



HAL
open science

Experimental and numerical study of transcritical Organic Rankine Cycles for low-grade heat conversion into electricity from various sources

Arnaud Landelle

► **To cite this version:**

Arnaud Landelle. Experimental and numerical study of transcritical Organic Rankine Cycles for low-grade heat conversion into electricity from various sources. Thermics [physics.class-ph]. INSA Lyon; CEA; ADEME, 2017. English. NNT: . tel-01731123v1

HAL Id: tel-01731123

<https://hal.science/tel-01731123v1>

Submitted on 13 Mar 2018 (v1), last revised 1 Feb 2019 (v2)

HAL is a multi-disciplinary open access archive for the deposit and dissemination of scientific research documents, whether they are published or not. The documents may come from teaching and research institutions in France or abroad, or from public or private research centers.

L'archive ouverte pluridisciplinaire **HAL**, est destinée au dépôt et à la diffusion de documents scientifiques de niveau recherche, publiés ou non, émanant des établissements d'enseignement et de recherche français ou étrangers, des laboratoires publics ou privés.



N°d'ordre NNT : 2017LYSEI090

THESE de DOCTORAT DE L'UNIVERSITE DE LYON
opérée au sein de
L'Institut National des Sciences Appliquées de Lyon

Ecole Doctorale N° 162
Mécanique, Énergétique, Génie Civil, Acoustique

Spécialité/ discipline de doctorat : Thermique Énergétique

Soutenue publiquement le 12/10/2017, par :

Arnaud LANDELLE

**Experimental and numerical study of
transcritical Organic Rankine Cycles for
low-grade heat conversion into
electricity from various sources**

Devant le jury composé de :

LEMORT, Vincent
GROSU, Lavinia
LANZETTA, François
REVELLIN, Rémi
TAUVERON, Nicolas
HABERSCHILL, Philippe

Professeur, Université de Liège
Maître de conférences, HDR, Université Paris Nanterre
Professeur, Université de Franche-Comté
Professeur, INSA-Lyon
Ingénieur de recherche, HDR, CEA
Maître de conférence, HDR, INSA-Lyon

Président
Rapporteur
Rapporteur
Directeur de thèse
Co-directeur de thèse
Examineur

Département FEDORA – INSA Lyon - Ecoles Doctorales – Quinquennal 2016-2020

SIGLE	ECOLE DOCTORALE	NOM ET COORDONNEES DU RESPONSABLE
CHIMIE	CHIMIE DE LYON http://www.edchimie-lyon.fr Sec : Renée EL MELHEM Bat Blaise Pascal 3 * étage secretariat@edchimie-lyon.fr Insa : R. GOURDON	M. Stéphane DANIELE Institut de Recherches sur la Catalyse et l'Environnement de Lyon IRCELYON-UMR 5256 Équipe CDFA 2 avenue Albert Einstein 69626 Villeurbanne cedex directeur@edchimie-lyon.fr
E.E.A.	ELECTRONIQUE, ELECTROTECHNIQUE, AUTOMATIQUE http://edcea.ec-lyon.fr Sec : M.C. HAVGOUDOUKIAN Ecole-Doctorale.eea@ec-lyon.fr	M. Gérard SCORLETTI Ecole Centrale de Lyon 36 avenue Guy de Collongue 69134 ECULLY Tél : 04.72.18 60.97 Fax : 04 78 43 37 17 Gerard.scorletti@ec-lyon.fr
E2M2	EVOLUTION, ECOSYSTEME, MICROBIOLOGIE, MODELISATION http://e2m2.universite-lyon.fr Sec : Sylvie ROBERJOT Bât Atrium - UCB Lyon 1 04.72.44.83.62 Insa : H. CHARLES secretariat.e2m2@univ-lyon1.fr	M. Fabrice CORDEY CNRS UMR 5276 Lab. de géologie de Lyon Université Claude Bernard Lyon 1 Bât Géode 2 rue Raphaël Dubois 69622 VILLEURBANNE Cédex Tél : 06.07.53.89.13 cordev@univ-lyon1.fr
EDISS	INTERDISCIPLINAIRE SCIENCES- SANTÉ http://www.ediss-lyon.fr Sec : Sylvie ROBERJOT Bât Atrium - UCB Lyon 1 04.72.44.83.62 Insa : M. LAGARDE secretariat.ediss@univ-lyon1.fr	Mme Emmanuelle CANET-SOULAS INSERM U1060, CarMeN lab, Univ. Lyon 1 Bâtiment IMBL 11 avenue Jean Capelle INSA de Lyon 696621 Villeurbanne Tél : 04.72.68.49.09 Fax : 04 72 68 49 16 Emmanuelle.canet@univ-lyon1.fr
INFOMATHS	INFORMATIQUE ET MATHÉMATIQUES http://infomaths.univ-lyon1.fr Sec : Renée EL MELHEM Bat Blaise Pascal, 3 * étage Tél : 04.72. 43. 80. 46 Fax : 04.72.43.16.87 infomaths@univ-lyon1.fr	M. Luca ZAMBONI Bâtiment Braconnier 43 Boulevard du 11 novembre 1918 69622 VILLEURBANNE Cedex Tél : 04 26 23 45 52 zamboni@maths.univ-lyon1.fr
Matériaux	MATERIAUX DE LYON http://ed34.universite-lyon.fr Sec : Marion COMBE Tél:04-72-43-71-70 –Fax : 87.12 Bat. Direction ed.materiaux@insa-lyon.fr	M. Jean-Yves BUFFIERE INSA de Lyon MATEIS Bâtiment Saint Exupéry 7 avenue Jean Capelle 69621 VILLEURBANNE Cedex Tél : 04.72.43 71.70 Fax 04 72 43 85 28 Ed.materiaux@insa-lyon.fr
MEGA	MECANIQUE, ENERGETIQUE, GENIE CIVIL, ACOUSTIQUE http://mega.universite-lyon.fr Sec : Marion COMBE Tél:04-72-43-71-70 –Fax : 87.12 Bat. Direction mega@insa-lyon.fr	M. Philippe BOISSE INSA de Lyon Laboratoire LAMCOS Bâtiment Jacquard 25 bis avenue Jean Capelle 69621 VILLEURBANNE Cedex Tél : 04.72 .43.71.70 Fax : 04 72 43 72 37 Philippe.boisse@insa-lyon.fr
ScSo	ScSo* http://recherche.univ-lyon2.fr/scso/ Sec : Viviane POLSINELLI Brigitte DUBOIS Insa : J.Y. TOUSSAINT Tél : 04 78 69 72 76 viviane.polsinelli@univ-lyon2.fr	M. Christian MONTES Université Lyon 2 86 rue Pasteur 69365 LYON Cedex 07 Christian.montes@univ-lyon2.fr

*ScSo : Histoire, Géographie, Aménagement, Urbanisme, Archéologie, Science politique, Sociologie, Anthropologie

Partenaires

Financier : Commissariat à l'Énergie Atomique et aux Énergies Alternatives



Thèse cofinancée par le CEA et réalisée au Laboratoire de Systèmes Thermiques et Thermodynamiques (LS2T), laboratoire du CEA-LITEN à Grenoble. Sous la responsabilité de S. Colasson et N. Tauveron.

Financier : Agence de l'Environnement et de la Maîtrise de l'Énergie

ADEME



Agence de l'Environnement
et de la Maîtrise de l'Énergie

Thèse cofinancée par l'ADEME et suivie par F. Streiff, Ingénieur efficacité énergétique en industrie.

Soutien scientifique : Centre d'Énergétique et de Thermique de Lyon (UMR 5008)



Thèse réalisée avec le soutien du CETHIL, laboratoire de recherche mixte : INSA de Lyon, CNRS et Université Claude Bernard Lyon 1. Sous la responsabilité de R. Revellin et P. Haberschill

Soutien : InnoEnergy PhD School



Thèse réalisée avec le soutien de l'InnoEnergy, dans le cadre de sa PhD School. Financier des mobilités à l'Université Agricole d'Athènes et à l'Université de Liège.

Observer,
Comprendre,
Agir.

Acknowledgments

Je commencerais par remercier mes directeurs de thèse. *Nicolas Tauveron*, pour ton soutien au quotidien et ta disponibilité sans faille. Merci de m'avoir laissé la liberté d'essayer, expérimenter, réussir et échouer, bref, mener un travail de recherche. Ce fût un sincère plaisir que de mener ce long travail doctoral sous ta tutelle. *Rémi Revellin*, pour la confiance que tu m'as accordée, ton expertise et tes remarques toujours pertinentes. J'aurais plaisir à poursuivre nos discussions sur le sens de l'entropie. *Philippe Haberschill*, pour son exigence et ses idées, toujours originales.

Je remercie également l'ensemble des membres du jury. *Lavinia Grosu* et *François Lanzetta* d'avoir accepté d'étudier et rapporter cette thèse de doctorat, avec enthousiasme. *Vincent Lemort*, d'avoir accepté d'examiner mes travaux et fait l'honneur de présider ce jury de thèse.

Il convient également de remercier les financeurs et soutiens de ces travaux de thèse. Le *Commissariat à l'Energie Atomique et aux Energies Alternatives* de Grenoble, ainsi que l'*Agence De l'Environnement et de la Maîtrise de l'Energie*, représenté en la personne de *Frédérique Streiff*.

Même si la thèse semble être une œuvre très individuelle, c'est en réalité un travail profondément collaboratif qui se construit et mûrit à mesure des échanges, discussions et réalisations. Ces travaux sont donc aussi l'œuvre d'une multitude de personnes qu'on ne pourrait tous citer, même si je souhaite m'y risquer.

Je remercie donc l'ensemble de mes collègues, techniciens, managers, ingénieurs du LS2T et plus généralement du CEA pour leur aide ponctuelle ou quotidienne. *Stéphane Colasson*, pour m'avoir accueilli dans son laboratoire et accordé sa confiance, *Nicolas Tauveron*, une seconde fois (qui n'est pas de trop), pour son soutien, *Jérôme Bentivoglio*, pour sa bonne humeur, ses coups de gueule et son maniement de la clé dynamo. Et bien d'autres qui m'ont apporté un petit ou grand coup de main : *Gilles, Amélie, Olivier, Franck, Lucas, Pierre, Geraud, Snoop, Tommy, Vincent, Quentin, Laura, Odin, Violette, Franck² ...*

Ayant eu le privilège de m'expatrier à plusieurs occasions, je souhaite remercier ici ceux qui m'ont accueilli en leur sein et ont accepté de partager leurs connaissances et leurs ressources.

I would like to thank very much the *Agricultural University of Athens* which hosted me during the summer 2015. Thanks to *Dimitris Manolakos* for welcoming me in his laboratory, a big thanks to *George Kosmadakis* who allowed me to perform my first experiments on a transcritical ORC and for his kindness, I really hope we will be able to work together once again. Thanks also to *Marija* from Genth and *Erika*. Σας ευχαριστώ, θα σας δούμε σύντομα.

Je remercie l'*Université de Liège* et le Laboratoire de Thermodynamique pour m'avoir accueilli à l'automne 2016 tantôt. Merci, une nouvelle fois, à *Vincent Lemort* pour son accueil chaleureux. Merci à *Adriano Desideri* de m'avoir initié à Dymola, pour le meilleur et pour le pire, merci à *Rémi Dickes* pour ta grande motivation et pour l'excellent modèle que tu as développé. Merci aussi à tous les autres membres du laboratoire, *Marco, Thomas, Ludo, Leonardo...*

J'en profite ici pour remercier *InnoEnergy* et *Isabelle Schuster* de m'avoir accepté au sein de la PhD School. Sans qui, je n'aurais pu rejoindre les équipes de recherche d'Athènes et de Liège. Et qui m'a également permis de rencontrer une multitude de doctorants avec qui j'ai eu plaisir à échanger et collaborer sur le développement des énergies dans l'Europe de demain : *Filip, Lucio, Clara, Ivan, Lisa, Trang, Rasha (#sister), Sandro, Mahendra, Mathilde, Anna, Rafael...*

Et puis il y a les soutiens du quotidien, à qui j'ai tenté, mais pas toujours su, expliquer la nature de mes travaux de recherches. Ceux que je connaissais et ceux que j'ai rencontré au cours de ces trois années, ceux que j'ai perdu de vue ou que j'ai retrouvé. Ceux que j'appellerais communément les amis, la famille, ou, devrais-je dire, *les familles*.

Ma famille : *Mathieu, Julie, mes parents*. La famille du 93 : *Elanie, Marion, Margaux, Martin, Olivier, Sarah, Alice, Grim*. La famille INP : *les DC, Renaud, Max, Mathieu, Alizée, Fab*. La famille EPUG : *Ben, Loic, Kévin, Noé, Coco, Thomas, Titi, Cam, Sam, Claire, Cha, Kév'* et ma chère et tendre *Fanny*.

Merci à vous,
Bisous Bisous !

Abstract

The Organic Rankine Cycle (ORC) is a technology used for low-grade thermal energy conversion into electricity. Transcritical ORC has been identified as a solution for efficient waste heat recovery. However, few experimental tests have been conducted to confirm the interest of transcritical ORC and investigate its operational behaviors.

The work presented focuses on the operation and the optimization of subcritical and transcritical Organic Rankine Cycles for low-grade heat conversion into electricity from various heat sources (solar, industrial waste heat). First, the thermodynamic framework of ORC technology is presented. Energetic and exergetic performance criteria, appropriate to each type of input source, are introduced and selected. The criteria are later applied to a database of ORC prototypes, in order to objectively analyze the state-of-the-art.

In a second step, the experimental and numerical tools, specifically developed or used in the present thesis, are presented. Three subcritical and transcritical ORC test benches (hosted by CEA and AUA) provided experimental data. Numerical models were developed under different environments: *Matlab* for steady-state modeling, data processing and energy/exergy analysis. The *Modelica/Dymola* environment, for system dynamics and transient operations.

Lastly, the different tools are exploited to investigate four different topics:

- The ORC pump operation is investigated, both under an energetic and volumetric standpoint, while semi-empirical models and correlations are exposed.
- Supercritical heat transfers are explored. Global and local heat transfer coefficients are estimated and analyzed under supercritical conditions, while literature correlations are introduced for comparison.
- Working fluid charge influence over the ORC performance and behavior is investigated. Optimal fluid charge is estimated under various operating conditions and mechanisms for charge active regulation are exposed.
- ORC system performances and behavior are discussed. Through both an energetic and exergetic standpoint, performances are compared with the state-of-the-art, while optimization opportunities are identified through an exergetic analysis.

Résumé

Le Cycle Organique de Rankine (abrégé ORC de l'anglais Organic Rankine Cycle) est une technologie permettant la conversion de chaleur basse température en électricité. L'ORC transcritique a été identifié comme une solution prometteuse pour la valorisation de la chaleur fatale. Cependant, peu d'installations expérimentales ont permis de confirmer ces performances.

Ce travail de thèse présente le fonctionnement et l'optimisation d'ORC sous-critique et transcritique pour la conversion de chaleur basse température en électricité à partir de différentes sources. Premièrement, les contextes thermodynamique et technologique de l'ORC sont présentés. Des critères de performance énergétiques et exergetiques sont définis et appliqués à une base de données d'installations expérimentales afin d'exposer l'état de l'art actuel des ORC.

Deuxièmement, les outils numériques et expérimentaux, spécifiquement développés ou utilisés pour ces travaux, sont présentés. Trois installations expérimentales d'ORC transcritique complet ou incomplet fournissent les données expérimentales. Différents modèles numériques sont utilisés : sous l'environnement *Matlab* pour la modélisation en permanent, l'analyse des données expérimentales et l'analyse énergétique/exergetique ; L'environnement *Modelica/Dymola* pour l'analyse des transitoires et de la dynamique du système.

Dans un troisième temps, ces différents outils sont utilisés pour étudier quatre différentes problématiques :

- Le fonctionnement de la pompe de circulation est étudié, d'un point de vue énergétique et volumétrique. Des modèles semi-empiriques et des corrélations de performance sont présentés.
- Les transferts thermiques en supercritique sont examinés, en local et en global. Les coefficients de transfert thermique sont comparés avec différentes corrélations de la littérature.
- L'influence de la charge de réfrigérant sur les performances et le comportement de l'ORC est analysée. La charge optimale est estimée pour différentes conditions de fonctionnement et des mécanismes de régulation de la charge sont présentés.
- Les performances énergétiques et exergetiques de l'ORC sont comparées avec la base de données. Une analyse exergetique du procédé a permis d'identifier des voies d'amélioration.

Résumé étendu

Le secteur de l'énergie traverse actuellement une profonde mutation. Le siècle à venir présente deux défis majeurs que ce secteur devra relever : fournir toujours plus de services et de puissance à une population mondiale croissante, tout en assurant la transition entre une industrie fortement émettrice de gaz à effet de serre à une industrie respectueuse du climat et de l'environnement. Pour relever ces deux défis, deux approches se combinent : produire une énergie sans CO₂ au travers des énergies renouvelables et, consommer moins d'énergie pour fournir les mêmes services, en améliorant l'efficacité des procédés.

Le cycle organique de Rankine (abrégié ORC de l'anglais Organic Rankine Cycle) est une technologie qui permet d'agir conjointement sur ces deux leviers d'amélioration. D'une part, en permettant la production d'énergie électrique propre à partir de sources renouvelables comme l'énergie solaire, géothermique ou provenant de la biomasse. D'autre part, en améliorant l'efficacité énergétique des procédés au travers de la récupération et de la valorisation des rejets thermiques, aussi appelé chaleur fatale, en électricité.

L'ORC est une technologie connue et utilisée depuis plusieurs siècles. Elle permet de transformer l'énergie thermique en énergie mécanique. Le principe est le même que la machine à vapeur de Rankine (voir Figure I-4). Un fluide de travail est pressurisé par la pompe et envoyé à l'évaporateur où il absorbe la chaleur en s'évaporant. Cette vapeur haute pression est détendue dans une machine de détente, qu'on nommera expandeur, en produisant un travail mécanique. Une fois détendue, la vapeur est ensuite refroidie et liquéfiée au condenseur avant d'être à nouveau pompée.

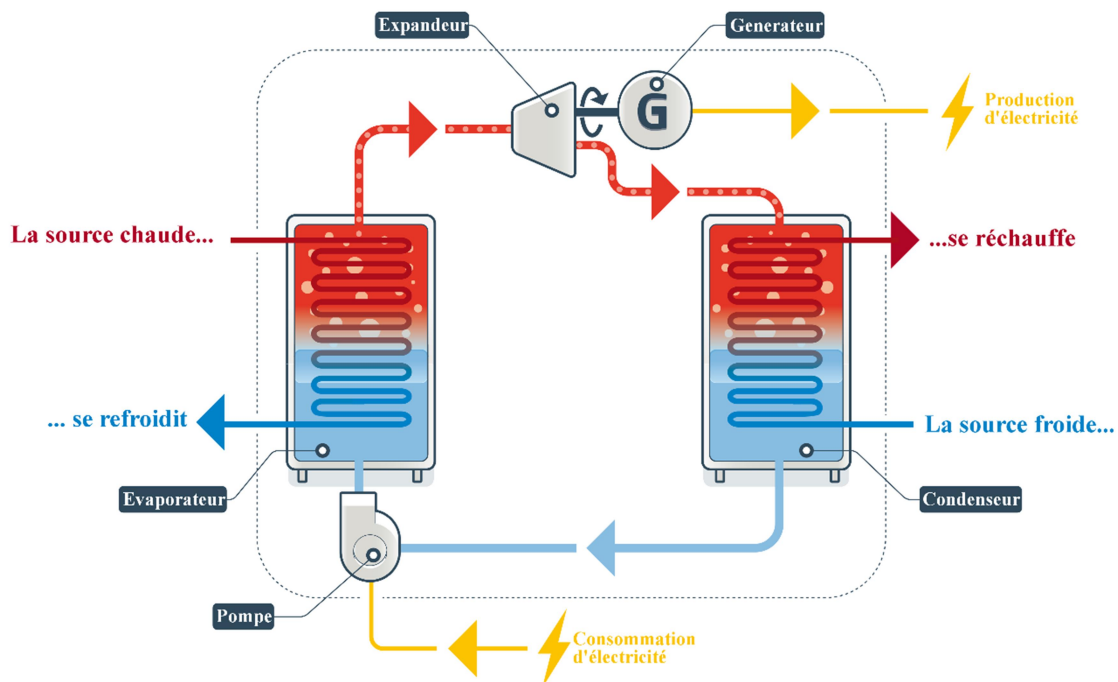


Figure I-4 : Fonctionnement du cycle organique de Rankine (ADEME 2015)

À la différence du cycle à vapeur de Rankine qui utilise de l'eau, le fluide utilisé dans l'ORC est dit « organique », c'est-à-dire comportant au moins un atome de carbone – À noter que l'usage exclue le CO_2 de ce groupe. Différents fluides organiques, avec diverses propriétés thermo-physiques, peuvent être utilisés afin d'optimiser les performances de l'ORC, selon la source chaude et froide. Ainsi, si le cycle à vapeur de Rankine devient difficilement utilisable pour des températures en dessous de 300 °C (Colonna et al. 2015), des machines ORC commerciales valorisent des sources de chaleur à partir de 60 °C . Actuellement, dans l'environnement des technologies de conversion de la chaleur en énergie mécanique, l'ORC se positionne dans une gamme de puissance allant de 1 kW à 10 MW , pour des sources de températures inférieures à 300 °C (voir Figure I-5).

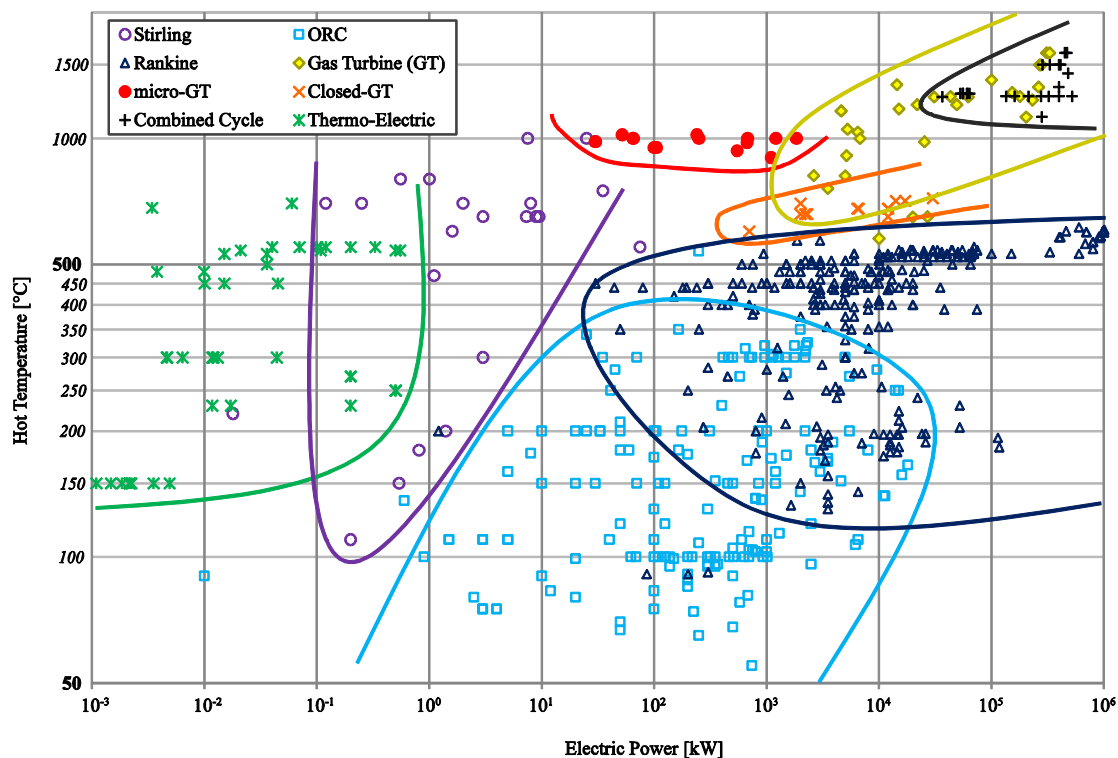


Figure I-5 : Carte des technologies de conversion de la chaleur en énergie mécanique (Tauveron, Colasson, and Gruss 2015)

Le concept de l'ORC fût breveté en 1826, mais il commença à réellement être utilisé un siècle plus tard, tout d'abord pour des applications de pompage à partir de l'énergie solaire, puis pour l'utilisation de l'énergie géothermique. Le choc pétrolier lança le concept de valorisation de la chaleur fatale des moteurs à combustion interne. Puis il fût utilisé dans certaines centrales biomasses fonctionnant en cogénération. Aujourd'hui, la valorisation de la chaleur fatale dans les procédés industriels est l'une des applications phare des ORC, représentant plus de 50 % des nouvelles installations.

L'ORC vise à s'étendre vers de nouvelles applications. D'une part les applications de faibles puissance et haute température telles que la micro-cogénération ou la valorisation de chaleur fatale pour moteurs automobiles. D'autre part les applications de grande capacité, mais avec de très faibles écarts de températures, en particulier l'énergie thermique des mers.

Pour répondre aux besoins des applications actuelles et futures, la recherche et le développement porte sur divers sujets : les machines de détente, composant critique de l'ORC sur lequel beaucoup de travaux portent ; les fluides de travail, que ce soit leur caractérisation, leur conception ou leur sélection ; l'architecture du cycle, notamment dans le cadre d'un fonctionnement en puissance variable ; la modélisation et la simulation de l'ORC, autant pour l'optimisation du design que pour la régulation des machines.

La présente thèse de doctorat est centrée sur l'utilisation des cycles organiques de Rankine pour la conversion de chaleur basse température et plus spécifiquement, le cas des cycles organiques de Rankine transcritiques. Le manuscrit s'articule en 8 chapitres :

- Le chapitre I présente le contexte de la thèse, ainsi que la technologie du cycle organique de Rankine
- Le chapitre II présente le cadre thermodynamique appliquée à l'ORC. Les définitions, les équations et les critères de performances utilisés y sont détaillés. Puis, l'état de l'art expérimental des ORC est présenté au travers d'une base de données libre compilée et analysée.
- Le chapitre III introduit les différents outils utilisés dans le cadre des travaux de thèse. Cela comprend les différentes installations expérimentales, la méthodologie de traitement des données ainsi que les outils de modélisation.
- Le chapitre IV se focalise spécifiquement sur la pompe de circulation de l'ORC, un composant peu étudié qui a pourtant un impact majeur sur les performances du cycle en transcritique. L'étude porte à la fois sur les performances énergétiques et volumétriques.
- Le chapitre V porte sur l'étude des transferts de chaleur, en particulier proche du point critique. Les coefficients de transfert thermique locaux et globaux sont étudiés, ainsi qu'une approche par efficacité.
- Le chapitre VI étudie l'influence de la charge de fluide sur le fonctionnement de l'ORC, à l'aide d'outils de simulation. Le potentiel d'optimisation de la charge de fluide comme vecteur d'amélioration des performances de l'ORC en fonctionnement variable est discuté.
- Le chapitre VII présente le fonctionnement et les performances générales de l'ORC. Avec dans un premier temps, un focus sur la machine de détente et équilibre avec la pompe de circulation. Puis une analyse des performances énergétiques et exégétiques des ORC étudiés, comparé avec l'état de l'art présent dans la littérature. Et finalement, une analyse exergetique des pertes ainsi qu'une analyse du comportement dynamique.
- Le chapitre VIII résume les principaux résultats et conclusions des travaux de thèse présentés, tout en exposant différentes opportunités pour de futurs travaux de recherche.

L'analyse de l'état de l'art nous a permis de mettre en évidence un manque d'uniformité et de standardisation dans la définition et la nomenclature de la puissance et des rendements appliqués à l'ORC. Ainsi, il convient de différencier la puissance isentropique, potentiel de puissance pour une machine idéale adiabatique et réversible ; la puissance dite adiabatique, correspondant à la différence d'enthalpie et supposant une machine adiabatique ; la puissance indiquée (ou hydraulique pour la pompe) correspondant au travail des forces de pression ; la puissance mécanique effective à l'arbre de la machine ainsi que la puissance électrique de la machine (voir Table II-1). Certaines de ces puissances sont équivalentes, à condition qu'un certain nombre d'hypothèses soient vérifiées. Ainsi la puissance adiabatique équivaut à la puissance mécanique à condition que l'expandeur soit une machine de détente dite « ouverte » et parfaitement adiabatique.

Table II-1 : Résumé des différents types de puissances présentes dans un ORC

Nom de la puissance	Equation
Puissance isentropique	$W_{is} = \dot{m} \cdot [h(T; P)_{in} - h(s_{in}; P_{out})]$
Puissance adiabatique	$W_{ad} = \dot{m} \cdot [h(T; P)_{in} - h(T; P)_{out}]$
Puissance indiquée (expandeur)	$W_{ind} = \dot{m} \cdot \int_{in}^{out} v \cdot dP$
Puissance hydraulique (pompe)	$W_{hy} = \dot{V} \cdot \Delta P$
Puissance mécanique	$W_{me} = \Gamma \cdot \dot{\Omega}$
Puissance électrique	$W_{el} = u \cdot i \cdot \cos(\varphi)$

Une fois les puissances discrétisées, il est possible de définir les rendements de machines, comme le rendement électrique et le rendement isentropique de l'expandeur :

$$\eta_{exp} = W_{el,exp} / W_{is,exp} \quad \text{Eq. II-1}$$

$$\eta_{is,exp} = W_{ad,exp} / W_{is,exp} \quad \text{Eq. II-2}$$

Pour la définition des critères de performance de l'ORC, il est nécessaire d'analyser l'environnement dans lequel vient se placer l'ORC et en particulier le type de source chaude utilisé. Celles-ci peuvent être divisées en deux catégories : les sources fermées et les sources ouvertes (Borsukiewicz-Gozdur 2013; Braimakis and Karellas 2017). Dans une source fermée, c'est une puissance thermique Q_{sup} qui est fournie à l'ORC. La température d'entrée de la source chaude (HF_{in}) dépend de sa sortie et du flux de chaleur. Les sources fermées incluent les applications de biomasse et solaire. Dans une source ouverte, c'est un flux de matière (Stream) qui est fourni, ce flux présente un certain débit et une certaine température d'entrée indépendante de la température de rejet de ce flux (HF_{out}). Les sources ouvertes incluent la géothermie et la valorisation de chaleur fatale (voir Figure II-4).

Alors que dans les sources fermées la puissance du fluide chaud en sortie d'évaporateur (HF_{out}) est récupérée, dans les sources ouvertes, cette puissance est rejetée à l'ambient et définitivement perdue. Ainsi, pour les sources fermées, il est essentiel d'augmenter le débit chaud pour avoir un profil de température chaude quasi-isotherme afin de s'approcher du cycle de Carnot. À l'inverse, pour les sources ouvertes, le cycle idéal est un cycle de Lorentz ou triangulaire pour lequel la température de sortie de source chaude approche la température ambiante.

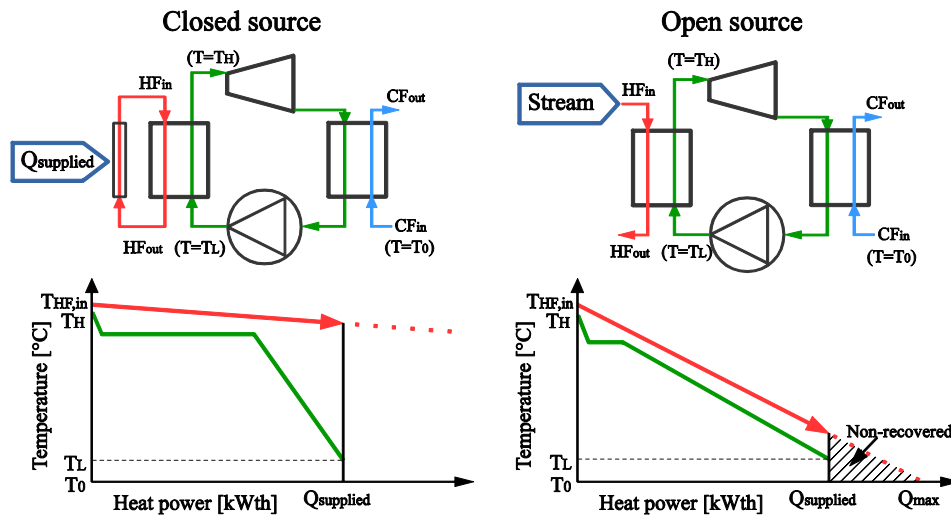


Figure II-4 : Schéma et diagramme de puissance-température des sources ouvertes et fermées

Il est donc nécessaire de définir des critères de performance adaptés à chaque type de source. On propose d'utiliser à la fois des critères de performance énergétique et exergetique (Table II-2). Le critère exergetique permettant de prendre en compte la qualité de la source chaude, au travers de sa différence de température avec l'ambient.

Table II-2 : Type puissance fournie à l'ORC selon le type de source chaude

	Énergie	Exergie
Source fermée	$Q_{sup} = \dot{m}_{hf} \cdot c_{p,hf} \cdot (T_{HF,in} - T_{HF,out})$ $\eta_{th} = W_{ORC}/Q_{sup}$: rendement énergétique	$E_{sup} = \dot{m}_{hf} \cdot (e_{HF,in} - e_{HF,out})$ $\epsilon_{ORC} = W_{ORC}/E_{sup}$: rendement exergetique
Source ouverte	$Q_{max} = \dot{m}_{hf} \cdot c_{p,hf} \cdot (T_{HF,in} - T_0)$ $\eta_{rec} = W_{ORC}/Q_{max}$: rendement de récupération	$E_{max} = \dot{m}_{hf} \cdot (e_{HF,in} - e_{HF}(T = T_0))$ $\epsilon_{rec} = W_{ORC}/E_{max}$: rendement exergetique de récupération

Le rendement énergétique est le plus communément utilisé pour définir les performances des machines de conversion d'énergie thermique en énergie électrique. On utilisera également les deux rendements exergetiques pour analyser les performances des ORC. Il convient de noter que dans un cas idéal de source chaude isotherme, le rendement exergetique de source fermée équivaut à la fraction de Carnot :

$$\lim_{T_{HF,out} \rightarrow T_{HF,in}} \left(\frac{W_{ORC}}{E_{sup}} \right) = \frac{W_{ORC}}{Q_{sup}(1 - T_0/T_{HF,in})} = \frac{\eta_{th}}{\eta_{Carnot}} = \eta_{II} \quad \text{Eq. II-12}$$

Ces critères de performance sont par la suite appliqués à une base de données d'installations ORC expérimentales. Cette base de données, mise en libre accès et développée dans le cadre de ces travaux de thèse, agrège les données de plus de 100 installations d'ORC (Figure II-7). Elle comporte des informations à la fois qualitatives et quantitatives sur l'ORC, ses composants et son environnement.

Cette base de données permet d'avoir une vue d'ensemble des recherches passées et actuelles sur les ORC. On constate par exemple une augmentation des prototypes utilisant des fluides de 4^{ème} génération (HFO) ou des mélanges zéotropiques de fluide. On peut également identifier la gamme d'utilisation de chaque technologie d'expandeur : les turbines étant utilisées pour une large gamme de rapports de pression et de puissance, mais avec des vitesses de rotation très élevées. Alors que les technologies spiro-orbitale (scroll),

rotative et à piston se placent dans une gamme de puissance similaire, mais pour différents rapports de pression.

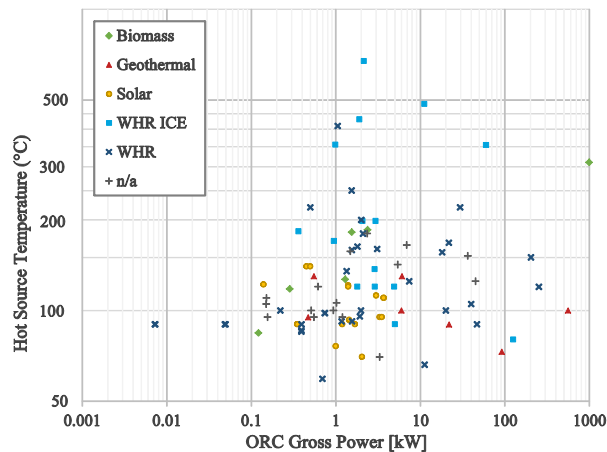


Figure II-7 : Carte des références d'ORC de la base de donnée expérimentale

D'un point de vue des performances, on constate une forte corrélation entre la puissance de l'installation ORC et le rendement, à la fois de l'expandeur, de la pompe et donc in-fine de l'ORC. La figure ci-dessous montre le rendement énergétique brut (η_{th}) et la fraction de Carnot brut (η_{II}) des références de la base de données, combinée avec les références commerciales de (Tauveron, Colasson, and Gruss 2015). Le rendement brut de l'ORC (ainsi que le rendement net) est très lié à la gamme de puissance de ce dernier. En observant la fraction de Carnot, on constate cependant une asymptote autour de 40 % et peu de référence au-delà du $\frac{1}{2}$ Carnot. Cette asymptote, qui semble être un maximum technologique pour l'ORC, a aujourd'hui un point d'inflexion situé aux environ de 10-50 kWe qu'on pourrait analyser comme la limite de maturité actuelle pour les ORC.

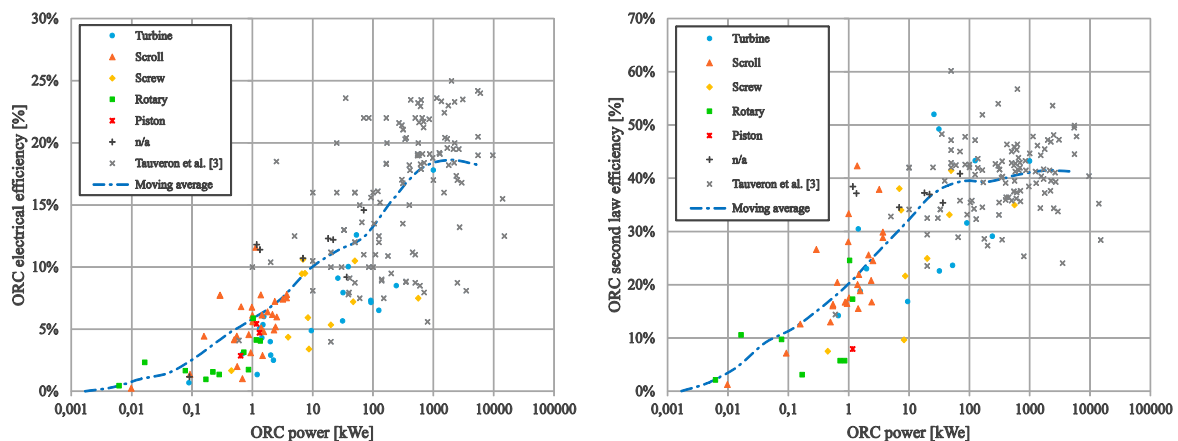


Figure II-17 & Figure II-19 : Rendement énergétique & fraction de Carnot brut en fonction de la puissance de l'ORC

En analysant à l'aide d'indicateur statistique l'influence de divers paramètres sur le rendement énergétique et la fraction de Carnot brut des ORC, on constate que le principal facteur d'influence est bien la puissance de l'ORC, ainsi que le rendement de la machine de détente. La température de la source chaude influence également, dans une moindre proportion, le rendement énergétique alors que par construction, il n'influence pas la fraction de Carnot.

Afin d'étudier les diverses problématiques citées en introduction, différents outils sont utilisés. Ces travaux de thèse s'appuient sur les données de 4 installations expérimentales :

- **CORSERE** : un banc d'ORC transcritique, hébergé au CEA-Grenoble, utilisant du R134a jusqu'à 50 bar et 150 °C et dédié à l'étude de la récupération de chaleur fatale. Ce banc, au cœur du projet de thèse, peut être utilisé en configuration classique ou en régénération. Ses données et caractéristiques sont utilisées pour la plupart des problématiques étudiées.
- **CPV-Rankine** : un banc d'ORC transcritique, hébergé à l'Université Agricole d'Athènes et conçu dans le cadre d'un projet européen FP7. Il utilise du R404a jusqu'à 45 bar et 100 °C, alimenté en chaleur par des collecteurs solaires à concentration. Utilisé pour l'étude du fonctionnement et des performances des ORC en transcritique.
- **SURCOUF** : un banc fluide, hébergé au CEA-Grenoble, utilisant du R134a et dédié à l'étude des transferts de chaleur grâce à une section d'essais spécifique. L'installation, qui ne dispose pas de machine de détente, est utilisée pour l'analyse comportementale d'une boucle hermétique, l'étude de la pompe de circulation et des transferts thermiques proches du point critique.
- **Solammor** : une machine à absorption utilisant un mélange eau-ammoniac et uniquement utilisée pour l'étude des pompes volumétriques.

Les données expérimentales sont post-traitées à l'aide de divers outils numériques, principalement *Matlab* et *Scilab*. Des critères sont définis pour détecter et compiler automatiquement les transitoires et les points statiques. Puis, divers paramètres complémentaires sont calculés, comme les enthalpies des différents fluides. Les propriétés thermo-physiques des fluides sont évaluées à l'aide de la librairie *CoolProp* (Bell et al. 2014).

Afin d'améliorer la précision des mesures, une méthode de réconciliation des données est appliquée aux points statiques. Cette méthode utilise la redondance des mesures et permet de faire varier les valeurs mesurées, dans la gamme d'incertitude du capteur correspondant, pour répondre à un certain nombre d'hypothèses et limites physiques. On impose notamment que les échangeurs soient parfaitement isolés de l'extérieur, qu'ils aient un pincement supérieur ou égal à zéro et que la pression soit monotonement décroissante entre la sortie de pompe et l'entrée de pompe.

D'autres outils numériques sont également utilisés pour simuler et modéliser le fonctionnement et les performances d'un ORC. Le logiciel *Engineering Equation Solver* permet des calculs de modèle d'ORC simplifiés, en sous et supercritique, et de résoudre des problèmes d'optimisation. Le logiciel *Dymola*, par l'intermédiaire de la librairie *ThermoCycle* (Sylvain Quoilin et al. 2014) du langage *Modelica* permet quant à lui la simulation dynamique du fonctionnement de l'ORC. Un modèle du banc d'essais CORSERE fut construit et partiellement validé.

En outre, la librairie *ORCmKit* (Dickes et al. 2017; Ziviani et al. 2016), utilisée sous *Matlab* permet la modélisation d'un ORC en régime statique. Cette librairie permet notamment de modéliser le taux de vide dans les échangeurs et donc de calculer ou

d'imposer la charge de fluide dans l'ORC. Un modèle du banc d'essais CORSERE a été construit à des fins de validation, puis une version simplifiée du banc d'essais et du modèle a été utilisée à des fins d'analyse comportementale pour des charges de fluide variables.

La première problématique étudiée porte sur le fonctionnement des pompes volumétriques à membrane pour les ORC. Dans un premier temps, l'étude se focalise sur l'analyse des performances énergétiques. Un modèle semi-empirique est développé, il discrétise les pertes au variateur et dans le moteur électrique des pertes dues à la pompe seule. Le modèle est initialement développé à l'aide des données du banc SURCOUF, il est ensuite affiné et plus largement validé à l'aide des autres bancs expérimentaux que sont le banc CPV-Rankine, CORSERE et Solammor.

Table VI-1 : Modèle énergétique de pompe

	Paramètres			Résultats par banc				
	Signe	Unité	Définition	Origine	SURCOUF	CPV-Rankine	CORSERE	Solammor
$W_{me} = K_2 \cdot \Omega_{pp} + K_3 \cdot V \cdot \Delta P$								
Puissance de pompe	Ω_{pp}	rpm	Vitesse de pompe	Entrée				
	ΔP	Pa	Différence de pression	Entrée				
	V	m ³ /s	Débit volumétrique	Entrée				
	K_2	W/rpm	Coefficient de friction	Constructeur	0.0711	0.1777	0.5922	0.0711
	K_3	-	Coefficient d'efficacité	Constructeur	1.174	1.174	1.174	1.174
$W_{el} = W_{me} + K_1 + W_{mot,n} \cdot (1/\eta_{mot,n} - 1) \cdot [k \cdot W_{me}^2 / W_{mot,n}^2 + (1-k) \cdot \Omega_{mot}^2 / \Omega_{mot,n}^2]$								
Puissance du moteur et variateur	W_{me}	W	Puissance mécanique	Entrée				
	Ω_{mot}	rpm	Vitesse de moteur	Entrée				
	$W_{mot,n}$	W	Puissance moteur nominale	Constructeur	1800	3000	5500	250
	$\Omega_{mot,n}$	rpm	Vitesse moteur nominale	Constructeur	1438	960	1447	1425
	$\eta_{mot,n}$	-	Rendement moteur nominal	Constructeur	0.794	0.864	0.856	0.694
	K_1	W	Coef. de pertes au variateur	Empirique	219*	904*	1555**	67.7*
	α	-	Répartition des pertes moteur	Empirique ou default (0.7)	0.78*	0.7	0.7	0.59*
Ecart-type entre le modèle et la valeur expérimentale					20.3 W	51.9 W	71.7 W	11.2 W

* : valeur empiriques

L'impact des performances de la pompe sur le design et les performances de l'ORC ont ensuite été étudiées. On constate notamment, une légère sous-estimation de la puissance d'évaporation optimale entre un modèle utilisant une efficacité de pompe constante et le modèle semi-empirique présenté.

Le modèle permet aussi d'analyser la répartition des pertes entre les différentes parties du système de pompage. Plus particulièrement, on constate que les performances de la pompe seule sont globalement bonnes et en adéquation avec les données du constructeur. En revanche, les pertes électromécaniques dues au variateur et au moteur peuvent

substantiellement grever les performances globales de la pompe. Plus particulièrement, le surdimensionnement du groupe électromécanique (variateur et pompe) entraîne un fonctionnement de celui-ci loin de son régime nominal et donc avec des performances fortement dégradées. Un dimensionnement approprié, sans marge excessive, permet de limiter la dégradation des performances.

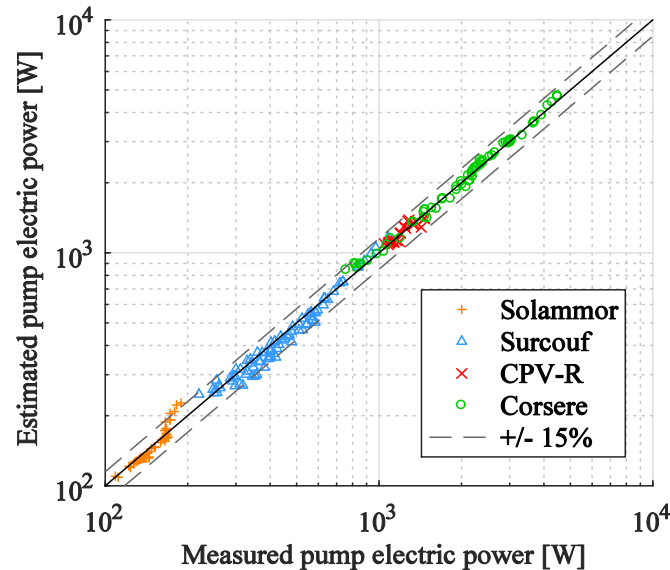


Figure IV-2 : Validation du modèle de pompe – puissance mesurée vs puissance estimée

Dans un second temps, l'étude des pompes d'ORC se focalise sur les performances volumétriques de celles-ci. Les pompes volumétriques à membre sont réputées pour avoir de bonnes performances volumétriques. Cependant, différents facteurs peuvent influencer ces performances. Un modèle volumétrique semi-empirique, développé à partir des éléments de la littérature, est proposé, il prend en compte à la fois la compressibilité isentropique du fluide (β_s) ainsi que les pertes dues aux fuites.

$$\eta_{vol} = \frac{\dot{V}}{\Omega \cdot V_{stroke}} = 1 - \Delta P \cdot \beta_s \left(1 + \frac{V_{dead}}{V_{stroke}} \right) - A \frac{\Delta P}{\mu \cdot \Omega \cdot V_{stroke}} \quad \text{Eq. IV-9}$$

De fait, le R134a possédant une compressibilité 10 fois supérieure à celle de l'eau, les performances volumétriques observées sur le banc SURCOUF sont inférieures à celles fournies par le constructeur.

Un autre élément peut substantiellement réduire les performances volumétriques de la pompe en fonction des conditions de fonctionnement : la cavitation. La cavitation d'une pompe intervient lorsque le fluide en entrée de pompe se trouve dans des conditions trop proches de sa saturation. Pour évaluer la marge à la saturation, on utilise communément le NPSH qui est la différence entre la pression en entrée et la pression de saturation pour la température d'entrée. Pour une pompe volumétrique, le NPSH requis est défini pour une réduction de 3 % du débit, on en a donc déduit un facteur correctif du rendement volumétrique proche de la limite de cavitation :

$$\eta_{vol} = \eta_{vol,nominal} \cdot \left(1 - 0.03 \frac{NPSH_{meas}}{NPSH_{req}} \right) \quad \text{Eq. IV-13}$$

Il est important de noter que les performances de l'ORC diminuent quand cette marge à la cavitation augmente, plus particulièrement pour les applications utilisant des sources à basse température. Il est donc nécessaire de trouver le bon équilibre de marge à la cavitation et de choisir des pompes ayant la plus faible marge à la cavitation requise.

La seconde problématique étudiée porte sur les transferts de chaleur proche du point critique. Dans un premier temps, le cas spécifique de la chauffe dans un tube lisse descendant est étudié. Des essais sont effectués avec un fluide largement sous-refroidi en entrée de section d'essais, puis avec une température d'entrée proche de la température critique, avec une pression légèrement supérieure à la pression critique.

En comparaison avec les transferts de chaleur en liquide, le coefficient d'échange thermique est largement amélioré proche du point critique, il semble cependant que celui-ci passe par un maximum. Ce maximum, déjà observé dans la littérature, se trouve cependant à des températures d'écoulement relativement éloignées de la température pseudo-critique, contrairement aux observations de la littérature. L'influence de divers paramètres comme la température d'entrée, le flux de chaleur, la vitesse massique ou la pression du fluide sont également étudiés.

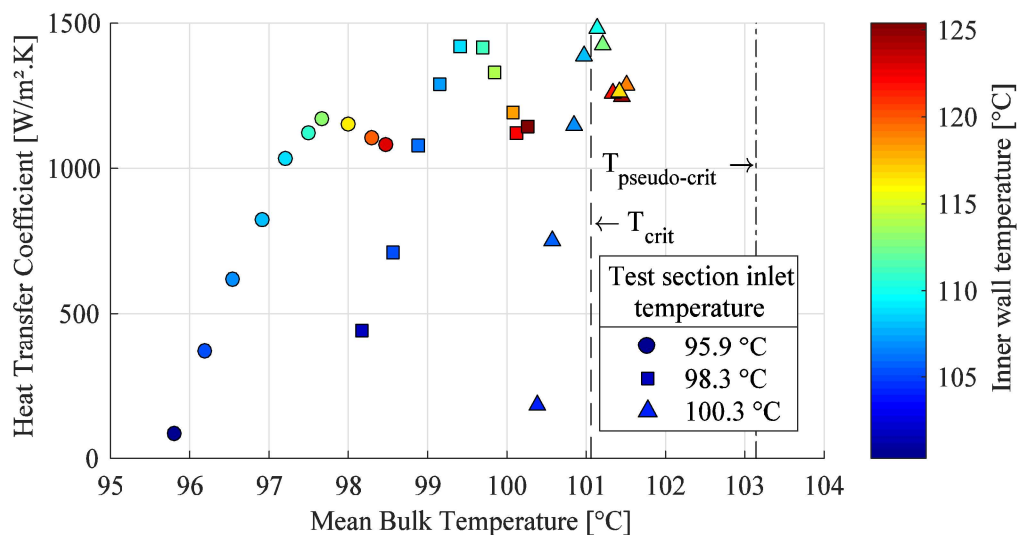


Figure V-4 : Transferts de chaleur proche du point critique

Les coefficients d'échange obtenus sont comparés avec les corrélations de la littérature données pour des fluides sous-critiques ou supercritiques, au travers du nombre de Nusselt. La plupart des corrélations semblent sous-estimer le coefficient de transfert thermique réel. Seule la corrélation de (Liao and Zhao 2002), pour les écoulements de CO_2 supercritique descendants, fournit des valeurs du même ordre même si on constate une forte dispersion par rapport aux valeurs expérimentales.

Certaines corrélations de la littérature sont adaptées au cas étudié en modifiant certains des coefficients. Les corrélations développées ont la particularité de posséder des exposants négatifs pour les paramètres faisant intervenir la différence de densité entre l'écoulement et la paroi, montrant que cette différence de densité tend à améliorer les coefficients d'échange.

De fait, il semble que l'écoulement et le transfert de chaleur étudiée remplissent les critères d'un échange en convection mixte opposée. Les données expérimentales sont donc comparées avec deux corrélations de la littérature développées pour ce cas spécifique (Fewster 1976; A. Bruch, Bontemps, and Colasson 2009).

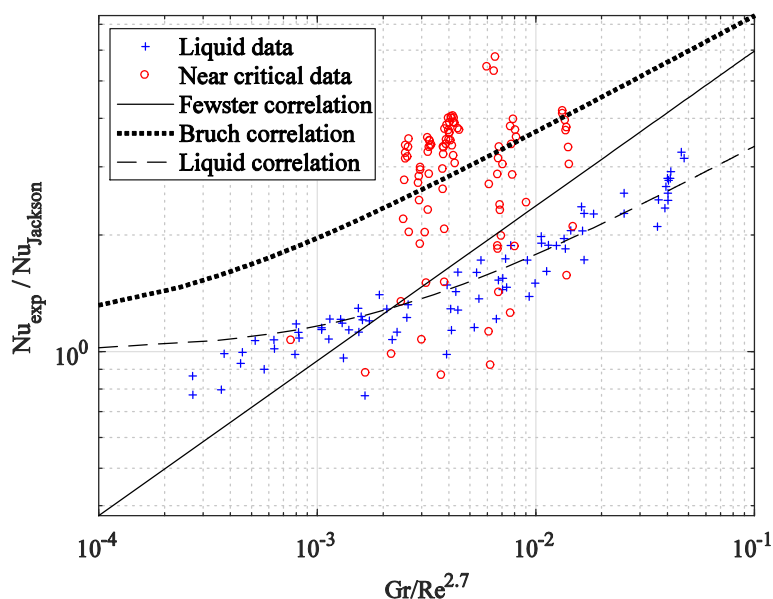


Figure V-9 : Corrélations en convection mixte

Il convient de noter que les transferts de chaleur autour du point critique sont encore mal compris (Huang et al. 2016). De plus, en raison des brusques variations de propriétés thermo-physiques, les incertitudes sont relativement grandes.

La troisième problématique concerne la charge de fluide de travail insérée dans la machine ORC. La plupart des installations ORC se doivent d'être parfaitement hermétiques. En effet, la majorité des fluides de travail présentent un risque environnemental, humain ou économique en cas de fuite. Ainsi, tout comme les pompes à chaleur ou les machines frigorifiques ayant un circuit hermétique, la densité moyenne dans l'ensemble de la machine est nécessairement constante, alors que ces machines présentent des niveaux de pression et de température très différents et variables en leur sein.

La charge de fluide est un sujet largement étudié pour les pompes à chaleur, l'industrie cherchant d'une part à minimiser la charge de fluide et d'autre part à maximiser les performances (Poggi et al. 2008). Pourtant, c'est une problématique peu étudiée pour les ORC. Seuls quelques travaux expérimentaux ont montré l'influence de la charge sur le comportement et les performances de l'ORC (Xu, Xi, and He 2013; T. Li et al. 2015).

Pour cette étude, l'effet de la charge de fluide est analysé grâce à un modèle du banc CORSERE simplifié (Figure VI-1), en utilisant la librairie *ORCmKit*. Les caractéristiques des composants sont gardées identiques à celles du modèle complet préalablement validé. Dans un premier temps, le modèle fonctionne à charge imposée. Celle-ci varie de 12 à 20 kg, tous les autres paramètres : source chaude et froide, vitesse de pompe et d'expandeur sont maintenues constantes.

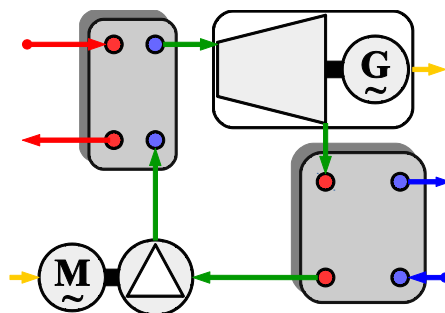


Figure VI-1 : Schéma simplifié du banc CORSERE modélisé

La variation de charge à un faible impact sur la zone de haute pression de l'ORC, la surchauffe et la pression d'évaporation reste quasi-constantes. En revanche, on constate un effet drastique sur la pression de condensation et le sous-refroidissement qui augmentent avec la charge de fluide. De cette augmentation du sous-refroidissement résulte une baisse des performances globales de l'ORC (Figure VI-2).

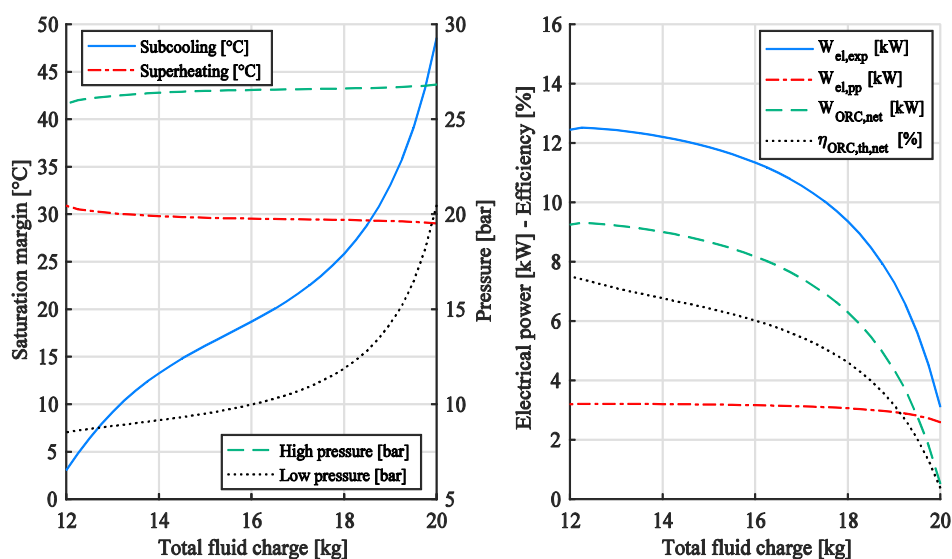


Figure VI-2 : Variations des principaux paramètres de l'ORC avec la charge de fluide

De fait, la grande majorité de la charge ajoutée dans l'installation vient se placer dans le condenseur (Figure VI-4). À très faible charge (12 kg), le condenseur manque de fluide, le pincement est situé au point de vapeur saturée. Seule une faible fraction du volume du condenseur est occupée par la phase liquide, donc une faible surface de transfert thermique dédiée au sous-refroidissement et une température de sortie plus élevée.

À charge moyenne (16 kg), le volume de condenseur occupé par chaque phase est équilibré, le fluide est correctement sous-refroidi et la pression n'est pas excessive. À l'inverse, à forte charge (20 kg), le condenseur est très largement noyé par la phase liquide et la phase vapeur s'en retrouve comprimée, ce qui fait augmenter la basse pression du cycle. Le pincement, qui tend vers zéro, se situe en sortie du fluide de travail.

La vitesse de rotation de l'expandeur n'a que peu d'influence sur le comportement de l'ORC lorsque la charge de fluide varie, la basse pression et le sous-refroidissement augmentent légèrement avec la vitesse de rotation. En revanche, l'ORC devient plus sensible à la variation de charge fluide à mesure que la vitesse de pompe et le débit de fluide augmente.

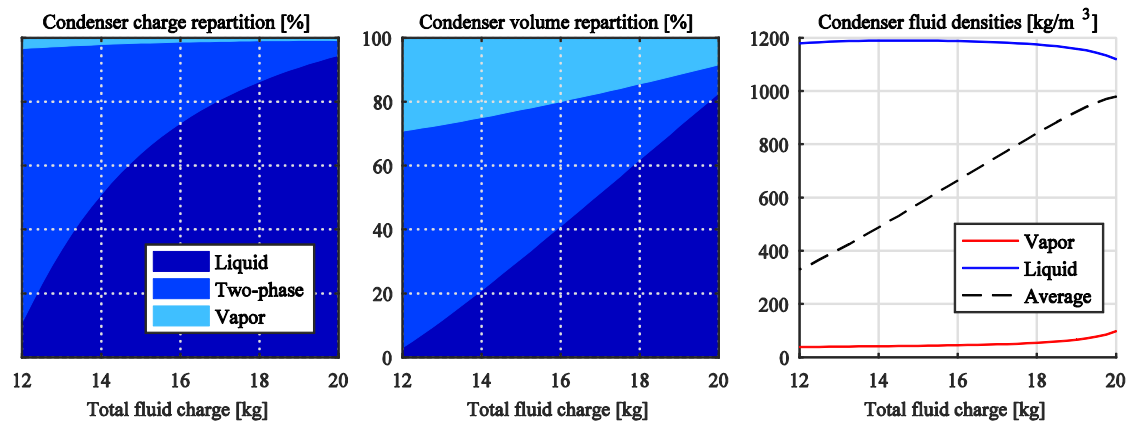


Figure VI-4 : Répartition massique et volumique de chaque phase au condenseur

La charge de fluide, au travers de son influence sur la basse pression et le sous-refroidissement, semble être un paramètre essentiel de l'optimisation des performances de l'ORC. Dans la suite de l'étude, on fixe un sous-refroidissement optimal de 10 °C, valeur permettant un fonctionnement sans cavitation de la pompe, sans pour autant dégrader les performances théoriques de l'ORC. La charge de fluide optimale est ensuite calculée pour diverses conditions de fonctionnement (Figure VI-15).

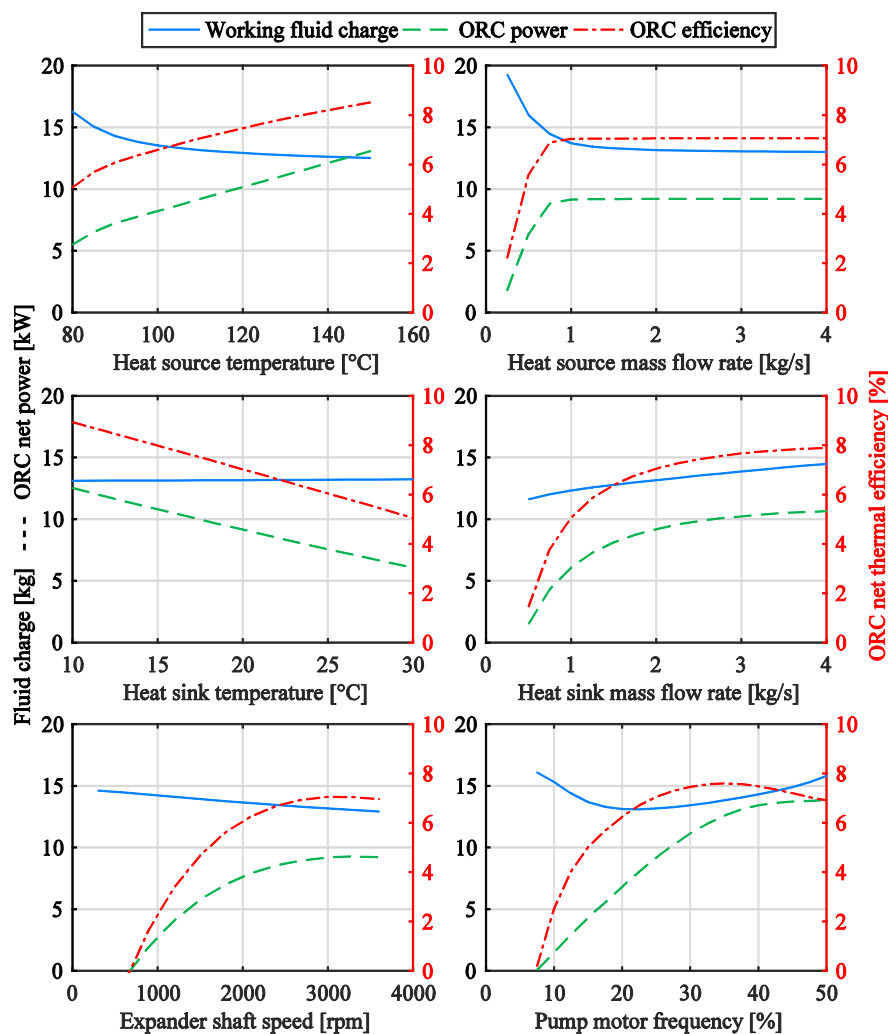


Figure VI-15 : Variation de la charge optimale de fluide en fonction de divers paramètres de l'ORC

L'augmentation du débit ou de la température de source chaude permet de réduire la charge de fluide optimale, par l'augmentation de la chauffe et donc la baisse de la densité moyenne à l'évaporateur. En revanche, la température de la source froide à une influence minimale, alors que l'augmentation du débit de source froide fait légèrement augmenter la charge optimale en augmentant la densité moyenne au condenseur.

L'augmentation de la vitesse d'expandeur, en réduisant la haute pression et donc la densité de vapeur haute pression, permet de diminuer la charge optimale. L'influence de la vitesse de pompe et donc du débit est plus complexe. À faible débit de fluide, la charge optimale est élevée, car le fluide au condenseur est rapidement refroidi donc très dense. Tandis qu'à fort débit, la puissance de chauffe n'est plus suffisante pour surchauffer le fluide en sortie d'évaporateur, la densité est élevée dans la zone haute pression et en entrée condenseur.

Tout comme la vitesse de pompe et d'expandeur, le contrôle de la charge de fluide devrait permettre de maximiser les performances des machines ORC en fonctionnement variable. Il convient cependant de noter que cette analyse et les effets observés dépendent fortement du design de l'ORC et des conditions de référence.

La dernière problématique porte sur le comportement et les performances globales de l'ORC, en sous-critique et en supercritique. La machine de détente étant un composant critique influençant les performances de l'ORC, il convient de commencer par son étude.

Dans le banc CORSERE et le banc CPV-Rankine, la machine de détente est un compresseur spiro-orbital commercial, modifié pour fonctionner en détente. Plusieurs éléments ont dû être modifiés et adaptés pour permettre un fonctionnement stable de ce composant. Ces machines étant des expandeurs volumétriques, il est important de faire correspondre le rapport de pression de l'ORC avec le rapport de volume de l'expandeur, imposé par sa géométrie. On constate également qu'à faible vitesse de rotation, les performances de l'expandeur sont fortement dégradées (Figure VII-6). Cette baisse de performance semble due à l'augmentation des fuites internes à très faible vitesse de rotation.

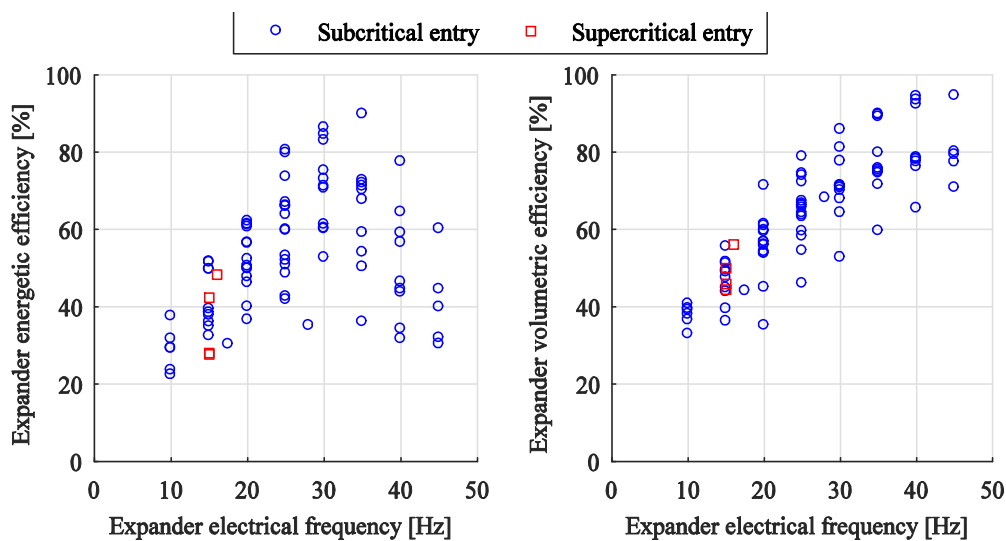


Figure VII-6 : Performances de l'expandeur du banc CPV-Rankine

Lors des essais sur les deux bancs, il s'est révélé complexe d'atteindre des pressions supercritiques tout en maintenant la pompe et l'expandeur à des vitesses de rotation proche de leurs vitesses nominales, afin de maximiser leur efficacité. Ces deux composants étant des machines volumétriques, il est important de bien faire correspondre leurs caractéristiques respectives lors du design de l'ORC.

En supposant un fluide toujours sous-refroidi en entrée de pompe, il est possible d'établir des cartes d'équilibrage des débits entre ces deux machines, pour diverses conditions de fonctionnement. Ainsi, pour le banc CORSERE (Figure VII-11), on constate qu'à vitesse nominale des deux composants (50 Hz), il faut maintenir la température d'entrée turbine entre 120 et 140 °C pour rester au-dessus de la pression critique et en dessous de la pression limite de l'ORC (50 bar)

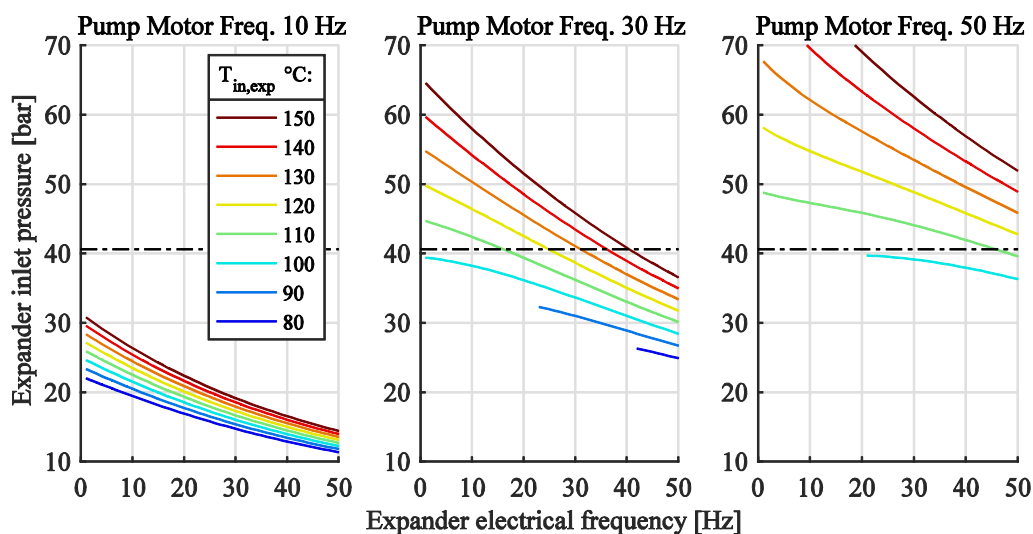


Figure VII-6 : Point d'équilibre des débits sur le banc CORSERE

Par la suite, on peut analyser les performances globales de l'ORC. Le banc CORSERE a atteint une production brute maximale de 6 kWe, pour un rendement énergétique net de 1,0 %, soit 4,24 % de fraction de Carnot et, un rendement exergetique de récupération de 1,81 %. Ces faibles performances sont pour partie due au fonctionnement en régime partiel et pour partie due à la forte consommation énergétique de la pompe.

Le banc CPV-Rankine a quant à lui produit jusqu'à 3,3 kWe brut, soit un rendement énergétique net de 4,2 % et une fraction de Carnot de 20 %. Les points transcritiques présentent des performances moindres en raison de la faible vitesse de rotation de l'expandeur nécessaires pour atteindre la pression critique (Figure VII-15).

Grâce à la base de données préalablement compilée, il est possible de comparer les performances brutes de ces deux installations avec d'autres installations expérimentales (Figure VII-18). Le banc CORSERE, dédié à la récupération de chaleur fatale, se place seulement en 84/100 et 71/100 pour respectivement le rendement énergétique et la fraction de Carnot. En revanche, il est dans le 1^{er} tiers en termes de rendement exergetique de récupération. À l'inverse, le banc CPV-Rankine, dédié au solaire à concentration, se place seulement 92/100 en rendement exergetique de récupération mais respectivement dans le 1^{er} quart et le 1^{er} cinquième pour le rendement énergétique et la fraction de Carnot.

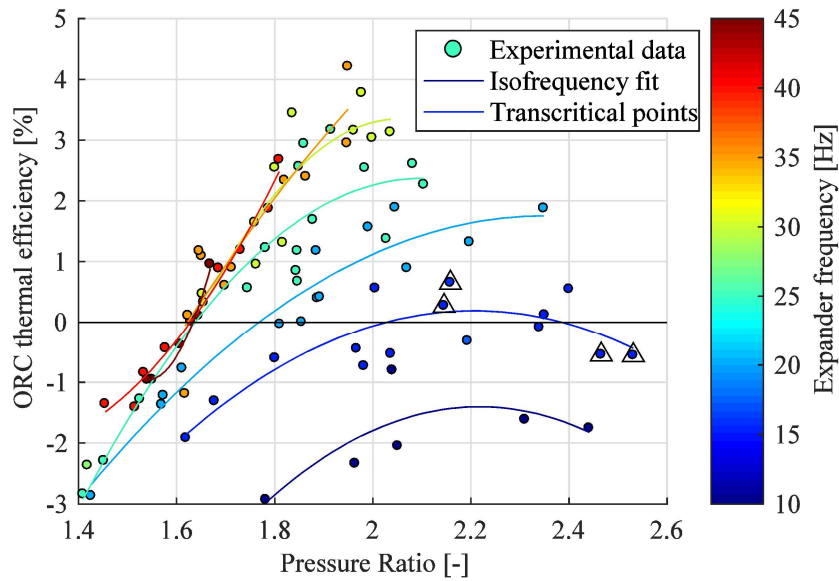


Figure VII-15 : Rendement énergétique du banc CPV-Rankine

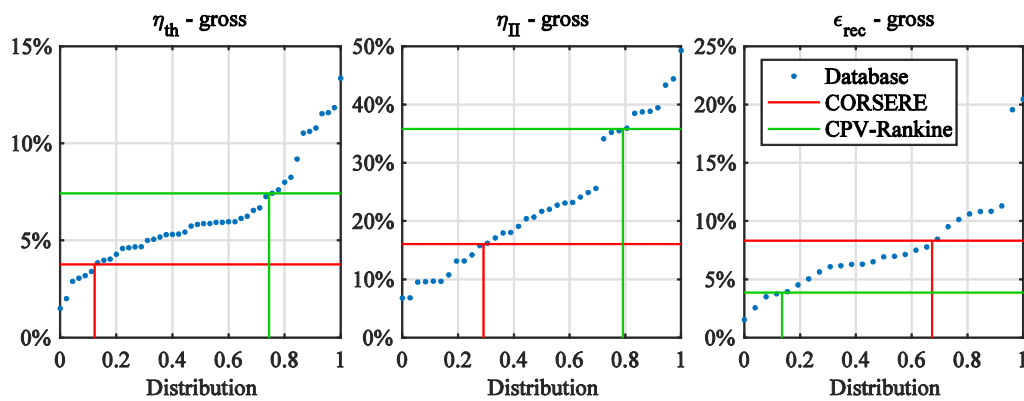


Figure VII-18 : Comparaison des bancs ORC étudiés avec l'état de l'art

L'analyse exergetique des pertes permet ensuite d'identifier, pour chaque machine ORC, les potentiels d'amélioration de l'installation. On note ainsi, qu'au point de rendement maximal du banc CORSERE, la perte maximale d'exergie se trouve au condenseur (Figure VII-19). Avec d'une part, l'exergie détruite lors du transfert thermique (7,3 kW) et d'autre part l'exergie dissipée par la source froide (7,4 kW). Ces pertes exergetiques peuvent être réduites en optimisant la pression de condensation du fluide et le débit de la source froide.

Vient ensuite l'évaporateur, qui est le premier composant à détruire l'exergie initialement apportée par la source chaude. Le transfert thermique est responsable de 6,1 kW de destruction d'exergie. On trouve ensuite la pompe et l'expandeur qui sont respectivement responsables de 2,4 et 1,9 kW d'exergie. Pourtant, la pompe a une efficacité exergetique (35 %) bien inférieure à celle de l'expandeur (92 %).

Pour finir, une quantité non négligeable d'exergie est perdue aux travers des différentes pertes de charge (2,2 kW). En particulier, une forte perte de charge a été identifiée sur la ligne de sortie condenseur du banc CORSERE. Si cette perte de charge ne détruit directement que 0,4 kW, elle est en partie responsable de la grande pression de condensation et donc de la perte de charge par transfert thermique au condenseur.

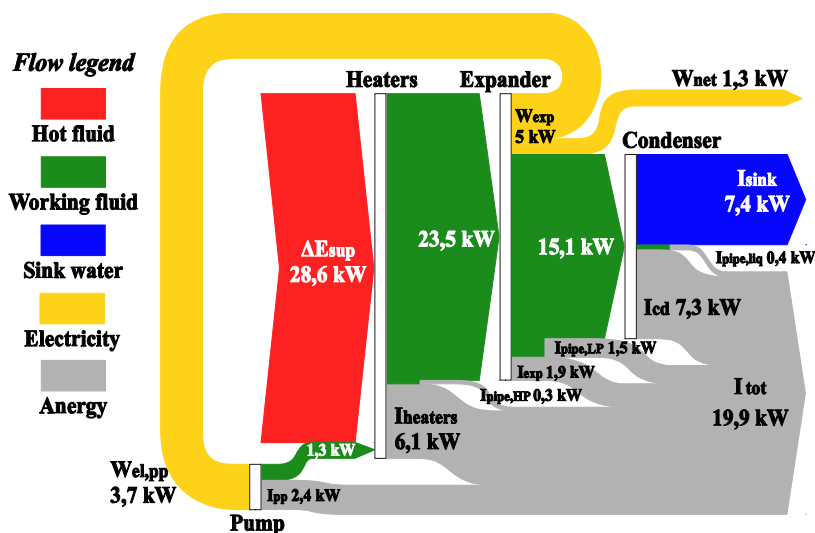


Figure VII-19 : Analyse des flux exergetiques du banc CORSERE

Sur le banc CPV-Rankine, le fonctionnement en transcritique a permis de réduire de 25 % la destruction d'exergie à l'évaporateur. En revanche, elle a augmenté à l'expandeur en raison de sa plus faible vitesse de rotation. D'autre part, la destruction au condenseur a augmenté de 40 % en raison de la plus grande pression de condensation.

Au cours de ces travaux de thèse, un état de l'art complet des recherches sur les ORC a pu être dressé à l'aide d'une base de données des installations expérimentales et d'une analyse approfondie de la thermodynamique appliquée aux ORC.

Par la suite, diverses problématiques originales ont été étudiées. Les performances énergétiques et volumétriques de la pompe de circulation ainsi que l'impact sur le design et les performances de l'ORC ; Les transferts de chaleur ayant cours proche du point critique ; L'effet de la charge de fluide sur le comportement et les performances de l'ORC ; Et une analyse des performances globales des ORC en sous-critique et en transcritique au travers d'une analyse énergétique et exergetique.

De ces travaux ressortent plusieurs perspectives de futurs travaux de recherche :

- Continuer la compilation de la base de données des installations ORC expérimentales tout en promouvant la standardisation des critères de performances.
- Etudier plus en profondeur la cavitation des pompes fonctionnant avec des fluides organiques, ainsi que les alternatives aux pompes mécaniques comme les ORC sans-pompes ou les pompes à énergie thermique.
- Etudier de façon plus précise les transferts thermiques autour du point critique à l'aide d'installations pleinement dédié, possédant une instrumentation de précision.
- Valider expérimentalement les modèles à charge variable ainsi que l'intérêt et les mécanismes permettant la régulation active de la charge de fluide.
- Améliorer les bancs d'essais transcritiques suite à l'analyse des pertes exergetiques réalisées. Poursuivre l'étude des ORC transcritiques pour la récupération de chaleur fatale.

List of publications

Journal papers:

- Kosmadakis G, **Landelle A**, Lazova M, Manolakos D, Kaya A, Huisseune H, et al. “Experimental testing of a low-temperature organic Rankine cycle (ORC) engine coupled with concentrating PV/thermal collectors: Laboratory and field tests”. *Energy* 2016;117:222–36. [doi:10.1016/j.energy.2016.10.047](https://doi.org/10.1016/j.energy.2016.10.047).
- **Landelle A**, Tauveron N, Revellin R, Haberschill P, Colasson S, Roussel V. “Performance investigation of reciprocating pump running with organic fluid for organic Rankine cycle”. *Applied Thermal Engineering* 2017;113:962–9. [doi:10.1016/j.applthermaleng.2016.11.096](https://doi.org/10.1016/j.applthermaleng.2016.11.096).
- **Landelle A**, Tauveron N, Haberschill P, Revellin R, Colasson S. “Organic Rankine cycle design and performance comparison based on experimental database”. *Applied Energy* 2017. [doi:10.1016/j.apenergy.2017.04.012](https://doi.org/10.1016/j.apenergy.2017.04.012).

Conference papers:

- **Landelle A**, Tauveron N, Haberschill P, Revellin R, Colasson S. “Study of reciprocating pump for supercritical ORC at full and part load operation”. *3rd International Seminar on ORC Power Systems*, Brussels: 2015. asme-orc2015.be
- **Landelle A**, Tauveron N, Haberschill P, Revellin R, Colasson S. “Performance Evaluation of Experimental Organic Rankine Cycle and Prototypes Comparison from Published Data”. *8th International Conference on Applied Energy*, Beijing; Energy Procedia; 2016, p. 1706–11. [doi:10.1016/j.egypro.2017.03.555](https://doi.org/10.1016/j.egypro.2017.03.555).
- **Landelle A**, Tauveron N, Revellin R, Haberschill P, Colasson S. “Experimental Investigation of a Transcritical Organic Rankine Cycle with Scroll Expander for Low-Temperature Waste Heat Recovery”. *4th International Seminar on ORC Power Systems*, Milano: 2017.

Database:

- **Landelle A**. 2017. “Experimental Organic Rankine Cycle database v2016.12”. [Data set]. Zenodo. [doi:10.5281/zenodo.218252](https://doi.org/10.5281/zenodo.218252)

Table of contents

ACKNOWLEDGMENTS	8
ABSTRACT	10
RÉSUMÉ.....	11
RESUME ETENDU	12
LIST OF PUBLICATIONS.....	30
TABLE OF CONTENTS.....	32
LIST OF FIGURES	36
LIST OF TABLES	39
NOMENCLATURE	40
CHAPTER I INTRODUCTION	44
Background.....	45
The Organic Rankine Cycle technology	47
Future applications and research trends.....	50
Scope of the thesis	52
CHAPTER II ORGANIC RANKINE CYCLE STATE-OF-THE-ART	54
1 Thermodynamics applied to ORC.....	55
1.1 Energy conversion chain.....	55
1.2 Types of heat sources.....	58
1.3 Performance criteria	59
2 Experimental ORC database.....	62
2.1 Data compilation	62
2.2 Database overview.....	64
2.3 Database statistical analysis	71
Chapter conclusion	77

CHAPTER III TOOLS & METHODOLOGY.....	78
1 Experiments.....	79
1.1 Setups presentation.....	79
1.2 Experimental procedures.....	85
2 Data processing.....	88
2.1 Steady-point & transient identification	88
2.2 Calculated parameters.....	90
2.3 Data reconciliation	92
3 Modeling.....	95
3.1 Process model	95
3.2 Charge sensitive model.....	95
3.3 Dynamic model	99
Chapter conclusion	102
CHAPTER IV RECIPROCATING PUMP FOR ORC.....	104
1 Energetic performances.....	105
1.1 Semi-empirical modeling	105
1.2 Model validation	106
1.3 Pump energetic performances effects on ORC design & operation	108
2 Volumetric performances	112
2.1 Fluid compressibility	112
2.2 Cavitation	114
2.3 Pump volumetric performances effects on ORC design & operation.....	116
Chapter conclusion	117
CHAPTER V SUPERCRITICAL HEAT TRANSFER.....	118
1 Smooth tube.....	119
1.1 Subcooled fluid entry.....	119
1.2 Near-critical point heat transfer.....	123
2 Plate heat exchanger	130
2.1 Global heat transfer coefficient	130
2.2 Exergetic analysis.....	132
Chapter conclusion	135
CHAPTER VI WORKING FLUID CHARGE.....	136
1 Effect of circulating charge on ORC behavior and performances	137

1.1	Charge variation at fixed conditions	137
1.2	Behavior at various expander and pump speeds.....	142
2	Circulating fluid charge optimization.....	148
2.1	Optimum charge under variable operating conditions	148
2.2	ORC design and charge regulation.....	153
	Chapter conclusion	157
	CHAPTER VII ORC OPERATION	158
1	Machineries	159
1.1	Expander operation.....	159
1.2	Volumetric machineries – flow rate balance.....	165
2	Cycle performances analysis.....	168
2.1	ORC efficiency: analysis and comparison	168
2.2	Exergetic analysis.....	172
2.3	ORC dynamics	176
	Chapter conclusion	179
	CHAPTER VIII CONCLUSION	180
	REFERENCES.....	188
	APPENDIXES.....	194

List of figures

<i>Figure I-1: Population and energy projection by 2040</i>	45
<i>Figure I-2: World energy flow (Lawrence Livermore National Laboratory 2007)</i>	46
<i>Figure I-3 : Global waste heat distribution (Forman et al. 2016)</i>	46
<i>Figure I-4: Organic Rankine Cycle working principle (ADEME 2015) - translated</i>	47
<i>Figure I-5: Heat-to-Power conversion systems map (Tauveron, Colasson, and Gruss 2015)</i>	48
<i>Figure I-6 : ORC installed capacity per application – from (Tartière and Astolfi 2017)</i>	49
<i>Figure I-7 : Number of installed ORC units (Tartière 2017) and WTI crude oil price evolution (International Energy Agency 2017)</i>	49
<i>Figure I-8 : Current and future scope of application of the ORC technology (Colonna et al. 2015)</i>	50
<i>Figure I-9 : Expander technological classification</i>	51
<i>Figure II-1 : Pump energetic conversion chain</i>	56
<i>Figure II-2 : Expander energetic conversion chain</i>	56
<i>Figure II-3 : Value diagram of an evaporator</i>	57
<i>Figure II-4: Scheme and temperature-heat diagram for closed and open heat sources</i>	58
<i>Figure II-5 : Efficiency boundaries (a) in the ORC unit - (b) ORC module vs plant</i>	60
<i>Figure II-6: Expander generator efficiency empirical correlation</i>	64
<i>Figure II-7: Map of ORC references - hot source temperature vs. gross power</i>	65
<i>Figure II-8: Target application proportions by regions and worldwide</i>	66
<i>Figure II-9: Type of refrigerant used as working fluid over time</i>	67
<i>Figure II-10: Patents and publications number of references trends</i>	67
<i>Figure II-11: Working fluids maximum operating conditions in the ORCs</i>	68
<i>Figure II-12: Expanders range of pressure ratio, shaft speed and power scale per technology</i>	68
<i>Figure II-13: Electric power and efficiency map of expanders</i>	69
<i>Figure II-14: Expander lubrication strategies</i>	69
<i>Figure II-15: (a) Pumps pressure lift vs. flow rate - (b) Pumps efficiency vs. hydraulic power</i>	70
<i>Figure II-16: Heat exchanger technologies</i>	70
<i>Figure II-17: ORC power and thermal efficiency map</i>	71
<i>Figure II-18: Hot temperature and ORC thermal efficiency map</i>	72
<i>Figure II-19: ORC power and second law efficiency map</i>	72
<i>Figure II-20: ORC power and exergetic recovery efficiency map for different target application types</i> ..	73
<i>Figure II-21: ORC power and back work ratio map</i>	74
<i>Figure II-22: Comparison of specific ORC with same scale ORCs: (a) transcritical ORC for solar – (b) transcritical ORC for WHR – (c) & (d) ORC with mixture fluid.</i>	75
<i>Figure III-1: CORSERE bench Process & Instrumentation Diagram</i>	79
<i>Figure III-2: CORSERE installation picture</i>	80
<i>Figure III-3: CPV-Rankine installation pictures</i>	80
<i>Figure III-4: CPVR bench PID (a) laboratory configuration - (b) field configuration</i>	81
<i>Figure III-5: SURCOUF bench PID</i>	82
<i>Figure III-6: (a) SURCOUF installation picture (b) Heat transfer test section</i>	82
<i>Figure III-7: Absorption chiller process diagram (Triché et al. 2017)</i>	83

<i>Figure III-8: Absorption chiller installation picture (Triché et al. 2017)</i>	83
<i>Figure III-9: CORSERE & CPV-Rankine operation maps</i>	87
<i>Figure III-10: Dynamic response time</i>	89
<i>Figure III-11: Example of steady-state detection</i>	89
<i>Figure III-12: Pinch point evaluation and localization</i>	91
<i>Figure III-13: Weight correction for each parameter of the CORSERE bench</i>	93
<i>Figure III-14: CORSERE heat exchangers energy balance before and after reconciliation</i>	94
<i>Figure III-15: Example of dead parts and fluid state depending on the bench configuration</i>	96
<i>Figure III-16: Heat exchangers heat power - Experimental vs. Simulation parity plot</i>	97
<i>Figure III-17: ORC mass inventory – Hughmark correlation</i>	99
<i>Figure III-18: ORC mass inventory - correlations comparison</i>	99
<i>Figure III-19: Dymola-Modelica model diagram of the CORSERE bench</i>	100
<i>Figure IV-1: Pump energetic power chain (copy of Figure II-1)</i>	105
<i>Figure IV-2: Pump energetic power model-experiment parity plot</i>	108
<i>Figure IV-3: Research of optimum pressure for different pump model and pump speed</i>	109
<i>Figure IV-4: SURCOUF pump operation scenarios</i>	110
<i>Figure IV-5: Relation between pump and expander efficiency for iso-ratio of real to isentropic ORC efficiency</i>	111
<i>Figure IV-6: Reciprocating pump discharge and suction operation</i>	113
<i>Figure IV-7: SURCOUF's pump experimental volumetric performances</i>	114
<i>Figure IV-8: Flow rate evolution near the cavitation limit</i>	115
<i>Figure IV-9: Impact of the minimum subcooling over the BWR and the ORC net efficiency</i>	116
<i>Figure V-1: Electrical and fluid heat power balance</i>	120
<i>Figure V-2: Data mappings: a) Mass velocity G vs. Heat flow q – b) Pressure vs. Test section inlet temperature (near-critical data only)</i>	120
<i>Figure V-3: Liquid data test: a) Experimental heat transfer evolution with mass velocity – b) Experiment vs. Dittus-Boelter comparison – c) Experiment vs. Sieder-Tate comparison – d) Experiment vs. Gnielinski comparison</i>	121
<i>Figure V-4: Near critical point heat transfer investigation: influence of the inlet temperature</i>	123
<i>Figure V-5: Near critical point heat transfer investigation: influence of the pressure, flow rate and inlet temperature over the maximum heat transfer coefficient location</i>	124
<i>Figure V-6 Near-critical point heat transfer investigation: comparison with Dittus-Boelter, Jackson and Liao downward correlations</i>	125
<i>Figure V-7: Near critical point heat transfer investigations: customized correlations</i>	127
<i>Figure V-8: Free-base correlation exponent sensitivity analysis</i>	127
<i>Figure V-9: Mixed convection effects: data and correlations</i>	128
<i>Figure V-10: CORSERE heat exchangers pinch point function of fluid flow rate</i>	130
<i>Figure V-11: Pre-heater and evaporator fluid heat transfer evolution with the flow rate in supercritical conditions</i>	131
<i>Figure V-12: Heat transfer investigation of pre-heater with supercritical outlet conditions - temperature and pressure influence</i>	132
<i>Figure V-13: Heater exergetic efficiency</i>	133
<i>Figure V-14: CPV-Rankine evaporator - exergy destruction rate</i>	134
<i>Figure VI-1: Simplified ORC process diagram</i>	138
<i>Figure VI-2: Reference case – evolution of the main ORC parameters with the working fluid charge</i> ..	139

Figure VI-3: Reference case – charge repartition in the ORC.....	139
Figure VI-4: Reference case – charge repartition in the condenser.....	140
Figure VI-5: ORC pressure zones elementary view.....	140
Figure VI-6: Condenser density and temperature evolution and Temperature-entropy diagram for different total fluid charge.....	142
Figure VI-7: ORC behavior investigation under various fluid charge, expander and pump speeds.....	143
Figure VI-8: Pump and expander speed optimization for a 15 kg charge.....	145
Figure VI-9: Pump and expander speed optimization for a 18 kg charge.....	147
Figure VI-10: Heat source parameters influence over the optimum fluid charge.....	148
Figure VI-11: Heat sink parameters influence over the optimum fluid charge.....	149
Figure VI-12: Expander speed influence over the optimum fluid charge.....	150
Figure VI-13: Pump speed influence over the optimum fluid charge.....	150
Figure VI-14: Ts diagrams for different pump speeds at the optimum fluid charge.....	151
Figure VI-15: Overview of the different parameters influence on the optimum fluid charge and resulting ORC performances.....	152
Figure VI-16: US-8800285 patent solution - modified from (Ernst and Nelson 2012).....	155
Figure VI-17: DE-102009050068 patent solutions proposed – modified from (Lutz, Motisi, and Bruemmer 2015).....	156
Figure VII-1: Scroll mechanism and parts – from (Harada 2010).....	159
Figure VII-2: Under and over expansion process in scroll expanders from (Lemort et al. 2009).....	160
Figure VII-3: Scroll compressor and expander: parts, mechanisms and modifications.....	161
Figure VII-4: CORSERE expander pictures: a) scroll body – b) body top view – c) top flange.....	161
Figure VII-5: Gross electrical production of the CORSERE and CPV-Rankine scroll expanders.....	162
Figure VII-6: CPV-Rankine expander electrical efficiency.....	162
Figure VII-7: CPV-Rankine modified scroll expander.....	163
Figure VII-8: CPV-Rankine expander volumetric efficiency.....	164
Figure VII-9: CORSERE expander electrical efficiency.....	164
Figure VII-10: CORSERE & CPV-Rankine expanders volumetric efficiency and empirical correlation.....	166
Figure VII-11: CORSERE expander and pump flow rate equilibrium.....	167
Figure VII-12: CPV-Rankine expander and pump flow rate equilibrium.....	167
Figure VII-13: CORSERE net efficiencies function of: (a) relative pressure (b) expander efficiency....	168
Figure VII-14: CORSERE Back Work Ratio and BWR efficiency evolution with the relative pressure..	169
Figure VII-15: CPV-Rankine net thermal efficiency function of the pressure ratio.....	169
Figure VII-16: CPV-Rankine 2 nd law efficiency function of expander inlet relative pressure.....	170
Figure VII-17: CPV-Rankine 2 nd law efficiency in the relative pressure-temperature map.....	171
Figure VII-18: ORCs comparison with state-of-the-art prototypes.....	171
Figure VII-19: Detailed exergetic flow diagram of the CORSERE bench at the most efficient point....	172
Figure VII-20: Condenser exergy destruction analysis: (a) CORSERE (b) CPV-Rankine.....	173
Figure VII-21: CORSERE bench - components exergetic destruction ratio for different case study....	174
Figure VII-22: CPV-R exergetic flow diagram: (a) subcritical optimum case (b) transcritical case....	175
Figure VII-23: CORSERE working fluid flow rate steps - Experiment & Model comparison.....	177
Figure VII-24: CORSERE bench - heat source flow rate downward step.....	177
Figure VII-25: CORSERE bench - heat sink flow rate upward step.....	178

List of tables

<i>Table II-1 : Summary of power types</i>	55
<i>Table II-2: ORC system possible inputs and resulting efficiencies</i>	60
<i>Table II-3: Experimental ORC database layout</i>	63
<i>Table II-4: Spearman’s correlations for ORC thermal and second law efficiency</i>	74
<i>Table II-5: Comparison of HFO R1233zdE with R245fa and same scale benches</i>	76
<i>Table III-1: Characteristics of each bench components and auxiliaries</i>	84
<i>Table III-2: Experimental setups control parameters</i>	85
<i>Table III-3: CORSERE sensors table</i>	86
<i>Table III-4: CPV-Rankine sensors table</i>	87
<i>Table III-5: SURCOUF sensors table</i>	87
<i>Table III-6: Uncertainty and experimental range of main calculated parameters</i>	92
<i>Table III-7: Heat transfer coefficient - correlation parameters for reference flow $m_0=1$ kg/s</i>	97
<i>Table IV-1: Pump energetic model summary</i>	107
<i>Table V-1: Main parameters of the Figure V-5 different test cases: mean value and standard deviation</i>	124
<i>Table V-2: Customized correlations: estimated coefficients</i>	126
<i>Table VI-1: Simplified model pipe and components volumes</i>	138
<i>Table VI-2: Summary of fluid charge and machineries speed effect over the ORC</i>	144
<i>Table VI-3: Parameters values for the reference case and range for the optimum fluid charge investigation</i>	148
<i>Table VI-4: Summary of main variables effect over the optimal fluid charge and ORC net power</i>	153
<i>Table VII-1: CORSERE exergetic performances – case study summary</i>	174

Nomenclature

A	Area [m^2]
c_p	specific heat capacity [$\text{J}/\text{kg}\cdot\text{K}$]
Dh	hydraulic diameter [m]
d	diameter [m]
E	exergy [W]
e	specific exergy [W/kg]
e_c	kinetic energy [W]
G	mass velocity [$\text{kg}/\text{m}^2\cdot\text{s}$]
g	standard gravity
h	specific enthalpy [J/kg]
I	exergy destruction [W]
i	electric current [A]
m	mass flow rate [kg/s]
P	pressure [Pa]
Q	heat power [W]
q	heat flux [W/m^2]
S	phase slip ratio [-]
s	specific entropy [$\text{J}/\text{kg}\cdot\text{K}$]
T	temperature [K]
t	thickness [m]
U	global heat transfer coefficient [$\text{W}/\text{m}^2\cdot\text{K}$]
u	electric tension [V]
V	volume flow rate [m^3/s]
v	volume [m^3]
W	power [W]

Greek symbols

α	local heat transfer coefficient [$\text{W}/\text{m}^2\cdot\text{K}$]
β_s	isentropic compressibility factor [Pa^{-1}]
Γ	torque [N.m]
Γ	void fraction [-]
Δ	difference
ε	exergetic efficiency [-]
η	energetic efficiency [-]
λ	thermal conductivity [$\text{W}/\text{m}\cdot\text{K}$]
μ	dynamic viscosity [$\text{Pa}\cdot\text{s}$]
v	specific volume [m^3/kg]
ξ	fluid saturated vapor slope [-]
ρ	density [kg/m^3]

Φ	dissipations [W]
φ	electric phase [rad]
Ω	rotating speed [Hz]

Subscripts

ad	adiabatic
amb	ambient
cp	compression
crit	critical
el	electric
esti	estimated
ev	evaporator
ex	exhaust
exp	expander
ext	external
f	fluid bulk
hf	hot fluid
hr	heat recovery
hy	hydraulic
in	inlet
ind	indicated
int	internal
is	isentropic
l	liquid
max	maximum
meas	measured
mot	motor
me	mechanic
out	outlet
pp	pump
rec	recovery
req	requested
sat	saturation
su	supply
sup	supplied
th	thermal (efficiency)
v	vapor
vol	volumetric
w	wall
wf	working fluid
0	reference
II	second law (efficiency)

Acronyms

AC	Alternative Current
BPHE	Brazed Plate Heat Exchanger
BVR	Built-in Volume Ratio
BWR	Back Work Ratio
CHP	Combined heat and power
DC	Direct Current
HEX	Heat Exchanger
HF	Hot Fluid
HTF	Heat Transfer Fluid
ICE	Internal Combustion Engine
IHE	Internal Heat Exchanger
LHV _f	Low Heating Value of a fuel
NPSH	Net Positive Suction Head
ORC	Organic Rankine Cycle
OTEC	Ocean Thermal Energy Conversion
P&ID	Process and Instrumentation Diagram
TS	Test Section
VSD	Variable Speed Drive
WHR	Waste Heat Recovery

Dimensionless numbers

Gr	Grashof
Nu	Nusselt
Pr	Prandtl
Re	Reynolds
rP	relative pressure [-]
rT	relative temperature [-]
Xtt	Lockhart and Martinelli parameter [-]

Chapter I

Introduction

Background

Sustainable development with a low-carbon and climate-resilient economy is one of the key challenges of the 21st century highlighted by the United Nations. As the world population is expected to grow, the energy sector is facing major challenges to provide the energy needed for economic growth while drastically reducing its impact on the environment, and the global warming issue. By 2040, energy demand is expected to increase by 37 % (International Energy Agency 2016b) while the world population is expected to increase by 22 % (United Nations Department of Economic and Social Affairs, Population Division 2015) as shown in Figure I-1.

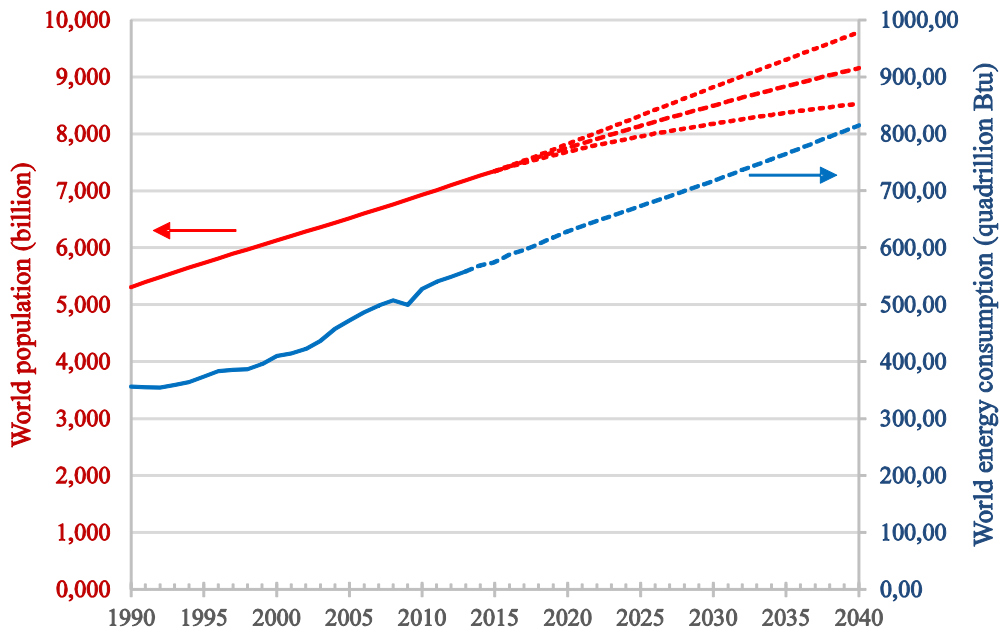


Figure I-1: Population and energy projection by 2040

In 2011, fossil resources represented more than 80 % of the world energy input flow. In the mean time, more than half of the world energy input was lost during conversion process (Figure I-2).

Therefore, two main levers could address those issues. First, by moving from carbon intensive energy sources to decarbonized sources, such as renewable energies (solar, biomass, hydro, wind, geothermal) or nuclear energy (4th generation, nuclear fusion), meeting the world demand for growth.

According to the 2016 Energy Technology Perspectives of the IEA (International Energy Agency 2016a), renewable energies represented 3.7 % of the total world energy input in 2013. According to the 2°C scenario, renewable energies may represent 10 % in 2030 and 22.9 % in 2050, for a total capacity of 150 EJ, 7.5 times the 2013 production.

Second, by improving the way energy is used through usage transformation and efficiency improvement (industrial process, insulation, machineries) to decrease the energy requested for the same services. According to (Forman et al. 2016), 245 EJ were rejected through exhaust or effluents in 2012 however, more than half of it was rejected below 100°C (Figure I-3). Assuming waste heat could be fully valorized with Carnot's engines, 48 EJ would be regenerated, representing $\frac{1}{3}$ of the useful energy consumed in 2013.

However, the technical potential largely differs from the economic potential. An Oak Ridge National Laboratory study estimates the US WHR technical potential to 14.6 GW, but estimated the market potential to only 2.9 GW (Elson, Tidball, and Hampson 2015). In France, the industry is estimated to waste 51 TWh of heat above 100 °C each year (ADEME 2015), half of it between 100 and 200 °C. 20 % could be recovered by existing district heating networks, and 1.1 TWh could be converted into electricity to deliver 140 MWe into the grid. Therefore, there still a strong need for recovery technologies improvement.

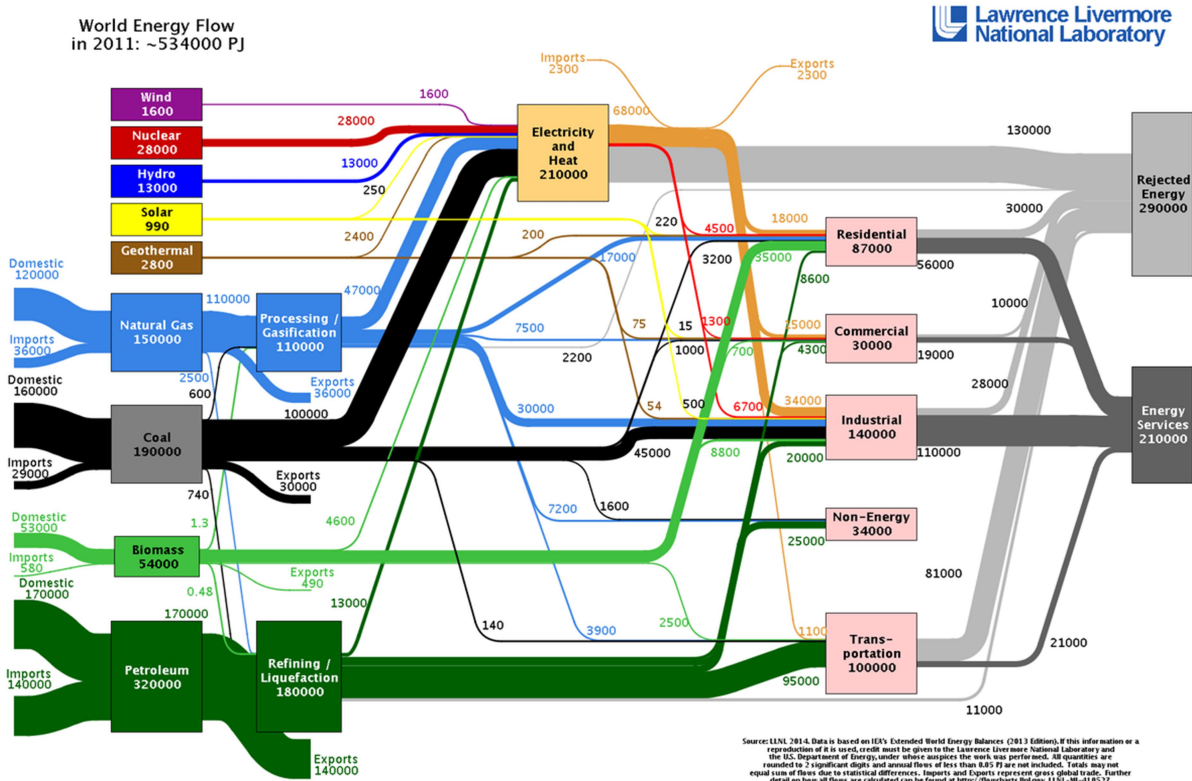


Figure I-2: World energy flow (Lawrence Livermore National Laboratory 2007)

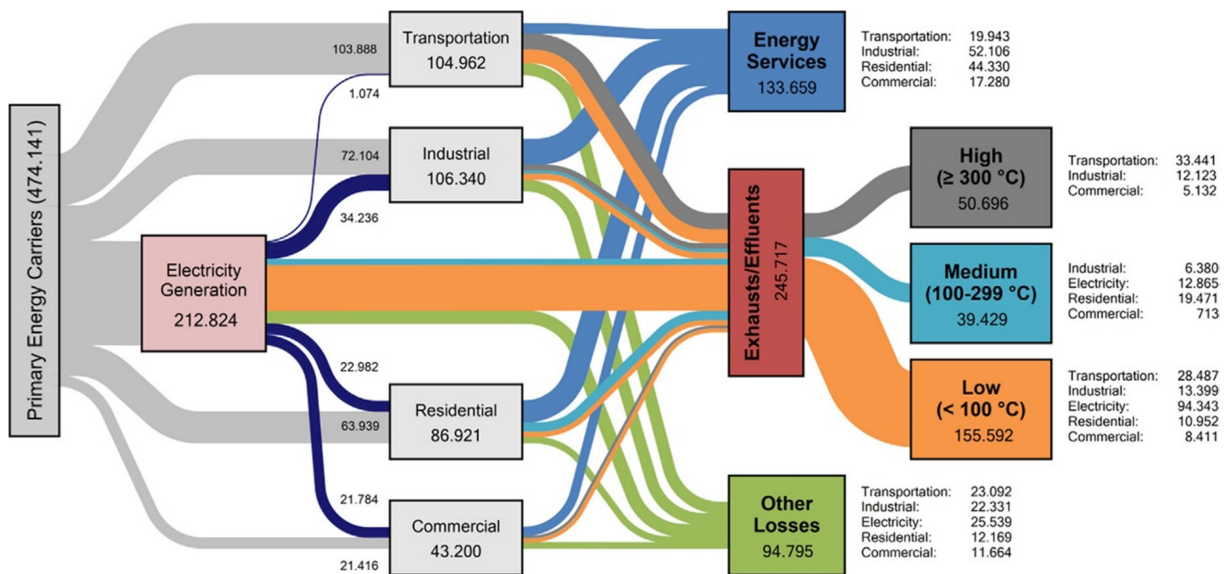


Figure I-3 : Global waste heat distribution (Forman et al. 2016)

Lastly, the climate-engineering (carbon capture, solar radiation management) could potentially decrease the global warming inducted by humans since the industrial revolution. However, geo-engineering represents substantial risks and will not address the natural resources depletion and other environment issues such as air pollution.

The Organic Rankine Cycle technology could play on both levers. First, by increasing the development of renewable energies such as thermal solar, biomass cogeneration or geothermal energy, three renewable sources which will grow from 11.2 EJ in 2013 to almost 100 EJ by 2050 according to the IEA, roughly a 6.3 % average annual growth. Second, by improving industrial processes and transport energy efficiency through the conversion of waste heat into useful power.

The Organic Rankine Cycle technology

The Organic Rankine Cycle is a heat to power conversion technology used since the 19th century to transform thermal energy from a variety of sources. The working principle of a Rankine engine is quite simple. The working fluid is pressurized by a pump and sent to the evaporator. In the evaporator, the heat source exchanges its thermal energy with the working fluid, which evaporates. The high pressure vapor is expanded in an expander, producing mechanical work, later converted into electrical energy by the generator. The low pressure fluid is cooled down in the condenser by means of a heat sink, and pumped back to the evaporator (Figure I-4).

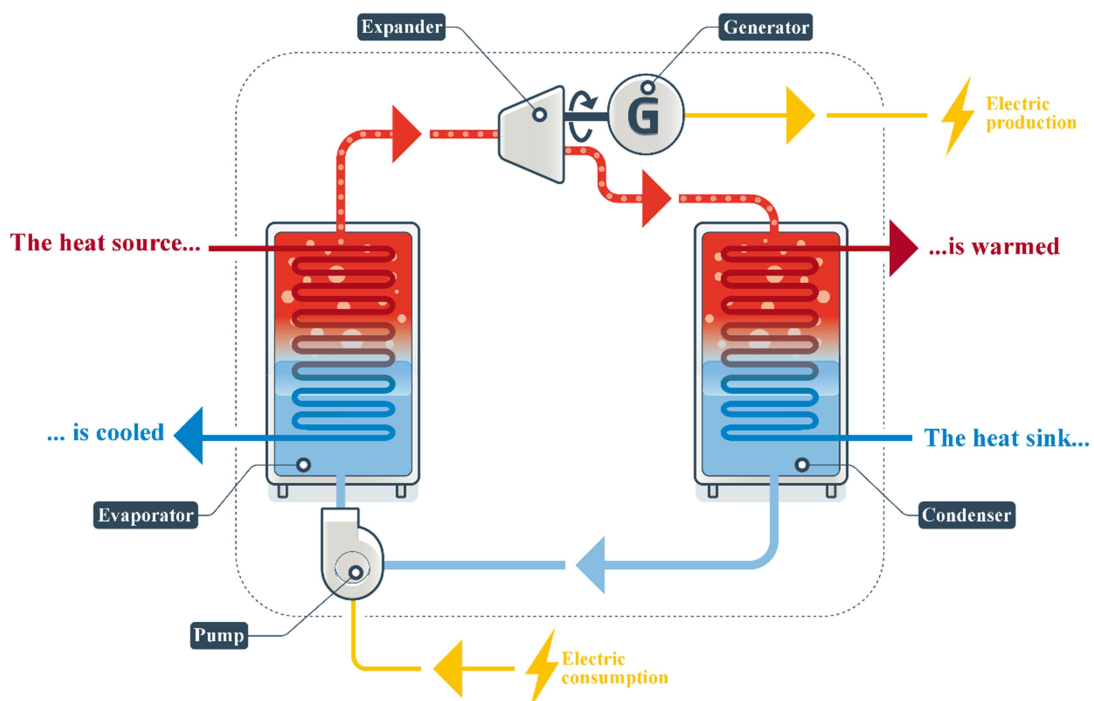


Figure I-4: Organic Rankine Cycle working principle (ADEME 2015) - translated

The classic Rankine cycle uses water as working fluid. In the ORC, the working fluid is an organic fluid, usually a refrigerant with a lower boiling point than water. Therefore, while classic Rankine cycle becomes complex to be designed and implemented for heat sources below 300 °C (Colonna et al. 2015), in ORC the working fluid can be selected to match the heat source for efficiency maximization. Some commercial ORC units can run with heat source temperature as low as 60 °C. In the current heat-to-power commercial units technological mapping (Figure I-5), the ORC is holding the 1 kW to 10 MW power range for hot sources below 300 °C but overlaps with the classic Rankine in the MW range.

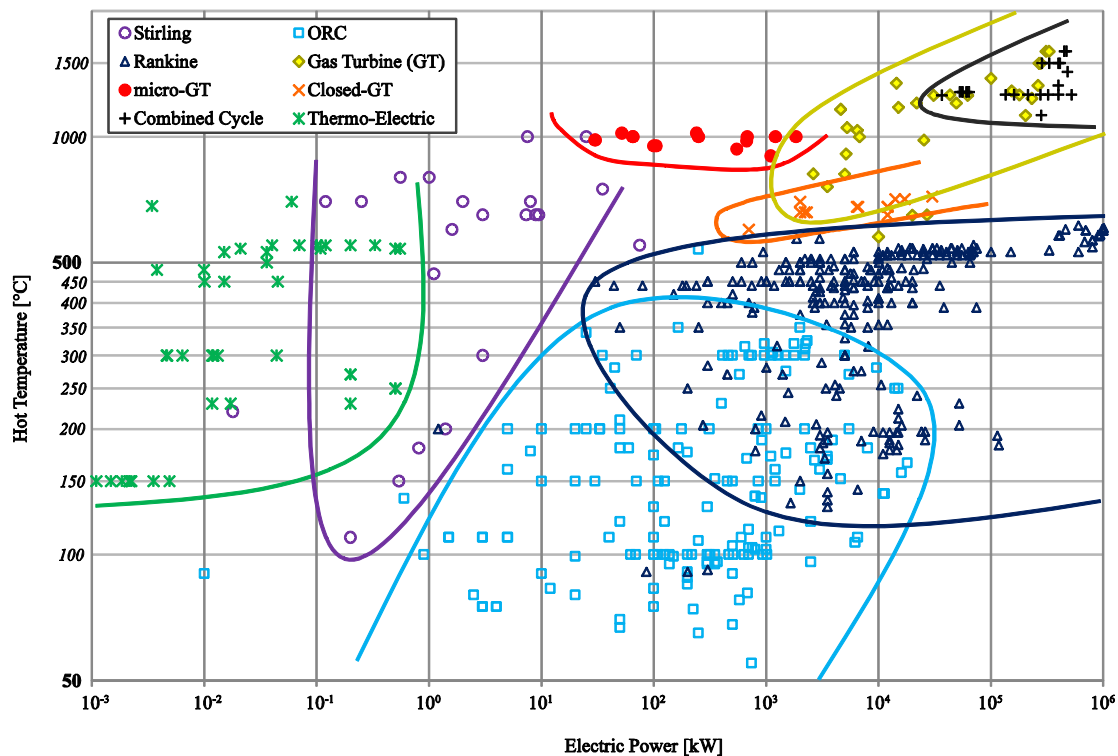


Figure I-5: Heat-to-Power conversion systems map (Tauveron, Colasson, and Gruss 2015)

T. Howard first patented a heat engine using ether as the working fluid in 1826, later replaced by engine running with Naphta. Then, by the 20th century, concept of ORC driven by solar flat collector was introduced by Shuman for irrigation purposes as cited in (Pytilinski 1978), followed by geothermal plant concept after World War II. The oil crisis led to a new usage of ORC for waste heat recovery (WHR) to improve process or internal combustion engines (ICE) energetic efficiency (Cipolla 1980; Casci et al. 1981). Bottoming cycles for waste-heat to power in long-haul truck were tested but never commercially developed (DiBella, DiNanno, and Koplw 1983). Use of ORC for biomass combined heat and power (CHP) plants started only in the late 90^s in Switzerland.

Nowadays, ORC still has the same four main applications: biomass combined heat & power (CHP), geothermal energy, thermal solar plants and waste heat recovery. However waste heat recovery can be split in two sub-categories: bottoming cycle of internal combustion engines (diesel, gas turbines) and industrial processes heat recovery (Sylvain Quoilin et al. 2013). According to the *ORC-world-map.org* database (Tartière 2017) and its last update (Tartière and Astolfi 2017), 984 ORC power plants are recorded worldwide for a

total capacity of 2.78 GWel and several plants for a total of 0.46 GWel are officially planned. In terms of installed capacity, geothermal applications represent three quarters of the total power while solar only a thousandth (Figure I-6). However, geothermal power plants are usually large scale units and in terms of units' number, there are now more biomass or heat recovery units. The number of installed units has experienced a rapid growth since 2003 but considerably slowdown a decade later, probably in relation with the crude oil price rise of the 2000's decade and the sudden drop in the late 2014 (Figure I-7).

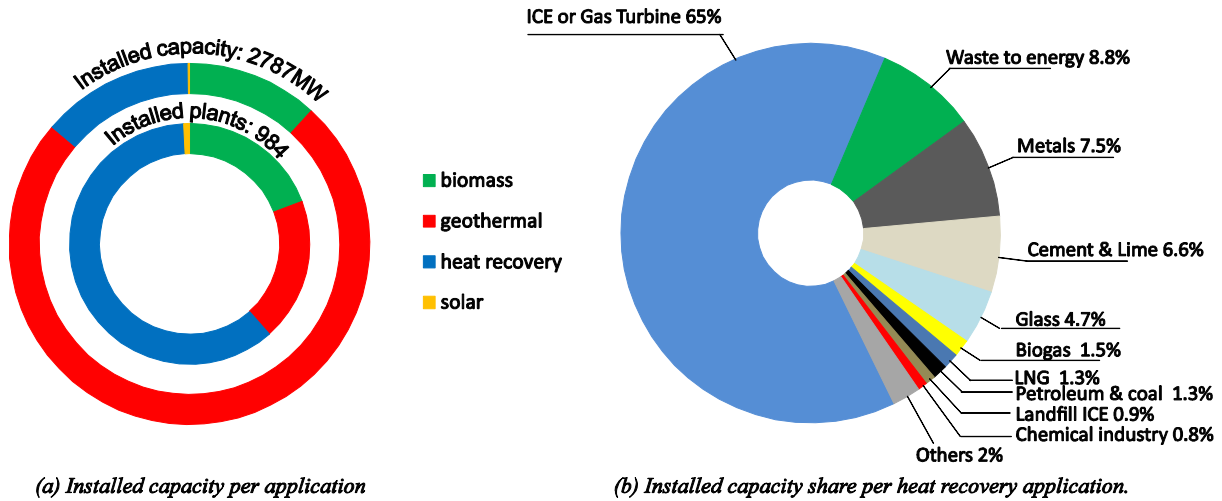


Figure I-6 : ORC installed capacity per application – from (Tartière and Astolfi 2017)

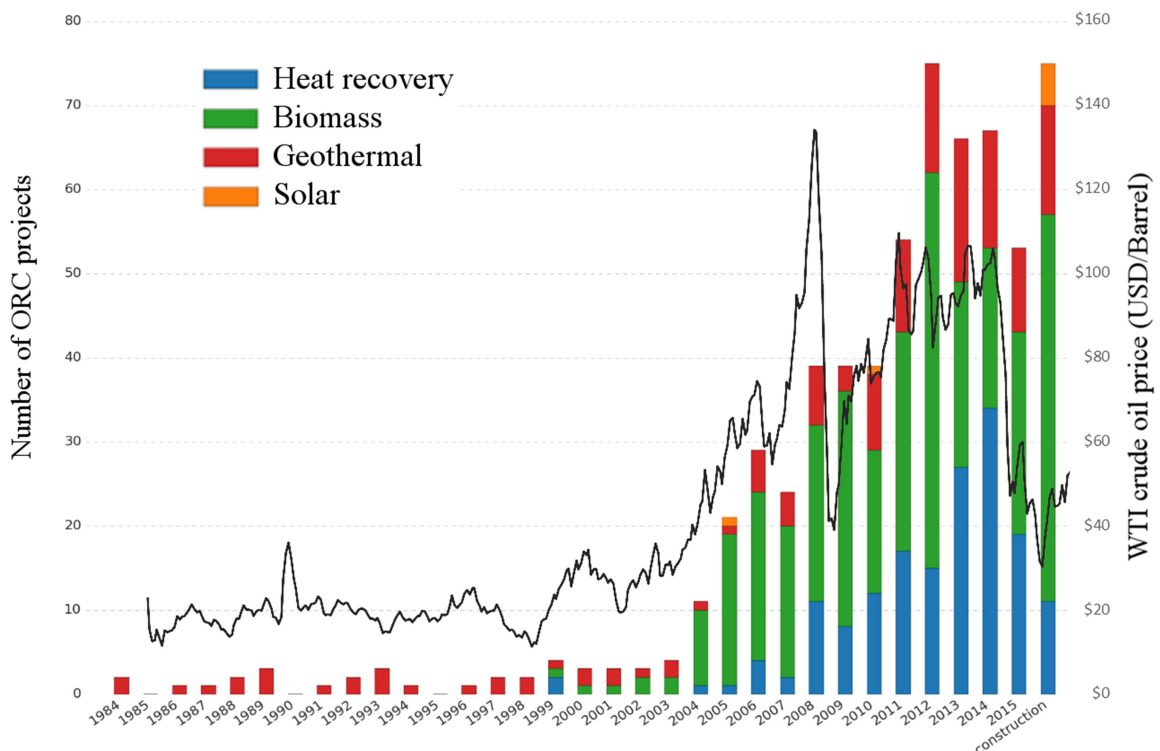


Figure I-7 : Number of installed ORC units (Tartière n.d.) and WTI crude oil price evolution (International Energy Agency 2017)

Future applications and research trends

The Organic Rankine Cycle technology is expected to reach new applications and markets. Small ORC unit becomes more efficient, smaller and less expensive, while large ORC unit can convert very low temperature heat sources. Therefore, the ORC technical and economical range of application is in expansion (Colonna et al. 2015) as shown in Figure I-8.

Among the potential future ORC applications, we can find automotive engines heat recovery for fuel consumption and pollution reduction of classic oil fueled engines. While ORC units' size and weight should be further reduced to be adopted by the automotive industry, the large market could drastically reduce the cost of small scale ORC units.

Domestic micro-CHP is expected to rise. Fueled by gas or biomass, small CHP units could respond to consumers' need for heat and electricity, especially in cold countries. Better recognition of the micro-CHP in the regulations with feed-in tariff and economies of scale could create a new market for small ORC.

Ocean Thermal Energy Conversion (OTEC) technology, while already tested in the 30's by Georges Claude (Popular Mechanics 1930), is still in the development stage. This technology uses the temperature difference between surface and deep water to drive the heat engine. As for geothermal energy, ORC is a promising technology for OTEC units. However, while for the geothermal energy, sources temperature differences are at least of 60 °C, OTEC has sources temperature difference of only 20 to 30 K.

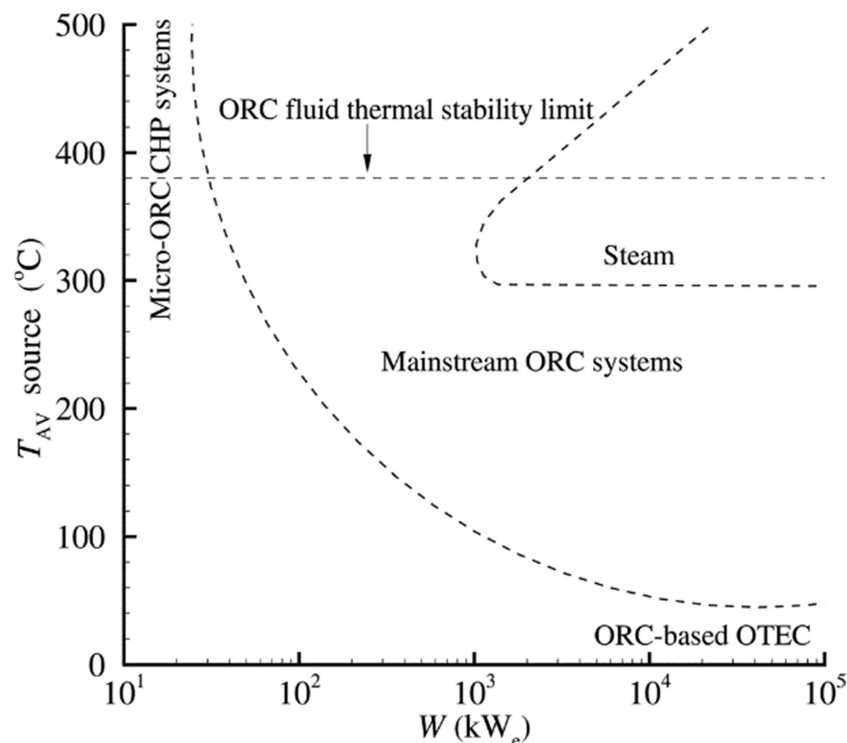


Figure I-8 : Current and future scope of application of the ORC technology (Colonna et al. 2015)

To answer those new markets requirements and current applications issues, research and development of the ORC technology is continuously ongoing. Main ORC topics of R&D can be divided as follows:

- Expanders

Expansion machines is one of the key components in an ORC, therefore, many researches focus on the improvement of expander efficiencies and range of use. Figure I-9 shows the classification of expander technologies applicable to ORC. Various factors should be considered for expander selection (Bao and Zhao 2013; Sylvain Quoilin et al. 2013); the unit power scale, the pressure or volumetric ratio between the high and low pressure working fluid vapor, the type of lubrication and its compatibility with the working fluid, or its efficiency at part load operation for variable process.

Turbines can be used in a wide range, from a few kW to more than a MW, but are complex to design. Volumetric machines received a large interest for small-scale applications (Song et al. 2015; Imran et al. 2016), since volumetric compressors can be deviated from their original purpose to be used as volumetric expanders (Zanelli and Favrat 1994).

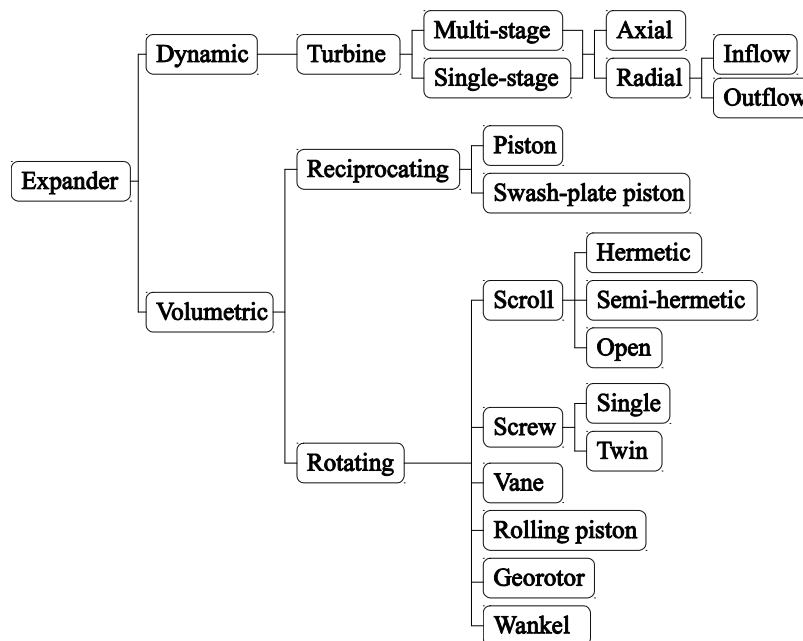


Figure I-9 : Expander technological classification

- Working fluid

The working fluid is the specific feature of the Organic Rankine Cycle technology. So, fluid selection and design have been widely investigated. Many factors should be considered for fluid selection (Bao and Zhao 2013; Chen, Goswami, and Stefanakos 2010): thermodynamic and physical properties maximizing the efficiency for the available heat source, fluid density (size of the installation), thermal stability, compatibility with other materials (lubricant, seals, metals), environmental aspects (Ozone Depletion Potential and Global Warming Potential), safety issue (flammability, toxicity) as well as availability and cost.

The ORC market was not large enough to justify high R&D and production investments for specific ORC fluids. Therefore, most fluids used in ORC units were designed for the refrigeration industry. Nevertheless, researches on ORC working fluids are very active. In particular, the use of fluid zeotropic mixture (Bamorovat Abadi and Kim 2017) to reduce irreversibility in the evaporator and better match the heat source and sink profile.

Nano-fluids could improve heat transfer but were not tested in ORC (Godson et al. 2010). Some studies proposed the Computer Aided Molecular Design for pure fluid and fluid mixture design and selection of the ORC working fluid (Papadopoulos, Stijepovic, and Linke 2010; Papadopoulos et al. 2013)

- Cycle architecture & operating conditions

From the simple Rankine cycle, many advanced cycles can be designed, using additional components or modifying fluid conditions at the expander inlet. A usual Rankine cycle improvement is the Hirn cycle, with superheated working fluid at the expander inlet, or the regenerative cycle with an additional heat exchanger to recover expander exhaust heat for high pressure working fluid pre-heating.

(Lecompte et al. 2015) summarize the different ORC architectures investigated. Some architectures are more specifically investigated, such as transcritical cycle, cascade or multi-pressure cycle, two-phase expansion... However, such architectures, while improving the ORC efficiency, substantially increase the specific cost due to additional components or arduous running conditions.

- Modeling & simulation:

Numerical tools are increasingly used for all engineering fields, and ORC models are becoming more complex, robust and accurate (Ziviani, Beyene, and Venturini 2014). ORC models and simulations have two distinct applications.

First, it can be used for ORC design, or virtual prototyping. Such tools could automate or at least assist engineers in the design phase for fluid selection, expander and cycle design to adapt each ORC unit to its environment (heat source and sink). Especially for small-scale units to reduce design cost, and waste heat recovery applications to better match each case and heat source.

Second, it can be used for ORC control and efficiency maximization, at full and part-load operation. Especially for upcoming applications such as automotive waste heat recovery or micro-CHP that request fully automated operation and can be highly dynamic.

Scope of the thesis

The present thesis is centered on the use of Organic Rankine Cycle for low-grade heat conversion into electricity. The origin of this thesis comes from the SURORC project sponsored by ADEME and carried out by Enertime, Separex, CEA and ENSAM Paris (Enertime et al. 2012). The SURORC project aimed at considering the techno-economical benefit of transcritical cycle for WHR of 100 °C to 150 °C sources. Based on this study, a 10 kWe prototype was built to better understand and evaluate the use of transcritical cycles within the framework of the SSORC project, a *Carnot Energies du Futur* project (Tauveron et al. 2014).

This thesis aims at investigating and improving the potential of transcritical ORC for WHR through experimental validation and numerical optimization. Two ORC prototypes were used in this study. The previously cited 10 kWe prototype CORSERE, developed for WHR application between 100 and 150 °C, hosted by the CEA. And a second 5 kWe

prototype, developed for solar application for the CPV-Rankine project¹, hosted by the Agricultural University of Athens.

Thesis background and scope are introduced in Chapter I, providing an overview of ORC technological and economic framework.

Chapter II presents the thermodynamic framework by detailing the definitions, equations and performance criteria used along the thesis. Then, the ORC experimental state-of-the-art, compiled in an open-access database, is exposed and analyzed.

In Chapter III, the different tools used in this thesis are introduced. The different experimental setups, the tools and methodology used for experimental data processing, as well as modeling tools for ORC systems understanding and optimization.

Chapter IV focuses on the working fluid pump, an underestimated but major component of transcritical ORC. Energetic and volumetric performances of reciprocating pumps are investigated.

Chapter V investigates supercritical heat transfer, first with a specific test set-up for local heat transfer study. Experimental heat transfer coefficients are compared with correlations from the literature. Then, a plate heat exchanger for global heat transfer study.

In Chapter VI, the influence of the working fluid charge over the ORC is discussed, using numerical tools. Influence and optimization potential of the working fluid charge under various operating conditions is investigated.

Chapter VII focuses on the ORC unit general operation. Expander performances are discussed, as well as the flow rate equilibrium with the ORC pump. ORC energetic and exergetic performances are investigated and compared with similar ORC from the prototype database. An exergetic analysis is presented, as well as the ORC dynamic behavior.

Chapter VIII summarizes the thesis results, as well as research and development opportunities.

¹ European Union funded project, grant agreement n° 315049 [CPV/RANKINE], FP7-SME-2012

Chapter II

Organic Rankine cycle state-of-the-art

1 Thermodynamics applied to ORC

1.1 Energy conversion chain

The core of the thermodynamic science is to study interaction between two types of energies: the work and the heat. The Organic Rankine Cycle is a thermodynamic process which converts heat into work; however different types of energies are involved in the process. Since those energies are different, they must clearly be identified and differentiated.

Table II-1 summarizes the different types of power that may be involved in the ORC. In addition, the required instrumentation for experimental measurement is introduced for practical consideration of each power.

Table II-1 : Summary of power types

Power name	Equation	Instrumentation required
Isentropic power	$W_{is} = \dot{m} \cdot [h(T; P)_{in} - h(s_{in}; P_{out})]$	Pressure and temperature sensors, flow-meter
Adiabatic power	$W_{ad} = \dot{m} \cdot [h(T; P)_{in} - h(T; P)_{out}]$	Pressure and temperature sensors, flow-meter
Indicated power (expander)	$W_{ind} = \dot{m} \cdot \int_{in}^{out} v \cdot dP = \int_{in}^{out} P \cdot dV$	Internal pressure sensors, tachometer
Hydraulic power (pump)	$W_{hy} = \dot{V} \cdot \Delta P$	Pressure and temperature sensors, flow-meter
Mechanical power	$W_{me} = \Gamma \cdot \dot{\Omega}$	Torque-meter and tachometer
Electrical power	$W_{el} = u \cdot i \cdot \cos(\varphi)$	Power-meter / Voltmeter

The isentropic power is the ideal power for a reversible adiabatic machine. The adiabatic power is derived from energy conservation and fluid enthalpy assuming an adiabatic machine. The indicated power is the pressure forces work only. For a pump, if the fluid can be considered as incompressible, it denotes to the hydraulic power and equals the isentropic power. The mechanical power is a pure work but can be complex or impossible to measure. The electrical power is easier to measure and can be considered as pure as the mechanical power.

While heat exchangers, as they are named, only exchange thermal energy, in the working fluid pump and expander, a complex energetic conversion chain is in place. This conversion chain and its relation with the working fluid and the environment depend on the technology used.

Figure II-1 shows pump conversion chain, locating the different powers. Δe_c denotes to the kinetic energy and Φ to the mechanical losses and frictions. Potential energy due to height difference and gravity force is neglected. Note that a variable speed drive (VSD) might be installed or not. For pumps, electromechanical losses are mostly dissipated through heat to the environment. Regarding practical experimental considerations, the adiabatic power is very sensitive to the temperature uncertainty and only the initial electrical input power can be easily measured.

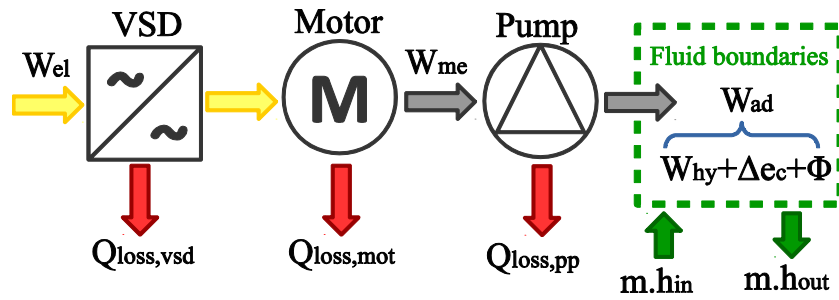


Figure II-1 : Pump energetic conversion chain

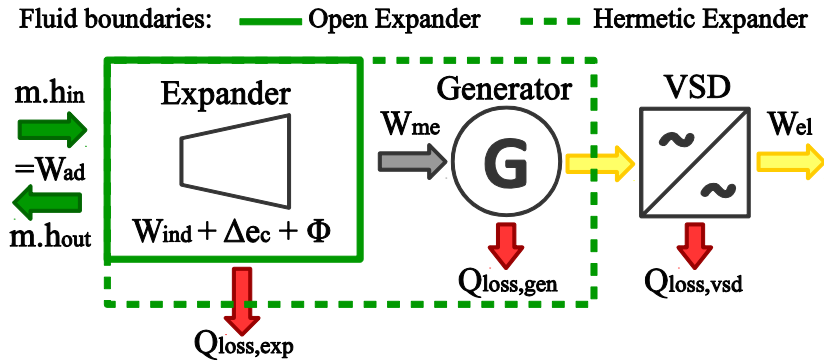


Figure II-2 : Expander energetic conversion chain

Figure II-2 shows expander conversion chain, the relation between the final output power and the adiabatic power depends on the expander type and the expander adiabatic assumption (heat dissipation negligible with respect to the output power). As (Lemort et al. 2009) has shown, volumetric machines cannot be considered as adiabatic. Especially, as most experimental volumetric expanders are modified compressors, and compressors are designed to dissipate heat to reduce the compression work. Large turbo-expanders are often considered as adiabatic machines, but this assumption should be validated for micro-turbines. Therefore, adiabatic power does not allow an appropriate comparison of different expander powers in practice. The mechanical power is more adapted but cannot be measured in hermetic expanders, so electrical power should be preferred, although some expanders only have direct mechanical output. To objectively compare expanders and pumps performances, the electrical efficiency (Eq. II-1) is preferred to the isentropic efficiency (Eq. II-2).

$$\eta_{exp} = W_{el,exp} / W_{is,exp} \quad \text{Eq. II-1}$$

$$\eta_{is,exp} = W_{ad,exp} / W_{is,exp} \quad \text{Eq. II-2}$$

Heat is more complex than it seems, and is closely related to its environment. While a liter of pure water at 40 °C will always have the same energy, it will warm up the air in the arctic, but do nothing in the desert. To account for the surroundings effect, and fairly compare the two types of energies used in thermodynamics: heat and work, the concept of exergy was introduced by J. Willard Gibbs (Gibbs 1873) based on the second law of thermodynamics, while the term of exergy was latter on introduced by Z. Rant (Rant 1956).

The exergy is the available or maximum useful work which can be extracted from a system as it reversibly comes into equilibrium with its environment (Tsatsaronis 2007). If energy is a quantity, exergy would be the quality. Unlike energy, exergy is destroyed during an irreversible process, as entropy increases. The destroyed exergy is called anergy. The exergy of heat is defined below, with T_0 the ambient temperature:

$$E_{heat} = Q \cdot \left(1 - \frac{T_0}{T}\right) \quad \text{Eq. II-3}$$

The specific exergy of a fluid is defined below, where the subscript 0 denotes to the environment or equilibrium conditions:

$$e = h - h_0 - T_0 \cdot (s - s_0) \quad \text{Eq. II-4}$$

In the present thesis, for ORCs, the environment temperature T_0 will be set to the heat sink temperature inlet $T_{sink,in}$. The pressure potential of heat source and heat sink will not be considered, and therefore the environment pressure P_0 will be set to their respective pressure outlet. Since the working fluid is in a fully hermetic loop, the equilibrium pressure will be set to the saturation pressure of the working fluid at the sink temperature: $P_0 = P_{sat}(T: T_{sink,in})$. This corresponds to the minimum pressure and energetic level achievable, if the fluid loop is fully cooled down by the heat sink.

For heat transfer with variable temperature, such as sensible heat sources, the thermal exergy transferred can be defined as:

$$\Delta e = \int \left(1 - \frac{T_0}{T}\right) \cdot dq \quad \text{Eq. II-5}$$

If the specific heat capacity is assumed to be constant, the thermal exergy becomes (Woudstra et al. 2010):

$$\Delta e = \int \left(1 - \frac{T_0}{T}\right) c_p \cdot dT = c_p \left(T - T_0 - T_0 \cdot \ln\left(\frac{T}{T_0}\right)\right) \quad \text{Eq. II-6}$$

Figure II-3 presents heat transfer in a fictive evaporator, in the form of a value diagram (Woudstra et al. 2010). Following the previous thermal exergy equation, the exergy destroyed during the heat transfer corresponds to the area between the red and blue curves.

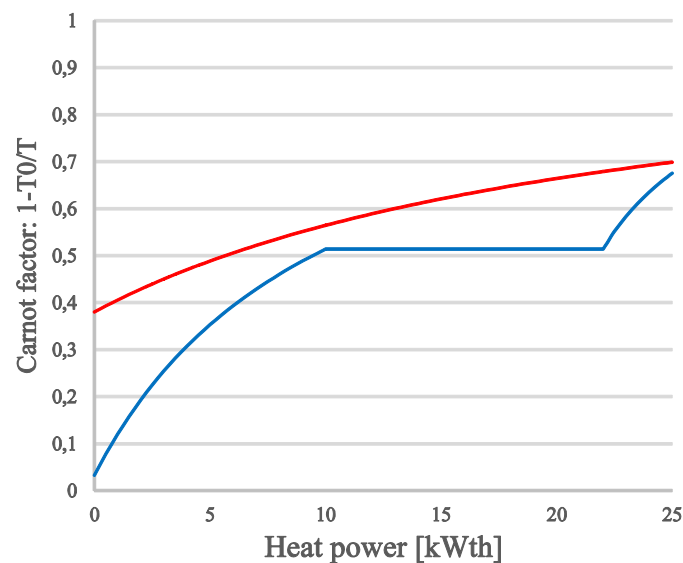


Figure II-3 : Value diagram of an evaporator

1.2 Types of heat sources

Organic Rankine Cycles can be used for a wide variety of heat sources. Each source, each application has its specificities, limitations, and objectives. Heat sources can be classified in two main categories based on the system input: the closed heat sources and the open heat sources (Borsukiewicz-Gozdur 2013; Braimakis and Karellas 2017).

In closed sources, the input is a heat flow Q_{sup} supplied to the ORC. The hot fluid (HF) inlet temperature depends on the hot fluid outlet and the heat flow (Figure II-4), and is usually limited by technological constraints. Closed sources includes biomass applications: the input is a mass flow rate of fuel m_{fuel} with a given lower heating value (LHV_f), resulting in a fuel heat flow $Q_{\text{fuel}} = m_{\text{fuel}} \cdot \text{LHV}_f$. And solar applications: the input is a solar irradiance q_{sol} in W/m^2 received by a given area of solar thermal collector A_{col} , resulting in a solar heat flow $Q_{\text{sol}} = q_{\text{sol}} \cdot A_{\text{col}}$.

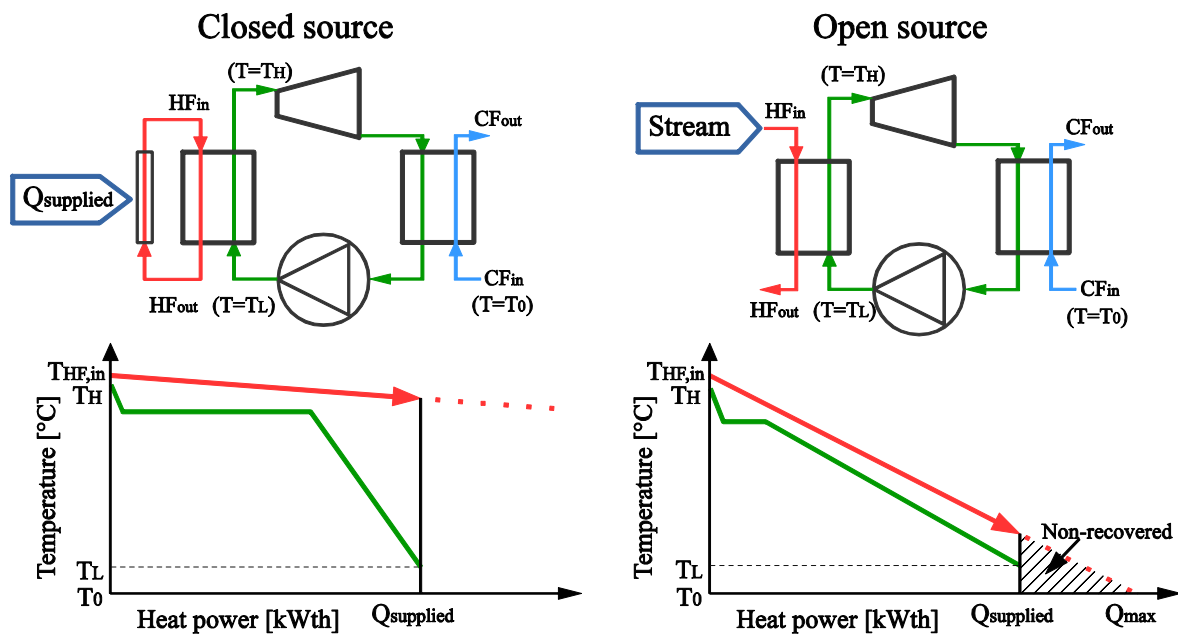


Figure II-4: Scheme and temperature-heat diagram for closed and open heat sources

In open sources, the input is a hot stream characterized by its mass flow rate (m_{HF}), specific heat (c_p) and temperature ($T_{\text{HF},\text{in}}$). This input is not influenced by the hot fluid outlet, which is not recovered. The actual supplied heat power Q_{sup} is lower than the maximum heat power Q_{max} that could be recovered if the stream was cooled down to the reference temperature T_0 . Open sources includes geothermal applications: the input is a stream with a maximum temperature corresponding to the ground temperature, this temperature HF_{in} is not influenced by the injection temperature HF_{out} , the mass flow rate and specific heat depend on the geothermal plant design. Open sources also includes waste heat recovery applications, or residual heat exergy from process as defined by (Bendig, Maréchal, and Favrat 2013): the input stream characteristics (m , c_p , $T_{\text{HF},\text{in}}$) are fully imposed since the ORC does not influence the process.

In closed sources, the hot fluid mass flow rate can be adjusted without or with limited influence over the system input Q_{sup} . Therefore, the flow rate can be adjusted to have an isothermal or quasi-isothermal heat source. In this case, we know the ideal thermodynamic

cycle would be the Carnot cycle (Carnot 1824). Note: closed sources are also called latent or quasi-latent sources due to their temperature profile.

In open sources, the hot fluid would be ideally cooled down to the reference temperature T_0 . If the heat capacity of the fluid is constant, the ideal thermodynamic cycle is the Lorentz or triangular cycle (Colonna et al. 2015; DiPippo 2007).

1.3 Performance criteria

There is a wide range of heat to power conversion systems, and a wide range of ORC modules for very different applications as we saw previously. It is therefore necessary to define clear, objective and fair criteria to evaluate and compare the performance of each unit: the efficiency.

There are many different efficiency definitions. Depending on who is building it, what the boundaries are and what the objective is. For ORC, a large number of efficiencies are often used; thermodynamic efficiencies, such as energetic or thermal efficiency, second law efficiency, exergetic efficiency etc... (Lecompte et al. 2015) Economic criteria such as the capital cost of power capacity in €/kW, the cost of power production in €/kWh, levelized cost of electricity or the return on investment (time or rate) (Astolfi et al. 2014; Toffolo et al. 2014). Some design studies also use hybrid criteria such as the heat exchanger area per installed capacity (m^2/kW) assuming that the exchanger area is proportional to the capital cost, or expander volume ratio (Branchini, De Pascale, and Peretto 2013). The following section will focus on thermodynamic criteria.

At first, efficiency is defined as the ratio of the output and the input. However, for energy, due to the first law, this ratio would always be 1. Therefore, functional efficiency is used instead (Woudstra 2004; Marmolejo-Correa and Gundersen 2012). The efficiency is the ratio of the useful product and the input source or fuel. However, it stills an ambiguity on what the useful product is and what the input source is, since it depends on the chosen boundaries of the system.

In the ORC unit, the pump consumption can be seen as an input (ORC_1) or as an internal consumption subtracted from the production (ORC_2) as shown in Figure II-5(a). Since the pump consumption is an input due to the implementation of the ORC unit, it should be subtracted from the useful production. We will define the efficiency as:

$$\text{Efficiency} = \frac{\text{Useful Production} - \text{Necessary Consumption}}{\text{Available Input}}$$

Note, for CHP units, the heat released by the condenser Q_{sink} is accounted for a useful production.

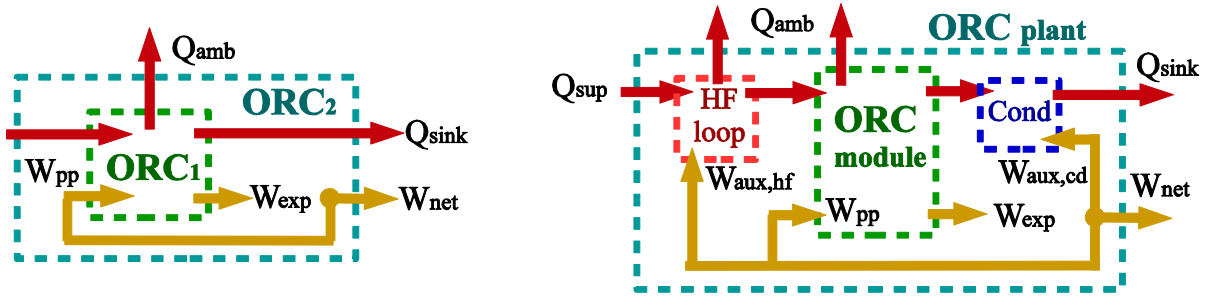


Figure II-5 : Efficiency boundaries (a) in the ORC unit - (b) ORC module vs plant

Another boundary ambiguity comes from the distinction between the ORC module and the ORC plant as shown in Figure II-5(b). In the ORC plant, the necessary consumptions also includes auxiliaries consumption such as hot fluid loop pumps, fans consumption of the air condenser or chiller, geothermal brine circulation pumps etc... Since those consumptions are related to constrains and choices exterior to the ORC, they should not be considered for ORC only comparison. Note, as we saw previously, different types of power co-exist in an ORC. For the net useful output W_{ORC} calculation, all the powers should be consistent. The electric power will be preferred in the present thesis since it is widely used and often corresponds to the final output power type:

$$W_{ORC} = W_{el,exp} - W_{el,pp} \quad \text{Eq. II-7}$$

Now the output is clarified, we can focus on the system input. In the efficiency definition, we can either use the energetic input or the exergetic input. Exergy is more appropriate to evaluate heat engine performances (DiPippo 2004; Schuster, Karellas, and Aumann 2010) since by definition, it is the maximum useful work available, and the exergetic efficiency would be a ratio of a real work by a maximum work.

Efficiency definition should also be made between closed and open sources. Table II-2 summarizes the input and efficiency for both closed and open source case, considering both the energetic and exergetic approach.

Table II-2: ORC system possible inputs and resulting efficiencies

	Energy	Exergy
Closed source	$Q_{sup} = \dot{m}_{hf} \cdot c_{p,hf} \cdot (T_{HF,in} - T_{HF,out})$ $\eta_{th} = W_{ORC}/Q_{sup}$: ORC thermal efficiency	$E_{sup} = \dot{m}_{hf} \cdot (e_{HF,in} - e_{HF,out})$ $\epsilon_{ORC} = W_{ORC}/E_{sup}$: ORC exergetic efficiency
Open source	$Q_{max} = \dot{m}_{hf} \cdot c_{p,hf} \cdot (T_{HF,in} - T_0)$ $\eta_{rec} = W_{ORC}/Q_{max}$: ORC recovery eff.	$E_{max} = \dot{m}_{hf} \cdot (e_{HF,in} - e_{HF}(T = T_0))$ $\epsilon_{rec} = W_{ORC}/E_{max}$: ORC exerg. recovery eff.

The exergy requires precise data on the fluid properties to be calculated. Considering only the thermal exergy for the hot fluid and assuming a constant specific heat, Eq. II-6 can be used to calculate the supplied exergy:

$$E_{sup} = \dot{m}_{hf} \cdot c_p \left[(T_{HF,in} - T_{HF,out}) - T_0 \cdot \ln \left(\frac{T_{HF,in}}{T_{HF,out}} \right) \right] = Q_{sup} \left[1 - T_0 \frac{\ln(T_{HF,in}/T_{HF,out})}{T_{HF,in} - T_{HF,out}} \right] \quad \text{Eq. II-8}$$

In the same way, we can derive the recoverable exergy of the hot fluid:

$$E_{max} = Q_{sup} \frac{T_{HF,in} - T_0 (1 + \ln(T_{HF,in}/T_0))}{T_{HF,in} - T_{HF,out}} \quad \text{Eq. II-9}$$

Additionally, we can introduce the heat recovery efficiency η_{hr} (Sylvain Quoilin et al. 2011) and the hot exergy recovery efficiency ε_{hr} :

$$\eta_{hr} = \frac{Q_{sup}}{Q_{max}} = \frac{(T_{HF,in} - T_{HF,out})}{(T_{HF,in} - T_0)} \quad \text{Eq. II-10}$$

$$\varepsilon_{hr} = \frac{E_{sup}}{E_{max}} = 1 - \frac{T_{HF,out} - T_0 (1 + \ln(T_{HF,out}/T_0))}{T_{HF,in} - T_0 (1 + \ln(T_{HF,in}/T_0))} \quad \text{Eq. II-11}$$

With those assumptions, ORC exergetic efficiencies (ε_{ORC} & ε_{rec}) only require heat power and inlet/outlet temperatures of the hot fluid to be computed.

For closed source applications, in the ideal case of a Carnot cycle with an isothermal source, the hot fluid temperature glide tends toward zero and the ORC exergetic efficiency ε_{ORC} tends toward the second law efficiency η_{II} , which is the ratio of the thermal efficiency η_{th} and the Carnot efficiency (Eq. II-12). The second law efficiency is useful to compare the degree of perfectness of the ORC without the influence of the heat source temperature. However, the thermal efficiency η_{th} is preferred when the heat source temperature is an optimization parameter of the ORC system.

$$\lim_{T_{HF,out} \rightarrow T_{HF,in}} \varepsilon_{ORC} = \frac{W_{ORC}}{Q_{sup}(1 - T_0/T_{HF,in})} = \frac{\eta_{th}}{\eta_{Carnot}} = \eta_{II} \quad \text{Eq. II-12}$$

For open source applications, the target is to maximize the power extracted from the hot stream. The ORC exergetic recovery efficiency ε_{rec} is more appropriate than the ORC recovery efficiency η_{rec} to compare systems with different heat source temperature.

2 Experimental ORC database

2.1 Data compilation

In order to get a global vision of the ORC experimental state-of-the-art, an extensive, collaborative open-access database is built (Landelle and Tauveron 2016; Landelle et al. 2017). The database presented in this section contains more than 100 unique ORC benches.

Data are collected from scientific journals, conference papers or theses. Only complete Rankine units are considered. Therefore, prototypes without expander (simulated with a valve), expander test benches (gas cycle), flash cycles and pumpless prototypes are excluded. Since this study focuses on organic Rankine cycle, classic Rankine cycles are excluded. It is decided to exclude CO₂ cycles due to the CO₂ specific properties.

References referring to identical test benches are identified and grouped together to avoid double counts, with a unique identifier sets to each reference and each test bench. However, changes of expander, working fluid or heat sources are tracked using additional identifier as they can provide useful information and significant changes on unit performances and behavior.

Both qualitative and quantitative information on prototypes are collected. Table II-3 summarizes the database layout and types of data collected, the complete database layout with description is available in Appendix A. For cycle numerical parameters (temperature, pressure, power...), both minimum and maximum reached values were collected. In addition, a second database gathers information at a specific running point – maximum efficiency and/or maximum power – but for a limited number of parameters: working fluid temperatures and pressures, expander & pump powers, heat & cold source temperatures, powers and flow rate.

Data are manually extracted from text, tables and graphs. Non-available parameters are calculated, when possible, using the *Coolprop* library (Bell et al. 2014) for fluid properties or left empty. A data reduction is processed on qualitative data in order to provide a uniform nomenclature (*e.g.*: fluid names, expander and pump technologies).

There are currently no standards for ORC power or efficiency nomenclature and definitions, although some authors urge and propose a shared terminology (Colonna et al. 2015). As we saw previously, many definitions are available and each author uses his own definition based on available instrumentation and personal choices, bringing confusion. Therefore, data are discriminated and classified in a harmonized frame.

Table II-3: Experimental ORC database layout

General Info	Working fluid	Cycle conditions	Heat & Cold source	Pump	Expander	Heat Exchangers	Lubrication	Additional Components	
Country	Name	Expander inlet temperature	Energy source	Technology	Technology	Evaporator Type	Oil proportion	Subcooler	
University	Category	Superheating	Temperature	Driver	Generator	Evaporator Area	Injection type	Filter	
Target application	Critical temperature	Pump inlet temperature	Heat power	Control	Control	Condenser Type	Separator	Vapor Tank	
Specificity	Critical pressure	Subcooling	Flow rate	Nominal power	Nominal power	Condenser Area	Pump	Liquid Tank	
CHP	Saturation slope (ξ)	High pressure	Heat transfer fluid	Shaft speed	Built-in volume ratio	Internal HEX	Tank	Other	
		Low pressure		Flow rate			Swept volume		Cooler
		Net power		Powers			Shaft speed		Filter
		Cycle efficiencies		Efficiencies			Pressure ratio		
					Powers				
					Efficiencies				

Empirical correlations, based on available data, are considered to estimate the expander electrical power; in order to increase available data for expander power.

First, the adiabatic assumption is considered. To evaluate the validity of such assumption, the adiabatic efficiency is calculated on available data:

$$\eta_{ad} = W_{el}/W_{ad} \text{ or } W_{me}/W_{ad} \quad \text{Eq. II-13}$$

The adiabatic efficiency is found to be of 56 % in average, with an inter-quartile between 35 and 77 %, whatever the expander technology. Therefore, adiabatic assumption is not valid and mechanical or electrical power cannot be derived from the adiabatic power.

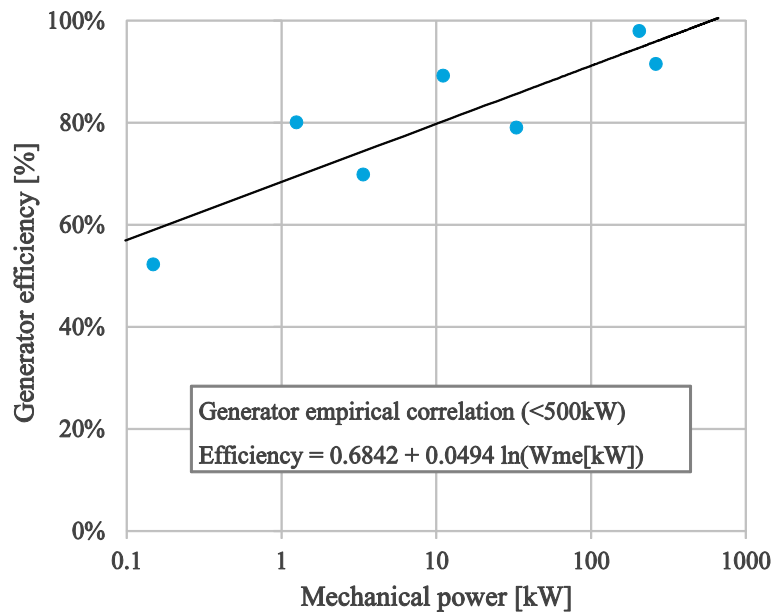


Figure II-6: Expander generator efficiency empirical correlation

Then, an empirical correlation of generator efficiency is built with available data, as shown in Figure II-6. The correlation is valid below 500 kW of mechanical power. Even if the correlation is not highly accurate and validated, it is deemed as sufficient to be used as a correction factor to estimate the expander electrical power from the mechanical power.

2.2 Database overview

Prototypes from the database cover a wide range of conditions. It goes from a few Watts to a MW of gross output power (expander electrical power), with hot source temperatures ranging from 60 to 675 °C. Figure II-7 shows a hot temperature – power map of the references classified by target application. 10 % of the units have hot sources below 90 °C, 10 % above 250 °C and the inter-quartile is between 100 and 160 °C. Prototypes are mostly in the kW scale range.

Regarding the prototypes targeted application, excluding not specified cases, 61 % are dedicated to waste heat recovery, including 19 % specifically for ICE WHR. 24 % are for solar application, including 6 % of solar combined with another heat source (biomass, gas, WHR), 11 % for geothermal, 4 % for biomass and 1 % for natural gas. WHR proportion is

similar to the proportion pointed out by (Tartière and Astolfi 2017) for commercial units, but they are drastically different for biomass, geothermal and solar applications. Likely, this is due to biomass and geothermal relative maturity and large scale, while solar application is still looking for a sustainable business model.

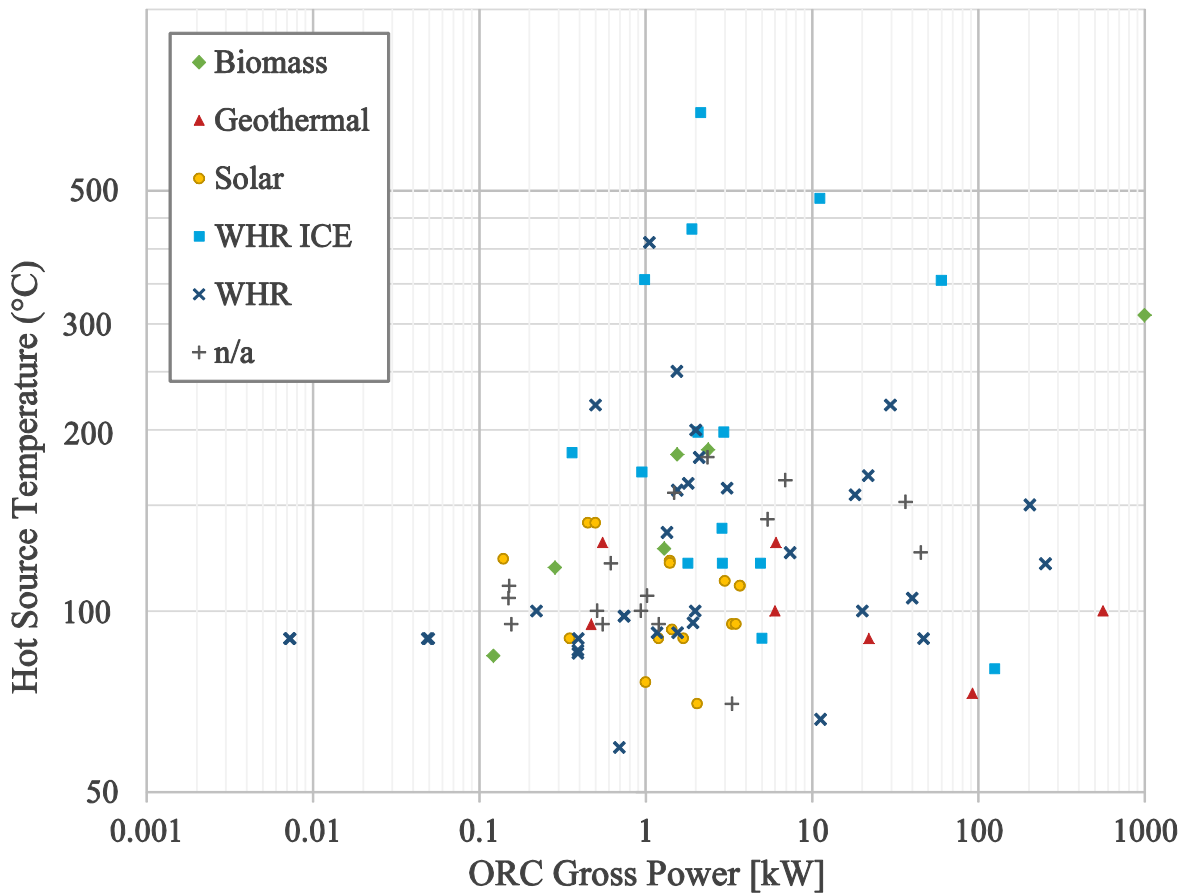


Figure II-7: Map of ORC references - hot source temperature vs. gross power

A great disparity among world regions is observed. Europe and Asia account for 86 % of the installed prototypes. Asia, especially China, as a large industrial sector and therefore mainly focus on industrial WHR. Europe, on the other hand, has very diversified target applications, with some country focusing on a single application and others investigating most of them.

In addition, 13 % of ORCs are dedicated to combined heat & power (CHP) production, but they are mostly closed sources: 100 % of biomass or gas units and 30 % of the solar units aim to produce CHP.

In practice, most prototypes use controllable and flexible heat source: 48 % use electric heaters and 20 % oil or gas burner versus 14 % for waste heat (including 11 % of engine waste heat), 9 % for solar field, 5 % biomass, 2 % geothermal stream. To transfer heat, water or glycol-water is widely used (54 %, including 8 % of steam) as well as thermal oil (27 %) or exhaust gas/air (15 %). In the same way, to condense the working fluid, 36 % use a cooling tower, 34 % water flow (sea or tap) and 27 % air chillers. 88 % of the references use water or water-glycol mixture as cooling transfer fluid, but 11 % performs direct condensation, usually with air chillers.

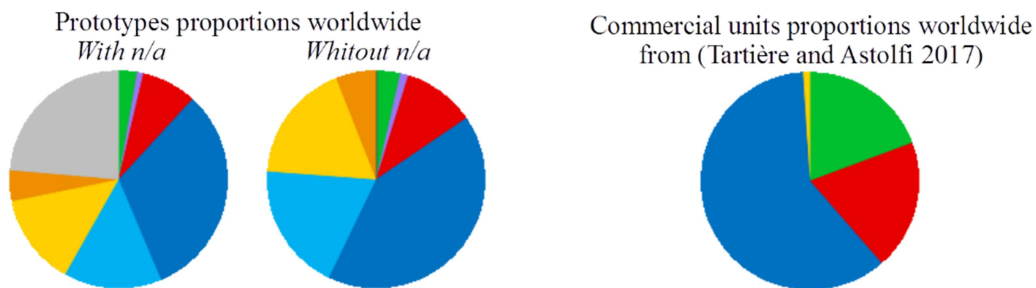
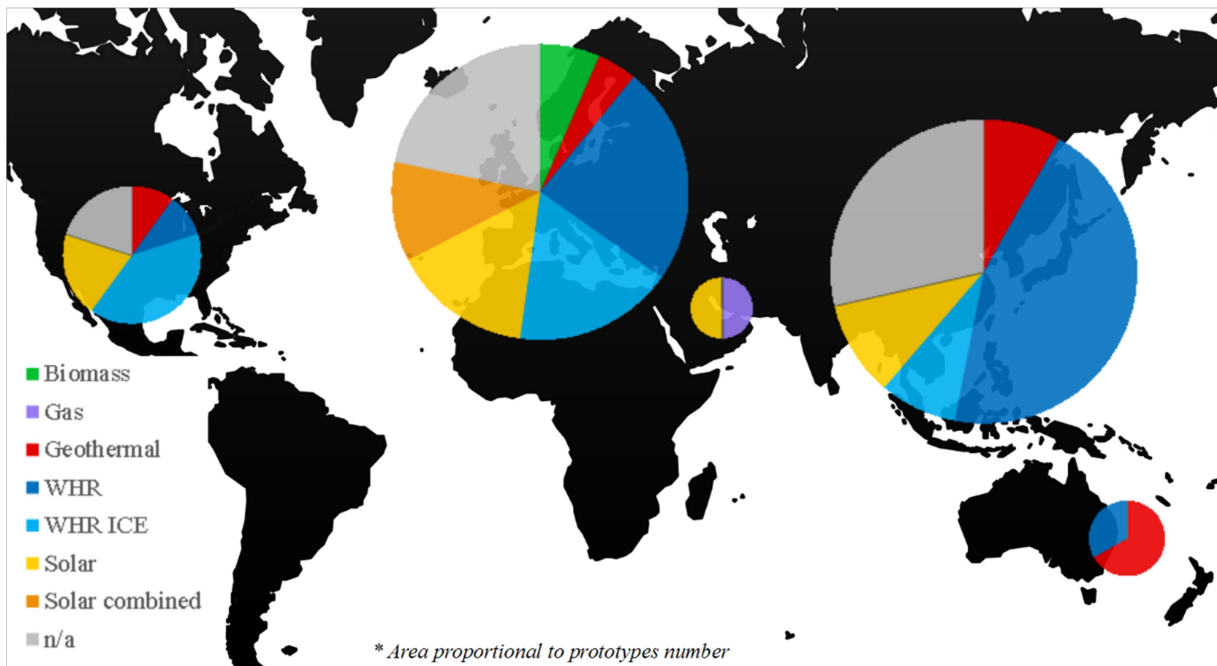


Figure II-8: Target application proportions by regions and worldwide

Figure II-9 shows the evolution of refrigerant categories used as ORC working fluids over time. CFC quickly declined in the 80s due to the Montreal protocol, mostly replaced by HCFC in the 2000 decade. HFC are now the dominant refrigerants even if HCFC are still used, mainly in Asia. Recently, HFO (R1233zdE) started to be tested on ORCs (Guillaume et al. 2016; Eyerer et al. 2016; Molés et al. 2016) and research on fluid mixtures increased (Bamorovat Abadi, Yun, and Kim 2015; T. Li et al. 2015; Jung, Taylor, and Krumdieck 2015; Wang et al. 2016). Overall, 52 % of the working fluids used are HFC, 20 % HCFC, 7 % Hydrocarbons, 6 % HFE, 4 % Mixtures, 2.5 % PFC, 2.5 % CFC, 2.5 % HFO and 5 % of others. There are over 30 different fluids, but only three fluids are used two times out of three: R245fa (38 %), R123 (18 %) and R134a (7 %).

The number of experimental references can be a good track of R&D investments on the ORC technology. The 2011-2015 period shows a strong increase in the number of references, but a decline is observed in 2016. Similar trend is observed by (Tartière and Astolfi 2017) for new commercial units, as discussed in the introduction chapter (0). A bibliometric analysis is performed on *Scopus* for the “Organic Rankine Cycle” keyword, relatively to the “Energy” keyword evolution, as shown in Figure II-10. Analysis is performed for scientific literature and patents, as previously done by (Fu, Hsu, and Liu 2014). Scientific literature shows a similar trend, with a mean annual growth rate of 40 %

from 2000 to 2014 in absolute number of references, and a proportion increase from 0.2 % to 3 % in the energy field, and followed by a relative slowdown since 2015. Similar trend is observed for patents with a clear growth since 2000, and a slowdown since 2012.

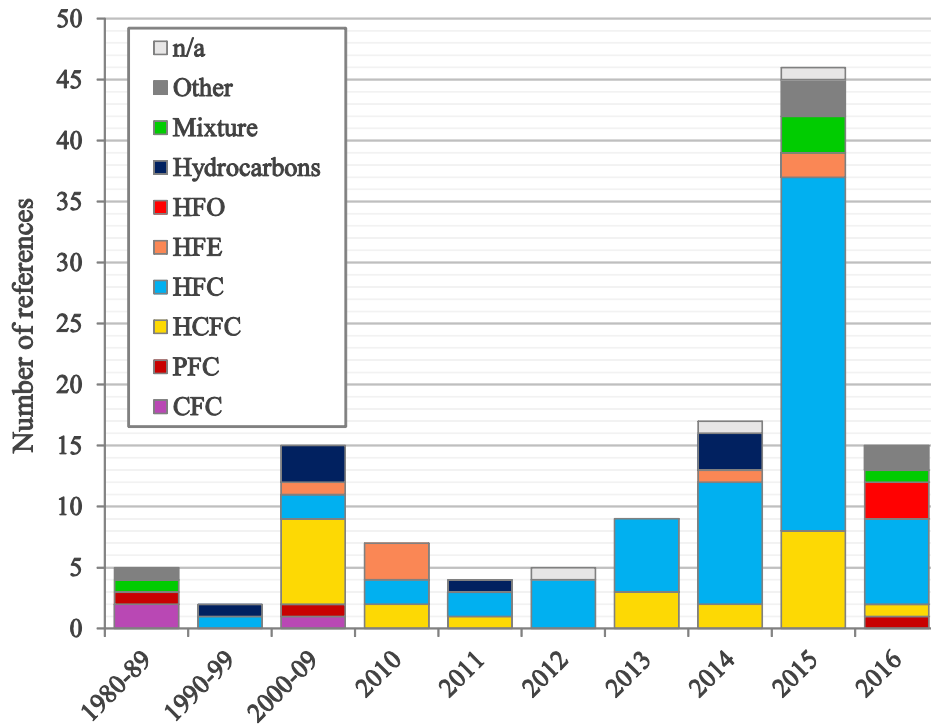


Figure II-9: Type of refrigerant used as working fluid over time

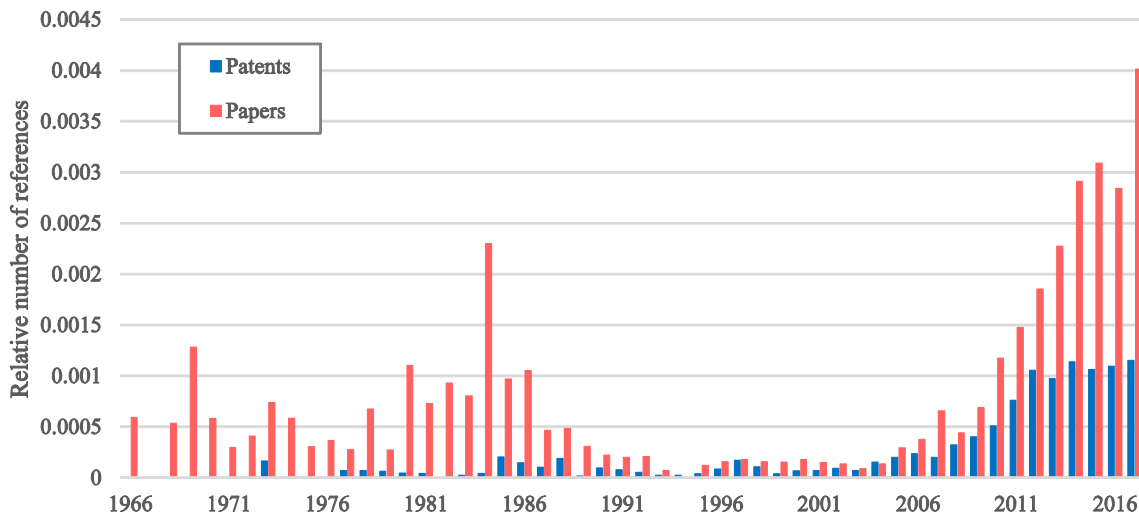


Figure II-10: Patents and publications number of references relatively to the energy field

Figure II-11 shows the maximum operating condition of those working fluids in the cycle. In average, the reduced temperature – ratio over the critical temperature in Kelvin – is about 0.9 at the evaporator outlet, and the reduced pressure is about 0.4. Four ORCs running at supercritical conditions are reported (Kosmadakis et al. 2016; Demierre, Rubino, and Schiffmann 2015; Hsieh et al. 2017; Cipolla 1980).

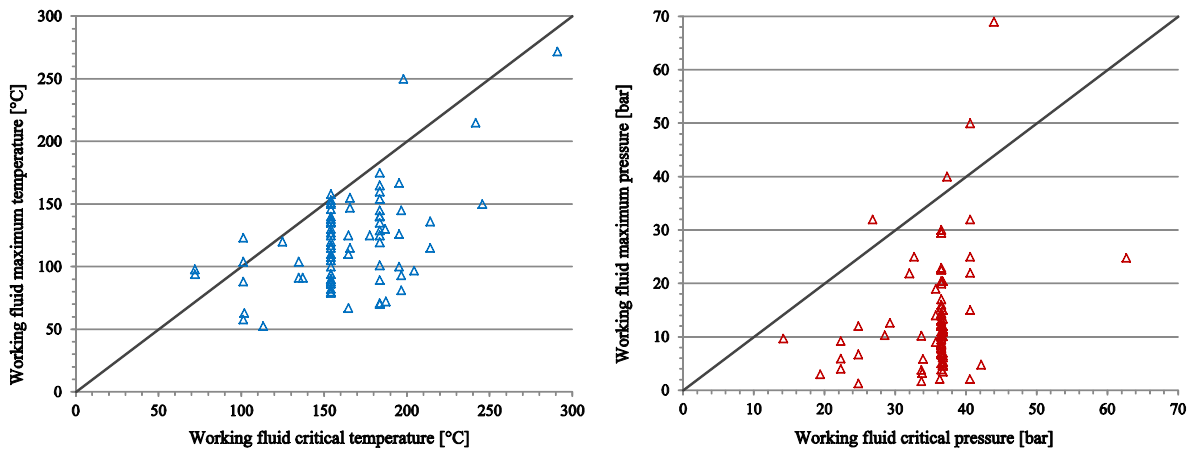


Figure II-11: Working fluids maximum operating conditions in the ORCs

The expander is the most investigated ORC component and many different technologies are tested. A fourth of the references are turbo-expanders, and 3/4 of them are radial type. Others technologies are volumetric expanders. Scroll is the most used (45 %), followed by screw and rotary expanders (12 % each) plus a few references of pistons expanders.

Figure II-12 shows boxplots of expander pressure ratio, shaft speeds and power scale for the main technologies. Turboexpander covers the all range of pressure ratio, and a wide range of power scale – from a kW to a MW; however its higher shaft speed – especially small scale turbines – requires high speed generator or speed reduction. If scroll, rotary and piston have the same power scale range, each one covers a different pressure ratio range. To control the expander speed, there are two main strategies. Two thirds controls the load with electrical resistances or mechanical brakes, the other third use variable frequency drive or connection to the electrical grid for electrical frequency control, mainly with AC asynchronous generators.

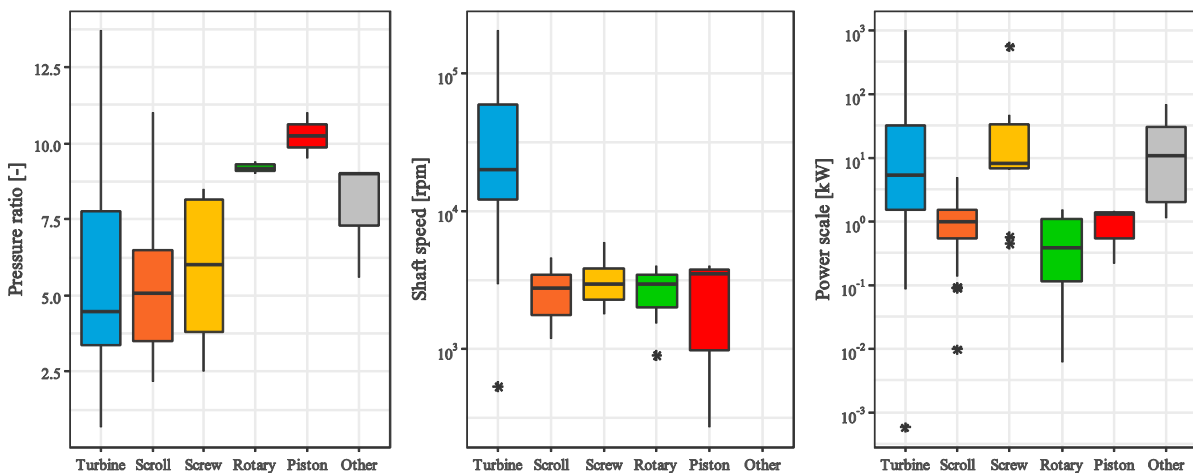


Figure II-12: Expanders range of pressure ratio, shaft speed and power scale per technology

Figure II-13 shows the expander electric power-efficiency map. Expander efficiency is strongly correlated with its power scale. As expected by (Sylvain Quoilin et al. 2012) there is an optimal technology depending on the power scale. Scroll expander seems more adapted below 5 kWe, screw expander for the 5-50 kWe scale and turboexpander above. Rotary technology is in the same power scale than scroll, but has a lower mean efficiency.

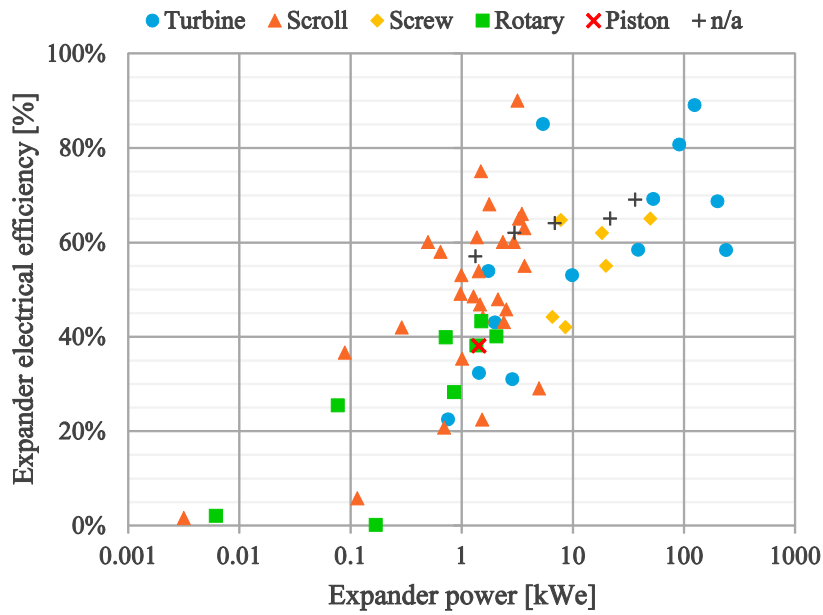


Figure II-13: Electric power and efficiency map of expanders

Different lubrication strategies are implemented depending on expander technology (Figure II-14). Turbines are mostly oil-free expanders, but bearings lubrication may be necessary. Some authors used working fluid liquid injection for bearings lubrication (Guillaume et al. 2016). Some volumetric expanders, especially scrolls, run without lubrication. When oil is added, there are two main strategies: create a mixture of working fluid and oil circulating in the ORC – in average 5 % of oil mass fraction; or use an additional oil-loop. This solution is more complex as it requires a secondary oil circuit to separate the oil from the fluid and pump it back to the expander inlet or bearings. However, it prevents oil to circulate in the heat exchangers, which would likely reduces the heat transfer coefficient and increases the pressure drop (Y. S. Chang et al. 2014). In average, the expander efficiency increases by 6 percentage points with a lubrication.

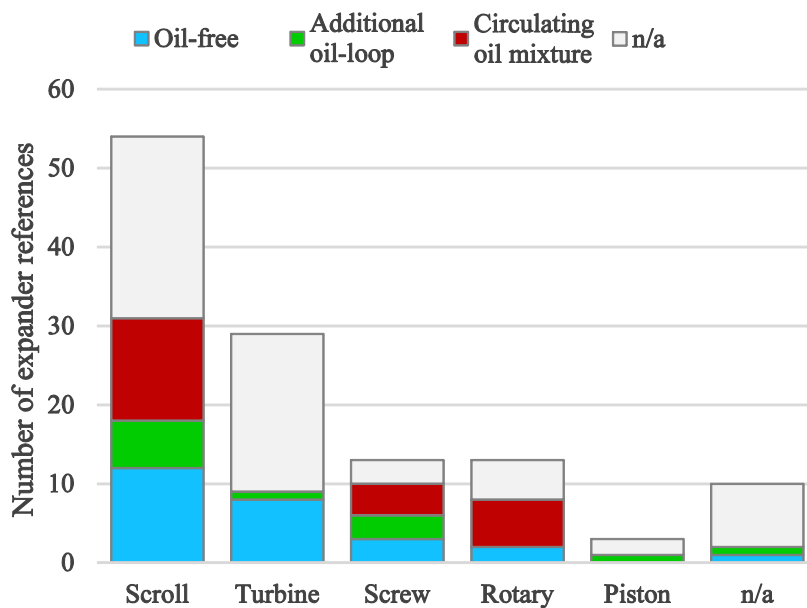


Figure II-14: Expander lubrication strategies

Many different pump technologies can be used on ORC, we group them in 3 categories: reciprocating (56 %) includes diaphragm, piston and plunger pumps; rotary (11 %) includes gear, rotary piston and rotary vane pumps; and centrifugal (30 %) mono or multistage pumps. A pumpless concept was experienced by (Yamada, Watanabe, and Hoshi 2013) or (Gao et al. 2015). 95 % of the pumps are driven by electric motor, while (Larjola 1995; Turunen-Saaresti et al. 2006) used direct expander mechanical shaft to drive the pump.

Figure II-15(a) shows pump operating condition map with the maximum mass flow rate and the maximum pressure lift. Figure II-15(b) shows a pump performance map. Centrifugal pump performs better above 1 kW of hydraulic power and are the dominant technology for flow rates above 1 kg/s. They can handle pressure lift as high as 20 bar, even at low flow rate. Reciprocating pump perform better below 1 kW of hydraulic power and can handle very high pressure lift. As for expanders, pump electric efficiency is correlated with its power scale.

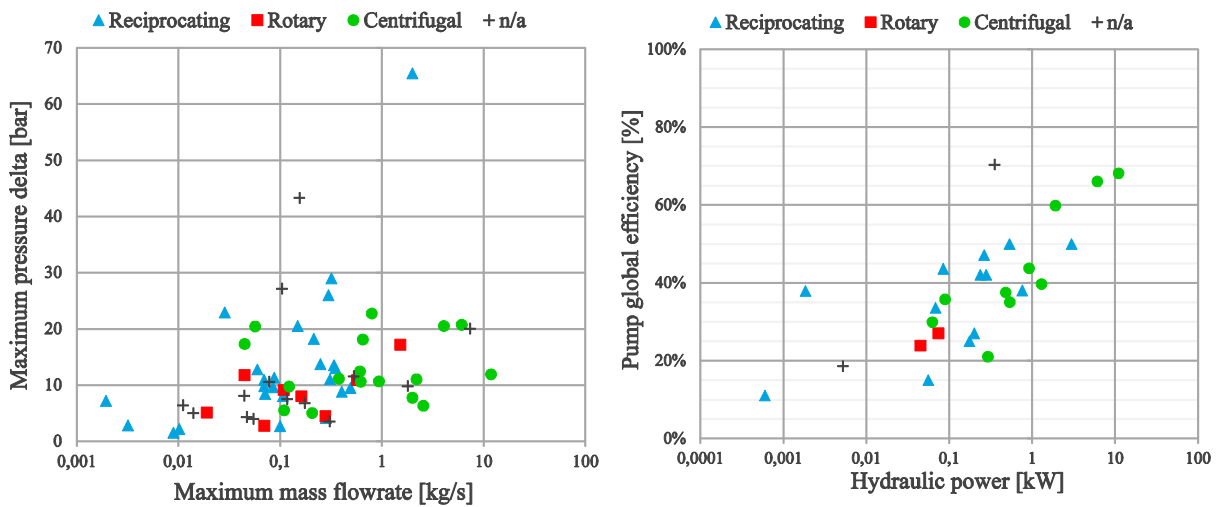


Figure II-15: (a) Pumps pressure lift vs. flow rate - (b) Pumps efficiency vs. hydraulic power

The ORC is usually composed by at least two heat exchangers: the evaporator and the condenser. A common supplementary heat exchanger is the internal heat exchanger (IHE) or regenerator. The IHE recovers expander exhaust superheat to pre-heat the pressurized liquid before entering the evaporator.

Figure II-16 shows the types of heat exchangers used for those 3 main ORC components. Plate heat exchanger is the major technology, almost 75 % of evaporators and condensers. Then, shell & tubes and various types of tube exchangers. Only 23 % of ORCs have an IHE. As expected by (Bao and Zhao 2013), the IHE usage increase with the organic fluid dryness, as they have a higher superheating at the expander outlet.

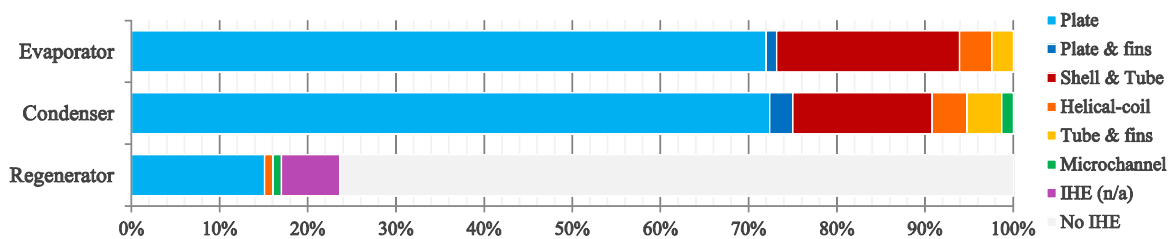


Figure II-16: Heat exchanger technologies

Auxiliary components are often added to the simple ORC configuration. 58 % of the authors declare using a liquid tank at the condenser outlet to absorb the charge variation. 18 % uses working fluid filter. 12 % use vapor separator or vapor tank at the evaporator outlet to avoid liquid droplets at the expander inlet. To prevent cavitation 6 % uses a subcooler prior to the pump and 3 % a pre-feed pump. A pulsation dumper can be added (3 %) to reduce reciprocating pumps pressure and flow rate pulsations.

2.3 Database statistical analysis

The prototype database is merged with a commercial ORCs database from (Tauveron, Colasson, and Gruss 2015), where possible duplicates are removed. The enlarged database now ranges to ORC units up to 10 MW and increased the number of references in the MW scale. Since only a few references provide the pump electrical consumption, the ORC gross electrical power $W_{\text{ORC,gross}} = W_{\text{exp,el}}$ is used as the ORC output in the different efficiencies definitions.

Figure II-17 and Figure II-18 show respectively the evolution of ORC thermal efficiency η_{th} with ORC power and hot temperature, distinction is made between the different expander technologies. A centered sliding average is plotted and provides the mean evolution. The ORC thermal efficiency is closely linked to its power scale, and as expected, to the hot source temperature. Commercial units are usually larger scale but also higher in temperature leading to higher efficiency.

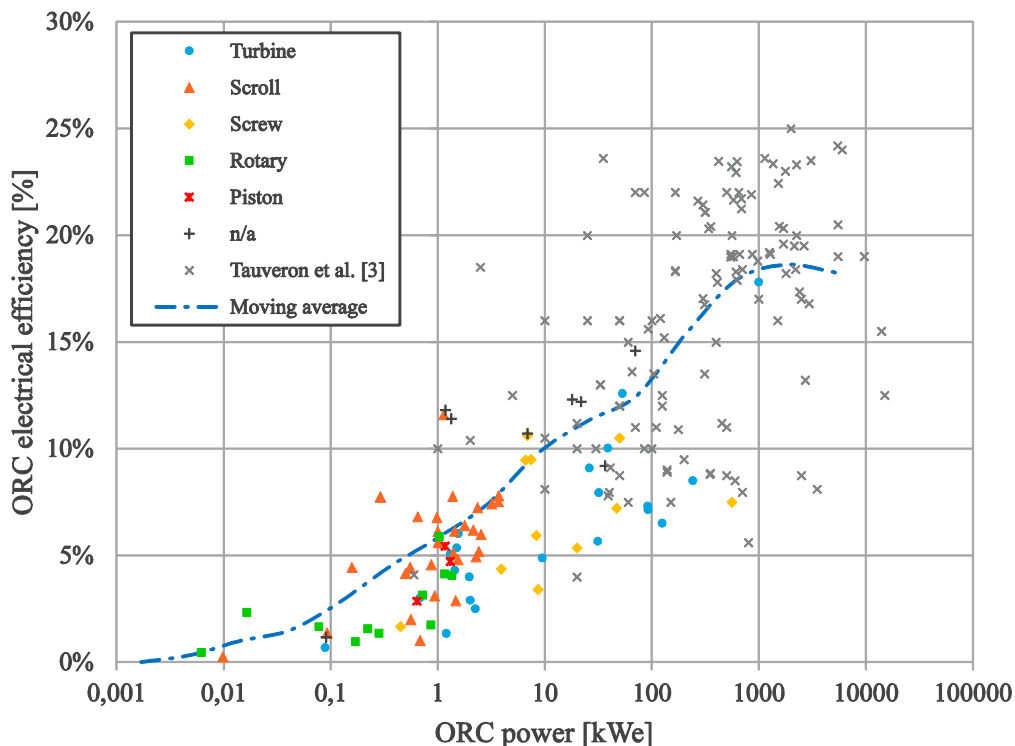


Figure II-17: ORC power and thermal efficiency map

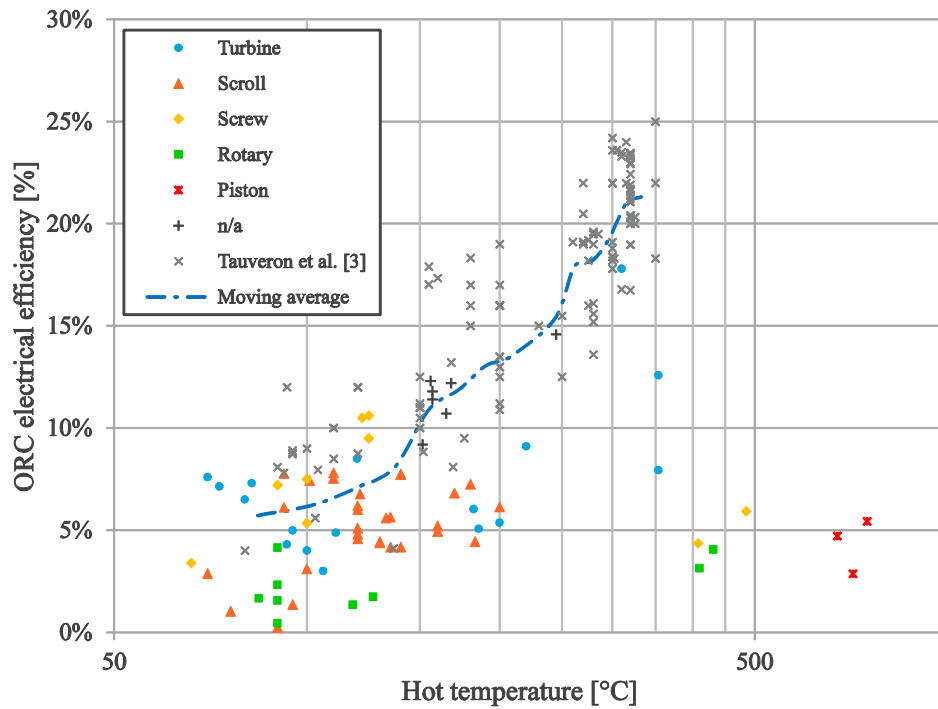


Figure II-18: Hot temperature and ORC thermal efficiency map

Figure II-19 shows a map of ORC second law efficiency η_{II} with ORC power scale. The moving average has an inflection point for ORC power around 20 to 50 kWe. This inflection point could represent the technological maturity limit. But it is located at the transition zone between both databases and may be due to intrinsic methodology difference between the two databases. The half-Carnot's efficiency ($\eta_{II} = 50\%$) seems to be a limit for Organic Rankine Cycle efficiency.

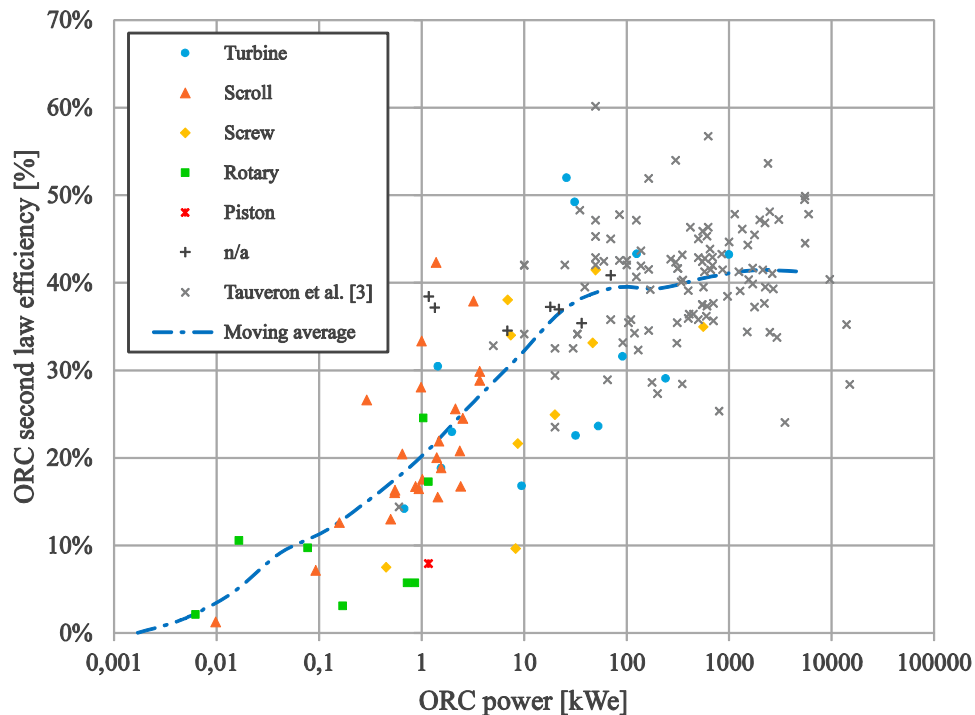


Figure II-19: ORC power and second law efficiency map

Figure II-20 shows the ORC exergetic recovery efficiency ε_{rec} , as defined in section II.1.3. Fewer references are available as it requires more information about the hot source to be computed. This efficiency follows the same relations with the power scale, but with some dispersion. Closed source target applications (biomass, gas, solar) and open source target applications (geothermal, WHR) are differentiated as exergetic recovery efficiency might be more appropriate to evaluate performances of open heat sources.

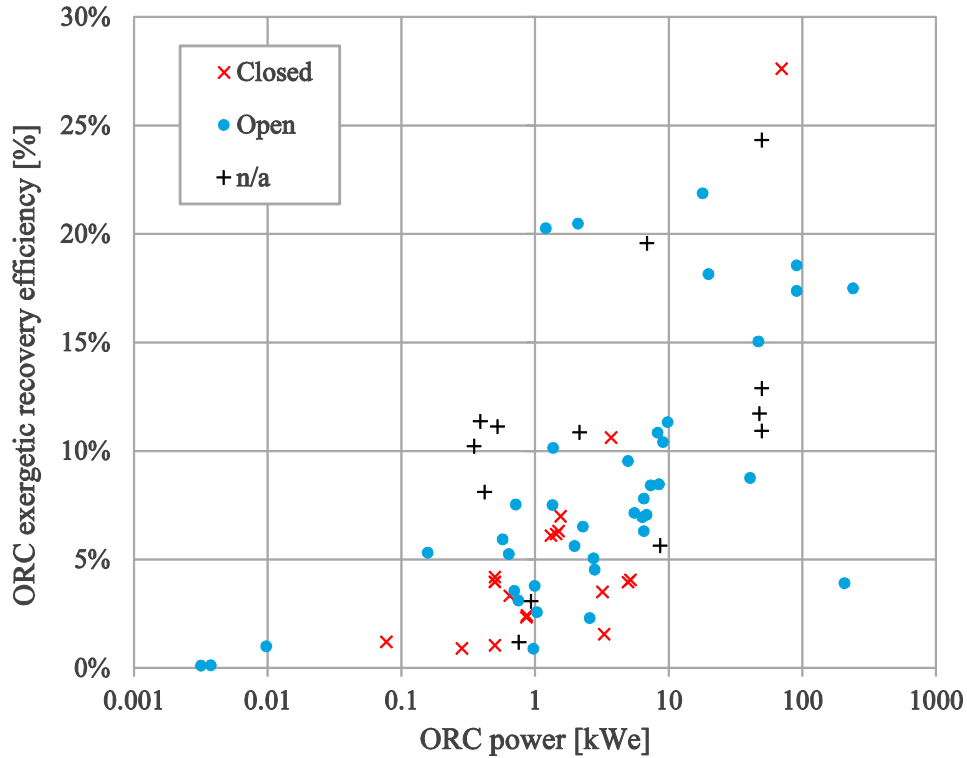


Figure II-20: ORC power and exergetic recovery efficiency map for different target application types

All the previous efficiencies and power are gross. The ORC net efficiency is linked to the back work ratio (BWR) and the gross efficiency by the equation (Eq. II-14) relation. Figure II-21 shows the BWR in relation with the ORC gross power. The BWR as well is closely linked to the power scale. From around 5 % at 100 kW scale, it reaches around 30 % at 1 kW scale. This is due to the combined relation of expander and pump efficiencies with the power scale. We can introduce the back work ratio efficiency (Eq. II-15) to compare actual BWR with the ideal BWR and to establish the relation with pump and expander efficiencies over the BWR. This efficiency reaches a maximum of 40 % for a 100 kW scale ORC and drops around 15 % for 1 kW scale ORC.

$$\eta_{net} = \eta_{gross}(1 - BWR) \quad \text{Eq. II-14}$$

$$\eta_{BWR} = \frac{BWR_{is}}{BWR} = \frac{W_{is,pp}/W_{is,exp}}{W_{el,pp}/W_{el,exp}} = \eta_{pp} \cdot \eta_{exp} \quad \text{Eq. II-15}$$

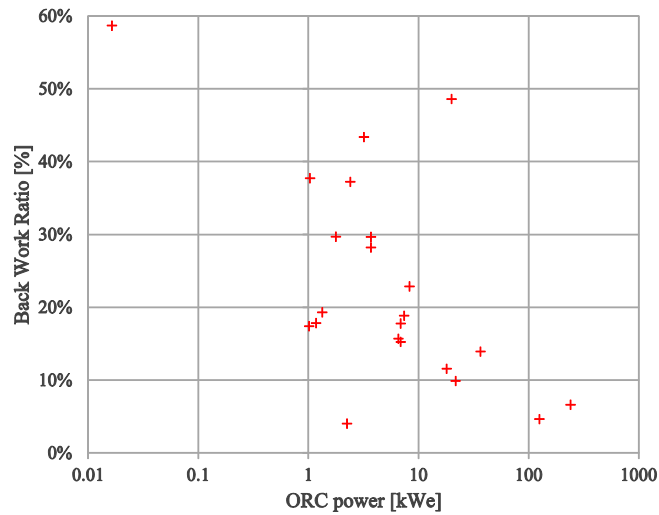


Figure II-21: ORC power and back work ratio map

With more than 100 unique prototypes from more than 175 references, the database has sufficient size to perform a statistical analysis. The Spearman's rank correlation is used to evaluate the influence of some parameters over the ORC efficiency. Spearman's correlation measures the monotonic relationship between two variables (Spearman 1904). The sign of the correlation coefficient ρ shows if variables have similar (positive) or opposed (negative) trends, its value reaches zero when there is no correlation and ± 1 for a strictly monotone correlation. The p-value decreases as the statistical significance of the correlation increase. According to the Fisher's approach of the p-value (Fisher 1925), for p-value below 0.01, the test result is considered as highly significant and not significant above 0.1.

Table II-4: Spearman's correlations for ORC thermal and second law efficiency

	ORC thermal efficiency		ORC second law efficiency	
	Spearman's coefficient	p-value	Spearman's coefficient	p-value
ORC power	0.6805	1.26 e-10	0.7197	4.38 e-11
Hot temperature	0.4363	5.51 e-4	-0.0558	0.67
Expander efficiency	0.7308	5.81 e-8	0.7655	2.16 e-8
IHE	0.2951	0.0125	0.1925	0.128
Lubrication	0.1942	0.250	0.1523	0.390

For this statistical analysis, duplicates are removed except change of expander or fluid. Table II-4 shows correlation results for ORC thermal and 2nd efficiency in relation with the power scale, the hot temperature, the expander efficiency, use of regenerator (IHE) or lubricant. Thermal efficiency is strongly and significantly related to power scale and expander efficiency, even more than the hot temperature. Regenerator also increases the efficiency, but in a smaller proportion. Lubrication increases the cycle efficiency but correlation is not statistically significant. ORC second law efficiency is also strongly related to power scale and expander efficiency. But, as theoretically expected, there is no more influence of the hot temperature on this efficiency. Regenerator influence on second law efficiency is weak, as well as lubrication. Influence of each factors are taken individually. But the strong relation between power scale or expander efficiency over the cycle efficiency might be all related together since expander efficiency and power scale are also strongly related.

Exergetic efficiency criteria are not affected by the heat source temperature, and therefore, are useful for different ORC comparison. Figure II-22 compare specific ORC with similar power scale ORC ($\pm 0.5 \log_{10}$) to eliminate power scale bias, with second law or exergetic recovery efficiency. ORCs in the selected power range are sorted by increasing efficiency. Based on its efficiency, the relative ranking of a specific ORC is identified.

Two transcritical ORC performances are evaluated. First, the ORC from (Kosmadakis et al. 2016), dedicated to a closed source (solar) and reached a power of 3.3 kW. It is compared with 1 to 10 kW range ORC, based on second law efficiency in Figure II-22 (a). With a 38.8 % efficiency, it ranks in the first fifth of same-scale ORC with a relative ranking of 0.84. The second transcritical ORC from (Hsieh et al. 2017) is dedicated to an open source (WHR) and reached a power of 20 kW. With 18.1 % of exergetic recovery efficiency, it has a relative ranks of 0.81 compared to ORC in the 5 to 50 kW range (Figure II-22 (b)). However, transcritical cycle has a large BWR, so similar evaluation based on net efficiency could lead to less optimistic results for transcritical ORC.

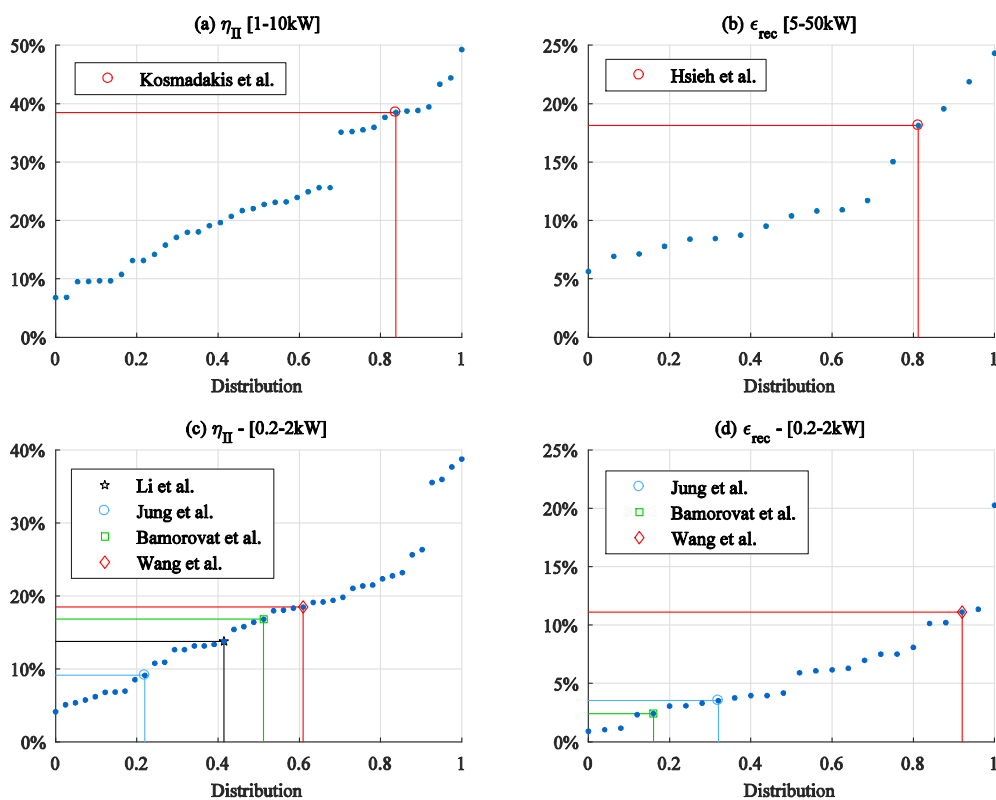


Figure II-22: Comparison of specific ORC with same scale ORCs: (a) transcritical ORC for solar – (b) transcritical ORC for WHR – (c) & (d) ORC with mixture fluid.

Four ORC using fluid mixture are evaluated. They reached a maximum power of 0.5 to 0.9 kW, and therefore are compared with ORC in the 0.2 to 2 kW power range. (T. Li et al. 2015) used a mixture of R245fa and R601 with a 0.72/0.28 fixed mixing ratio of and proposed a comparison with pure R245fa. (Jung, Taylor, and Krumdieck 2015) used a 0.485/0.515 mixture of R245fa and R365mfc exhaust gas recovery. (Bamorovat Abadi, Yun, and Kim 2015) tested a 0.6/0.4 mixture of R245fa and R134a, while Wang et al. (Wang et al. 2016) tested mixture of R601a and R600a with different fluid ratio and achieved the

highest efficiency at the 0.6/0.4 ratio. Based on the second law efficiency (Figure II-22 (c)), ORC using mixture does not have significantly higher potential for heat conversion since they are in the mean of same-scale ORC. For recovery potential, (Wang et al. 2016) performs very well, but others do not. However, the average relative ranking of ORC using fluid mixture is higher based on exergetic recovery efficiency (0.47) than based on second law efficiency (0.44). Therefore, fluid mixture may have a good potential for open heat source applications and fluctuating heat sources (Bamorovat Abadi, Yun, and Kim 2015).

In the same way, three ORC using last generation of organic fluids, the HFO R1233zdE are evaluated. The three reference tested their ORC both with R245fa and R1233zdE as working fluid. Table 7 summarize for each bench its power scale for statistical comparison, performance and relative ranking base on both second law and exergetic recovery efficiency for both R245fa and R1233zdE. Based on second law efficiency, R1233zdE seems to have slightly higher efficiency – 1 % efficiency increase in average. However, based on exergetic recovery efficiency, R1233zdE has efficiency decreased by 10 %. If R1233zdE seems to be a great R245fa replacement fluid for closed source applications, a deeper evaluation must be performed for open source applications.

Table II-5: Comparison of HFO R1233zdE with R245fa and same scale benches

	Power Scale	ORC second law efficiency		ORC exergetic recovery efficiency	
		R245fa	R1233zdE	R245fa	R1233zdE
(Eyerer et al. 2016)	0.1 – 1.2 kW	η_{II} : 19.2 % Rel. Rank: 0.73	η_{II} : 19.4 % Rel. Rank: 0.80	ϵ_{rec} : 11.3 % Rel. Rank: 0.95	ϵ_{rec} : 10.2 % Rel. Rank: 0.89
(Guillaume et al. 2016)	0.9 – 8.9 kW	η_{II} : 9.6 % Rel. Rank: 0.10	η_{II} : 9.5 % Rel. Rank: 0.08	ϵ_{rec} : 5.0 % Rel. Rank: 0.27	ϵ_{rec} : 4.5 % Rel. Rank: 0.23
(Molés et al. 2016)	0.4 – 4.2 kW	η_{II} : 37.7 % Rel. Rank: 0.93	η_{II} : 38.7 % Rel. Rank: 0.98	n/a	n/a

Chapter conclusion

In this chapter, we first exposed and clarified the thermodynamic and technologic framework of the Organic Rankine Cycle.

The different types of powers involved in the ORC (electrical, mechanical, and adiabatic) are named and defined, as well as component efficiencies. Exergy is introduced to make the link between heat and work.

A thought on relevant system input and system efficiency is proposed, based on the targeted application of the ORC. Three efficiencies are selected as ORC global performance criteria: the classic thermal efficiency, ratio of the ORC output power and input heat; the second law efficient, ratio of the thermal efficiency and the Carnot maximum efficiency; and the exergetic recovery efficiency, to account for non-recovered thermal energy from the heat source.

Then, an experimental state-of-the-art overview is proposed by creating a database of ORC prototypes. References analysis provided a view of current and new research trends, as well as opportunities for innovation.

The database provides qualitative and quantitative data on ORC components. Previously introduced criteria are applied to the references for ORC performances evaluation.

A statistical methodology is proposed to evaluate innovative prototypes performance compared to simple ORC performance and identify the main parameters affecting the performances: the ORC power scale and expander efficiency.

From this literature survey and through simple thermodynamic analysis, we draw a number of research and innovation opportunities for ORC and waste heat recovery applications:

- The transcritical ORC for waste heat recovery, since its potential is confirmed thanks to comparison of prototypes with the state-of-the-art and a thermodynamic analysis based on exergetic recovery criteria.
- The working fluid pump performances analysis, since measured performances are lower than expected, the components raises various practical questions, and has a large influence on transcritical ORC.
- The working fluid charge, since this question is sparsely investigated but might end up to be an optimization parameter (T. Li et al. 2015; Xu, Xi, and He 2013)
- And other research opportunities not investigated: fluid mixtures, HFO fluids, modeling and design assistance tools, monitoring & control, supercritical heat transfer, advanced cycle architectures... which will not be investigated in the present thesis.

Chapter III

Tools & methodology

1 Experiments

1.1 Setups presentation

To investigate the different opportunities and queries, different tools are used. Experiment provides real system data and behaviors to understand the different mechanisms involved. The present work relies on four different experimental setups. Two complete and functional transcritical ORCs, a fluid test bench without expander and anecdotally, an absorption chiller experimental setup.

The first transcritical ORC, the CORSERE test bench, is one of the outcome of the SURORC project and was financed by the *Institut Carnot Energies du Futur* (Tauveron et al. 2014). This ORC is designed to run at supercritical pressure up to 50 bar with R134a as the working fluid (critical pressure 40.6 bar) for industrial waste heat recovery of source between 100 and 150 °C. The bench can switch from a classic configuration to a regenerative configuration. The scroll expander can be by-passed and isolated if necessary.

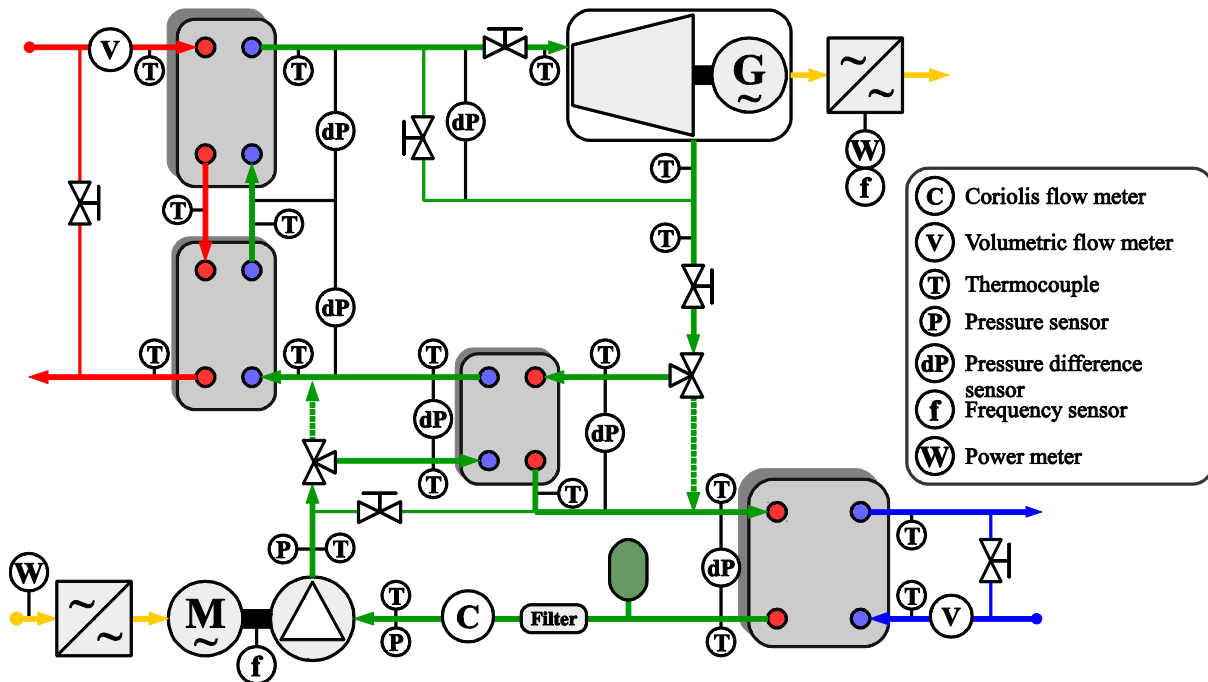


Figure III-1: CORSERE bench Process & Instrumentation Diagram

Figure III-1 and Figure III-2 show the CORSERE test bench process and instrumentation diagram (P&ID) and installation picture, while all the characteristics of the components and auxiliaries are summarized in Table III-1. The waste heat source is simulated by a 250 kW electrical boiler; heat is transferred by pressurized water. Since the loop is filled with nearly 3 m³ of water, it results in a large thermal inertia of the heating loop. The maximum heat source temperature increase rate is found to be 1.2 °C/min and the decrease rate 0.7 °C/min at the ORC nominal power. Tap water flow is used as the ORC heat sink.

The working fluid R134a was selected based on different criteria: theoretical ORC efficiency (Zabek, Penton, and Reay 2013), environmental constrains, technical constrains, price and availability. The expander is originally a hermetic scroll compressor modified to run as an expander: Non return valves are removed, thermal protection is deactivated and the floating seal is fixed to the top cover in order to force the fluid flow to enter in the scroll mechanism. All heat exchangers are brazed plate heat exchangers (BPHE) selected for their strength to high pressure and compactness. The working fluid pump is a triplex diaphragm pump driven by a variable speed electric motor.



Figure III-2: CORSERE installation picture



Figure III-3: CPV-Rankine installation pictures

The second transcritical ORC, the CPV-Rankine test bench, was financed and designed under the European FP7 project grant [CPV/RANKINE], and hosted at the Agricultural University of Athens (Figure III-3). This ORC is also designed to run at supercritical pressure up to 45 bar with R404a as the working fluid (critical pressure 37.2 bar) for solar heat source around 95 °C.

The ORC bench is first tested in a laboratory configuration, with regulated and modular heat source and heat sink to widely characterize the ORC under different conditions and draw a performance map for control and optimization. Then, the ORC bench is tested in a field configuration. The heat source comes from concentrated photovoltaic panels. Photovoltaic cells are cooled by a heat transfer fluid (HTF); the heat is transferred to the ORC for additional energy production.

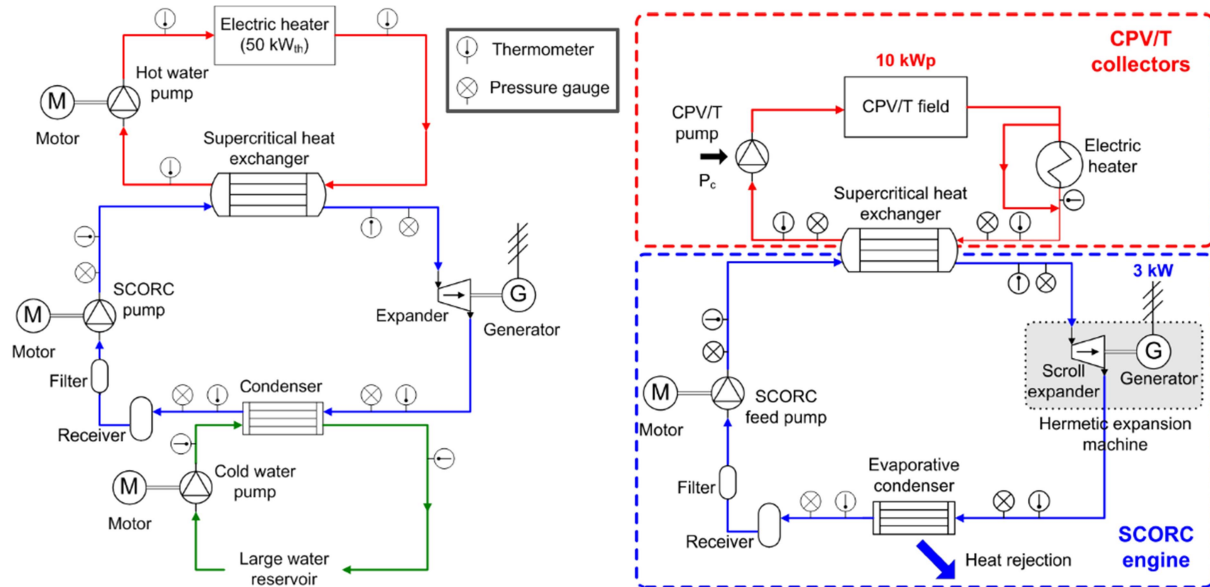


Figure III-4: CPVR bench P&ID (a) laboratory configuration - (b) field configuration

Figure III-4 shows the CPV-R test bench P&ID, as for the CORSERE bench, auxiliaries and components characteristics are summarized in Table III-1. In the laboratory configuration, the heat source is simulated by a 48 kW electric boiler, using pressurized hot water as heat transfer fluid (HTF) up to 100 °C. The heat sink is a water reservoir, large enough (320 m³) to ensure stable temperature during the test.

The working fluid R404a is selected using environmental, cost and ORC theoretical efficiency criteria (Maizza and Maizza 2001). The expander is a modified hermetic scroll compressor installed in a new casing re-designed to better match expansion operation and handle higher pressure. The evaporator is a helical coil with two concentric shell cylinders heat exchanger (Lazova et al. 2016), and the condenser is a classic shell and tube heat exchanger. The working fluid pump is a triplex diaphragm pump driven by a variable speed electric motor.

As previously explained, in the field configuration, the heat sources come from the cooling of photovoltaic cells. Ten concentrated collectors with a concentration ratio of 10 are installed. The total collectors' surface is 100 m²; the photovoltaic cells are expected to produce 10 kW_e and their cooling 41 kW_{th} at 95 °C to supply the ORC unit. The HTF used is a mixture of glycol and water (0.2/0.8) instead of pure water to avoid freezing in winter. In the field configuration, the cooling circuit is replaced by a direct evaporative condenser, with a forced air flow thanks to a series of fans.

The fluid test bench, SURCOUF, is an experimental setup initially designed for heat transfer investigation. Therefore in this test bench, there is no expander but a throttling

valve instead. Figure III-5 and Figure III-6a shows the SURCOUF P&ID and installation picture, while auxiliaries and components characteristics are summarized in Table III-1.

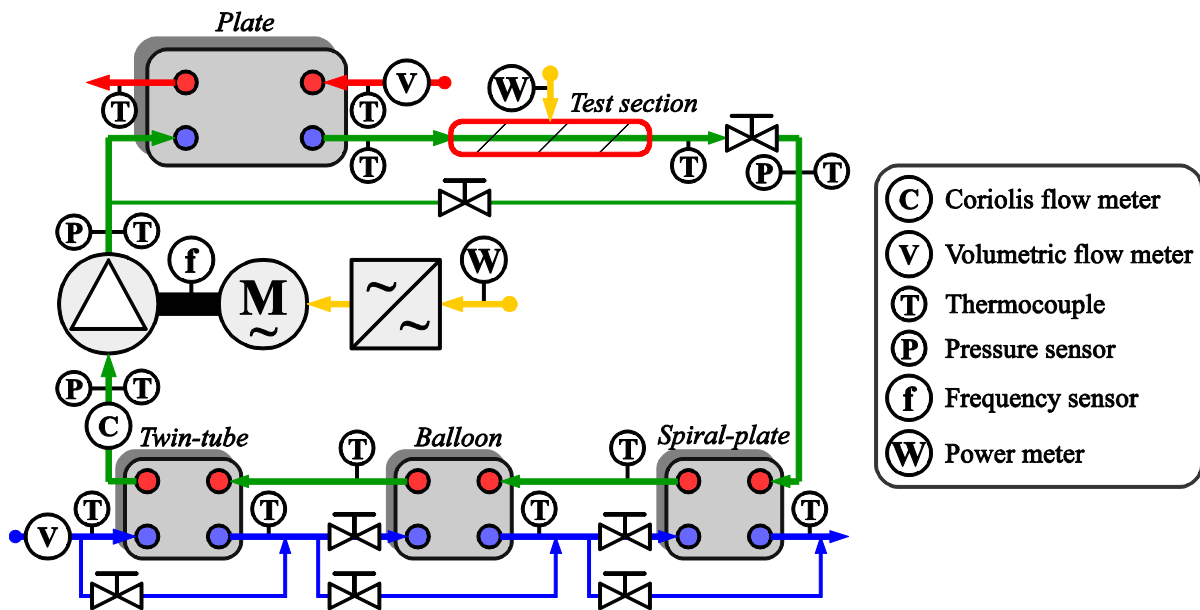


Figure III-5: SURCOUF bench PID

Working fluid R134a is pre-heated through a plate heat exchanger. The heat source is a 10 kW electric boiler using thermal oil as heat transfer fluid, the oil can be heated up to 250 °C. Then, the working fluid enters the heat transfer test section. The test section consists of two electric heating cord wound around working fluid circuit tube, with a capacity of 1.3 kW each. The tube has an U-shape with different internal diameters on each branch, as shown in Figure III-6b, and can be turned either vertically or horizontally.

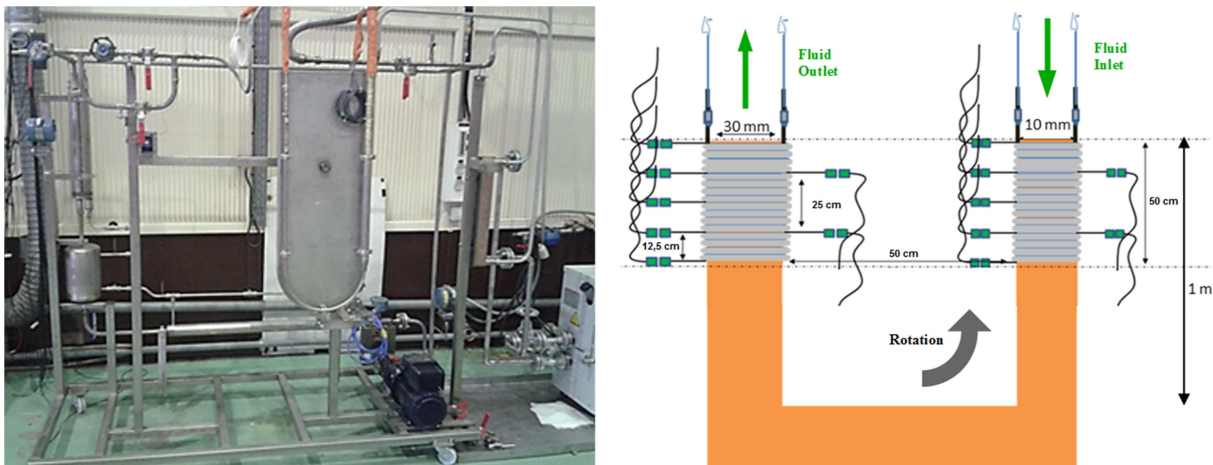


Figure III-6: (a) SURCOUF installation picture (b) Heat transfer test section

Working fluid is expanded through the throttling valve and condensed in a series of three heat exchangers. Tap water is used as cooling medium and heat sink. The water flows also consecutively in the three heat exchangers in counter-flow of the working fluid, but water flow rate can be individually regulated on each exchanger. The high temperature working fluid enters first a spiral plate heat exchanger, then a balloon condenser or “shell and twist”, and finally a twin or concentric tube heat exchanger. The working fluid pump is

a triplex diaphragm pump driven by a variable speed electric motor. The working fluid can be pressurized up to 50 bar.

The last test bench, Solammor, is an ammonia-water absorption chiller (Triché et al. 2017). This bench is only used to investigate diaphragm pump and motor operation with different fluids. Figure III-7 and Figure III-8 show the process diagram and installation picture of the chiller. Mass fraction of ammonia is constantly changing along the circuit and with the boundary conditions of the hot, medium and cold source. The rich solution pump investigated is a triplex diaphragm pump driven by a variable speed electric motor. Pump and motor characteristics are summarized below:

- **Pump:** Hydra-Cell G03X, triplex diaphragm pump. Stroke 6.8 cm^3 ; Shaft speed 1750 rpm; maximum pressure: 70 bar; required NPSH: from 0.3 to 0.6 bar.
- **Motor:** Leroy-Somer LS71M. 3-phase 380V at 50 Hz input; rated power: 0.25 kW; nominal efficiency: 69 %; shaft speed 1425 rpm; speed reducer: 5 to 1; integrated variable speed drive.

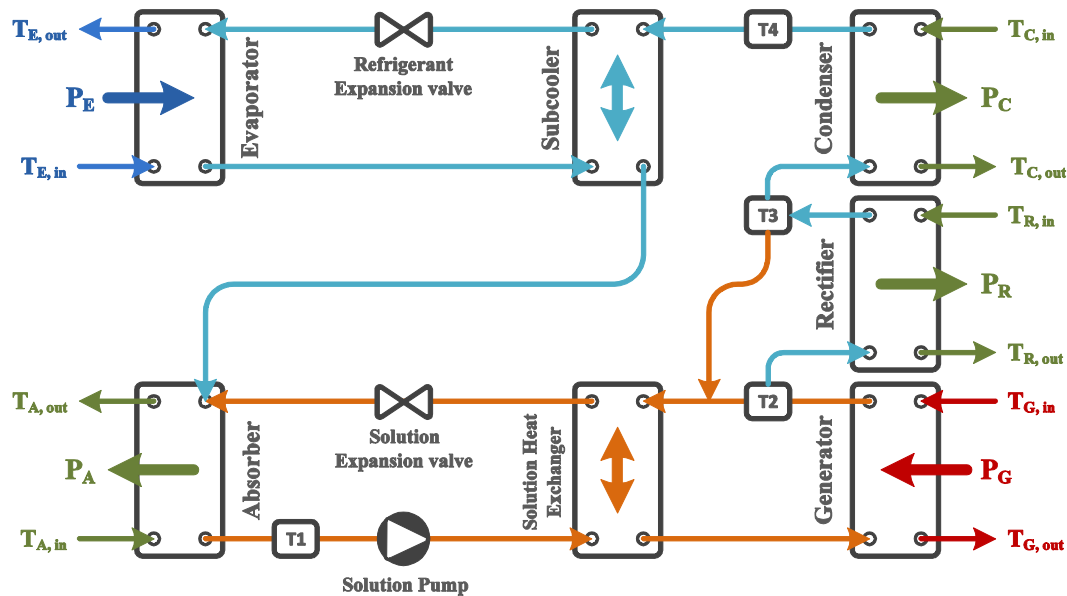


Figure III-7: Absorption chiller process diagram (Triché et al. 2017)



Figure III-8: Absorption chiller installation picture (Triché et al. 2017)

Table III-1: Characteristics of each bench components and auxiliaries

	CORSERE	CPV-Rankine	SURCOUF
Working fluid	<ul style="list-style-type: none"> ● <u>R134a</u>: 1,1,1,2-Tétrafluoroéthane - Critical pressure: 40.6 bar - Critical temperature: 101.1 °C - Point of decomposition: 370 °C - ODP: 0 - GWP: 1320 	<ul style="list-style-type: none"> ● <u>R404a</u>: mixture of R143a, R125 and R134a (0.52/0.44/0.04) - Critical pressure: 37.4 bar - Critical temperature: 72.1 °C - ODP: 0 - GWP: 3922 	<ul style="list-style-type: none"> ● <u>R134a</u>: 1,1,1,2-Tétrafluoroéthane - Critical pressure: 40.6 bar - Critical temperature: 101.1 °C - Point of decomposition: 370 °C - ODP: 0 - GWP: 1320
Pump	<ul style="list-style-type: none"> ● <u>Pump</u>: Hydra-Cell G25S triplex diaphragm. - Stroke: 54.2 cm³ - Shaft speed: 1150 rpm - Max. pressure: 70 bar - Required NPSH: 0.4 - 0.6 bar ● <u>Motor</u>: Leroy-Somer LS132S asynchronous motor - Input: 3-phase 380V at 50 Hz - Power: 5.5 kW - Efficiency: 85.6 % - Shaft speed: 1447 rpm - Speed reducer: 100:71 - Integrated variable speed drive 	<ul style="list-style-type: none"> ● <u>Pump</u>: Hydra-Cell G10X triplex diaphragm. - Stroke: 27 cm³ - Shaft speed: 1450 rpm - Max. pressure: 70 bar - Required NPSH: 0.35 - 0.55 bar ● <u>Motor</u>: Valiadis K132S, 6-poles asynchronous motor - Input: 3-phase 380V at 50 Hz - Power: 3 kW - Efficiency: 86.4 % - Shaft speed: 960 rpm ● <u>Variable Speed Drive</u>: Siemens SED2-4/32B - Power: 4 kW - Efficiency: 96 % 	<ul style="list-style-type: none"> ● <u>Pump</u>: Hydra-Cell G03X triplex diaphragm. - Stroke: 6.8 cm³ - Shaft speed: 1750 rpm - Max. pressure: 70 bar - Required NPSH: 0.3 - 0.6 bar ● <u>Motor</u>: Leroy-Somer LS90L asynchronous motor - Input: 3-phase 380V at 50 Hz - Power: 1.8 kW - Efficiency: 80 % - Shaft speed: 1438 rpm - Integrated variable speed drive
Evaporator	<ul style="list-style-type: none"> ● <u>Pre-heater</u>: SWEP B25 - 40 plates of AISI 316 steel - Parallel configuration - Weight: 11.6 kg - Transfer area: 2.39 m² - Cross-section: 2.25 cm² - Volume: 2.22 dm³ per fluid ● <u>Evaporator</u>: SWEP B25 - 80 plates of AISI 316 steel - Parallel configuration - Weight: 21 kg - Transfer area: 4.91 m² - Cross-section: 2.26 cm² - Volume: 4.5 dm³ per fluid 	<ul style="list-style-type: none"> ● <u>Evaporator</u>: Ghent University shell & coil design. - Coil in P235GH steel - Coil length: 66 m - Coil internal diam.: 25.7 mm - Weight: 580 kg - Transfer area: 6.99 m² - Cross-section: 5.19 cm² - Volume: 34.24 dm³ of fluid 	<ul style="list-style-type: none"> ● <u>Evaporator</u>: SWEP B25 - 20 plates of AISI 316 steel - Parallel configuration - Weight: 6.9 kg - Transfer area: 1.13 m² - Cross-section: 2.26 cm² - Volume: 1.1 dm³ per fluid
Expander	<ul style="list-style-type: none"> ● <u>Expander</u>: Copeland scroll compressor ZR190KCE-TFD - Suction volume: 250 cm³ - Built-in Volume Ratio: ~3 - Internal volume: 14.03 dm³ ● <u>Generator</u>: Integrated asynchronous motor - Input: 3-phase 380V at 50 Hz - Power: 15 kW - Shaft speed: 3000 rpm ● <u>Variable Speed Drive</u>: ABB ACS800 4-quadrants inverter - Power: 15 kW - Efficiency: 97 % - Grid re-injection 	<ul style="list-style-type: none"> ● <u>Expander</u>: Copeland scroll compressor ZP137KCE-TFD - Suction volume: 127 cm³ - Built-in Volume Ratio: ~2.6 - Max. pressure: 48 bar ● <u>Generator</u>: Integrated asynchronous motor - Input: 3-phase 380V at 50 Hz - Power: 10.2 kW - Shaft speed: 3000 rpm ● <u>Variable Speed Drive</u>: Lenze AC Tech, SMVECTOR NEMA1 AC/DC ● <u>Load</u>: Bonitron M3452, DC transistor brake 	None (throttling valve)
Condenser	<ul style="list-style-type: none"> ● <u>Condenser</u>: SWEP B200T - 90 plates of AISI 316 steel - Parallel configuration - Weight: 45.8 kg - Transfer area: 11.4 m² - Cross-section: 2.26 cm² - Volume: 10.7 dm³ per fluid 	<p>Laboratory configuration</p> <ul style="list-style-type: none"> ● <u>Condenser</u>: Shell and tube - Volume: 18.4 dm³ of fluid <p>Field configuration</p> <ul style="list-style-type: none"> ● <u>Condenser</u>: Direct evaporative condenser 	<ul style="list-style-type: none"> ● <u>Condenser 1</u>: Spiral-plate SPIREC H.07.48 - Volume: ~1.6 dm³ ● <u>Condenser 2</u>: Coil in balloon - Volume: ~0.25 dm³ - Transfer Area: ~0.07 m² ● <u>Condenser 3</u>: Concentric-tubes - Volume: ~0.16 dm³ - Transfer Area: ~0.04 m²

	CORSERE	CPV-Rankine	SURCOUF
Other	<ul style="list-style-type: none"> ● Economizer: SWEP B12 - 60 plates of AISI 316 steel - Parallel configuration - Weight: 8.64 kg - Transfer area: 1.62 m² - Cross-section: 4.77 cm² - Volume: 1.86 dm³ per fluid ● Liquid tank: - Volume: 30 dm³ ● Fluid filter 	<ul style="list-style-type: none"> ● <u>Liquid tank</u>: in-line - Volume: 30 dm³ ● Fluid filter 	<ul style="list-style-type: none"> ● Heating cord: - 2 cords - Power: 1.3 kW each
Heat source	<ul style="list-style-type: none"> ● <u>Source</u>: Electrical boiler - Max. power: 250 kW ● <u>HTF</u>: Liquid water - Max. temperature: 150 °C - Max. flow rate: 5 m³/h - Pressure: 4 to 6 bar 	<p>Laboratory configuration</p> <ul style="list-style-type: none"> ● <u>Source</u>: Electrical boiler - Max. power: 50 kW ● <u>HTF</u>: Water-Glycol (0.7/0.3) - Max. temperature: 100 °C - Flow rate: 10 m³/h - Pressure: 2.5 bar <p>Field configuration</p> <ul style="list-style-type: none"> ● <u>Source</u>: Solar collectors - Estimated power: 41 kW ● <u>HTF</u>: Water-Glycol (0.7/0.3) - Max. temperature: 95 °C - Max. flow rate: 7 m³/h 	<ul style="list-style-type: none"> ● <u>Source</u>: Electrical boiler - Max. power: 10 kW ● <u>HTF</u>: Oil (Therminol 66) - Max. temperature: 250 °C - Max. flow rate: 2.5 m³/h - Pressure: around 10 bar
Heat sink	<ul style="list-style-type: none"> ● <u>Source</u>: Tap water ● <u>HTF</u>: Liquid water - Temperature: 18.5 ± 1 °C - Max. flow rate: 4 m³/h - Pressure: 1 bar 	<p>Laboratory configuration</p> <ul style="list-style-type: none"> ● <u>Source</u>: Water tank ● <u>HTF</u>: Liquid water - Temperature: 16.5 ± 1 °C - Flow rate: 12 m³/h <p>Field configuration</p> <ul style="list-style-type: none"> ● <u>Source</u>: Air (direct condenser) 	<ul style="list-style-type: none"> ● <u>Source</u>: Tap water ● <u>HTF</u>: Liquid water - Temperature: 10 to 20 °C - Max. flow rate: 0.65 m³/h - Pressure: 5 bar

1.2 Experimental procedures

The specificity of experimental setups is the flexibility, controllability and the measurement of a wide range of parameters. On ORC test bench, different parameters can be controlled or regulated, in order to investigate performances and behavior of the ORC. Table III-2 summarizes the different parameters and the control possibilities for each test bench.

Table III-2: Experimental setups control parameters

	CORSERE	CPV-Rankine		SURCOUF	Solammor
Heat Source Temperature	Regulated	Lab: Reg.	Field: Imposed	Regulated	n/a
Heat Source Flow rate	Manual	Lab: Fix	Field: Manual	Manual	n/a
Sink Temperature	Fix	Lab: Fix	Field: n/a	Imposed	n/a
Sink Flow rate	Manual	Lab: Fix	Field: n/a	Manual	n/a
Pump speed	Manual	Manual/Regulated		Manual	Man./Reg.
Expander speed	Manual	Manual/Regulated		None	n/a
Throttling valve (or bypass)	Manual	None		Manual	Man./Reg.

Some parameters can be regulated with a dedicated controller; usually it is the case of the heat source temperature, with a regulation of the heat power. Some parameters can be manually adjusted: the flow rate with bypass valves or pump speed. Others cannot be

adjusted or controlled. They can be either a fixed value or imposed by the environment (sun, ambient temperature...)

The CORSERE bench can be set in different configurations. The economizer can be by passed or not to evaluate its influence on the cycle behavior and performances. However the working fluid must be shut down before switching from one configuration to another.

The scroll expander is doubled with a bypass valve and can be isolated. The bypass valve is used during the start-up process to avoid excessive liquid injection in the expander and is fully closed when the expander is running. The bypassed configuration is also used to perform precise heat exchangers test. Then, the CORSERE bench has 4 different running configurations: with/without economizer, with/without expander.

In addition, injection and rejection throttling valves are installed respectively at the expander inlet and outlet to control the expander inlet pressure and back pressure regardless the rest of the cycle conditions.

Components and operators safety requires a number of procedures and additional components such as safety shutdown above limit pressure or temperature, in case of lack of cooling. Safety valves are installed to avoid overpressure. Start-up and shutdown procedure should limit liquid injection in the expander and high pressure transient.

A number of sensors are installed on each bench for performances and behavior analysis. Process and instrumentation diagram of each bench (Figure III-1, Figure III-4 and Figure III-5) shows the location of each sensor.

The types of measurement, sensors, their ranges and uncertainties as well as the range experimentally reached by the parameter are summarized in three tables. The Table III-3 is dedicated to the CORSERE bench, the Table III-4 to the CPV-Rankine bench and the Table III-5 to the SURCOUF bench. While the Figure III-9 shows the CORSERE and CPV-Rankine relative pressure and temperature of the recorded data points.

The CORSERE and SURCOUF bench used an Agilent 3470A data logger for acquisition and recording. The acquisition frequency is around 1 Hz, which is sufficient for thermal or mass dynamic effect investigation but not fast enough for some pressure dynamics. The CPV-Rankine used a 1 Hz acquisition system but data were recorded manually, therefore, only static point can be investigated.

Table III-3: CORSERE sensors table

Sensor	Type	Sensor range	Experimental range	Precision
Temperature	K-type thermocouple	-50:250 °C	Hot in. 55:120 °C Cold in. 17.5:20 °C Exp. in. 100:118 °C Cond. out. 17.5:40 °C	± 1.5 °C
High pressure	Rosemount 3051CA	0:55 bar	12.3:43.9 bar	± 0.1 bar
Low pressure	Danfoss MBS33	0:25 bar	7.3:12.9 bar	± 0.2 bar
Expander pressure dif.	Rosemount 2051CD	0:137 bar	3:33.7 bar	± 0.1 bar
Hot water flow rate	Vortex E+H Prowirl 72F	0:5 m ³ /h	2.6:4.8 m ³ /h	± 0.004 m ³ /h
Cold water flow rate	Rosemount 8711	0:20 m ³ /h	1:3.8 m ³ /h	± 0.05 m ³ /h
Fluid flow rate	Micromotion F050S	0:2.25 kg/s	0.15:0.76 kg/s	± 0.0023 kg/s
Expander elec. pow.	ABB ACS800	-	0:6 kW	-
Expander elec. freq.	ABB ACS800	-	0:27 Hz	-
Pump elec. pow.	Fluke 345	0:1200 kW	1.3:4.5 kW	± 80 W
Pump shaft speed	Laser Extech 461880	0:100 Hz	0:10.7 Hz	± 0.05 Hz

Table III-4: CPV-Rankine sensors table

Sensor	Type	Sensor range	Experimental range	Precision
Temperature	Pt100	-40:125 °C	Hot in. 50:101 °C Exp. in. 43.5:99.8 °C Cond. out. 23.8:38.6 °C	± 0.2 °C
High Pressure	Keller 21Y	0:60 bar	20.6:42.3 bar	± 0.6 bar
Low Pressure	Keller 21Y	0:30 bar	12.2:18 bar	± 0.3 bar
Hot flow rate	n/a	0:18 m ³ /h	6:10 m ³ /h	-
Expander elec. pow.	Lenze AC Tech (Inverter)	0:6 kW	0:3.2 kW	-
Expander elec. freq.	Lenze AC Tech (Inverter)	-	10:40 Hz	-
Pump elec. pow.	Siemens SED2 (Inverter)	0:6 kW	1:1.5 kW	-
Pump elec. freq.	Siemens SED2 (Inverter)	-	20:45 Hz	-

Table III-5: SURCOUF sensors table

Sensor	Type	Sensor range	Experimental range	Precision
Temperature	K-type thermocouple	-50:250 °C	Hot in. 30:150 °C Cold in. 12:17 °C Det. in. 50:150 °C Cond. out. 14:55 °C	± 1.5 °C
High pressure	Keller	0:100 bar	9.6:45 bar	± 0.5 bar
Low pressure	Danfoss AKS33	0:20 bar	7:17 bar	± 0.1 bar
Water flow rate	Rosemount 8711	0:15 m ³ /h	0.1:0.63 m ³ /h	± 0.05 m ³ /h
Fluid flow rate	Rosemount S25S	0:0.2 kg/s	0.042:0.201 kg/s	± 0.0004 kg/s
Pump elec. pow.	Fluke 345	0:1200 kW	0.25:1.08 kW	± 20 W
Pump shaft speed	Laser Extech 461880	0:100 Hz	5:50 Hz	± 0.05 Hz

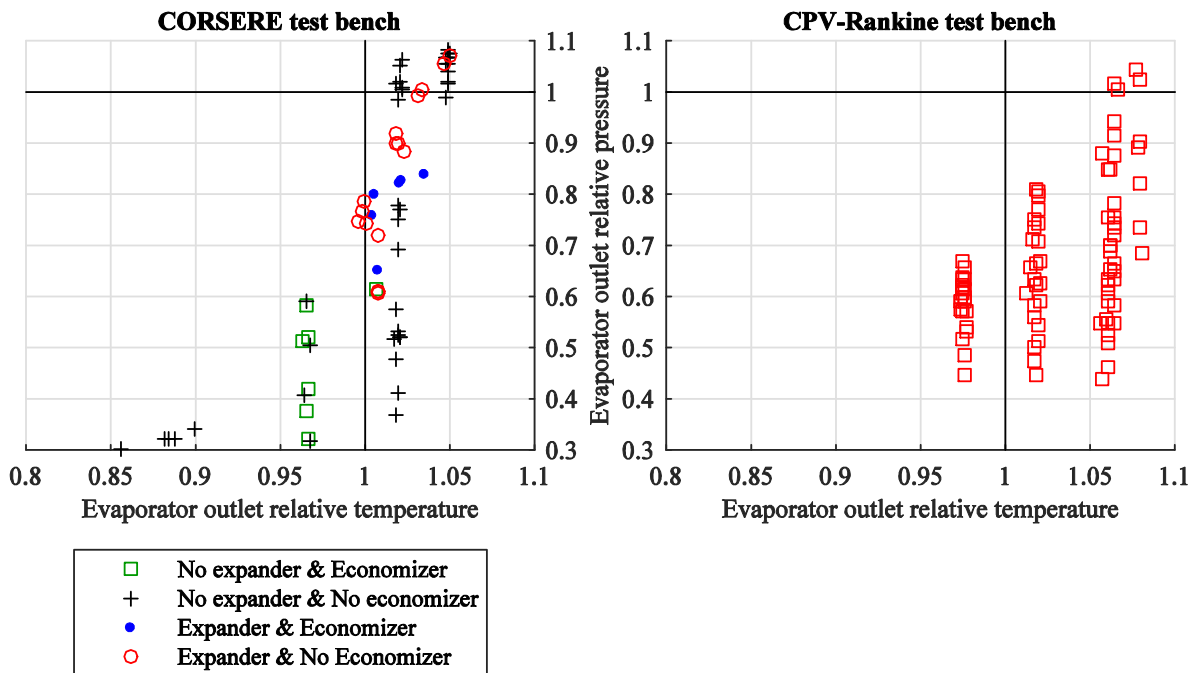


Figure III-9: CORSERE & CPV-Rankine operation maps

2 Data processing

2.1 Steady-point & transient identification

Several hours of experiments have been performed and recorded on the different test benches. In order to speed up and simplify test analysis, part of the data processing has been automated.

In a first step, the signal is smoothed to remove the process and sensors noise, the signal is also resampled, usually at 1/30 Hz, to reduce calculation time due to fluid properties computation.

Several factors contribute to the signal noise. The inherent sensor and electronic noise, and the noise due to the process itself. In the present processes, reciprocating pump is creating mass and pressure pulsation resulting in a highly noisy pressure signal. Some authors added a pulsation dampener to solve this issue (Sylvain Quoilin, Lemort, and Lebrun 2010; S. Quoilin 2007).

Different filters can be used to smooth a noisy signal. The Gaussian filter will be preferred as it enables to correctly reduce white or periodic noise while keeping sharp variations. The Gaussian filter uses a Gaussian as weight function; the standard deviation parameter is empirically adjusted, with the time window size, to smooth the signal without over attenuating signal variations.

$$f(X) = \frac{1}{\sigma\sqrt{2\pi}} \cdot e^{-\frac{X^2}{2\sigma^2}} \quad \text{Eq. III-1}$$

Once the signal is correctly filtered, the dynamic of system can be computed. Transient test evaluates the dynamic response of the system to a sharp variation of one of the inputs, such as the pump shaft speed, the hot or the cold fluid flow rate. Two main parameters are computed to characterize the dynamic of a system. The 5 % settling time and the ramp time.

The 5 % settling time is the time elapsed from the initial process disruption to the time which the selection variable remained within a specified error band. The error band is between 95 and 105 % of the signal final gain. The ramp time is the time to pass from 10 % of the signal gain to 90 % of the signal gain. Figure III-10 shows an example of response time analysis.

The next step is the steady-point automatic detection and recording. Some thermodynamic balances such as the energy balance cannot be checked during transients. Therefore, it is necessary to ensure that the process is fully stabilized to apply such balance. A system is considered in steady-state conditions when all its state parameters have a null time derivative.

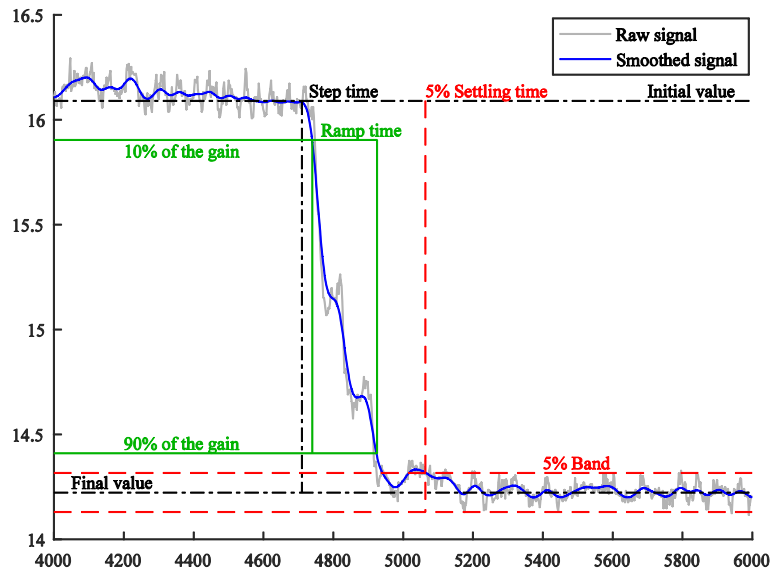


Figure III-10: Dynamic response time

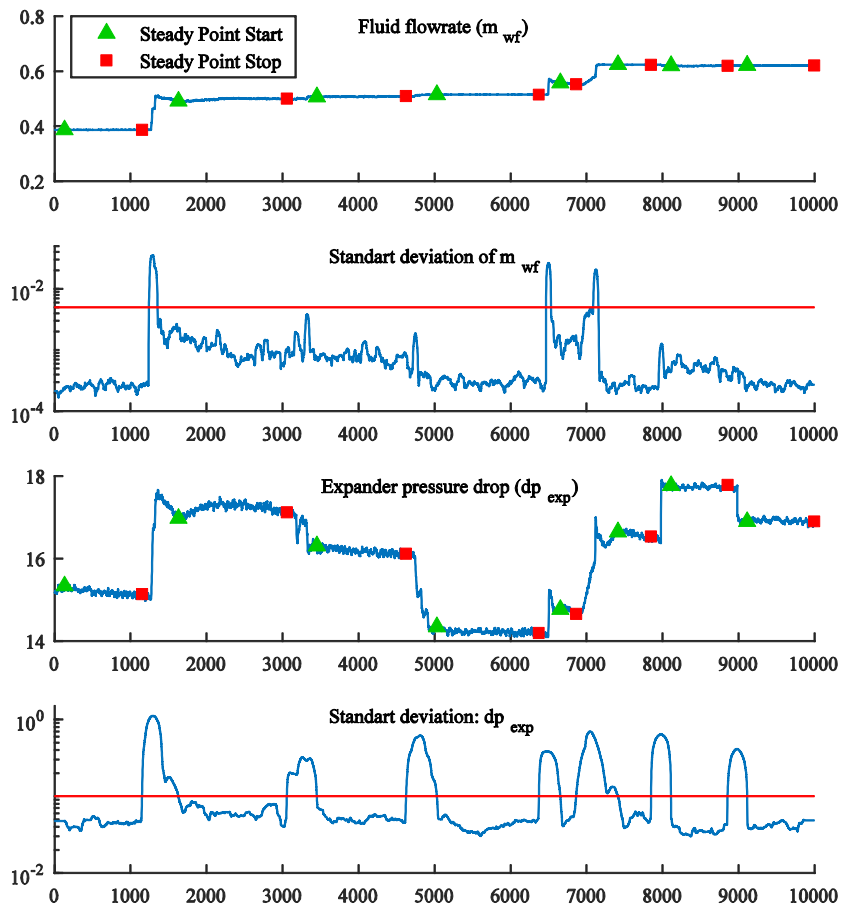


Figure III-11: Example of steady-state detection

One of the solution would be to compute and check the time derivative to detect steady and transient periods. Another solution use the moving window standard deviation, as presented by (Kim et al. 2008), to automatically detected steady conditions and transients. A number of variables, representative of the different test bench dynamics are selected; for example, hot, cold and working fluid flow rates, pump outlet pressure, hot water inlet temperature or expander pressure difference, power, frequency and outlet temperature. For each variable, the standard deviation is calculated on a moving window. In practice, the window size ranges from 30 to 120 seconds and is set up to remove sensors noise while keeping a good level of standard deviation for transient detection.

Limits on standard deviation between transient and steady state are individually and empirically set for each variables. A steady point is created when all variables are considered in steady state based on their standard deviation level. If the steady point lasts more than 60 seconds, the point is recorded and all variables are averaged in the steady state period.

Figure III-11 shows an example of steady-state detection using only two variables: the working fluid flow rate and the expander pressure drop. The flow rate signal has low noise, so moving window size for standard deviation computation is set to 30 seconds, and the limits between transient and steady-state at 5.10^{-3} . The expander pressure drop has high noise so the window is set to 120 seconds. The standard deviation limit is set to 0.1. With those detection parameters, 8 steady points can be identified.

2.2 Calculated parameters

Once the steady-points are detected and recorded, we can compute the fluid properties and the balance equation along the cycle. The fluid properties are computed with the open-source library *CoolProp* developed by (Bell et al. 2014). The enthalpy and the pressure are used as the main state variables for the cycle modeling and analysis.

A number of assumptions and simplifications are made to simplify calculations. Circuits heat dissipation to the ambient is neglected, pressure drop in heat exchangers are neglected and replaced by single pressure drop afterwards. If possible, thermal power of heat exchangers is estimated both on the hot and cold fluid side:

$$Q_{hot} = m_{hot} \cdot (h_{in} - h_{out}) \quad \text{Eq. III-2}$$

$$Q_{cold} = m_{cold} \cdot (h_{out} - h_{in}) \quad \text{Eq. III-3}$$

A typical characteristic of heat exchangers in thermodynamic design study is the pinch point. The pinch is the minimum temperature different between the hot and cold fluid streams. For pressure below 90 % the critical pressure, a simple 3-part discretization (liquid, two-phase, vapor) of the heat exchange is used to estimate the pinch point, assuming steady fluids heat capacity on each part. Close and above the critical pressure, the fluid specific heat capacity has high variation. Therefore, an enthalpy discretization is used to locate and estimate the pinch point, as shown in Figure III-12.

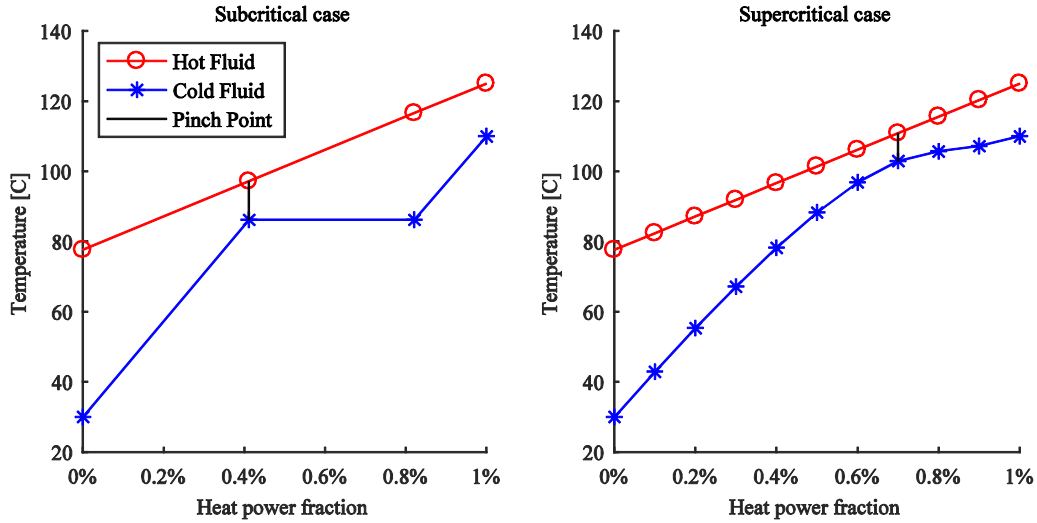


Figure III-12: Pinch point evaluation and localization

The saturation margin is an essential parameter for expander and pump operation. The superheating is the temperature difference between the expander inlet temperature and the saturation temperature of the fluid for the expander inlet pressure. In the same way, the subcooling is the difference between saturation and actual temperature at the pump inlet, while the Net Positive Suction Head (NPSH) is the difference between the actual and the saturation pressure at the pump inlet.

$$\text{Superheat} = T_{in,exp} - T_{sat}(P_{in,exp}) \quad \text{Eq. III-4}$$

$$\text{Subcool} = T_{sat}(P_{in,pp}) - T_{in,pp} \quad \text{Eq. III-5}$$

$$\text{NPSH} = P_{in,pp} - P_{sat}(T_{in,pp}) \quad \text{Eq. III-6}$$

Some dimensionless parameters are also calculated to better describe and analyze the ORC operation. The relative temperature rT and pressure rP is the ratio of the temperature/pressure over the critical temperature/pressure.

In addition, many of the previously cited parameters are calculated, such as the machineries adiabatic and isentropic powers, their different efficiencies, the back work ratio, the net and gross ORC power and the different ORC efficiencies (thermal, 2nd law, exergetic recovery).

The exergy destruction of each component of process is calculated. The exergy destruction I_k is the difference between the exergy input and output (see Chapter II-1), where electrical power input is considered as pure exergy.

$$I_k = \sum E_{in} - E_{out} + W_{el,in} - W_{el,out} \quad \text{Eq. III-7}$$

Note, for the condenser, distinction is made between the exergy destroyed during the heat transfer I_{cd} and the exergy extracted by the heat sink I_{sink} . The exergy extracted by the heat sink can either be considered as destruction (rejection to the ambient) or used for other purposes (combined heat and power).

$$I_{cd} = E_{wf,in} - E_{wf,out} + E_{sink,in} - E_{sink,out} \quad \text{Eq. III-8}$$

$$I_{sink} = E_{sink,out} - E_{sink,in} \quad \text{Eq. III-9}$$

The accuracy of the calculated parameters is estimated using the NIST method for uncertainty propagation (Taylor and Kuyatt 1994). Assuming the individual measurements X_i are uncorrelated and random, with a known uncertainty u_{X_i} , the uncertainty u_Y of the calculated parameter $Y=f(X_1, \dots)$ is determined as:

$$u_Y = \sqrt{\sum_i \left(\frac{\partial Y}{\partial X_i}\right)^2 \cdot u_{X_i}^2} \quad \text{Eq. III-10}$$

Table III-6 shows the relative measurement error of some calculated parameters, at their maximum value. The experimental range of the parameters, on each test bench, is also written down.

Table III-6: Uncertainty and experimental range of main calculated parameters

Parameter	CORSERE		CPV-Rankine		SURCOUF	
Hot power Q_{hot} [kW _{th}]	28-130	± 9 %	12-48	± 2.6 %	0-11.1	± 5 %
Pressure ratio (exp.) [-]	1.3-4.6	± 1.5 %	1.4-2.6	± 1.4 %	0-3.2	± 1,3 %
Expander efficiency η_{exp} [%]	0-66	± 3 %	20-85	± 2.7 %	-	-
Pump efficiency η_{pp} [%]	7-46	± 2 %	7-32	± 8 %	0-52	± 3 %
Back Work Ratio BWR [%]	73-190	± 3 %	43-263	± 7 %	-	-
Thermal net eff. η_{th} [%]	0-1.16	± 12 %	0-4.2	± 3.7 %	-	-
2 nd law net eff. η_{II} [%]	0-4.78	± 15 %	0-19.6	± 8 %	-	-
Exergetic rec. eff. ϵ_{rec} [%]	0-2.12	± 15 %	0-1.8	± 8 %	-	-

2.3 Data reconciliation

The study of uncertainty propagation over calculated parameters and performance criteria shows a relatively large uncertainty and a high sensitivity in some cases. For example the heat power calculated on the working fluid side used temperature and pressure sensors and can have very large uncertainty for inputs or outputs close to the saturation.

Furthermore, a number of measurements are redundant or can become redundant through a number of hypotheses. For example, assuming negligible heat dissipation to the ambient on heat exchangers, the heat power on the hot and cold sides should be equal and therefore some measures are redundant.

In order to take advantage of measurement redundancy and justified assumptions or physical limits, a reconciliation method is implemented. The reconciliation method presented by (Dumont, Quoilin, and Lemort 2016) changes the process variables in their uncertainty ranges to satisfy a number of imposed limits in order to improve the accuracy of the global system measurement.

The reconciliation function minimizes Eq. III-11 with m_i the i^{th} measured value, c_i the corrected value and σ_i the uncertainty of the value. Additionally, a number of constrains are imposed. Pinch points must be null or positive, heat exchangers are assumed adiabatic and pressure must always decrease from the pump outlet. The weighted deviations k_i (Eq. III-12) are checked and points including weighted deviation above 1 – variation above the uncertainty – are removed. Figure III-13 shows the weighted deviations of the 23 control

parameters (flow rates, pressure drops, working fluid enthalpy or sink and hot fluids temperatures) for 5 random steady-points. Point B experienced a weighted deviation above 1 for the working fluid flow rate, the low pressure and the expander pressure difference: the point is not kept. Similarly, Point A is excluded due to overrun for the low pressure and expander pressure difference weighted deviation. Other points (C, D and E) are kept. Overall, 17 steady-points are eliminated over the 70 points, due to non-respected criteria.

$$f = \sum_i \frac{(m_i - c_i)^2}{\sigma_i^2} \tag{Eq. III-11}$$

$$k_i = \frac{|m_i - c_i|}{\sigma_i} \tag{Eq. III-12}$$

Figure III-14 shows the thermal energy balance of the combined pre-heater & evaporator of the CORSERE bench, as well as for the condenser, before and after the data reconciliation. The heat dissipation to the ambient of the heat exchangers is estimated using heat exchanger external surface, free convection heat transfer coefficient (10 W/m².K), maximum and ambient temperatures. The dissipation of the evaporators was estimated to be below 0.5 kW and therefore negligible.

Data reconciliation is a useful tool to improve the global accuracy of the system state estimation. In addition, it checks balance equation such as energy conservation, accurately estimates unmeasured parameters and allows detecting sensors error or deviation.

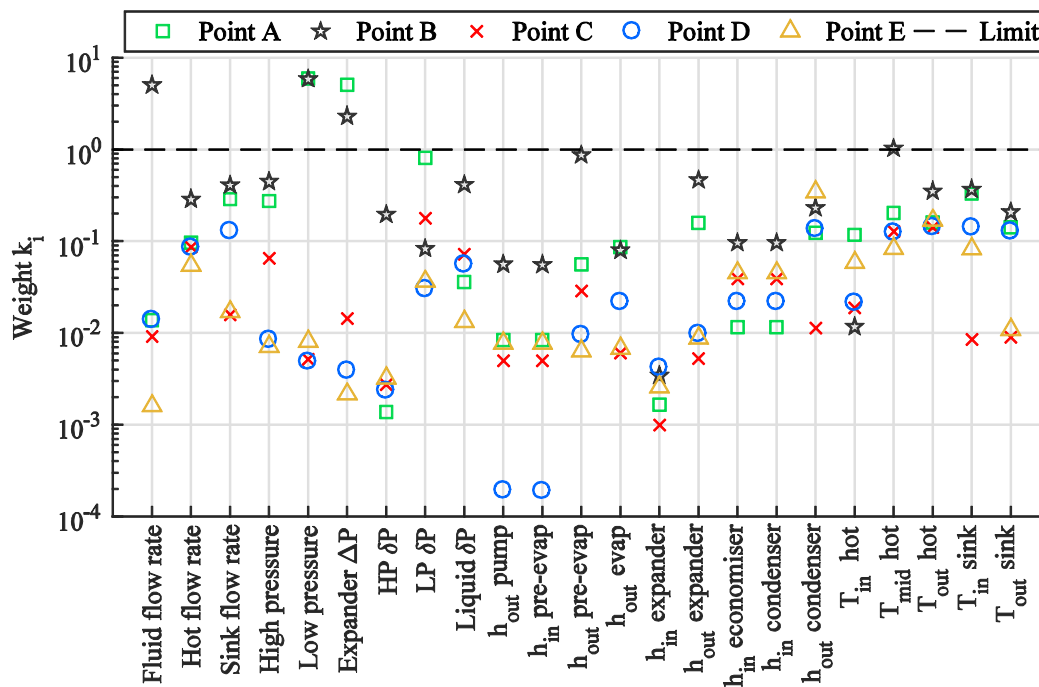


Figure III-13: Weight correction for each parameter of the CORSERE bench

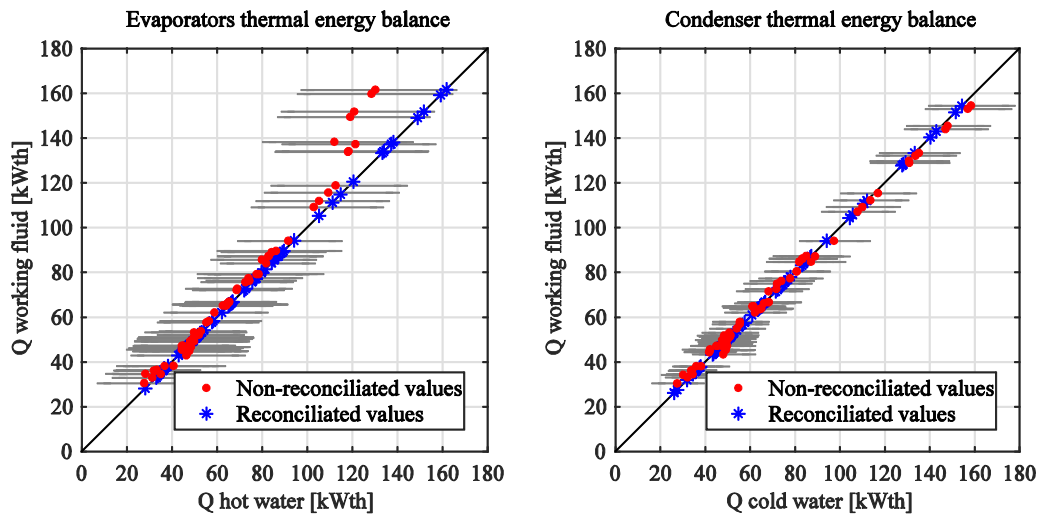


Figure III-14: CORSERE heat exchangers energy balance before and after reconciliation

3 Modeling

3.1 Process model

Different modeling tools can be used to simulate and optimize thermodynamic processes. The *Engineering Equation Solver* software (Klein 2015) is an acausal equation solver which originally includes a fluid physical properties library. The *EES* software also includes optimization tools such as genetic algorithm optimizer.

This tool is easy to handle, however, it has a limited number of options and programming possibilities, along with visualization options. It is appropriate for steady-state modeling of various cycle architectures and working fluid screening or automatic selection and for parametric optimization. Energy balances and equations can be directly written down thanks to the acausal feature of the software.

3.2 Charge sensitive model

ORCmKit is an open-source library for ORC systems steady-state modeling, co-developed by the University of Liège and the University of Ghent (Dickes et al. 2017; Ziviani et al. 2016). The library is developed for three environments: *Python*, *Matlab* and *EES*. The *Matlab* environment is selected for its flexibility, usability and the large number of options and additional tools available.

The specificity of the *ORCmKit* library is the possibility to develop a charge sensitive model of an ORC. The developed model includes all the geometries and volumes of the different components. Then, either the fluid charge of the subcooling at the pump inlet can be imposed. For design purpose, the subcooling is imposed and the model can provide the necessary fluid charge. For simulation purpose, the experimental fluid charge is imposed and the model estimates the subcooling.

The enthalpy and the pressure are used as the main fluid state variables. From those variables, the fluid density is directly computed to estimate the fluid mass in each part of the ORC. A model is developed for the CORSERE test bench. Pipe volumes are estimated using pipe length and internal diameter, heat exchanger volumes and expander volumes are extracted from manufacturer datasheets. For more complex and unknown volumes, such as the high pressure part of the expander, the component is filled with a measured volume of water.

In addition, in contrast with the conceptual architecture, the experimental test bench has a number of so called dead volumes. The dead volumes are the portions of the ORC circuits, where the working fluid is not or almost not circulating. For example, the bypass lines are dead volumes if the bypass is closed. In the CORSERE test bench, depending on the configuration used (simple/regenerative, expander/bypass) the dead parts differ (see P&ID

Figure III-1). On steady-state conditions, fluid in the dead parts is assumed to be at the ambient temperature and therefore in the liquid state since the ambient temperature is always lower than the low pressure saturation temperature. However, depending on the geometries, the position of the pipes, and the fluid state in the circulating parts, some dead portions might always be at the saturated conditions.

For example, between the simple and the regenerative configuration, the dead parts of the circuits drastically change, as well as the fluid conditions in the pipes and the components. Figure III-15 shows a partial scheme of the CORSERE test bench in both configurations. With the regenerative configuration (a), the dead parts are the liquid bypass pipe and the pipe between the 3-way valve and the economizer outlet junction. Even if those pipes are at the ambient temperature, the fluid in those parts condenses but the saturated liquid drops down to the condenser. Therefore, the fluid in those volumes is considered as saturated vapor fluid, and the liquid mass fraction is considered as negligible.

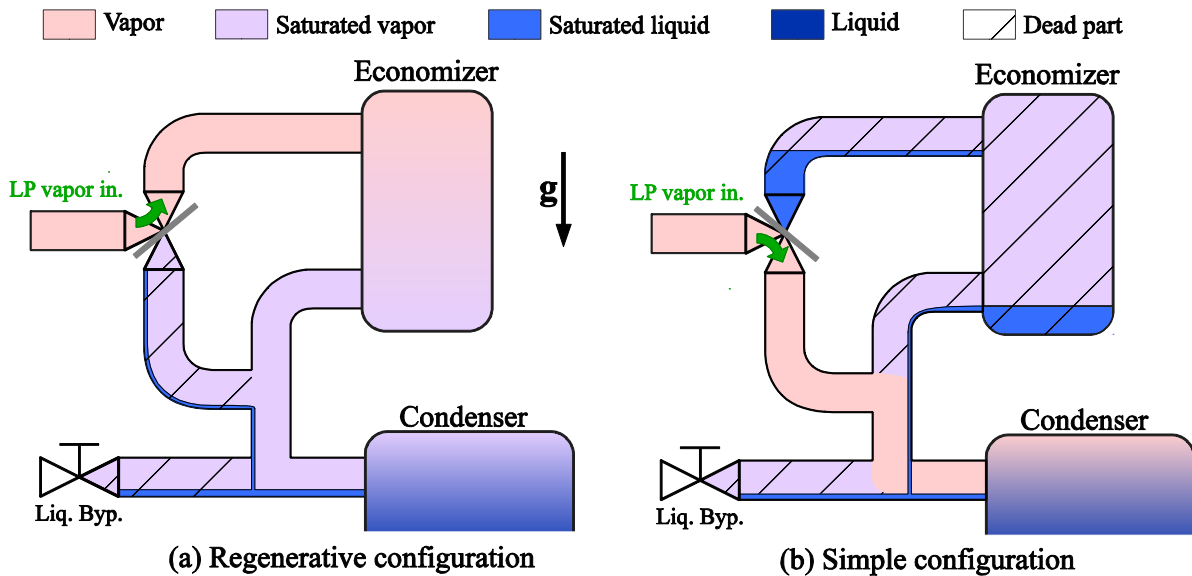


Figure III-15: Example of dead parts and fluid state depending on the bench configuration

In the simple configuration, liquid bypass pipe is still a dead part, but now, the pipe between the 3-way valve and the economizer outlet junction is active while economizer and related pipes is now a dead zone. Those zones are at the ambient temperature and therefore the fluid is condensing. In this case, some parts of the dead volumes can trap liquid fluid, which could correspond to a non-negligible portion of the total fluid charge, and therefore should be estimated. In other non-trapping section, the fluid is considered as saturated vapor.

Heat exchangers are the most complex and sensitive components in this charge sensitive model of ORC since the enthalpy of the fluid and therefore its density is constantly changing along the heat exchangers. In addition, in case of two-phase portions, a slip ratio model might be necessary to estimate the void fraction and the total fluid charge in the heat exchanger.

Heat transfer coefficient is determined and set for each fluid (hot and cold), on each heat exchanger. For multi-phase flow, a coefficient is set to each phase (liquid, two-phase, vapor). In the used correlation, the heat transfer coefficient U is flow rate m dependent,

through Eqt. III-13, with U_0 the heat transfer coefficient at the reference flow rate m_0 . U_0 and n are estimated based on manufacturer data. Table III-7 summarizes the U_0 and n coefficients for the different fluids and heat exchangers. The heat transfer correlations used resulted in a good matching with experimental results as shown in the model vs. experimental heat power parity plot of the different heat exchangers (Figure III-16).

$$U = U_0 \cdot \left(\frac{m}{m_0}\right)^n \quad \text{Eqt. III-13}$$

Table III-7: Heat transfer coefficient - correlation parameters for reference flow $m_0=1$ kg/s

Fluid and state	Pre-heater	Evaporator	Condenser	Economizer (HP)	Economizer (LP)
Water	U_0 : 16.5 kW/m ² n: 0.8	U_0 : 10.1 kW/m ² n: 0.8	U_0 : 3.5 kW/m ² n: 0.8	n/a	n/a
R134a liquid	U_0 : 4.1 kW/m ² n: 0.7	U_0 : 2.5 kW/m ² n: 0.7	U_0 : 1.0 kW/m ² n: 0.7	U_0 : 2.75 kW/m ² n: 0.7	unknown
R134a 2-phase	U_0 : 8.8 kW/m ² n: 0.3	U_0 : 7.05 kW/m ² n: 0.3	U_0 : 3.3 kW/m ² n: 0.4	unknown	U_0 : 2 kW/m ² n: 0
R134a vapor	U_0 : 3.6 kW/m ² n: 0.7	U_0 : 2.5 kW/m ² n: 0.7	U_0 : 0.78 kW/m ² n: 0.7	unknown	U_0 : 2.1 kW/m ² n: 0.7

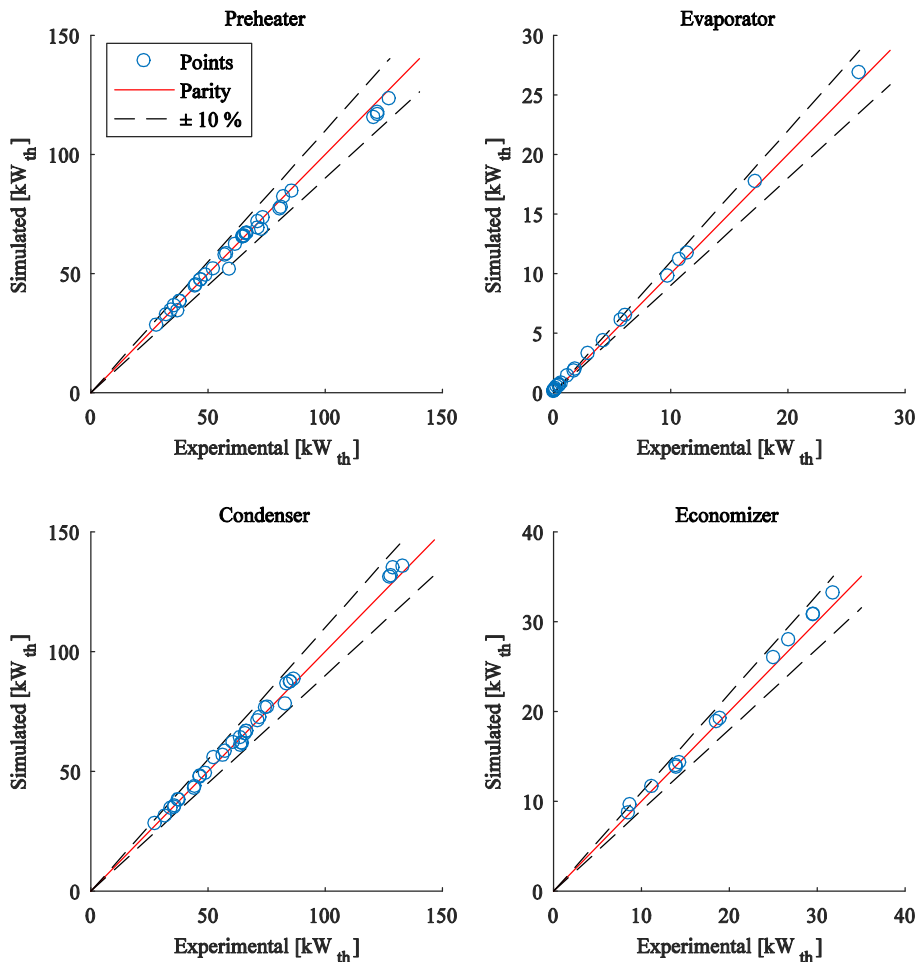


Figure III-16: Heat exchangers heat power - Experimental vs. Simulation parity plot

Different void fraction correlations can be used to compute the working fluid mass in the heat exchangers (Woldesemayat and Ghajar 2007). In the *ORCmKit* library, 5 correlations are available. Correlations can directly provide the void fraction γ or the phase slip ratio S which is used to compute the void fraction through the following relation, with x the vapor quality and ρ_v and ρ_l the vapor and liquid densities (Poggi et al. 2008):

$$\gamma = \left[1 + S \cdot \frac{1-x}{x} \cdot \frac{\rho_v}{\rho_l} \right]^{-1} \quad \text{Eq. III-14}$$

The simplest void fraction correlation is the *Homogenous* model, in this case, the vapor and liquid phases are assumed to have the same velocity and therefore the slip ratio is 1. (Zivi 1964) used a slip ratio in relation with the phases density: $S_{zivi} = \rho_v / \rho_l^{-1/3}$. (Premoli, Francesco, and Prina 1970) proposed a more complex slip ratio correlation based on the phase densities, the Reynolds and the Weber dimensionless numbers:

$$S = 1 + F_1 \sqrt{\frac{y}{1+y \cdot F_2}} - y \cdot F_2 \quad \text{Eq. III-15}$$

With Re_l the saturated liquid Reynolds number and:

$$F_1 = 1.578 \cdot Re_l^{-0.19} \cdot (\rho_l / \rho_v)^{0.22}$$

$$F_2 = 0.0273 \cdot We \cdot Re_l^{-0.51} \cdot (\rho_l / \rho_v)^{-0.08}$$

$$y = \left[\left(\frac{1-x}{x} \right) \cdot \frac{\rho_v}{\rho_l} \right]^{-1}$$

(Domanski and Didion 1983) proposed a correlation based on the Lockhart and Martinelli parameter X_{tt} (Lockhart and Martinelli 1949). A first correlation is valid for $X_{tt} > 10$ and the other below.

$$X_{tt} = \left(\frac{1-x}{x} \right)^{0.9} \cdot \left(\frac{\rho_v}{\rho_l} \right)^{0.5} \cdot \left(\frac{\mu_l}{\mu_v} \right)^{0.1} \quad \text{Eq. III-16}$$

With:

$$X_{tt} > 10: \gamma = 0.823 - 0.157 \cdot \ln(X_{tt})$$

$$X_{tt} \leq 10: \gamma = (1 - X_{tt}^{0.8})^{-0.378}$$

Finally, (Hughmark 1965) proposed a correlation, applicable to any horizontal or vertical flows, based on vapor quality, phase densities and viscosities, mass flux and channel geometry. This correlation is known to provide good results (Poggi et al. 2008), however its computation requires an iterative process as the void fraction γ is one of the correlation parameter. Figure III-17 shows the calculated mass inventory on each part of the circuit for different experimental cases, using the Hughmark void fraction correlation. The real experimental fluid charge is 24.0 kg, the mean calculated total mass inventory is found to be very close, at 24.02 kg with a standard deviation of 1.3 kg. The Hugmark correlation showed higher precision and less dissipation in the mass calculation compared to other correlations and is latter used for cycle simulation (Figure III-18).

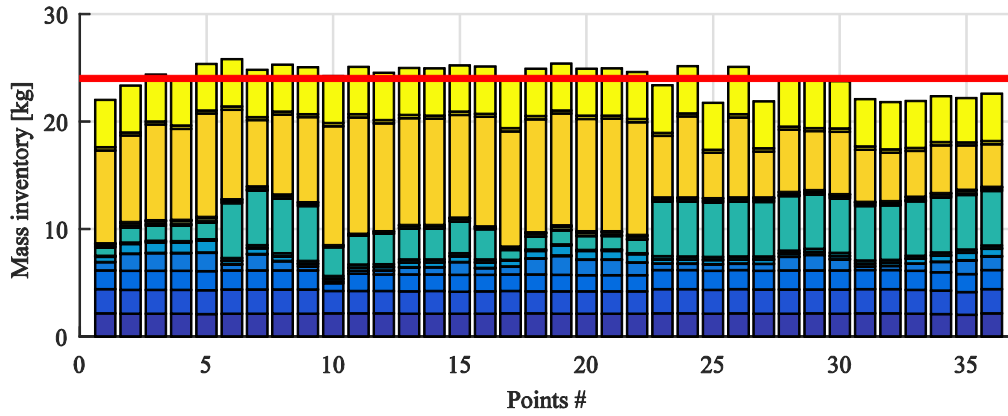


Figure III-17: ORC mass inventory – Hughmark correlation

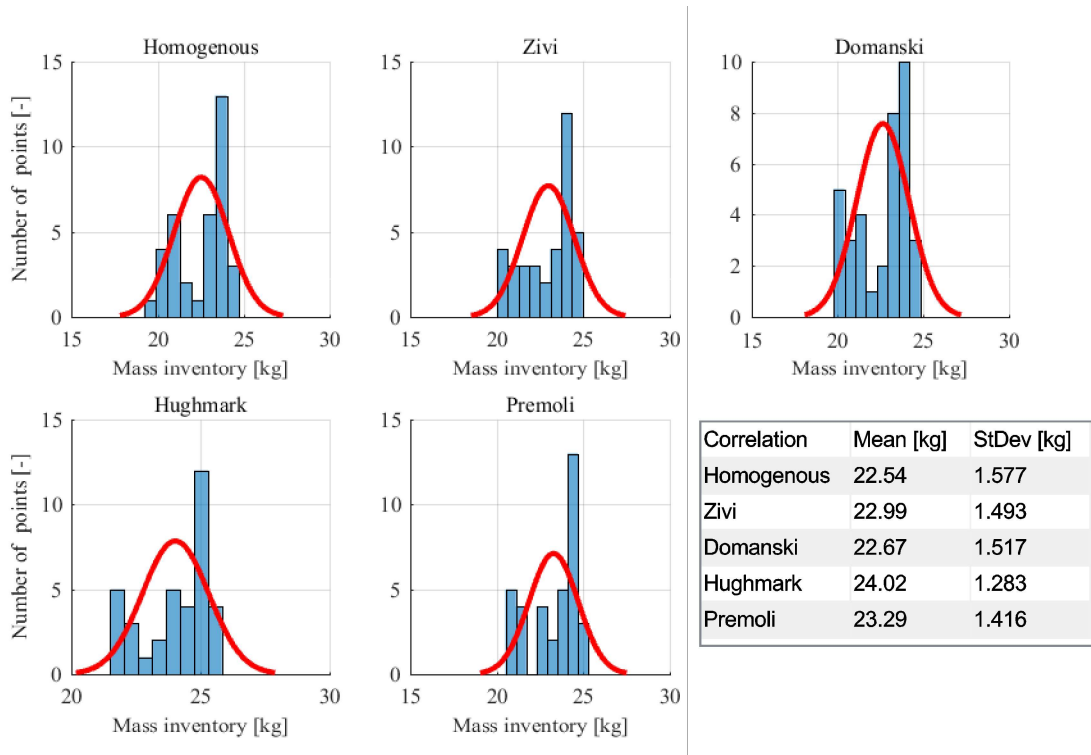


Figure III-18: ORC mass inventory - correlations comparison

3.3 Dynamic model

Modelica is a free, object-oriented, multi-physic modeling language for complex systems and dynamic simulation. The *Modelica* language is used under the *Dymola* environment.

Many proprietary and open-source libraries have been developed under the *Modelica* language. The *ThermoCycle* (Sylvain Quoilin et al. 2014) library was initially developed for thermal and thermodynamic systems modeling such as heat pumps and ORC by the

University of Liège. The library is coupled to the *CoolProp* fluid properties library previously cited. The use of a single fluid library in the present work is preferred for consistency and appropriate results comparison.

The *ThermoCycle* library already includes basic components models such as expanders (scroll, screw ...), tanks, moving boundaries model for heat exchangers, with a large number of options and personalization capabilities. Some of the latter detailed work on reciprocating pump models has been added.

A model is developed for the CORSERE test bench. The connection diagram is shown in Figure III-19. The expander model has no dynamics and no thermal energy losses. Volumetric and energetic performances are estimated using an empirical performance curve for the expander efficiency and volumetric efficiency. The pump model has no dynamics either, and use the reciprocating pump model introduced in the following chapter for energetic and volumetric performances.

Heat exchangers use a spatial finite difference discretization scheme. The pre-heater is discretized into 15 parts, the evaporator into 10 parts and the condenser into 15 parts. The heat transfer correlations are identical to the charge sensitive model correlations previously validated.

Heat exchanger model has no pressure drop; therefore, three fictive valves are added in the model to account for pipes and heat exchangers pressure drop along the cycle. The first valve is at the evaporator outlet and accounts for the high pressure side pressure drop (from pump outlet to expander inlet); the second is at the expander outlet and accounts for the low pressure vapor pressure drop (from expander outlet to condenser outlet). A last valve is added at the condenser outlet to account for pressure drop in the liquid line (from condenser outlet to pump inlet) since the preliminary analysis of experimental results showed a large pressure drop in this zone (due to the filter).

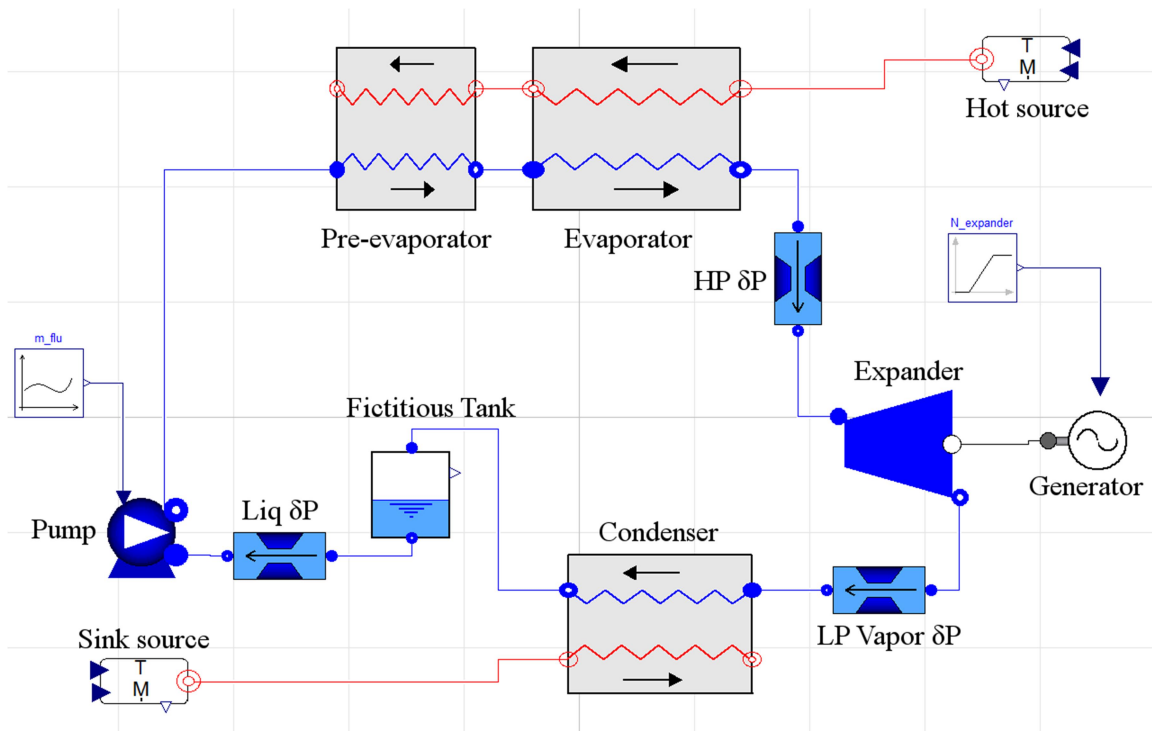


Figure III-19: Dymola-Modelica model diagram of the CORSERE bench

The valves model can use a three parameters input to account for the static fluid head (h), volumetric flow rate linear pressure drop (k) and valve throat area (A) quadratic pressure drop:

$$\delta P = (h \cdot \rho \cdot g) + (k \cdot \dot{V}) + \left(\frac{\dot{m}^2}{A^2 \cdot 2 \cdot \rho} \right) \quad \text{Eq. III-17}$$

However, the valve throat area quadratic pressure drop is found to be sufficient to accurately correlate the different pressure drops. The valve throat areas are empirically determined to be: $1.5935 \cdot 10^{-4} \text{ m}^2$ for the high pressure vapor pressure drop, $1.4031 \cdot 10^{-4} \text{ m}^2$ for the low pressure vapor pressure drop and $1.4601 \cdot 10^{-5} \text{ m}^2$ for the liquid pressure drop.

A fictitious tank is added at the condenser outlet. The tank also includes a partial pressure of non-condensable gaz. The addition of the tank is found necessary to achieve the model initialization, and get the appropriate condensation pressure value initially.

However the addition of the tank disturbs the low pressure behavior when the condenser is liquid flooded, *i.e.* when the pinch point at the condenser outlet between the working fluid and the heat sink becomes very small.

Chapter conclusion

In this chapter, the different tools and methodologies implemented to perform the present work are presented. Four different experimental test benches are used and described:

- **CORSERE**: a complete ORC, using R134a as working fluid and a scroll expander. Designed to run in transcritical conditions, it can be switched from simple to regenerative configuration. This test bench is at the core of the present work and is largely investigated.
- **CPV-Rankine**: a transcritical ORC prototype installed at the Agricultural University of Athens. It uses R404a as working fluid and a scroll compressor. The bench was first tested on a controlled laboratory environment and then connected to concentrated solar panel field.
- **SURCOUF**: a fluid loop, without expander, designed for heat transfer experiments. It uses R134a as circulating fluid and is mainly used for supercritical heat transfer and pump investigation.
- **Solammor**: a ammonia-water absorption chiller, only used for reciprocating pump investigation.

Process and instrumentation of each bench is presented, as well as the data processing methodology. Steady-point and transient automatic identification is introduced, as well as signal filtering.

The main calculated parameters are presented with their propagated uncertainty. The reconciliation methodology is introduced, the reconciliation uses measurements redundancy, carefully addressed assumptions and physical limits to improve the precision on the cycle state parameters.

Modeling tools are presented. The first tool, *Engineering Equation Solver* is used for simple thermodynamic simulation and optimization. The *ORCmKit*, a library for steady-state ORC modeling, is used under the *Matlab* environment because of its ability to integrate the fluid charge through heat exchangers void fraction correlations to simulate an ORC bench.

Dynamic modeling is performed with the *ThermoCycle* library, coded with the *Modelica* language and used under the *Dymola* environment. This tool is able to simulate the ORC dynamic response but does not include void fraction options for heat exchangers. The different libraries were already validated, while the models of the CORSERE bench were presently validated.

Chapter IV

Reciprocating pump for ORC

1 Energetic performances

1.1 Semi-empirical modeling

The experimental ORC database shows real pump electrical efficiency in the 20 to 60 % range, while most parametric optimization study uses pump efficiency between 60 and 90 % (Sylvain Quoilin et al. 2011; Yekoladio, Bello-Ochende, and Meyer 2015). On this basis, pump losses origin should be investigated to justify optimization study efficiency assumptions and improve operating pump efficiency. The pump energetic conversion chain of Figure II-1, previously discussed, is drawn again as a reminder (Figure IV-1).

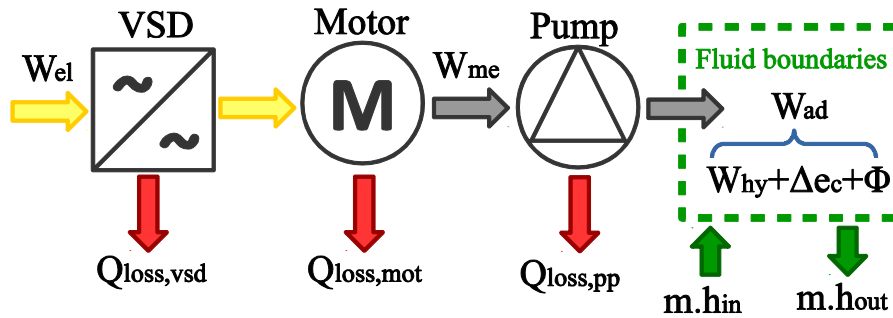


Figure IV-1: Pump energetic power chain (copy of Figure II-1)

In the semi-empirical model proposed, the pumping is assumed to be fast enough and the fluid temperature difference with the ambient low enough to neglect the heat transfer between the fluid and the pump body or the environment. Losses are located either in the electro-mechanical parts, and dissipated to the ambient, or in the fluid through irreversible dissipations and turbulences (Φ) which increases the fluid outlet temperature.

Model parameters are estimated from manufacturer data or from experimental pump data through the minimization of the error-objective function between the estimated and the measured pump electric consumption:

$$f = \sum \left(\frac{W_{el,measured} - W_{el,calculated}}{W_{el,measured}} \right)^2 \quad \text{Eq. IV-1}$$

According to the IEC 60034-31 standard (IEC 2010) and (De Almeida et al. 2014), VSD have static losses, plus losses proportional to the output power and output frequency. (Kari 2009) performed experiments on modern VSDs and showed that losses increase with speed and torque. At low torque, losses are nearly constant and independent from rotational speed. (Deprez et al. 2010) investigated efficiency of a 11kW motor and VSD combination.

As a first approximation, VSD power losses can be considered constant. Under this assumption, $Q_{los,VSD} = K_1$, with K_1 is a constant model parameter to estimate from experiments.

Induction motors have been deeply investigated under variable speed and load. The IEC 60034-31 standard provides a part load efficiency correlation based on motor manufacturer data. In this correlation, motor losses are a linear function of W_{me}^2 . (Y. Li et al. 2015)

proposed a new correlation for motor efficiency driven by a VSD, under variable speed and load. VSD control is assumed to be a constant U/f command type, meaning voltage is proportional to the frequency at the VSD output.

The motor losses correlation uses motor nominal performance provided by the manufacturer:

$$Q_{los,mot} = W_{mot,nom} \left(\frac{1}{\eta_{mot,nom}} - 1 \right) \left[k \frac{W_{me,mot}^2}{W_{mot,nom}^2} + (1 - k) \frac{\Omega_{mot}^2}{\Omega_{mot,nom}^2} \right] \quad \text{Eq. IV-2}$$

The k model parameter is set to 0.7 by default, but it can be estimated from experimentation (limit values: [0;1]).

HydraCell, the manufacturer of the diaphragm pumps used in the different test benches proposed a correlation to estimate the required power based on pump shaft speed and hydraulic power: $W_{me} = K_2 \cdot \Omega_{pp} + K_3 \cdot W_{hy}$. K_2 and K_3 parameters are given by *HydraCell*, but they can be estimated from experiments. This correlation does not discriminate losses to the environment $Q_{los,pp}$ and internal fluid dissipation Φ . Other authors (Miller 1995; Tackett, Cripe, and Dyson 2008) showed similar type of pump efficiency correlation with the hydraulic power for other type of reciprocating pumps.

The adiabatic power $W_{ad,pp}$ can be computed with pressure and temperature measurements for enthalpy estimation and leads to an estimation of Φ by subtracting the hydraulic power W_{hy} . However, it is highly sensitive to the temperature measurement. A 0.5 °C uncertainty on both temperatures results in a pump isentropic efficiency uncertainty up to 30 % for an R-134a fluid. By definition, isentropic efficiency is higher than pump efficiency. So as a first approximation, the isentropic efficiency is estimated to be constant and equal to $1/K_3$.

1.2 Model validation

Different tests are performed to characterize the pumping system. Motor standalone test, with the pump shaft disconnected from motor shaft, are performed to characterize the VSD and motor static losses (only performed in the SURCOUF and CORSERE bench). Pumping test, at different shaft speeds and pump pressure differences to cover different pump loads, are performed. Subcooling is kept high enough to avoid cavitation during those tests.

The semi-empirical model is validated on three different pumping systems. The SURCOUF pump, a *HydraCell* G03X with R134a as working fluid. The CPV-Rankine pump, a bigger pump (G10X) with another type of refrigerant (R404a). The CORSERE pump is even bigger (G25S) and runs with R134a. Finally, the Solammor pump, similar to the SURCOUF pump, with a smaller motor and a drastically different fluid (ammonia-water). The diversity of pumps, motors and fluid allows a reliable validation of the semi-empirical model.

The CORSERE variable speed drive losses coefficient K_1 was not set to a fixed value. Since uncoupled test shown a linear increase of the VSD losses with the power, the coefficient K_1 was replaced by a linear relation for motor power below 1000 W and a

constant value above. This difference might be due to the bigger size of the CORSERE motor and VSD, and therefore an optimized technology of VSD:

$$Q_{los,vsd,CORSERE} = \begin{cases} \rightarrow 535 + 1.019 \cdot W_{el,mot} & \text{for } W_{el,mot} < 1000W \\ \rightarrow 1555 & \text{for } W_{el,mot} \geq 1000W \end{cases} \quad \text{Eq. IV-3}$$

Table IV-1 summarizes the pump energetic model, the different parameters with their origins and their values for the different test bench. The parameters extracted from the manufacturer datasheets could also be empirically estimated. The Figure IV-2 compares the electric power measured and the electric power estimated with the calibrated model for the different pumps.

The model is found to accurately estimate the pump consumption at various flow rates and pressure lift. The model standard deviation to the maximum measured power is 1.8 % for the SURCOUF bench, 3.7 % for the CPV-Rankine bench, 1.6 % for the CORSERE bench and 5.6 % for the Solammor bench.

Table IV-1: Pump energetic model summary

Parameters		Results per bench						
Sign	Unit	Definition	Origin	SURCOUF	CPV-Rankine	CORSERE	Solammor	
$W_{mc} = K_2 \cdot \Omega_{pp} + K_3 \cdot V \cdot \Delta P$								
Pump power	Ω_{pp}	rpm	Pump shaft speed	Input				
	ΔP	Pa	Pressure differential	Input				
	V	m ³ /s	Volumetric flow	Input				
	K_2	W/rpm	Friction coefficient	Manufacturer	0.0711	0.1777	0.5922	0.0711
	K_3	-	Efficiency coefficient	Manufacturer	1.174	1.174	1.174	1.174
$W_{el} = W_{mc} + K_1 + W_{mot,n} \cdot (1/\eta_{mot,n} - 1) \cdot [k \cdot W_{mc}^2 / W_{mot,n}^2 + (1-k) \cdot \Omega_{mot}^2 / \Omega_{mot,n}^2]$								
VSD & motor power	W_{mc}	W	Shaft power	Input				
	Ω_{mot}	rpm	Motor shaft speed	Input				
	$W_{mot,n}$	W	Motor nominal power	Manufacturer	1800	3000	5500	250
	$\Omega_{mot,n}$	rpm	Motor nominal speed	Manufacturer	1438	960	1447	1425
	$\eta_{mot,n}$	-	Motor nominal efficiency	Manufacturer	0.794	0.864	0.856	0.694
	K_1	W	VSD losses coefficient	Empirical	219*	904*	1555**	67.7*
	k	-	Motor losses repartition	Empirical or default (0.7)	0.78*	0.7	0.7	0.59*
Electric power standard deviation between model and experiment				20.3 W	51.9 W	71.7 W	11.2 W	

* : value established from experiments

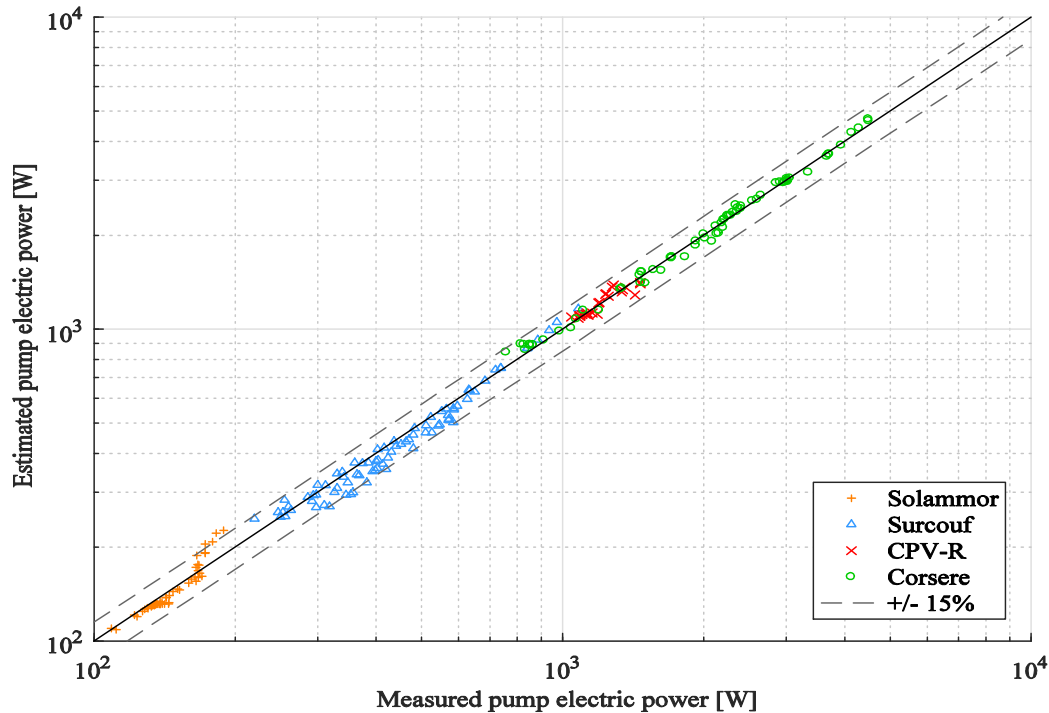


Figure IV-2: Pump energetic power model-experiment parity plot

1.3 Pump energetic performances effects on ORC design & operation

Compared to a constant pump efficiency model, the semi-empirical model could change the ORC parametric optimization results, in particular, the evaporation pressure. Figure IV-3 shows, for different pump models, the second law efficiency evolution with the evaporation pressure, as well as the pump global efficiency (pump standalone and driving motor efficiency combined). For the constant efficiency case, a pump isentropic efficiency of 85 % and a motor efficiency of 80 % are chosen for the maximum case, and respectively 80 % and 60 % for a more realistic case. For the pump model case, the SURCOUF's pump parameters are used, the cases of half and full shaft speeds are investigated. Other ORC model parameters are: an expander efficiency of 70 %, heat exchangers pinch of 10 K, 10 K of subcooling with a heat sink at 20 °C and a hot source at 150 °C. The working fluid is R134a.

Using a constant pump efficiency models using the nominal efficiency (68 %) slightly overestimates the optimal pressure compared to the detailed model. However, using a constant pump efficiency model with a more realistic pump efficiency (48 %) underestimates the optimal pressure.

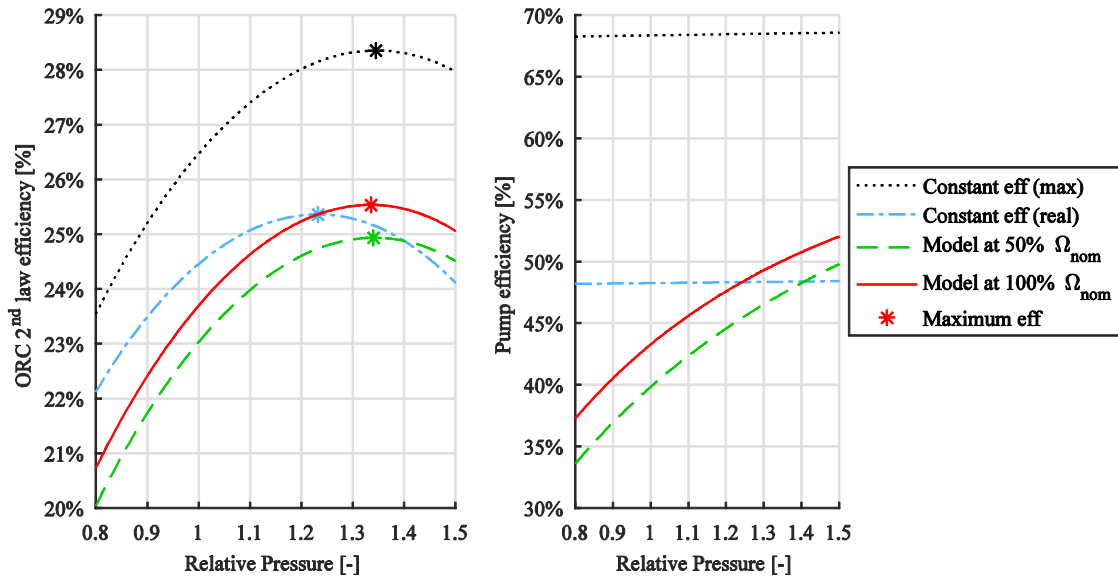


Figure IV-3: Research of optimum pressure for different pump model and pump speed

Electro-mechanical losses of the driving part can represent a substantial portions of the total pumping system losses. VSD losses represent about 1/3 of the consumption and should be deeply investigated. Its benefits should be compared with other flow variation methods such as gearbox or fluid bypass. In the test bench maximum operating conditions, motor loads is always below 50 % of its nominal load, leading to very low efficiency, especially as the motor rated power is low (IEC 2010).

Model analysis also gives an overview of losses location in the power chain. The SURCOUF pump model is run for different shaft speeds and pressure differences. Some scenarios are shown in Figure IV-4.

According to the pump power correlation, the pump mechanical efficiency is only function of the pressure differential, since the volumetric flow is ideally proportional to the pump shaft speed ($V = v_{stroke} \cdot \Omega_{pp}$):

$$\eta_{me,pp} = \frac{W_{hy,pp}}{W_{me,pp}} = \frac{V \cdot \Delta P}{K_2 \cdot \Omega_{pp} + K_3 \cdot V \cdot \Delta P} = \frac{\Delta P}{K_2 / V_{disp} + K_3 \cdot \Delta P} \quad \text{Eq. IV-4}$$

Therefore, reciprocating pumps are increasingly efficient as the pressure difference increases.

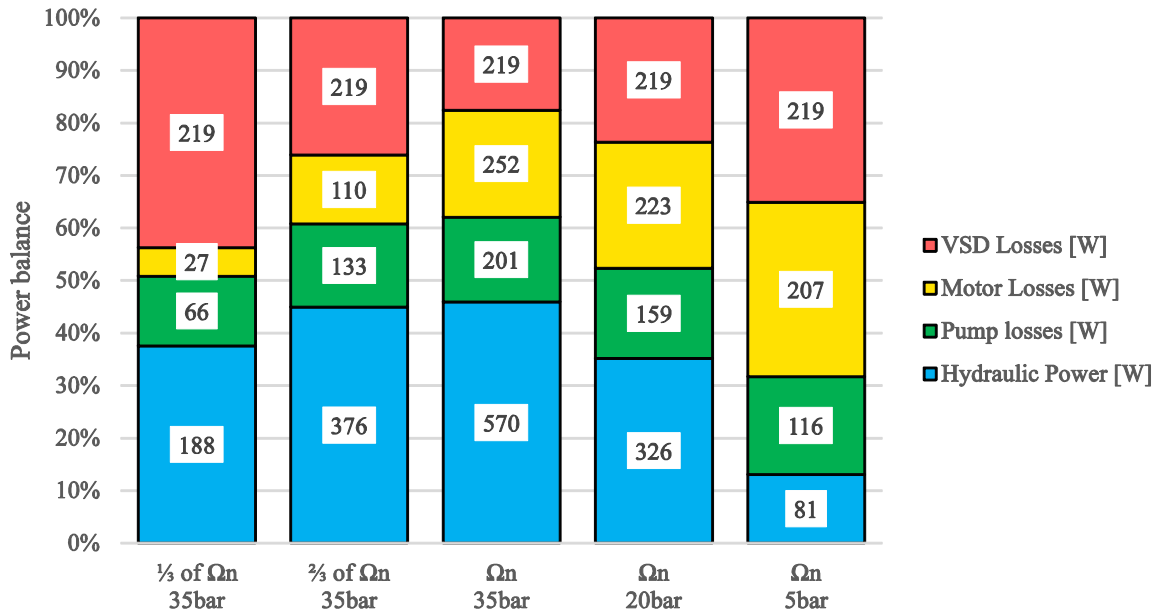


Figure IV-4: SURCOUF pump operation scenarios

Design matching between components and cycle should be carefully checked in commercial units. Accumulation of power margins at each stage of the ORC design and component selection can lead to a harmful oversizing. Reciprocating can handle very high pressure lift, however the ORC operating pressure is likely much lower. Therefore pump driving motor should be selected according to the ORC maximum conditions rather than the pump limits.

For example, the nominal conditions of the SURCOUF pump are 1450 rpm and 35 bar of pressure lift, resulting in a hydraulic power of 0.57 kW or a theoretical pump shaft power of 0.77 kW. Therefore, the selection of the *Leroy-Somer* motor LS80L, with a nominal power of 0.9 kW and nominal efficiency of 73.2 %. And assuming VSD static losses of 0.11 kW, proportional to the nominal power. The pumping system global efficiency η_{pp} could increase by 7 % at the nominal conditions, and by 20 % in average for the 5 scenarios presented in the Figure IV-4.

The Back Work Ratio is useful to emphasize the pump power compared to the expander power. For a given working fluid an operation conditions – pressure level and temperature – we can also emphasize the pump efficiency influence on the ORC net efficiency compared to the expander efficiency influence. For a given case, we can determine the isentropic power of the expander and the pump, and therefore the ORC isentropic net power and the isentropic BWR (see Eq. II-15). The ratio between the real ORC net efficiency and the ORC isentropic net efficiency equals the ORC isentropic and real net power and can be linked to the expander and pump efficiencies:

$$\frac{\eta_{ORC,real}}{\eta_{ORC,is}} = \frac{W_{net,real}}{W_{net,is}} = \frac{W_{el,exp}}{W_{is,exp}} \cdot \frac{1-BWR}{1-BWR_{is}} = \frac{\eta_{exp-BWR_{is}}/\eta_{pp}}{1-BWR_{is}} \quad \text{Eq. IV-5}$$

Figure IV-5 shows cases with three different isentropic BWR (5, 10 and 20 %). Different iso-ratio of ORC real to isentropic efficiency (Eq. IV-5) are plotted function of

the expander and pump efficiency. For example, with an isentropic BWR of 5 %, to reach 70 % of the ORC isentropic net efficiency, we can either use a combination of a 80 % efficiency expander with a 40 % efficiency pump, or a 75 % expander with a 60 % pump.

The more horizontal the iso-ratio lines are, the more predominant the expander efficiency is, compared to the pump efficiency. Reversely, vertical iso-ratio lines mean predominant pump efficiency effect over the ORC efficiency. Similarly, closer the iso-ratio lines are, higher is the combined effect of the expander and pump efficiency over the ORC efficiency.

For example, at isentropic BWR of 5 % and expander efficiency of 80 %, for low pump efficiency, the iso-ratio lines are very close; therefore a small improvement of pump efficiency will drastically increase the ORC efficiency. Similarly, for high isentropic BWR, the iso-ratio lines are less horizontal, even for high pump efficiency, since high BWR means more preponderant pump efficiency effect over the ORC net efficiency.

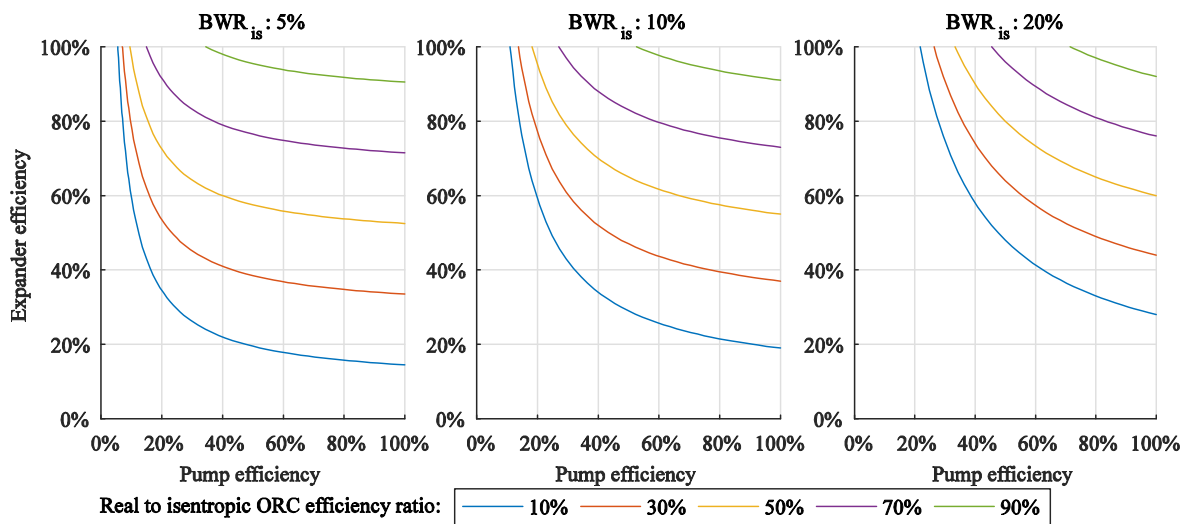


Figure IV-5: Relation between pump and expander efficiency for iso-ratio of real to isentropic ORC efficiency

2 Volumetric performances

2.1 Fluid compressibility

Pump manufacturers, usually, provide pump performances for water. However, refrigerant used in ORC have different viscosity or compressibility properties. Therefore, it is necessary to investigate the volumetric performances of reciprocating pumps running with organic fluids.

In this first section, we will investigate and discuss the effect of fluid properties over the volumetric efficiency of the pump. In the second section, we will focus on the specific case of reciprocating pump running near the cavitation limit.

In reciprocating pump, the volume flow rate without pressure V_0 is proportional to the pump shaft speed Ω_{pp} and the stroke volume v_{stroke} . V_0 is used as the reference flow to compute the volumetric efficiency $\eta_{vol} = V/V_0$. The volumetric flow rate and therefore the volumetric efficiency can be either estimated at the pump inlet (V_{in}), as proposed by (Tackett, Cripe, and Dyson 2008) or outlet (V_{out}), as proposed by (Miller 1995). In the first case, this is a non-compressed volume, while it is a compressed volume in the second. This leads to confusion in efficiency definition and difference in the efficiency value. In this study, the outlet flow is used.

Different factors affect the volumetric efficiency. First, valves leakage. (Johnston 1991) explained that valve leakage is mainly due to delays in valve closing. This delay is assumed inversely proportional to the shaft speed, while the number of openings per unit of time is proportional to the shaft speed. Therefore, valve leakage flow rate is independent of the speed and can be modeled by a continuous average leakage flow rate using the equation proposed by (De Chargerés and Rey 2009), with A an empirical geometric coefficient and μ the fluid dynamic viscosity.

$$\dot{V}_{leak} = A \cdot \Delta P / \mu \quad \text{Eq. IV-6}$$

Second, the fluid compressibility. Figure IV-6 presents the pump discharge and suction process with the evolution of the internal volume along pump operation. The isentropic compressibility coefficient β_S is introduced to define the output volume per stroke:

$$V_{out} = V_{max} - \delta V_{comp} - V_{dead} = V_{stroke} - \Delta P \cdot \beta_S \cdot (V_{stroke} + V_{dead}) \quad \text{Eq. IV-7}$$

Combining leakage and compressibility equations, the output volumetric flow rate and efficiency equations are:

$$\dot{V} = \Omega \cdot V_{stroke} \cdot \left(1 - \Delta P \cdot \beta_S \left(1 + \frac{V_{dead}}{V_{stroke}} \right) \right) - A \frac{\Delta P}{\mu} \quad \text{Eq. IV-8}$$

$$\eta_{vol} = \frac{\dot{V}}{\Omega \cdot V_{stroke}} = 1 - \Delta P \cdot \beta_S \left(1 + \frac{V_{dead}}{V_{stroke}} \right) - A \frac{\Delta P}{\mu \cdot \Omega \cdot V_{stroke}} \quad \text{Eq. IV-9}$$

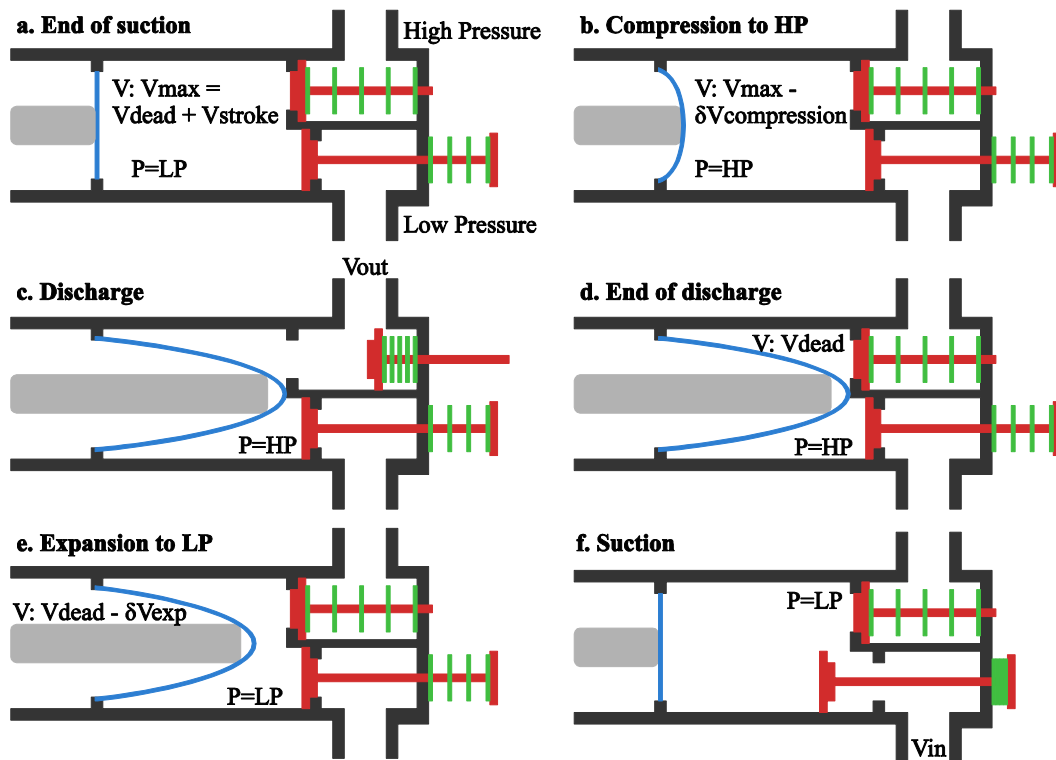


Figure IV-6: Reciprocating pump discharge and suction operation

Unloaded pump test are done to estimate the unloaded volume flow (V_0), valves are open to reduce the pressure differential at the pump ends (ΔP) to a negligible value. From manufacturer datasheet, we can derive the pump stroke. For the SURCOUF pump, the manufacturer stroke V_{stroke} is 6.84 cm^3 while the experimental stroke is found to be 7.15 cm^3 .

Manufacturer provides volumetric performances. Volumetric efficiency is proportional to the pressure lift and no dependence with the shaft speed is shown. Assuming null valve leakage on the manufacturer volumetric performances, we can derive the theoretical dead volume V_{dead} , using isentropic compressibility coefficient of water at 1 bar and 20°C , computed with the fluid density and speed of sound:

$$[\text{water}, 1\text{bar}, 20^\circ\text{C}]: \beta_s = \frac{1}{\rho \cdot c^2} = 4.554 \cdot 10^{-10} \text{ Pa}^{-1} \quad \text{Eq. IV-10}$$

Since manufacturer declared a 94.4 % volumetric efficiency for a pressure lift of 70 bar, the dead volume is estimated to be around 113 cm^3 .

Volumetric efficiency is investigated under various shaft speeds and pressure differential as shown in Figure IV-7. Influence of the pressure difference on the volumetric efficiency is linear as expected. Experimental volumetric efficiency is lower than manufacturer correlation. However water, which is usually used for manufacturer correlation, has a compressibility coefficient ten times lower compared to the R-134a organic fluid at the pump inlet conditions. Using the previously estimated dead volume of 113 cm^3 , we can draw the model volumetric efficiency for R134a, using the average pump inlet conditions (16.7°C , 12 bar). The model predicted a much lower efficiency than

recorded – 83.7 % at 35 bar versus 93 % measured. However the dead volume computation and the model assume negligible valve leakage.

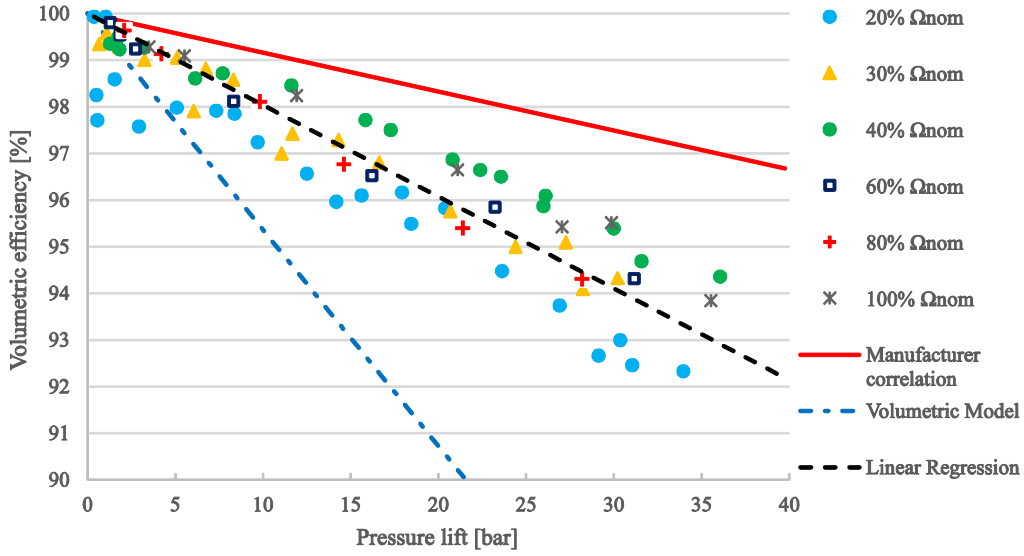


Figure IV-7: SURCOUF's pump experimental volumetric performances

Influence of the pump shaft speed is unclear and not in agreement with the behavior expected from the valve leakage model. Therefore it is impossible to properly estimate the valve leakage coefficient A and the dead volume V_{dead} for a proper model validation.

2.2 Cavitation

A major issue of pump operation in ORC is the cavitation. Cavitation occurs when fluid at the pump inlet gets too close to saturation, it leads to flow rate reduction and pump vibrations. Consequently, cavitation undermines pump performance and lifetime. Cavitation is believed to be more serious with organic fluid since compared to water, they have lower latent heat of vaporization and evaporation temperature (Yang et al. 2015).

In reciprocating pump, the point of cavitation is defined by a volumetric flow drop of 3% compared to non caviting conditions (Miller 1995). Two parameters are used to assess the cavitation in a closed fluid circuit; both describe the margin to the fluid saturation at the pump inlet conditions. The Net Positive Suction Head (NPSH) in pressure unit, commonly used by pump manufacturers, who provides the minimum NPSH for pump operation:

$$NPSH = P_{in,pp} - P_{sat}(T_{in,pp}) \quad \text{Eq. IV-11}$$

And the subcooling in temperature unit, commonly used for cycle thermodynamic analysis:

$$dT_{\text{subcool}} = T_{\text{sat}}(P_{in,pp}) - T_{in,pp} \quad \text{Eq. IV-12}$$

For example, in ORC, (Yang et al. 2015) reported cavitation in piston pump for subcooling under 20°C. (Dumont, Quoilin, and Lemort 2015) or (J.-C. Chang et al. 2015) used plunger pumps which requested respectively 10°C and 11°C of subcooling to avoid

cavitation. (Leontaritis et al. 2015) used a diaphragm pump which required 0.5 bar of NPSH or a 2°C subcooling for smooth operation.

An experimental investigation is performed on the SURCOUF bench to investigate cavitation limits. For cavitation test, shaft speed and pressure lift are kept constant, while subcooling is reduced through sink flow rate reduction until working fluid flow rate drops significantly.

Figure IV-8 shows evolution of R134a volumetric flow function of subcooling and NPSH at the pump nominal speed. Cavitation limit at the nominal speed is 0.24 bar for NPSH or 4.4°C of subcooling, while for water, the pump manufacturer specified 0.53 bar of requested NPSH. The minimum subcooling is slightly increasing with the pump shaft speed, ranging from 2.5°C to 4.4°C for a shaft speed between 20 and 100% of the nominal speed, as expected from the manufacturer datasheet. Influence of the pump pressure differential on the minimum subcooling has been studied at 70% of the nominal speed for pressure difference between 5 and 35 bar but no relation could be highlighted, the minimum subcooling seems independent of the pressure difference.

In order to model the cavitation impact over the volumetric efficiency, an empirical correlation has been developed to correct volumetric efficiency, measured or calculated using Eq. IV-9, from the cavitation effect:

$$\eta_{vol} = \eta_{vol,nominal} \cdot \left(1 - 0.03 \frac{NPSH_{meas}}{NPSH_{req}} \right) \quad \text{Eq. IV-13}$$

With $NPSH_{meas}$ the measured Net Positive Suction Head, and $NPSH_{req}$ the requested NPSH which can be the NPSH specified by the manufacturer or the actual NPSH experimentally measured. In Figure IV-8, the correlation is plotted using the measured NPSH of 0.24 bar for the $NPSH_{req}$ parameter.

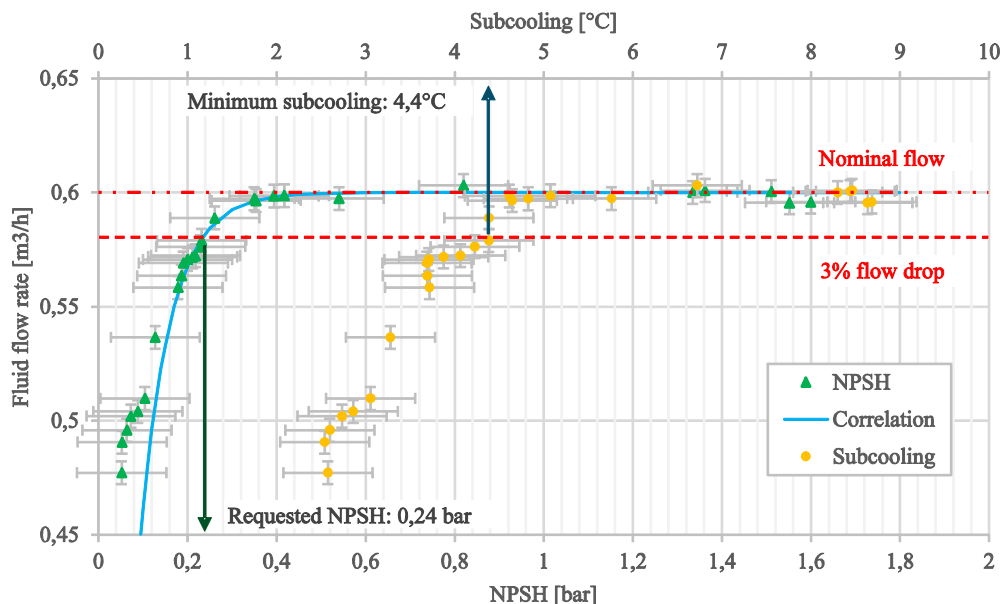


Figure IV-8: Flow rate evolution near the cavitation limit

2.3 Pump volumetric performances effects on ORC design & operation

Volumetric and cavitation performances of the pump impact the ORC design and operation. Figure IV-9 shows a parametric study performed for an ORC running with R134a and with a 70 % constant pump and expander efficiency, at three different expander inlet temperature. Turning from 5 °C of subcooling to 10 °C causes a 5 to 10 % ORC efficiency drop. For a subcooling turning from 5 °C to 20 °C, it is a 20 to 25 % ORC efficiency drop. Therefore, requested NPSH and subcooling should be reduced as much as possible through proper pump technology selection, working fluid selection and operational subcooling management.

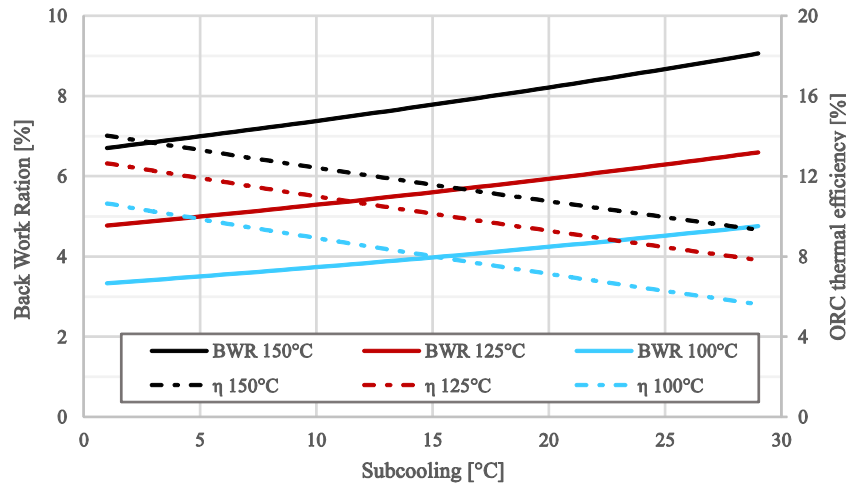


Figure IV-9: Impact of the minimum subcooling over the BWR and the ORC net efficiency

(Sylvain Quoilin et al. 2013) summarized different technical solutions to avoid cavitation. The addition of a pre-feed pump as (Miao et al. 2015) did, which requires a very small NPSH. It can drastically reduce the requested subcooling but adds a new components with additional power consumption.

The addition of a liquid subcooler as (Dumont, Quoilin, and Lemort 2015; Galindo et al. 2015; Leontaritis et al. 2015) did, placed after the condenser and the tank or integrated into the fluid tank. It does not decrease the requested subcooling but enables to control it.

The addition of non-condensing gases in the tank to pressurize it. This solution is low-cost and easier to implement but compatibility of the non-condensing gas with the working fluid and leakage risk should be carefully considered if no separation membrane is implemented.

Finally, the use of gravity and fluid hydrostatic pressure. By placing the working pump at lower level than the condenser, the available pressure at the pump inlet increases. This solution may not be possible for compact or on-board ORC units.

Another solution for subcooling management could come from working fluid circulating load management. Some patents in that way were already published (Duparchy 2011; Smague 2015; Lutz, Motisi, and Bruemmer 2015), working fluid can be stored in a separated tank. Fluid injection or suction is performed through pumps, pressure difference or neutral gas pressurization.

Chapter conclusion

In this chapter, two main aspects of ORC working fluid pump are investigated. The energetic performances and the volumetric performances. The study is limited to the case of volumetric, reciprocating pumps.

For the energetic investigation, a semi-empirical model is proposed, combining correlations from the literature or manufacturers with field investigation of the pump operation.

The model discretizes the losses between the variable speed drive, the electric motor driving the pump and the reciprocating pump. Parameters are extracted from motor and pump manufacturer datasheet or empirically determined.

The model is validated on four different test benches, running with different working fluids, pump and motor size and model. It is able to estimate pump electric consumption at full and part load operation with less than 5 % deviation.

Impact of pump energetic performance on ORC design and operation is discussed. Effect of pump and pump driver oversizing is highlighted. Excessive oversizing results in performance decrease, especially for small-scale units.

For volumetric performances, first a focus is made on fluid properties effect over the volumetric efficiency. In particular, the impact of fluid compressibility and viscosity is highlighted.

A semi-empirical model for reciprocating pump volumetric efficiency is proposed, considering both the fluid compressibility effect and the valve leakage effect combined with the fluid viscosity. However, no robust validation of the model is achieved.

Then, the specific case of pump cavitation is discussed. Cavitation is experimentally investigated and shown results similar to manufacturer data for water. A correlation is proposed and validated to take into account the cavitation on the pump volumetric efficiency.

Chapter V

Supercritical heat transfer

1 Smooth tube

1.1 Subcooled fluid entry

One of the major inquiries of transcritical ORC is the actual heat transfer performances and heat transfer coefficient correlations accuracy. Supercritical heat transfers are investigated in two configurations. First, a downward flow in smooth tube case. Second, a commercial plate heat exchanger. The smooth tube case is performed on the SURCOUF test bench, using the dedicated test section.

By way of reminder, the test section is a 30 mm inner diameter (d_{int}) smooth tube, homogeneously heated by a 1.3 kW electrical cord on 0.5m of the tube length, resulting in an internal tube heat transfer area S_{hex} of 0.0471 m² and a maximum heat flux q of 27.6 kW/m². The tube has a 2.5 mm thickness and is made of stainless steel 316L, with an estimated thermal conductivity λ_{316L} of 16 W/m.K. Thermocouples are inserted between the tube and the electrical cord. Therefore, a thermal conductivity equation of a smooth tube is used to derive the inner wall temperature $T_{w,int}$ based on the external wall temperature $T_{w,ext}$ measured:

$$T_{w,int} = T_{w,ext} - q \cdot \frac{d_{in}}{2} \cdot \ln\left(\frac{d_{ext}}{d_{int}}\right) / \lambda_{316L} \quad \text{Eq. V-1}$$

Measures are averaged to provide a mean wall temperature. In the same way, the mean fluid bulk temperature T_f is the average of the test section inlet and outlet fluid temperature. The experimental heat transfer coefficient α_{exp} is calculated through the following equation:

$$\alpha_{exp} = \frac{q}{T_{w,int} - T_f} \quad \text{Eq. V-2}$$

The heat flux is calculated using the test section fluid heat power Q_{TS} , itself derived from the measured inlet and outlet fluid temperatures. Since the test section outlet temperature measurement is not close to the actual test section outlet, a heat dissipation study has been performed to derive a constant ambient dissipation heat transfer coefficient (α_{amb}) and correct the fluid heat power as well as the test section outlet temperature and enthalpy h^*_{out} :

$$Q_{TS} = m \cdot (h^*_{out} - h_{in}) = m \cdot \left((h_{out} + \alpha_{amb} \cdot (T_{out} - T_{amb})) - h_{in} \right) \quad \text{Eq. V-3}$$

The corrected fluid heat power is compared to the electrical power input through the parity plot in Figure V-1. The difference between the two powers remains within the electrical power measurement uncertainty (100 W), with a standard deviation of 101 W. The mass velocity G is the ratio of the fluid mass flow rate over the cross-sectional area of the tube. However, the fluid heat power uncertainty is very large. The relative uncertainty ranges from 6 % to more than 200 %, with an average of 41 %, and is mainly due to temperature sensors uncertainties. The relative uncertainty increases with the mass flow rate and decreases with the heat flux. Following results and conclusions about heat transfer should be carefully considered, regarding the high uncertainties (25 % in average on the HTC).

Figure V-2 shows two mappings of the recorded data. Figure V-2a shows a G - q map of data. A series of heat transfer tests, called “Liquid data”, were performed in fully liquid conditions, with a test section inlet temperature of 50 °C, and a pressure ranging from 37 to 45 bar (saturation pressure 13 bar). Those tests aim at validating the protocol and the test setup. A second series of heat transfer tests, called ‘Near critical data”, were performed with test section pressure near or above the critical pressure and inlet temperature below or near the critical temperature, as shown in Figure V-2b.

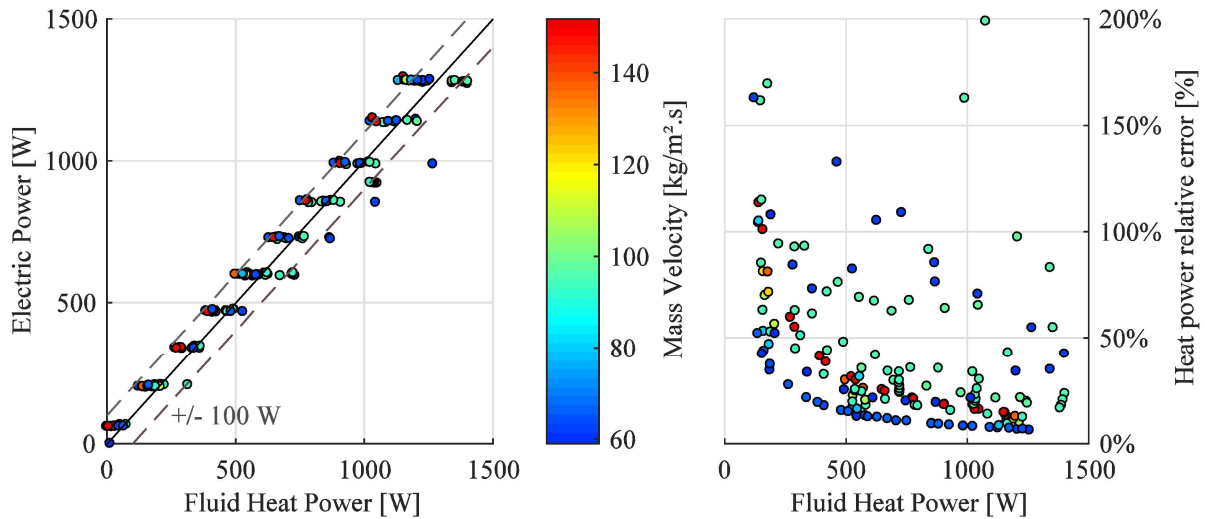


Figure V-1: Electrical and fluid heat power balance

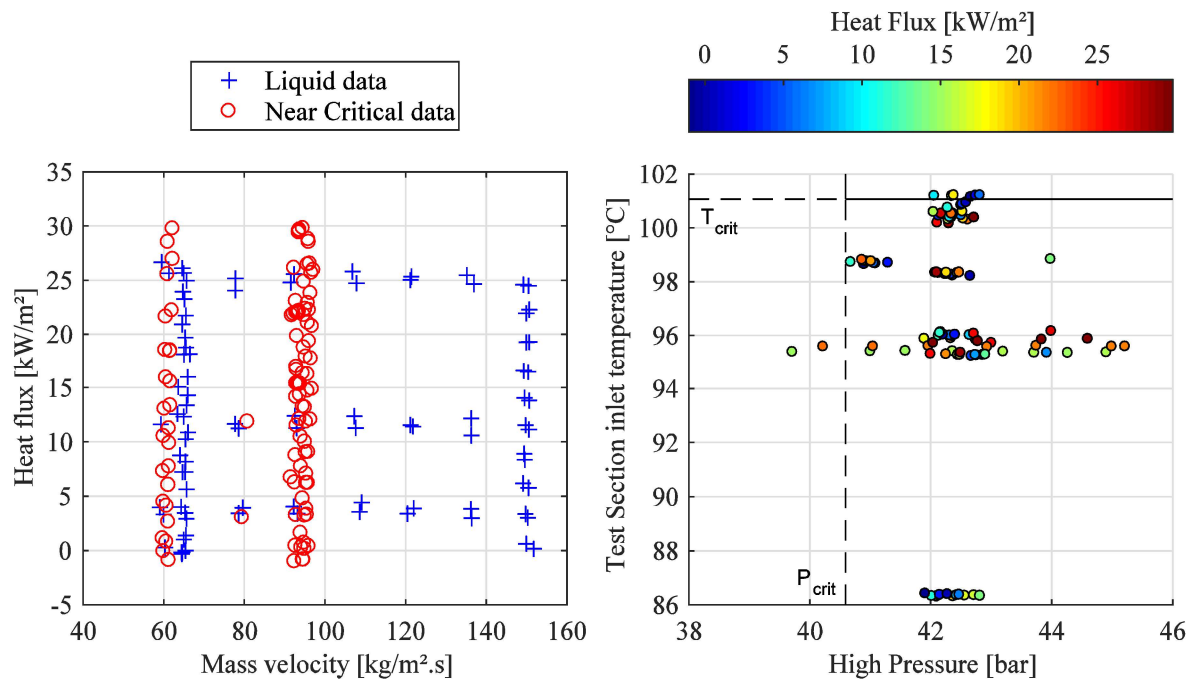


Figure V-2: Data mappings: a) Mass velocity G vs. Heat flow q – b) Pressure vs. Test section inlet temperature (near-critical data only)

As shown in Figure V-3a, the heat flux has a major effect on the heat transfer coefficient, compared to the mass velocity effect. For a given heat flux, passing from a mass velocity of 65 kg/m².s to 150 kg/m².s only increased by 30 %, in average, the heat transfer

coefficient. While passing from a heat flux of 10 kW/m² to 20 kW/m² increased the heat transfer coefficient by 35 % and 15 % for respectively the 65 kg/m².s and the 150 kg/m².s mass velocity.

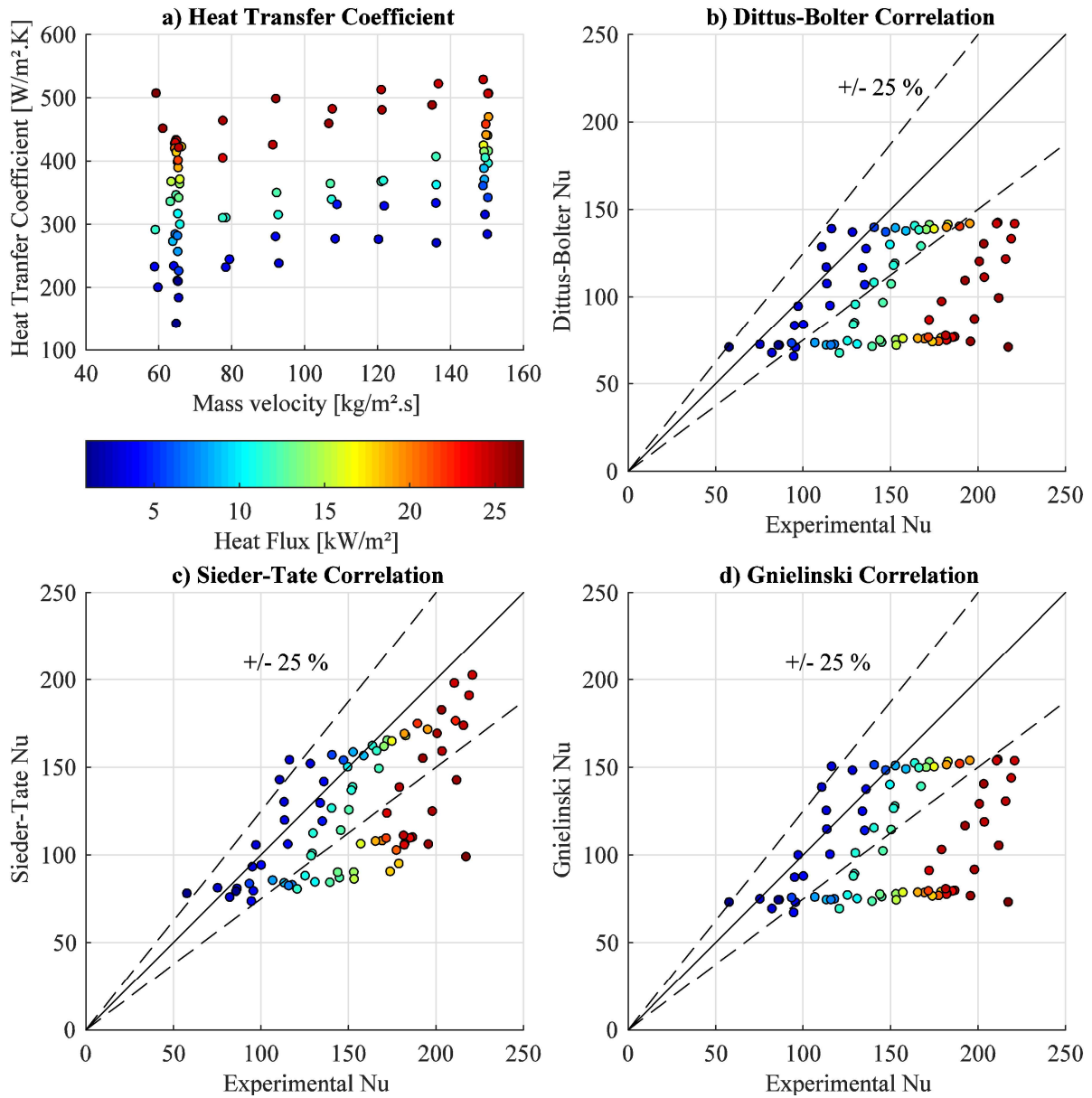


Figure V-3: Liquid data test: a) Experimental heat transfer evolution with mass velocity – b) Experiment vs. Dittus-Boelter comparison – c) Experiment vs. Sieder-Tate comparison – d) Experiment vs. Gnielinski comparison

Experimental liquid data heat transfer coefficients are compared with different literature correlations, using the Nusselt number (Nu):

$$Nu = \frac{\alpha \cdot d_{int}}{\lambda_f} \tag{Eq. V-4}$$

Data are first compared with the Dittus-Boelter correlation (Dittus and Boelter 1930) in Figure V-3b:

$$Nu_{Dittus} = 0.023 \cdot Re^{0.8} \cdot Pr^{0.4} \tag{Eq. V-5}$$

With Re , Pr and λ_f respectively the fluid Reynolds number, Prandtl number and fluid thermal conductivity. All those numbers or properties are calculated using the test section pressure and fluid bulk mean temperature T_f .

The Dittus-Boelter correlation is found to be in good agreement with the experimental values for low heat flux only – below 10 kW/m². At high heat flux and low mass velocity, the correlation derives from the experimental values.

The Sieder-Tate correlation (Sieder and Tate 1936) is derived from the Dittus-Boelter correlation but adds a correction coefficient based on the fluid dynamic viscosity ratio between the bulk (μ) and wall (μ_w) conditions:

$$Nu_{Sieder} = 0.027 \cdot Re^{0.8} \cdot Pr^{1/3} \cdot \left(\frac{\mu}{\mu_w}\right)^{0.14} \quad \text{Eq. V-6}$$

Comparison between experimental Nusselt and Sieder-Tate Nusselt is shown in Figure V-3c. The correlation better matches the experimental data compared to the classic Dittus-Boelter correlation, but not at high flux and low mass velocity. This suggests that deviation in the Dittus-Boelter correlation might be due to drastic change of fluid properties at the inner wall interface.

Indeed, by analyzing the saturation margins of the fluid at the inner wall interface. It turns out that the Sieder-Tate correlation deviates from experimental data (error above 25 %) when the inner wall temperature approaches or exceeds the fluid saturation temperature (or pseudo-critical temperature for supercritical pressure). This boiling (or pseudo-boiling) condition at the wall interface might explain the experimental heat transfer increase compared to the correlations.

The increase of Nusselt number with the heat flux was previously observed by many researches for supercritical fluids heat transfer (Huang et al. 2016), but only for heated downward flow (opposed). For heated upward flow (aided), the influence is reversed. As (Huang et al. 2016) stated, influence of heat flow on heat transfer is rather complicated since both enhancing and deteriorating effects are combined, and even more near pseudo-critical temperature. Finally, a comparison between experimental data and the Gnielinski correlation (Gnielinski 1976) is performed and shown in Figure V-3d:

$$Nu_{Gnielinski} = \frac{f/8 \cdot (Re-1000) \cdot Pr}{1 + 12.7 \cdot \sqrt{f/8} \cdot (Pr^{2/3} - 1)} \quad \text{Eq. V-7}$$

With f the Darcy friction factor for smooth tube as defined by (Petukhov 1970):

$$f = (0.79 \cdot \ln(Re) - 1.64)^{-2} \quad \text{Eq. V-8}$$

The Gnielinski correlation has a drastically different approach from the Dittus-Boelter correlation. However, predicted Nusselt are similar and as for the Dittus-Boelter correlation, the Gnielinski correlation deviates from experimental data at high flux and low mass velocity. The reason of the deviation was previously discussed.

Note, all liquid data are within the different correlations validity boundaries, with a Reynolds number between $1 \cdot 10^4$ and $3 \cdot 10^4$, and the Prandtl number between 3 and 3.1.

1.2 Near-critical point heat transfer

Near-critical point test are also performed to investigate the heat transfer around the critical point. Figure V-4 shows the heat transfer coefficient evolution with the fluid mean bulk temperature, for three different test section inlet temperature. Fluid pressure and mass velocity are constant for the different cases, respectively at 42.35 bars (standard deviation 0.22 bars) and 95.5 kg/m².s (standard deviation 0.8). The heating power is increased in ten steps, resulting in a heat flux ranging from 0.37 kW/m² to 28.75 kW/m².

The heat transfer coefficient reaches a maximum for each case, at 1.17, 1.42 and 1.48 kW/m².K for the test section inlet temperature of respectively 95.9, 98.3 and 100.3 °C. (Shen et al. 2016) and (Zhang et al. 2014) noted that the maximum heat transfer is found to be at bulk temperature (or enthalpy) near the pseudo-critical temperature (or enthalpy). The pseudo-critical point of a fluid, at a given pressure, is defined as the point of maximum specific heat capacity. In the present experiment, the maximum heat transfer coefficients are found to be located at different bulk temperatures, and below the pseudo-critical temperature. However, it should be noted that properties and bulk temperatures are averaged over the full test section length, and therefore the local and real location of the heat transfer maximum is unknown. It should be noted that maximum heat transfer coefficients are found to be located at similar inner wall temperature of respectively 112, 109 and 110 °C.

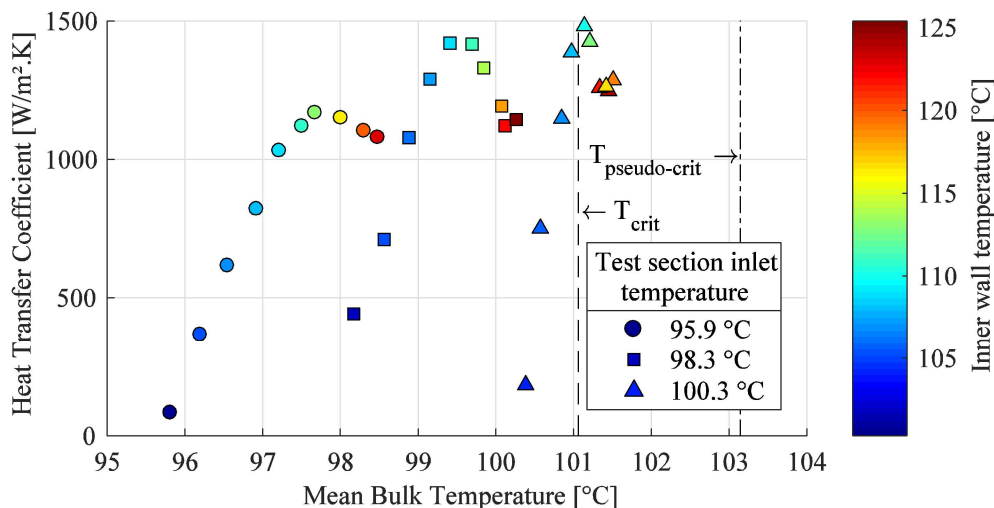


Figure V-4: Near critical point heat transfer investigation: influence of the inlet temperature

Influence of the pressure, the flow rate and the test section inlet temperature is separately studied in Figure V-5. Mean value of main parameters and their standard deviations for the different heat fluxes are detailed in the Table V-1, for each case study.

As previously discussed, the test section inlet temperature changes the maximum heat transfer coefficient, partly because parameters values used are averaged on the overall test section length.

As expected, the heat transfer coefficient increases with the mass flow rate. A 60 % increase of the mass flow rate induced a 35 % increase of the heat transfer coefficient, in average, for the four first cases. This is lower than the Dittus-Boelter mass flow rate correlation coefficient ($Re^{0.8}$), with an experimental coefficient about $Re^{0.65}$. In contrast, the

inner wall temperature at maximum heat transfer coefficient location doesn't seem to change with the mass flow rate.

Table V-1: Main parameters of the Figure V-5 different test cases: mean value and standard deviation

Legend	Mass flow rate m [kg/s]	Mass velocity G [kg/m ² .s]	Test section inlet temperature $T_{TS,in}$ [°C]	Fluid pressure [bar]
Fig a) – Filled blue dot	$0.0427 \pm 3.5 \text{ E-4}$	60.4 ± 0.5	95.3 ± 0.03	42.5 ± 0.3
Fig a) – Filled red dot	$0.0435 \pm 4.2 \text{ E-4}$	61.6 ± 0.6	100.7 ± 0.2	42.4 ± 0.3
Fig a) – Empty blue dot	$0.0680 \pm 3.4 \text{ E-4}$	96.3 ± 0.5	95.9 ± 0.1	42.4 ± 0.2
Fig a) – Empty red dot	$0.0676 \pm 4.3 \text{ E-4}$	95.7 ± 0.6	100.3 ± 0.1	42.4 ± 0.2
Fig b) – Filled blue dot	$0.0675 \pm 2.2 \text{ E-4}$	95.4 ± 0.3	98.7 ± 0.04	41.0 ± 0.2
Fig b) – Filled red dot	$0.0669 \pm 3.9 \text{ E-4}$	94.6 ± 0.5	98.3 ± 0.04	42.3 ± 0.1

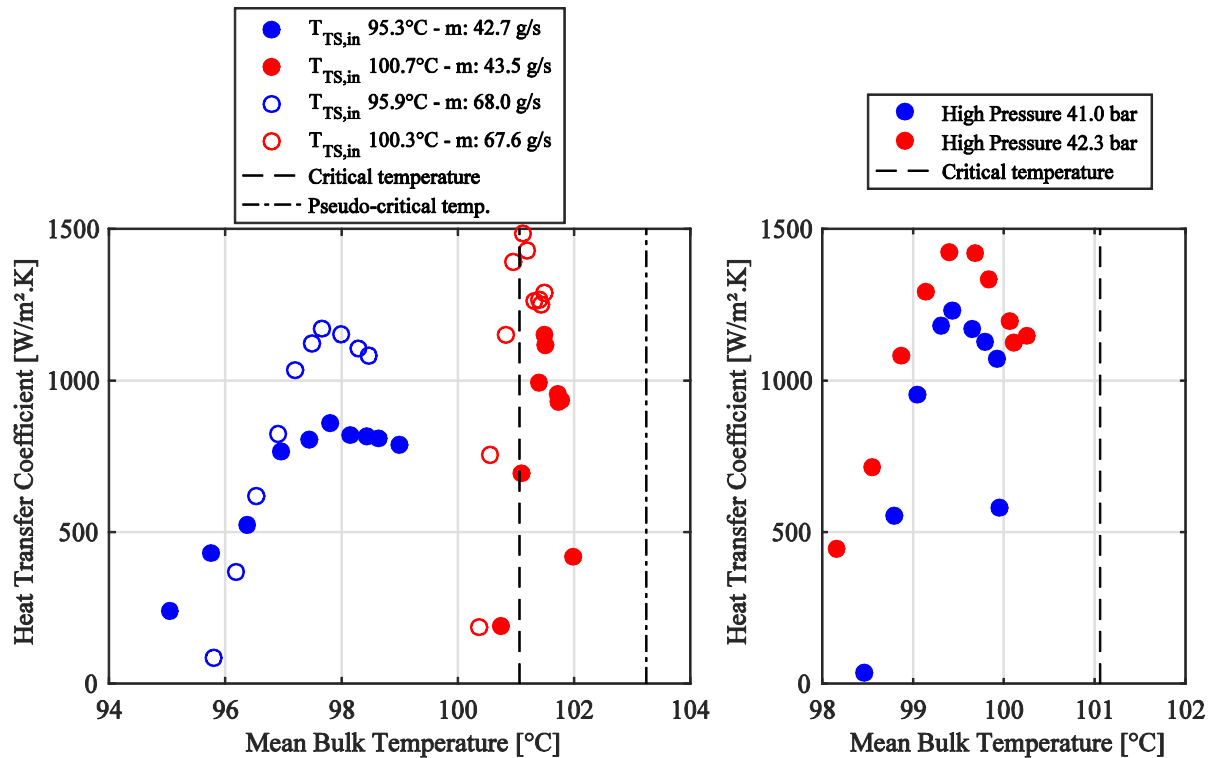


Figure V-5: Near critical point heat transfer investigation: influence of the pressure, flow rate and inlet temperature over the maximum heat transfer coefficient location

In Figure V-5b, the effect of the fluid pressure is investigated. For both pressure levels, the maximum heat transfer coefficient is located at the same mean bulk temperature, largely below the critical point and pseudo-critical points of each pressure level. However, the heat transfer coefficient is found to be higher at high pressure (42.3 bar case), above the critical pressure, rather than just above the critical pressure (41 bar case), which is in conflict with (Shen et al. 2016) conclusions of maximum heat transfer coefficient at the critical pressure and temperature.

As (Arnaud Bruch 2006) noted, supercritical fluids present different heat transfer regimes depending on the heat flux, the mass velocity and the ratio of both parameters. Research conducted shown a deterioration of the heat transfers as the heat flux to mass velocity ratio q/G increases. Different authors proposed correlations of this ratio to predict the deterioration. Some are summarized by (Huang et al. 2016), the present data are found

to be below the q/G limit of correlations developed for water (non-deteriorated heat transfer), but above the limit of correlation developed for CO_2 .

Different correlations were developed for supercritical water and CO_2 heat transfer coefficients determination. (Arnaud Bruch 2006) concluded that the Krasnoshchekov correlation (Krasnoshchekov et al. 1967) and its upgrade by Jackson (Jackson 2002) provided the best results for supercritical water and carbon dioxide.

The Jackson correlation is calculated as shown below:

$$\text{Nu}_{\text{Jackson}} = 0.0183 \cdot \text{Re}^{0.82} \cdot \text{Pr}^{0.5} \cdot \left(\frac{\rho_w}{\rho}\right)^{0.31} \cdot \left(\frac{\overline{C_p}}{C_p}\right)^n \quad \text{Eq. V-9}$$

with:

$$n = \begin{cases} 0.4; & T_w < T_{\text{crit}} \text{ and } T_b > 1.2 \cdot T_{\text{crit}} \\ 0.4 + 0.2 \left(\frac{T_w}{T_{\text{crit}}} - 1\right); & T_b < T_{\text{crit}} < T_w \\ 0.4 + 0.2 \left(\frac{T_w}{T_{\text{crit}}} - 1\right) \left[1 - 5 \left(\frac{T_b}{T_{\text{crit}}} - 1\right)\right]; & T_{\text{crit}} < T_b < 1.2 \cdot T_{\text{crit}} \end{cases} \quad \text{Eq. V-10}$$

$$\overline{C_p} = \frac{C_{p,b} + C_{p,w}}{2} \quad \text{Eq. V-11}$$

(Liao and Zhao 2002) developed correlations for horizontal, upward and downward supercritical CO_2 flow in small tubes. The downward correlation is also calculated for comparison, as tests were performed in downward flow configuration:

$$\text{Nu}_{\text{Liao}} = 0.643 \cdot \text{Re}^{0.8} \cdot \text{Pr}^{0.4} \cdot \left(\frac{\rho_w}{\rho}\right)^{2.154} \cdot \left(\frac{\overline{C_p}}{C_p}\right)^{0.751} \cdot \left(\frac{\overline{Gr}}{\text{Re}^{2.7}}\right)^{0.186} \quad \text{Eq. V-12}$$

with Gr the Grashof number as defined below – g is the gravitational acceleration and D_h the pipe hydraulic diameter:

$$\overline{Gr} = \frac{(\rho - \bar{\rho})\rho \cdot g \cdot D_h^3}{\mu^2} \quad \text{Eq. V-13}$$

Figure V-6 shows the parity plot of experimental Nusselt number with correlations Nusselt numbers for the Dittus-Boelter correlation, the Jackson correlation and the Liao downward correlation.

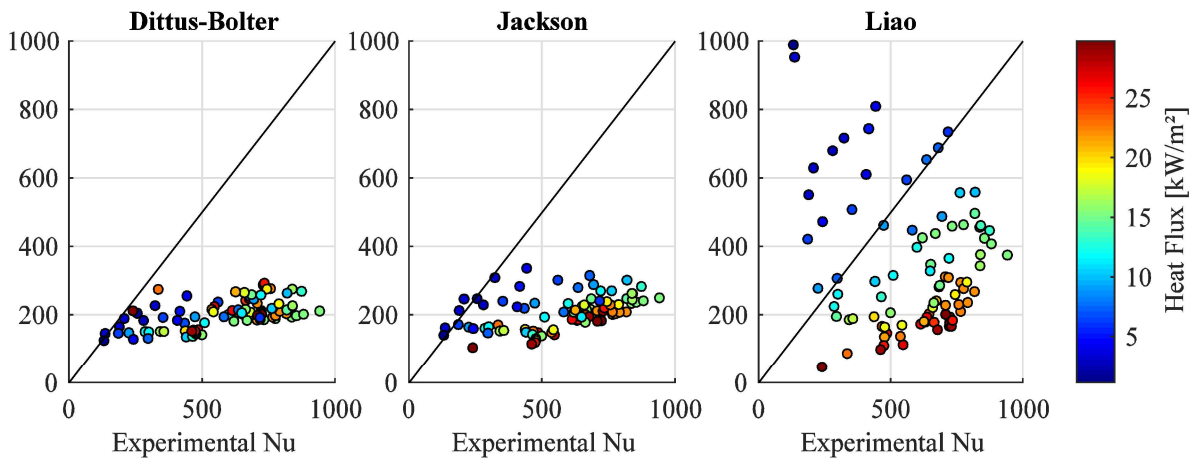


Figure V-6 Near-critical point heat transfer investigation: comparison with Dittus-Boelter, Jackson and Liao downward correlations

Dittus-Boelter and Jackson correlations are found to drastically underestimate the actual Nusselt number up to 500 %. Therefore, it is clear that those correlations are not adapted to this case study.

The Liao correlation, by taking into account the buoyancy forces through the Grashof number seems to provide same order Nusselt number but doesn't match perfectly the experimental data.

The Jackson and the Liao correlations frame are used to create customized correlations:

$$Nu_{Frame} = C_1 \cdot Re^a \cdot Pr^b \cdot \left(\frac{\rho_w}{\rho}\right)^c \cdot \left(\frac{C_p}{C_{p0}}\right)^d \cdot \left(\frac{Gr}{Re^{2.7}}\right)^e \quad \text{Eq. V-14}$$

In the Jackson-base correlation, only the proportional coefficient C_1 and the density ratio exponent (c) are unconstrained. The Reynolds (a), Prandtl (b), and specific heat capacity ratio (d) exponents are set to the Jackson value, respectively 0.82, 0.5 and n (see Eq. V-9) while the Grashof exponent (e) is set to 0 since this coefficient is not used by Jackson.

In the Liao-base correlation, every coefficients are unconstrained, except the Reynolds and Prandtl exponents, set respectively to the Dittus-Boelter values: 0.8 and 0.4. A last free-base correlation is also tested. In this correlation, all the coefficients (C_1, a, b, c, d, e) are unconstrained.

To estimate the correlation coefficients, a relative least squares minimization function is introduced to fit the experimental and the estimated Nusselt numbers (Nu_{exp} and Nu_{esti}):

$$f_{min} = \sum (1 - Nu_{esti}/Nu_{exp})^2 \quad \text{Eq. V-15}$$

The minimization is run on near-critical points only, and estimated coefficients are shown in Table V-2.

Table V-2: Customized correlations: estimated coefficients

Base	C_1	a	b	c	d	e	Max rel. err.	Mean rel. err.	Standard dev.
Jackson	0.0123	*0.82*	*0.5*	-0.8166	*n*	*0*	107.22 %	31.95 %	34.73 %
Liao	0.0124	*0.8*	*0.4*	-0.7226	0.02244	-0.1028	101.69 %	30.36 %	34.14 %
Free	0.0071	0.8311	0.8165	-0.6526	0.3231	-0.0416	99.84 %	29.43 %	33.57 %

Figure V-7 shows the parity plot between experimental and estimated Nusselt numbers from customized correlations. Both customized correlations seem to fit equally the experimental data. Indeed, the mean relative error and the standard deviation of the three correlations are very close. Inherently, correlation with higher degree of freedom performs slightly better but not significantly.

Therefore, the two coefficients unconstrained in the Jackson-base correlation should be preponderant in the data fitting. If the proportional coefficient C_1 is of the same order between the original Jackson correlation (0.0183) and the customized Jackson-base correlation (0.0123), the density ratio exponent is drastically different, passing from 0.31 to -0.82. The Liao-base and free-base customized correlations, also experienced a sign and amplitude change for the density ratio exponent and the Grashof exponent (e).

The negative sign of the density ratio exponent means that an increase of the temperature difference between the inner wall interface and the fluid bulk increases the

density difference in the fluid flow and this density difference tends to improve the heat transfer coefficient.

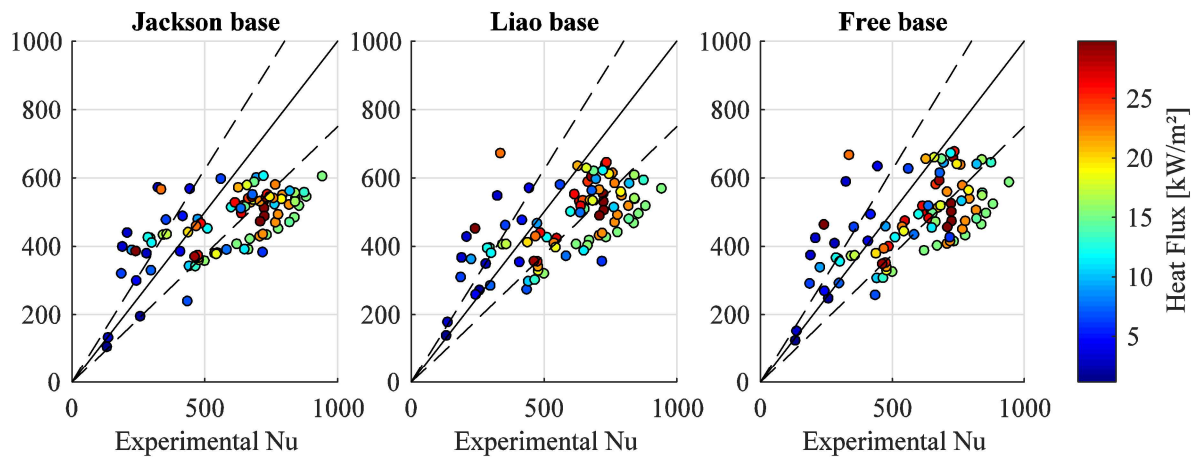


Figure V-7: Near critical point heat transfer investigations: customized correlations

An exponent sensitivity analysis is performed for the Free-base correlation. All the exponents except one are set to the estimated value to evaluate the sensitivity of the correlation to each non-dimensional number (Layssac et al. 2017). Figure V-8 shows the evolution of the relative mean square deviation (see Eq. V-15) with the exponents' values. The correlation is found to be highly sensitive to the $Gr/Re^{2.7}$ and the Reynolds exponents, however, the $Gr/Re^{2.7}$ exponent is very close to zero. On the opposite, the correlation is not highly sensitive to the C_p exponent, therefore uncertainty on its value is higher. The sensitivity to the density ratio (ρ_w/ρ) exponent is moderate but its value is definitely negative.

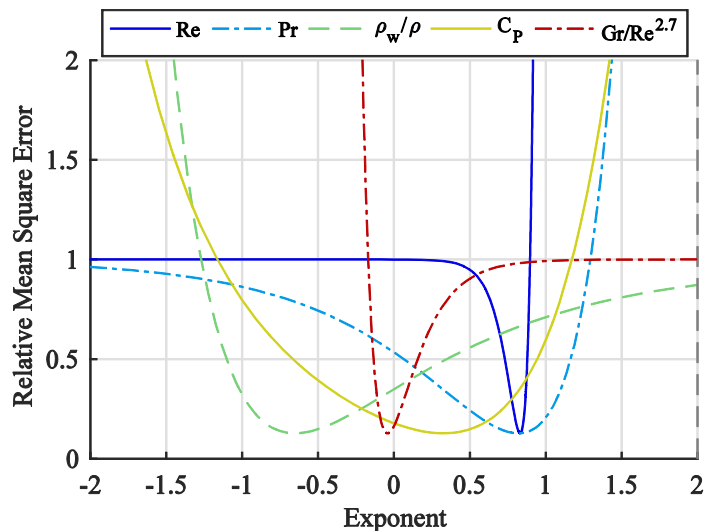


Figure V-8: Free-base correlation exponent sensitivity analysis

This suspected effect could result from the downward flow. The fluid heated at the wall tends to flow backward due to the density difference with the fluid main flow. This effect might not be observed by (Liao and Zhao 2002), since their tests and correlations are performed on small tubes, with diameters ten to fifty times smaller than the present experiment. More investigations, with different tube diameters, horizontal and upward flow

should be performed to further understand and justify the present assumption and correlations.

Furthermore, as explained by (A. Bruch, Bontemps, and Colasson 2009), for the specific flow and heat transfer conditions of turbulent opposing mixed convection, results in heat transfer enhancement due to buoyancy effects. And as summarized by (Huang et al. 2016), effect of buoyancy force on heat transfer might also depend on the tube diameter.

A recognized criterion to distinguish forced and mixed convection was proposed by (Jackson and Hall 1979). Mixed convection should be considered if:

$$Gr/Re^{2.7} > 10^{-5} \quad \text{Eq. V-16}$$

In the present experiment, this criterion is ranging between $2 \cdot 10^{-4}$ and $5 \cdot 10^{-2}$, which validates the turbulent mixed opposing convection case.

Some correlations were developed for supercritical CO_2 heating in mixed convection by (Fewster 1976), correction the Jackson correlation (Eq. V-9) with a $Gr/Re^{2.7}$ coefficient to correct from buoyancy effects, as for the Liao correlation (Eq. V-12):

$$\frac{Nu_{Fewster}}{Nu_{Jackson}} = 15 \cdot \left(\frac{\overline{Gr}}{Re^{2.7}} \right)^{0.4} \quad \text{Eq. V-17}$$

Derived from Fewster's work and correlation, (A. Bruch, Bontemps, and Colasson 2009, 200) developed a correlation for supercritical CO_2 cooling in turbulent opposing mixed convection:

$$\frac{Nu_{Bruch}}{Nu_{Jackson}} = \left(1.542 + 3243 \cdot \left(\frac{\overline{Gr}}{Re^{2.7}} \right)^{0.91} \right)^{1/3} \quad \text{Eq. V-18}$$

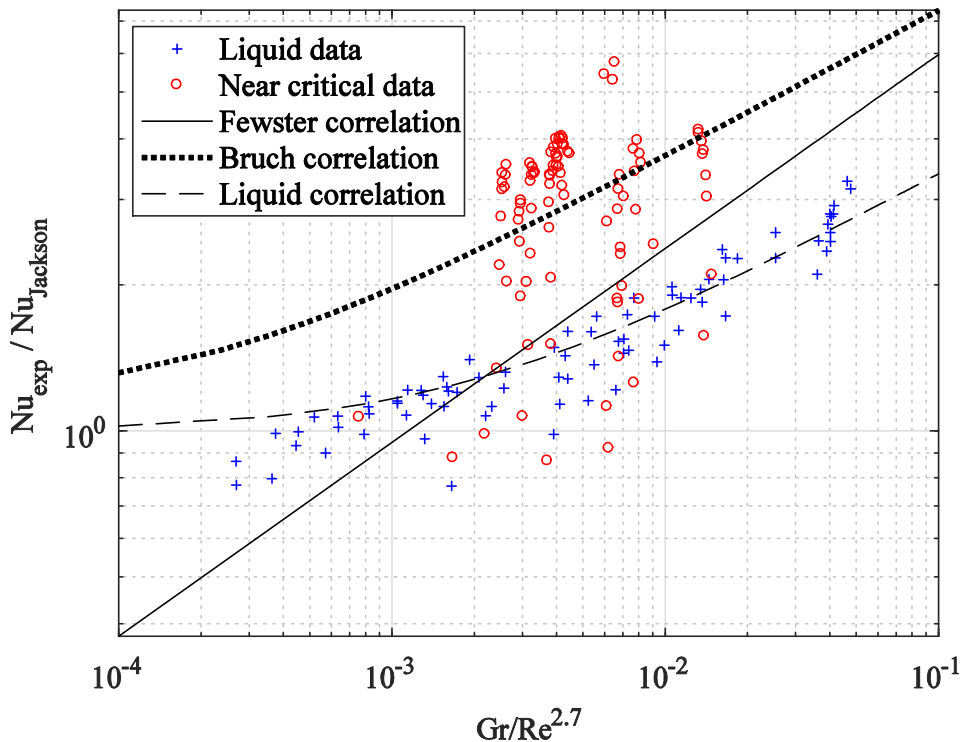


Figure V-9: Mixed convection effects: data and correlations

The liquid entry data and near critical data are distinguished on the Figure V-9. This figure shows the experimental to Jackson Nusselt ratio, function of the mixed convection criterion $Gr/Re^{2.7}$. Liquid entry data showed a similar trend than data obtained by (A. Bruch, Bontemps, and Colasson 2009). However, the Bruch correlation largely overestimates the Nusselt number compared to liquid entry data Nusselt. A new correlation is developed for liquid entry data, based on the Bruch correlation:

$$\frac{Nu_{liquid}}{Nu_{Jackson}} = \left(1 + 308 \cdot \left(\frac{\overline{Gr}}{Re^{2.7}} \right)^{0.91} \right)^{1/3} \quad \text{Eq. V-19}$$

The 308 coefficient is empirically estimated and it is ten times smaller than the original Bruch coefficient. But test case are also drastically different, Bruch experiment is performed for supercritical CO₂ cooling, largely above the critical point. While present liquid entry test are performed with R134a heating at near-critical pressure, with bulk temperature above the critical temperature and wall temperature near or above the critical temperature. In contrast, the Bruch correlation better fits the near-critical data. However, those data are disparate: near-critical data with low heat flux are overlying the liquid entry data.

As explained by (Huang et al. 2016), even today, near-critical point heat transfer are not deeply investigated and understood, both numerical and experimentally. Thermo-physical properties undergo sharp and large changes. Therefore, further investigation should be done.

2 Plate heat exchanger

2.1 Global heat transfer coefficient

The CORSERE test bench is equipped with two brazed plate heat exchangers from SWEP© in series for working fluid heating. The first heat exchanger, called pre-heater has a heat transfer area of 2.39 m², while the second exchanger, called evaporator has a two times bigger heat transfer area of 4.91 m².

Heat exchangers were tested in various conditions. However, since the CORSERE test bench did not run at full load, heat exchangers were slightly oversized for the running conditions. It results in quasi-null pinch point in the evaporator, and in the condenser and pre-heater at very low flow rates, as shown in Figure V-10.

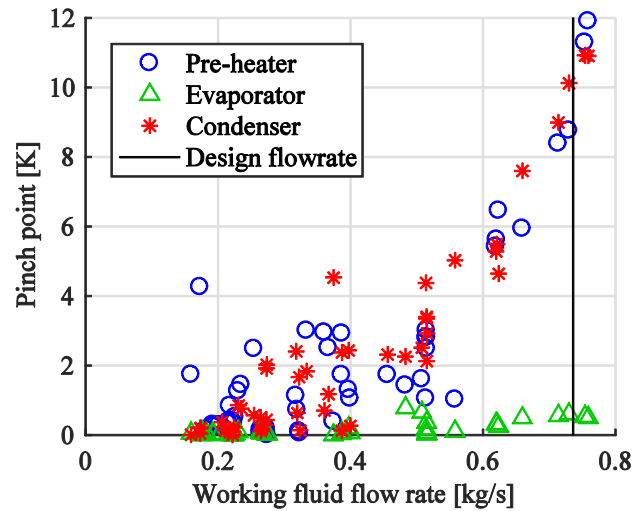


Figure V-10: CORSERE heat exchangers pinch point function of fluid flow rate

The global heat transfer coefficient U is determined from:

$$\frac{1}{U} = \frac{1}{h_{wf}} + \frac{1}{h_{water}} + \frac{t_{wall}}{\lambda_{wal}} \quad \text{Eq. V-20}$$

h_{wf} is the unknown working fluid heat transfer coefficient, t_{wall} and λ_{wall} the plates thickness and thermal conductivity, respectively 0.6 mm and 16.3 W/m.K. h_{water} is the water side heat transfer coefficient, calculated using the experimental correlation determined during subcritical test:

$$h_{water} = h_0 \cdot m_{water}^{0.8} \quad \text{Eq. V-21}$$

With h_0 for the pre-heater and the evaporator estimated respectively at 16.5 and 10.1 kW/m².K.

Since the specific heat capacity of the working fluid is drastically changing near the critical point, the log mean temperature difference (LMTD) cannot be used to estimate the

global heat transfer coefficient of the heat exchanger and then the working fluid heat transfer coefficient.

Instead, the working fluid heat transfer coefficient is estimated by dichotomy. The hypothetical fluid heat transfer coefficient is used to calculate a mean global heat transfer coefficient U over the complete heat exchanger. The heat exchanger is discretized in N segments of same heat rate $\delta q = Q/N$. The working fluid – water temperature difference is calculated on each segment $\delta T = (T_{\text{water,in}} + T_{\text{water,out}} - T_{\text{wf,in}} - T_{\text{wf,out}})/2$. Then, the necessary heat transfer area for each segment is calculated from $\delta A = \delta q / (U \cdot \delta T)$, and every segment necessary area are summed to get the estimated heat transfer area $A_{\text{esti}} = \sum \delta A$. The mean fluid heat transfer coefficient h_{wf} is identified, using a solver minimizing the difference between the estimated heat transfer area and the heat exchanger real area.

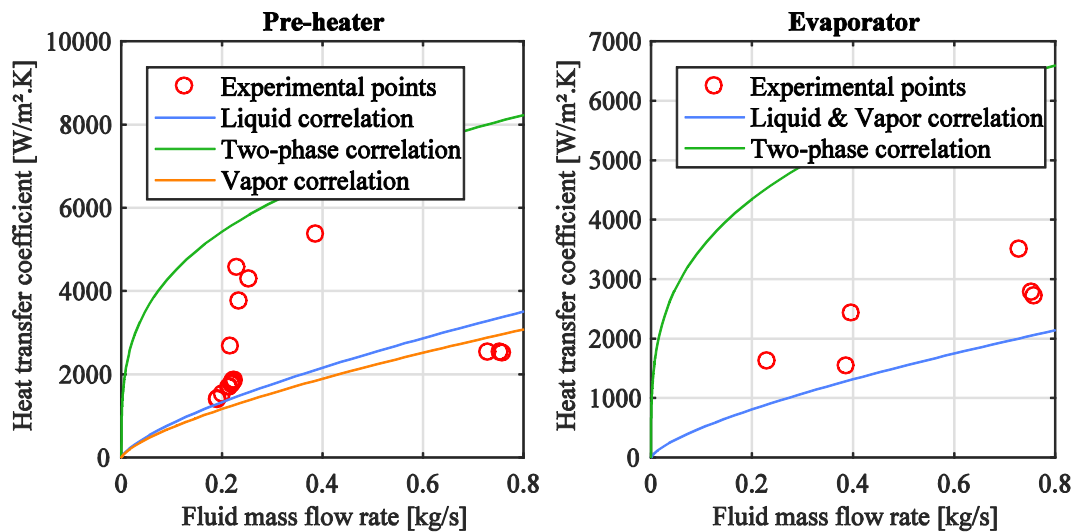


Figure V-11: Pre-heater and evaporator fluid heat transfer evolution with the flow rate in supercritical conditions

Figure V-11 shows the evolution of the fluid heat transfer coefficient with the fluid flow rate for the pre-heater and the evaporator when they respectively reached supercritical outlet conditions. Note, evaporator data with quasi-null pinch – or negligible heat transfer – are removed.

For comparison, the heat transfer correlation, validated for both exchangers for the different fluid phases are plotted. In the evaporator, heat transfer coefficient of supercritical fluid is 20 to 80 % higher than the expected liquid heat transfer coefficient, and 50 % higher in average.

The pre-heater heat transfer coefficient with supercritical outlet is also 50 % higher, in average, than the expected liquid coefficient. However, it ranges from -25% to $+400\%$ and never surpasses the expected two-phase coefficient. Therefore, more investigations are necessary, with a better control of each influencing parameter.

Figure V-12 shows the heat transfer coefficient ratio evolution with the pre-heater outlet temperature or fluid pressure. The heat transfer coefficient ratio is the ratio the of heat transfer coefficient h_{wf} with the expected liquid heat transfer coefficient based on the previously validated correlations. Ratio above one means enhance heat exchanges compared to liquid heat transfer.

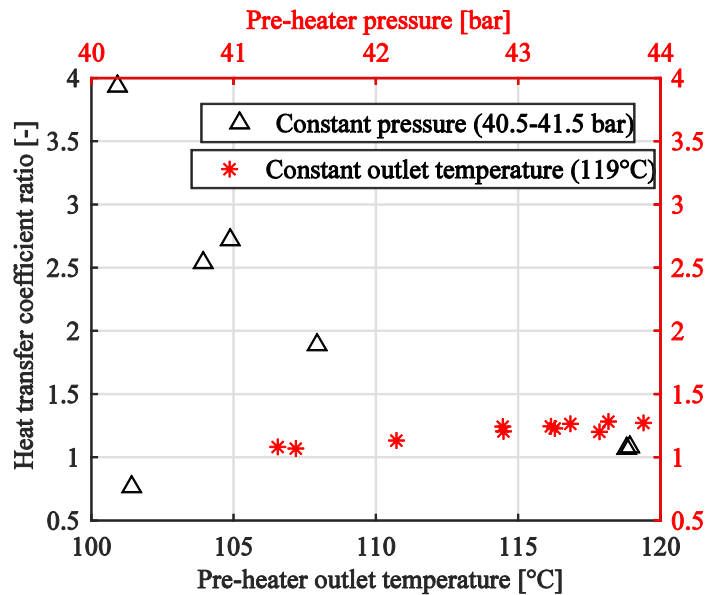


Figure V-12: Heat transfer investigation of pre-heater with supercritical outlet conditions - temperature and pressure influence

At constant outlet temperature, the fluid pressure increase slightly increases the heat transfer ratio. Passing from +5 % at 41.5 bar to +25 % at 44 bar. Function of the pre-heater outlet temperature, the effect is much more drastic. For outlet at the supercritical temperature, the heat transfer enhancement reached nearly +400 %, but quickly drops to +200 % 7 °C above the critical temperature and only +5 % 18 °C above the critical temperature.

It should be noted that the calculated heat transfer coefficient is not the local heat transfer coefficient of the working fluid but a global coefficient. Therefore, since the fluid enters the pre-heater near the ambient temperature (20 °C), the local heat transfer coefficient near the pseudo-critical point might even be higher.

However, available data are limited and further investigation might be necessary to fully understand and propose a robust correlation for supercritical heat exchanges. It should be noted that while a point is found to be +400 % enhanced, near the critical temperature, another points shown a 20 % degradation for similar temperature level.

2.2 Exergetic analysis

Heat exchangers are analyzed from an exergetic standpoint. For this analysis, the CORSERE pre-heater and evaporator were considered as a single heat exchanger called heaters. Figure V-13 shows the heaters exergetic efficiency evolution with the fluid mass flow rate, both when the economizer is on line and bypassed. For evaporator, we defined two different exergetic efficiencies. The simple evaporators' exergetic efficiency, ratio of the exergy accumulated by the working fluid and the exergy rejected by the hot fluid, which only accounts for the exergy destruction during heat transfer:

$$\varepsilon_{ev} = \frac{\Delta E_{wf, ev}}{E_{sup}} = \frac{(E_{wf, out} - E_{wf, in})}{(E_{HF, in} - E_{HF, out})} = 1 - \frac{I_{ev}}{E_{sup}} \quad \text{Eq. V-22}$$

And the evaporators' exergetic recovery efficiency, to account for heat source non-recovered exergy, useful to analyses process with open heat sources:

$$\varepsilon_{ev, rec} = \frac{(E_{wf, out} - E_{wf, in})}{(E_{HF, in} - E(T_0; P_{out})_{HF})} \quad \text{Eq. V-23}$$

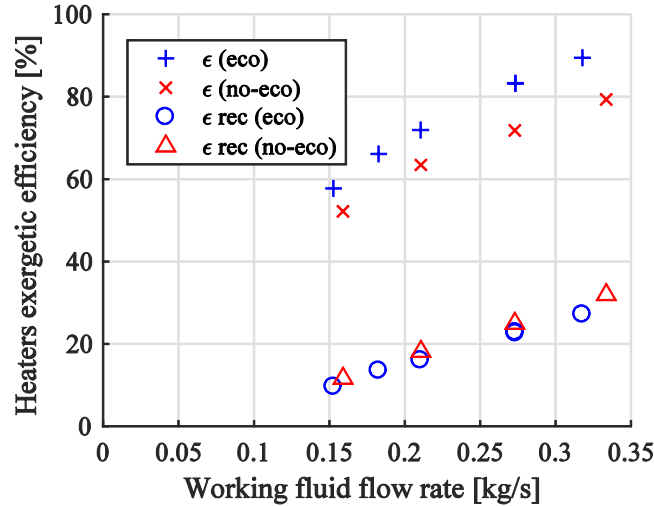


Figure V-13: Heater exergetic efficiency

For every case (with/without eco) and both efficiency definitions, the exergetic efficiency increases with the working fluid mass flow rate and the fluid pressure. The economizer configuration increases the heat exchanger exergetic efficiency of 5 to 10 %, since the working fluid enters the pre-heater at higher temperature, the mean temperature difference is reduced and so the exergy destruction during the heat transfers. However, economizer configuration slightly decreases the heat exchanger exergetic recovery efficiency by 2 to 3%, since the working fluid entering at higher temperature is less able to lower the hot water temperature by recovering heat, this effect counteract the previous effect.

Effects of other parameters on the heat exchanger efficiencies are tested. The classic exergetic efficiency decreases with higher hot water temperature inlet since the mean temperature difference increases, but increases with higher working fluid pressure, especially at low working fluid flow rate. The exergetic recovery efficiency is not or slightly influence by the hot water temperature inlet and working fluid pressure, but drops at high hot water flow rate since the hot water temperature outlet is increased for similar heat power.

Similar results are also observed on the CPV-Rankine evaporator. Figure V-14 shows the evaporator exergy destruction ratio (I_{ev}/E_{sup}) for a large set of outlet temperature and fluid pressure. Exergy destruction rate increases as the outlet temperature increases, however, increases of the fluid pressure drastically reduces the exergy destruction rate. Minimum destruction rate are achieved at supercritical pressure and outlet temperature.

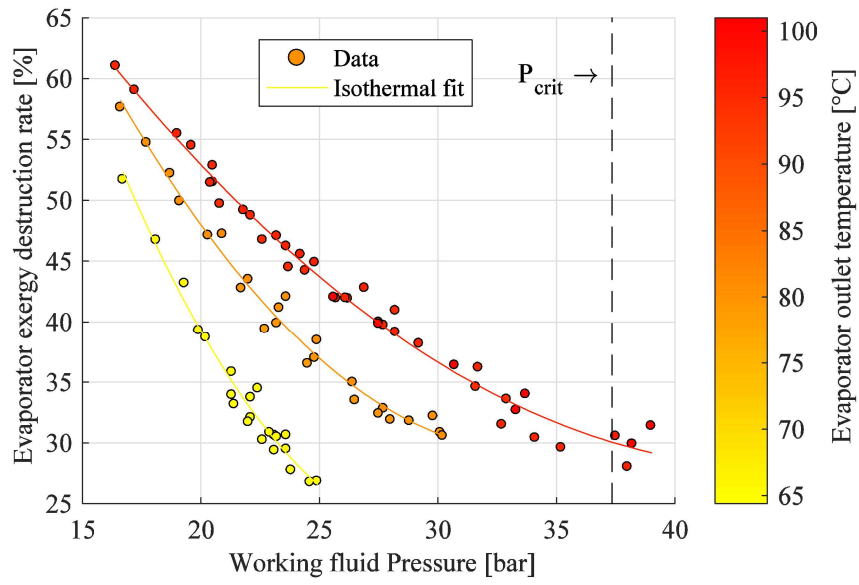


Figure V-14: CPV-Rankine evaporator - exergy destruction rate

Chapter conclusion

This chapter proposed a focus on supercritical heat transfers. In a first step, a dedicated experimental setup is presented and used. The setup consists of a smooth tube, homogeneously heated by a controlled power electric cord. The flow in the tube is in downward configuration.

In a first set of tests, subcooled fluid enters the test section. In this case, heat transfer coefficient is found to be very sensitive to the heat flux. Experimental Nusselt number is compared with classic correlations from the literature. The Sieder-Tate correlation is found to better estimates the experimental value, by adding a bulk to wall viscosity ratio coefficient.

Then, near-critical point heat transfer is investigated. Fluid enters the test section at pressure slightly above the critical pressure, and temperatures slightly below the critical temperature. Effects of different parameters are investigated: inlet temperature, fluid pressure and mass flow rate.

Finally, experimental Nusselt is compared with Nusselt numbers computed with some supercritical fluid heat transfer correlations from the literature. The Liao downward flow correlation is found to give the best results, even if dispersion is very high. The Jackson correlation largely underestimated the heat transfer coefficient. Indeed, the present flow and heat transfer is found to be a mixed convection. Then a new correlation derived from Bruch's correlation is proposed.

In a second step, a commercial plate heat exchanger is investigated under transcritical conditions. A global heat transfer coefficient is determined for the pre-heater and the evaporator of the CORSERE test bench.

Supercritical global heat transfer coefficient is found to be higher than the liquid state heat transfer coefficient but below the two-phase heat transfer coefficient. Effects of the pressure and the fluid temperature over the heat transfer coefficient are discussed. However, no clear and precise conclusion could be drawn from the present experiment and data.

Finally, the heat exchanger performances are investigated using exergetic efficiency criterion. Heaters exergy destruction rate is found to decrease with the fluid pressure, and to be minimized under supercritical pressure.

In addition, regenerator is found to be useful to improve heaters exergetic efficiency in closed-source applications but unnecessary to improve the exergetic heat recovery efficiency for open-source applications.

Chapter VI

Working fluid charge

1 Effect of circulating charge on ORC behavior and performances

1.1 Charge variation at fixed conditions

The working fluid charge is a significant parameter for closed volume thermodynamic engines such as heat pumps or organic Rankine cycles. Working fluid used in those engines should be fully isolated from the environment to avoid leakage, for environmental, health and economic reasons. Therefore, heat pumps and ORCs have constant hermetic volume and working fluid total charge, resulting in a constant average density in the circuit. In addition, such engines work at different temperature and pressure levels resulting in a complex charge repartition in the circuits and the different components.

Fluid charge is largely investigated for heat pumps. Industries are seeking ways to both minimize the total fluid charge due to economic and environmental constraints, and optimize the fluid charge to maximize engine performances (Poggi et al. 2008). Fluid charge is investigated numerically and experimentally. For different working fluids (Afshari et al. 2016), for transcritical CO₂ heat pumps (Aprea, Greco, and Maiorino 2015), and under different source and sink conditions (Corberán et al. 2011).

On the opposite, fluid charge has been barely investigated for organic Rankine cycles. (Xu, Xi, and He 2013) experimentally investigated an ORC running with R123 as working fluid and found an optimal charge to maximize the power output. (T. Li et al. 2015) experimentally investigated an ORC running with R245fa and a 0.72/0.28 mixture of R245fa and R601a. For both the pure fluid and the fluid mixture, authors found different fluid charge optima to maximize the ORC thermal efficiency or the output power. Fluid charge is also found to influence heat exchangers global heat transfer coefficients.

Many ORCs include a working fluid reservoir place in-line between the condenser exhaust and the pump intake. In normal conditions, the reservoir is at saturation conditions and has a liquid and vapor zone. During transient or under various operating conditions, the reservoir can absorb fluid charge variations to smooth fluid charge effect. The fluid usually exits the reservoir near the saturated liquid conditions, an additional subcooler, an elevation difference or addition of non-condensable gas can be necessary to increase the NPSH at the pump intake.

Recently, an open-source library for charge sensitive ORC modeling was released by (Ziviani et al. 2016) and (Dickes et al. 2017) as previously introduced in Chapter III-3.2. A charge sensitive model enables to compute the fluid charge repartition in the ORC and the components. Model parameters were previously validated against the CORSERE test bench.

For numerical convergence and computation time constraints, a simplified model of ORC based on the CORSERE test bench was developed to numerically investigate the working fluid charge influence on the ORC behavior and performances. The simplified ORC is composed of the CORSERE pump, evaporator, expander and condenser, as shown in Figure VI-1. Pre-heater, economizer as well as pressure drops are removed. However,

realistic pipe lengths were kept to connect the components. Table IV-1 summarizes the pipes and components volumes. To deeply investigate the working charge effect, no in-line reservoir is placed on the CORSERE test bench. Only a 2 liters balloon is added to trap non-condensable gas. In the simplified model, the balloon volume is assumed to be part of the condenser exhaust line.

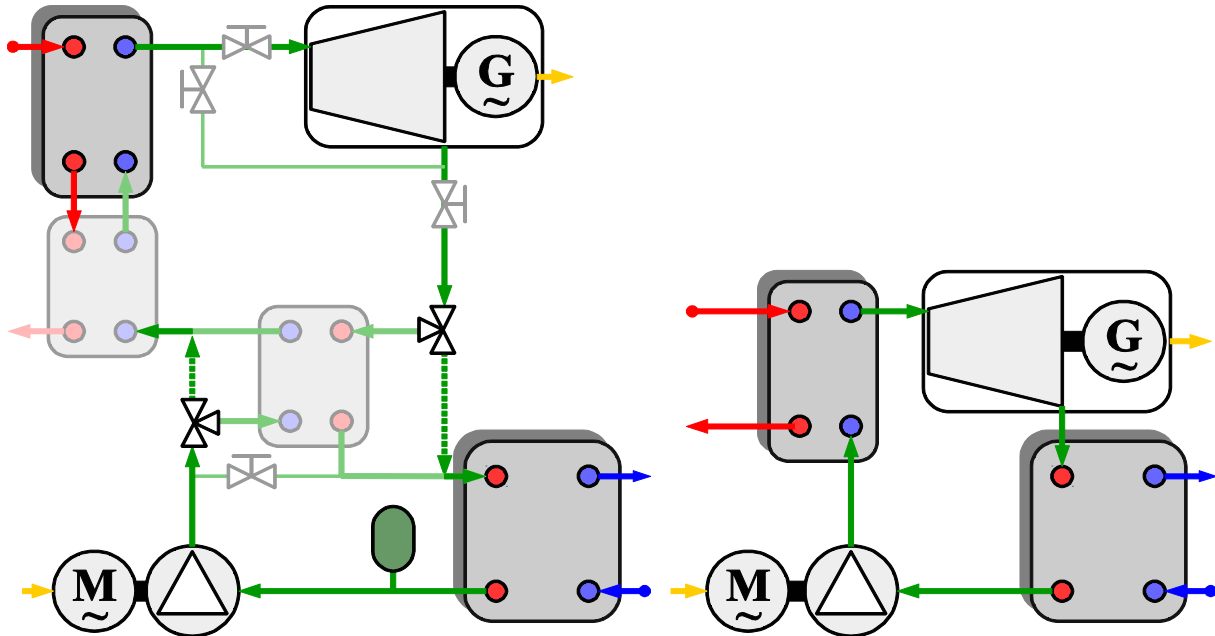


Figure VI-1: Simplified ORC process diagram

Table VI-1: Simplified model pipe and components volumes

Component	Volume	Piping	Volume
Pump	0 m ³	Pump to evaporator	1.6.10 ⁻³ m ³
Evaporator	4.45.10 ⁻³ m ³	Evaporator to expander	6.6.10 ⁻⁴ m ³
Expander (High P)	1.92.10 ⁻³ m ³	Expander to condenser	7.1.10 ⁻⁴ m ³
Expander (Low P)	1.211.10 ⁻² m ³	Condenser to pump	3.8.10 ⁻³ m ³
Condenser	1.060.10 ⁻² m ³		

In a first step, working fluid charge effect is investigated under constant operating conditions. In this reference case, the expander is fixed at the nominal speed of 3000 rpm, the pump motor frequency at half its maximum speed (25 Hz). The heat source, pressurized hot water, is set to 110 °C and 2 kg/s, while the heat sink, cold water, is set to 20 °C and 2 kg/s. The fluid charge is imposed to the model, ranging from 12 to 20 kg of R134a.

Figure VI-2 shows the evolutions of the ORC main parameters with the working fluid charge. High pressure and superheating is found to be barely sensitive to the fluid charge, for charge between 12 and 20 kg, they respectively varied by about 1 bar and less than 2 °C. However, the low condensing pressure and the subcooling are largely impacted by the charge variation. They respectively ranged from 8.5 to 20.5 bar and from 3.1 to 48.6 °C.

As expected, the subcooling increases and the pressure ratio reduction results in a drastic decrease of the ORC net output power and net thermal efficiency. Assuming a minimum subcooling of 10 °C for smooth pump operation (Chapter IV-2.2), the optimal fluid charge for this reference case is about 13.2 kg resulting in a theoretical net power of

9.2 kW and the thermal efficiency of 7 %. Increasing the charge to 16 kg would result in a 1 kW drop of net power and a 1 points of efficiency drop.

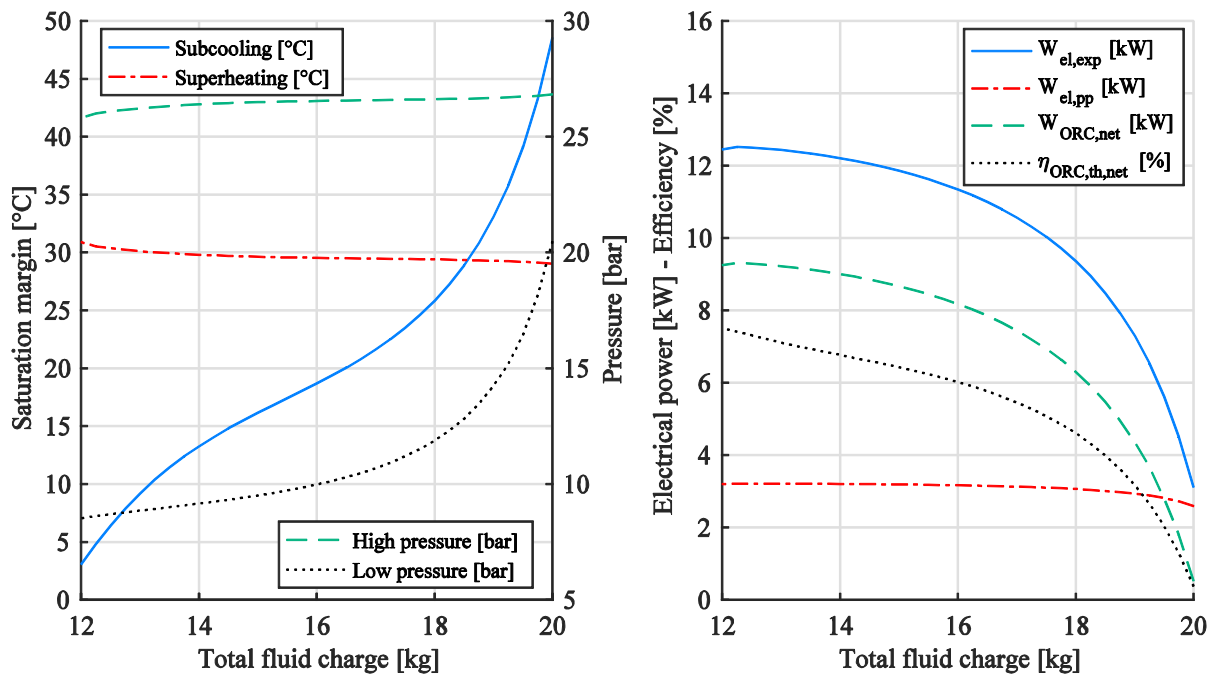


Figure VI-2: Reference case – evolution of the main ORC parameters with the working fluid charge

To understand such behavior, charge repartition in the ORC is shown in Figure VI-3. Adding working fluid does not drastically change the charge in the evaporator or the pipes. The charge in the expander is slightly increasing due to low pressure increase which increases the vapor density at the expander exhaust.

Indeed, most of the working fluid added goes to the condenser. Over the 8 kg of charge added, 7.33 kg are located in the condenser. Relatively to the total charge, the condenser charge proportion increases from less than 30 % to more than 50 % for a total charge increase from 12 to 20 kg.

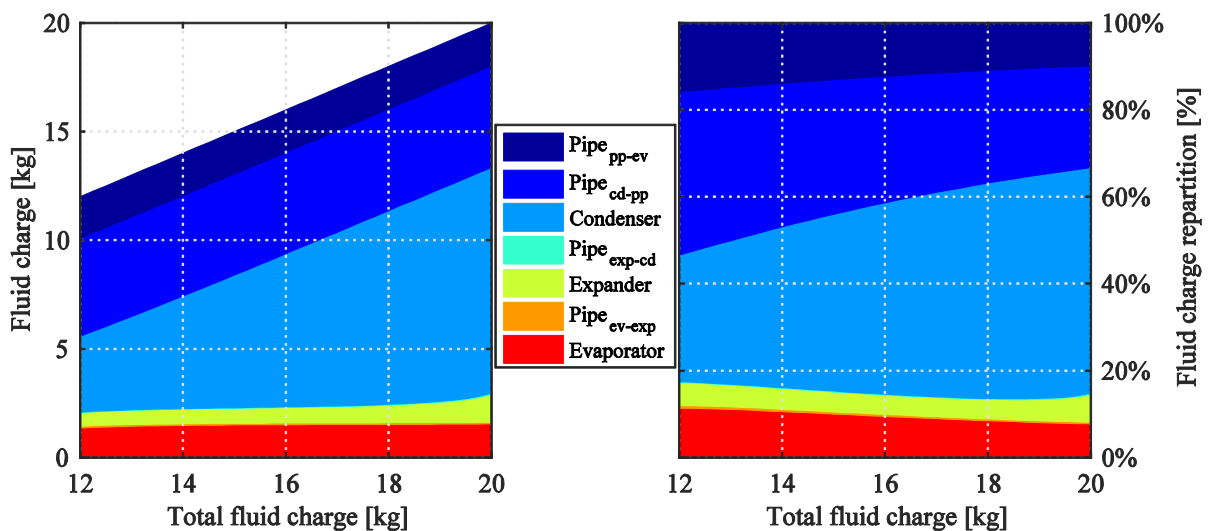


Figure VI-3: Reference case – charge repartition in the ORC

Figure VI-4 focuses on the mass repartition inside the condenser between the different fluid phases. Figure VI-4a and b show respectively the charge and volume repartition by the liquid phase, the two-phase and the vapor phase. As the total fluid charge increases, the liquid represents an increasing proportion of the charge and the condenser volume. In absolute terms, the vapor charge is almost constant and two-phase charge decreases from 3 kg to 0.5 kg when the total fluid charge increases from 12 to 20 kg. Indeed, as the total fluid charge increases by 8 kg, the condenser liquid portion charge increases by 9.4 kg.

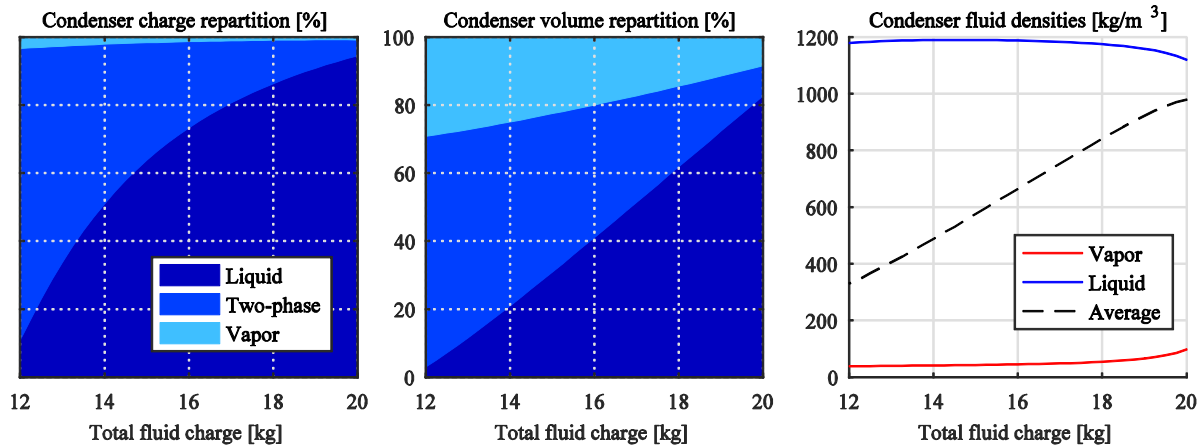


Figure VI-4: Reference case – charge repartition in the condenser

From an elementary view, the ORC can be divided in two zones (Figure VI-5): the high pressure zone and the low pressure zone. In this schematic ORC, the volumes are assumed to be only the evaporator and condenser volumes, pump and expander volumes are neglected. The volume of both high and low pressure zones (V_{HP} and V_{LP}) are constant, as well as the total fluid charge M_{tot} .

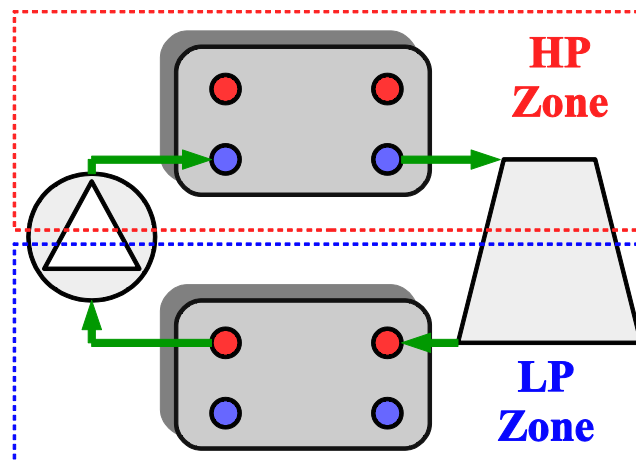


Figure VI-5: ORC pressure zones elementary view

Assuming an ideal pump and a subcooled pump intake, the pump fixes the mass flow rate entering the HP zone. Assuming ideal expander, the expander fixes a constant intake volumetric flow rate. At equilibrium, pump and expander mass flow rates are equivalent, therefore the expander inlet density is fixed. The expander inlet enthalpy is fixed by the heat source. Therefore, the expander inlet pressure is also fixed. Consequently, the high pressure

and average enthalpy in the high pressure zone is constant, resulting in a constant average density and charge in that zone.

Since the total charge is constant, remaining charge is located in the low pressure zone: $M_{LP} = M_{tot} - M_{HP}$. This charge is also constant, as well as the average density in the low pressure zone. The average enthalpy in the low pressure zone is controlled by the heat sink. The remaining free parameter is the low pressure. Indeed, if some charge is added to the total charge, in this ideal ORC, the low pressure zone density would proportionally increase and so the low pressure. This is the observation made in the modeling result in Figure VI-4c. The average density in the condenser is more or less proportionally increasing with the total fluid charge.

Figure VI-6 shows the density and temperature evolution along the condenser volume and T-s diagrams for three different total fluid charges: 12, 16 and 20 kg. The area below the fluid density in the condenser corresponds to the condenser fluid charge.

In the 12 kg charge case, the condenser volume is mostly in vapor (30 %) and two-phase (67 %). Only a small fraction of the condenser length (3 %) is dedicated to the subcooling. Indeed, the pinch point is located at the saturated vapor and the mean temperature difference between the heat sink and the working fluid is rather small, resulting in reduced heat transfer and a longer condenser length for fluid cooling. As the pinch point is located at the saturated vapor point, the condensation pressure could be decreased and the subcooling increased by increasing the heat sink flow rate (assuming the sink inlet temperature is fixed).

In the 16 kg charge case, the different phases are equally shared in volume proportions. The length dedicated to the subcooling is large enough to get a fluid outlet temperature close to the minimum temperature: the heat sink inlet temperature. Pinch point is shifted from the saturated vapor to the sink inlet. Heat sink flow rate increase would slightly decrease the subcooling by reducing the average condenser enthalpy and so the condensation pressure. This effect was observed experimentally.

In the 20 kg charge case, the condenser is almost fully liquid. The condensation pressure is high, as well as the mean temperature difference between working fluid and heat sink. It results in an efficient heat transfer, a rapid de-superheating and fluid condensation. The length dedicated to the subcooling is large enough to have a fluid outlet temperature equals to the heat sink inlet temperature. A heat sink flow rate increase would not further increase the subcooling or reduce the condensing pressure since heat transfer is already very efficient. The only way to reduce the condensing pressure would be to remove some fluid charge to get back to the 16 kg case.

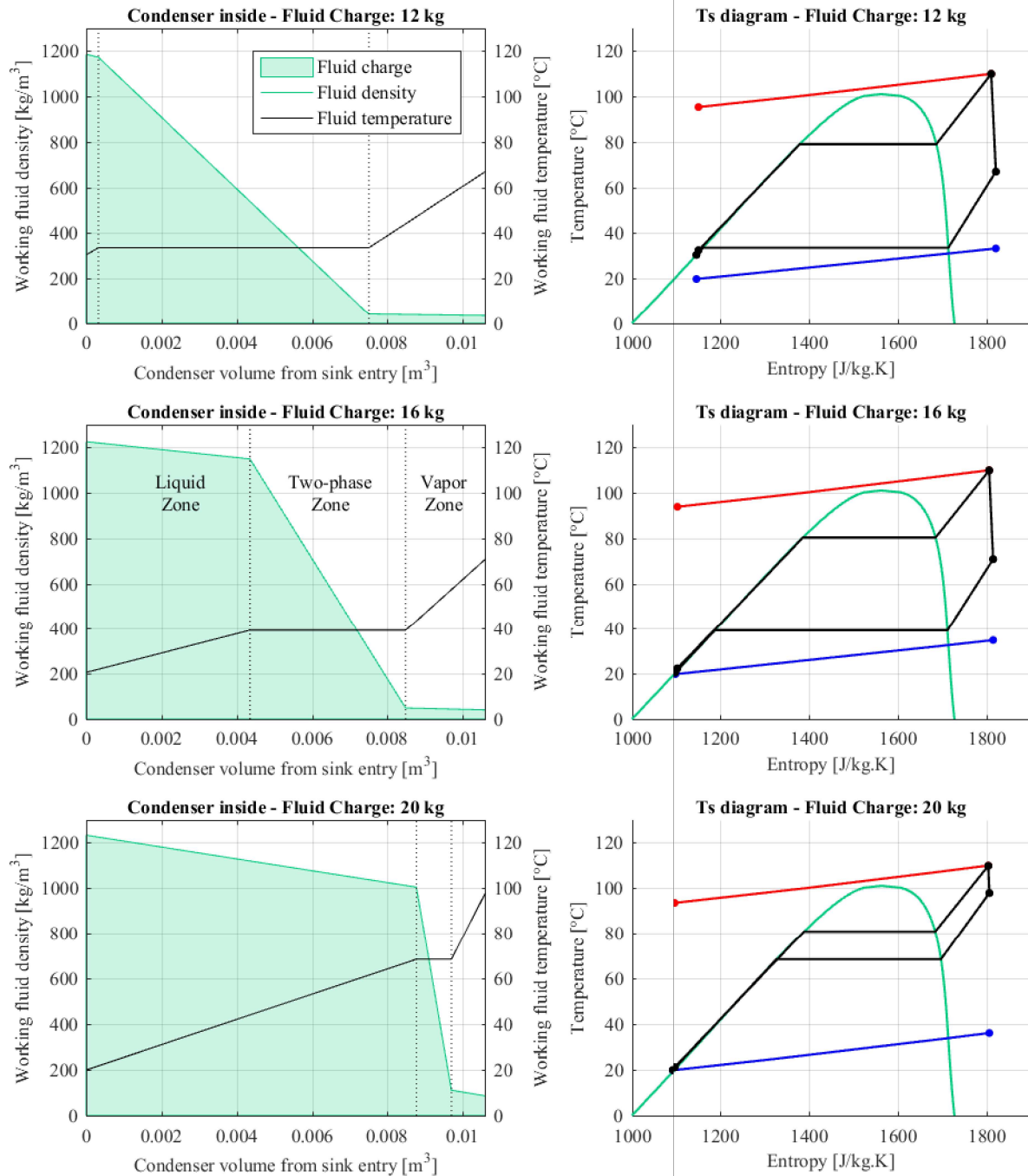


Figure VI-6: Condenser density and temperature evolution and Temperature-entropy diagram for different total fluid charge

1.2 Behavior at various expander and pump speeds

In a second step, influence of the fluid charge was investigated under various expander and pump speeds. Heat source and heat sink are kept constant to the same values as the reference case previously discussed. Figure VI-7 shows the main ORC parameters evolution with the fluid charge. In the left graphs, the pump motor frequency is maintained at 25 Hz, and the expander shaft speeds ranges from 600 to 3600 rpm. In the right graphs, expander speed is set to 1200 rpm, and pump motor frequency ranges from 15 to 35 Hz.

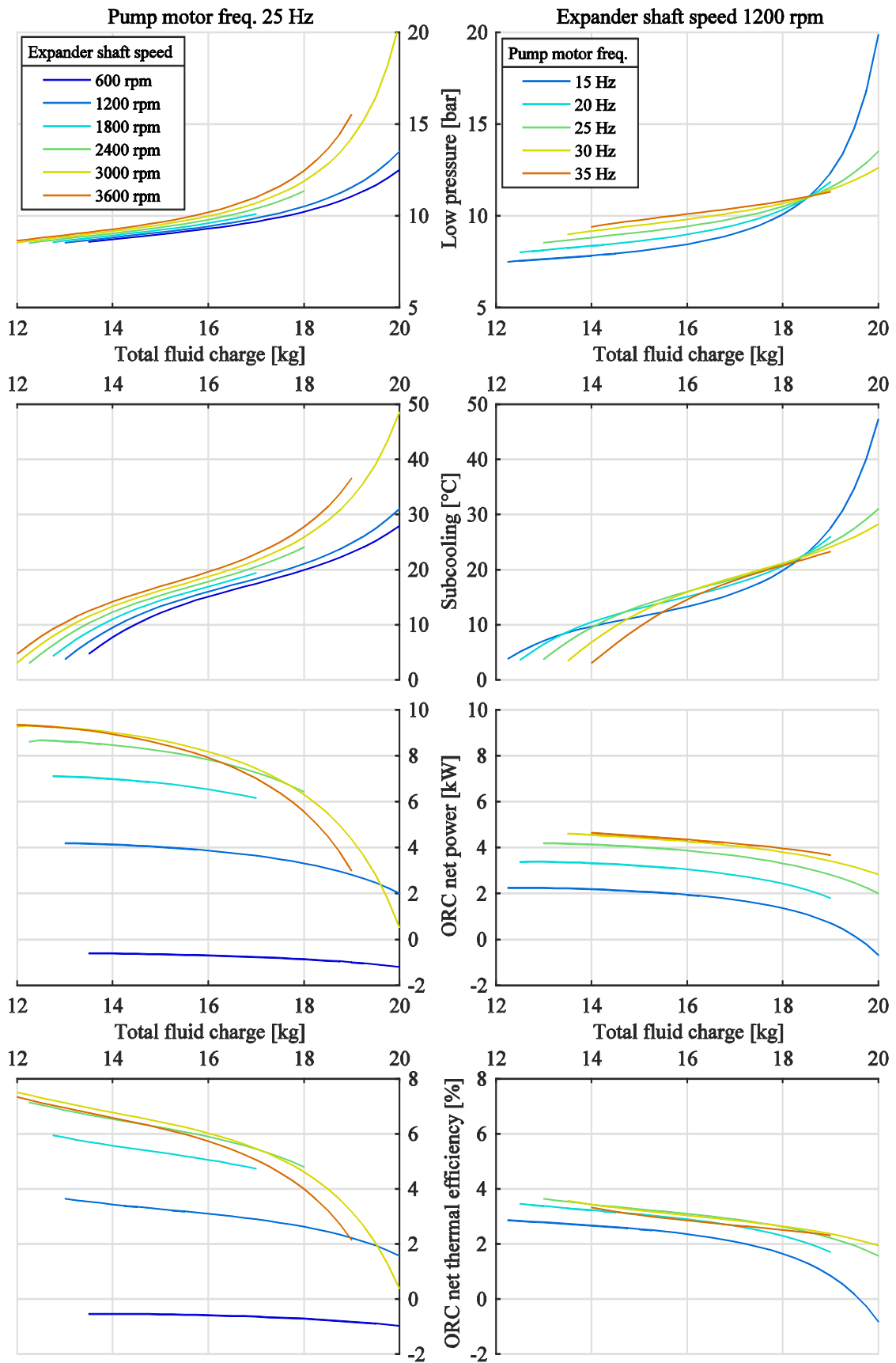


Figure VI-7: ORC behavior investigation under various fluid charge, expander and pump speeds

The low pressure is increasing with the expander shaft speed. The rate of low pressure rate of increase with the fluid charge rises as the expander speed increase. Behavior of the low pressure with the pump speed is more complex. Low pressure is more sensitive to the fluid charge as pump speed is decreasing. However, the influence of the pump speed on the low pressure increase or reduction depends on the fluid charge. It does exist a pivot point charge around 18.5 kg. Below the pivot point charge, the low pressure is increasing with the pump speed, but decreases as the pump speed increase above the pivot point.

Similarly, the subcooling is increasing with the expander shaft speed. However, in contrast with the low pressure, there is a range of fluid charge where the low pressure rate of increase with the fluid charge is smaller. This plateau of fluid charge shift at lower fluid charge as the expander shaft speed increase.

As for the low pressure, the subcooling is found to be more sensitive to the fluid charge at high pump speed. The plateau previously cited tends to decrease – in charge range – as the pump speed increases. In addition, the bottom subcooling limit is reached at higher fluid charge as the pump speed increase; while the ORC reached a 5 °C subcooling for a 12.5 kg charge at the minimum pump motor frequency of 15 Hz, it already reaches this subcooling for a 14.3 kg for a frequency of 35 Hz.

The ORC net power and net thermal efficiency have similar behaviors under various expander shaft speeds. Above 2400 rpm (80 % of the nominal speed), power and efficiency do not changes with the expander speed, since expander efficiency is quite constant. Except at high fluid charge, where higher expander speed leads to faster power and ORC efficiency decline, probably in relation with the subcooling and low pressure increase. Below 2400 rpm, ORC power and efficiency drastically decline and even turn to be negative for 600 rpm, probably due to the expander volumetric and isentropic efficiency decline at very low shaft speed.

Similarly, ORC power increases with the pump speed and reaches an asymptote from 30 Hz (60 % of the nominal speed). The ORC net thermal efficiency is relatively independent of the pump speed, since both the ORC output power and heat power is decreasing at lower working fluid mass flow rate. The ORC starts to decline above 15 Hz. Whatever the pump speed, relation between ORC power and efficiency with the fluid charge is quite similar: almost constant and then declining starting from the pivot point previously cited (around 18.5 kg). The decline is found to be sharper at lower pump speed.

Table VI-2 summarizes the influence of the fluid charge, expander speed and pump speed over the ORC main parameters.

Table VI-2: Summary of fluid charge and machineries speed effect over the ORC

ORC parameter	Fluid charge	Expander speed	Pump speed
High pressure	+	--	++
Superheating	-	--	++
Low pressure	= / ++	+	+
Subcooling	+++	+	=
Net power	= / --	++ / =	- / =

Finally, a last investigation of expander and pump speed is made for a constant and fixed total fluid charge of 15 kg. Model is computed for expander speed ranging from 600 rpm to 3600 rpm (maximum speed), and pump motor frequency from 5 to 50 Hz (nominal speed), in order to create a mapping for ORC performances and behavior at fix fluid charge.

Figure VI-8 shows the maps of ORC net power, ORC net thermal efficiency, subcooling and condenser volume fraction occupied by liquid fluid, for a fluid charge of 15 kg. A cubic interpolation is performed to create the maps. However for some pump and expander speeds, the model did not converge. At high pump speed and low expander speed, the subcooling was tending to zero and the high pressure to supercritical pressure; while at low pump speed and high expander speed, pressure difference tended to zero.

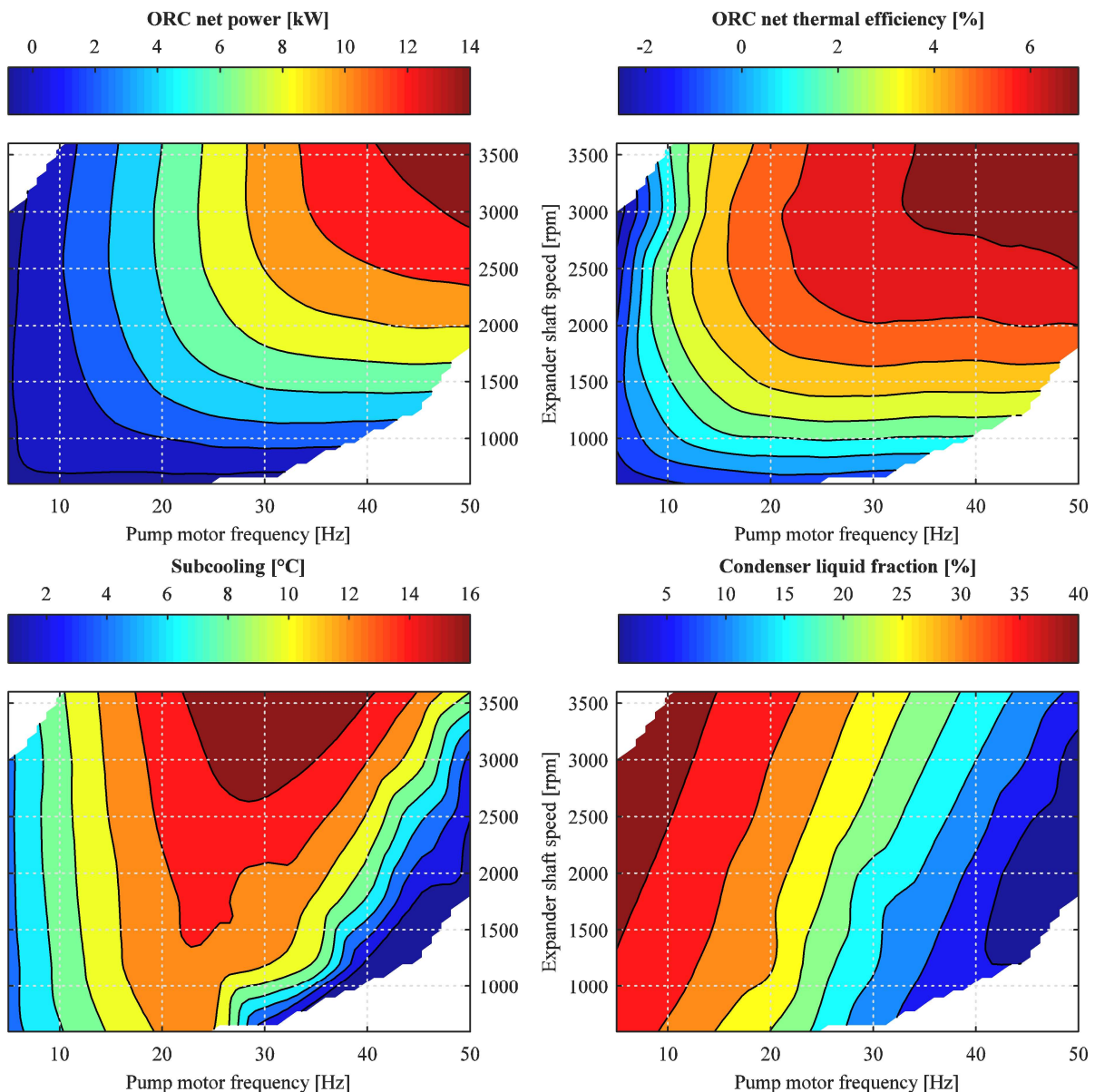


Figure VI-8: Pump and expander speed optimization for a 15 kg charge

As expected from previous observations, ORC power and efficiency keeps increasing with expander and pump speed, without reaching an optimum point. However, the ORC power is found to increase constantly, while the ORC efficiency quickly increases for low pump or expander speed and then increase more slightly above half the machineries nominal speed.

The subcooling, however, seems to have an optimum pump speed to be maximized. This optimum speed varies with the expander shaft speed. Indeed, for pump motor frequency below 20 Hz, the subcooling is quite independent from the expander speed and the condenser is largely flooded with a liquid fraction above 25 % of the condenser volume. This is the configuration depicted in Figure VI-6c, for the 20 kg charge case. The condenser is flooded, with a pinch point located at the sink inlet and close to zero. Expander speed variation does not change the subcooling since the charge variation in the HP zone due to pressure variation is not significant compared to the total fluid overcharge in the condenser. In contrast, subcooling is found to decrease as pump speed further decrease. This is mainly due to low pressure reduction since fluid outlet temperature is already about the sink inlet temperature. At low pump speed, fluid flow rate is reduced so does the heat load at the condenser, therefore fluid is cooled down faster and the average enthalpy is reduced, decreasing the low pressure in the meantime to maintain a constant average density in the condenser.

On the other side, after the subcooling maximum is reached, the subcooling quickly decreases as the pump shaft speed increases. In this case, the liquid fraction in the condenser is much smaller, below 10 %. This is the configuration depicted in Figure VI-6a, for the 12 kg charge case. The pinch point is shifted to the fluid saturated vapor point and the cooling power is not sufficient to subcool the working fluid. Pump speed increase or expander speed reduction increases the high pressure and so the charge in the HP zone, reducing by the same way the charge in the LP zone deteriorating further the subcooling. Additionally, pump speed increase raises the heat load at the condenser, which further reduces the condenser length for fluid subcooling.

Note, the optimum operating point is found to be at the maximum pump and expander speed. At this running point, both output power and ORC efficiency are maximized while the subcooling can be maintained about 10 °C and the liquid fraction in the condenser is minimized.

Figure VI-9 shows similar maps for total fluid charge of 18 kg. The ORC output power map is quite similar, the maximum power reached is located at the same expander and pump speed as for the 15 kg case but is slightly lower, mainly due to the subcooling increase (from about 10 °C to 25 °C). ORC net efficiency is also slightly lower, but is relatively constant for a larger range of expander and pump speed.

The subcooling is substantially increased by 15 to 20 °C, as well as the condenser liquid fraction, homogeneously increased by 25 %. The subcooling map is significantly modified between the 15 kg and the 18 kg fluid charge case. Condenser is in the flooded configuration starting from pump motor frequency about 35 to 40 Hz and does not switch to the empty configuration even at the maximum pump speed. However, subcooling is found to be more sensitive to the expander speed than for the 15 kg charge case. This is mainly due its influence over the low pressure.

Even if the subcooling is substantially increased, running points at high pump speed and low expander speed could not be simulated. Indeed, the model is limited to subcritical cycle, due to thermo-physical library limitations nears the critical zone, which explains the missing data in this zone even if the subcooling is sufficient thanks to the fluid charge increase.

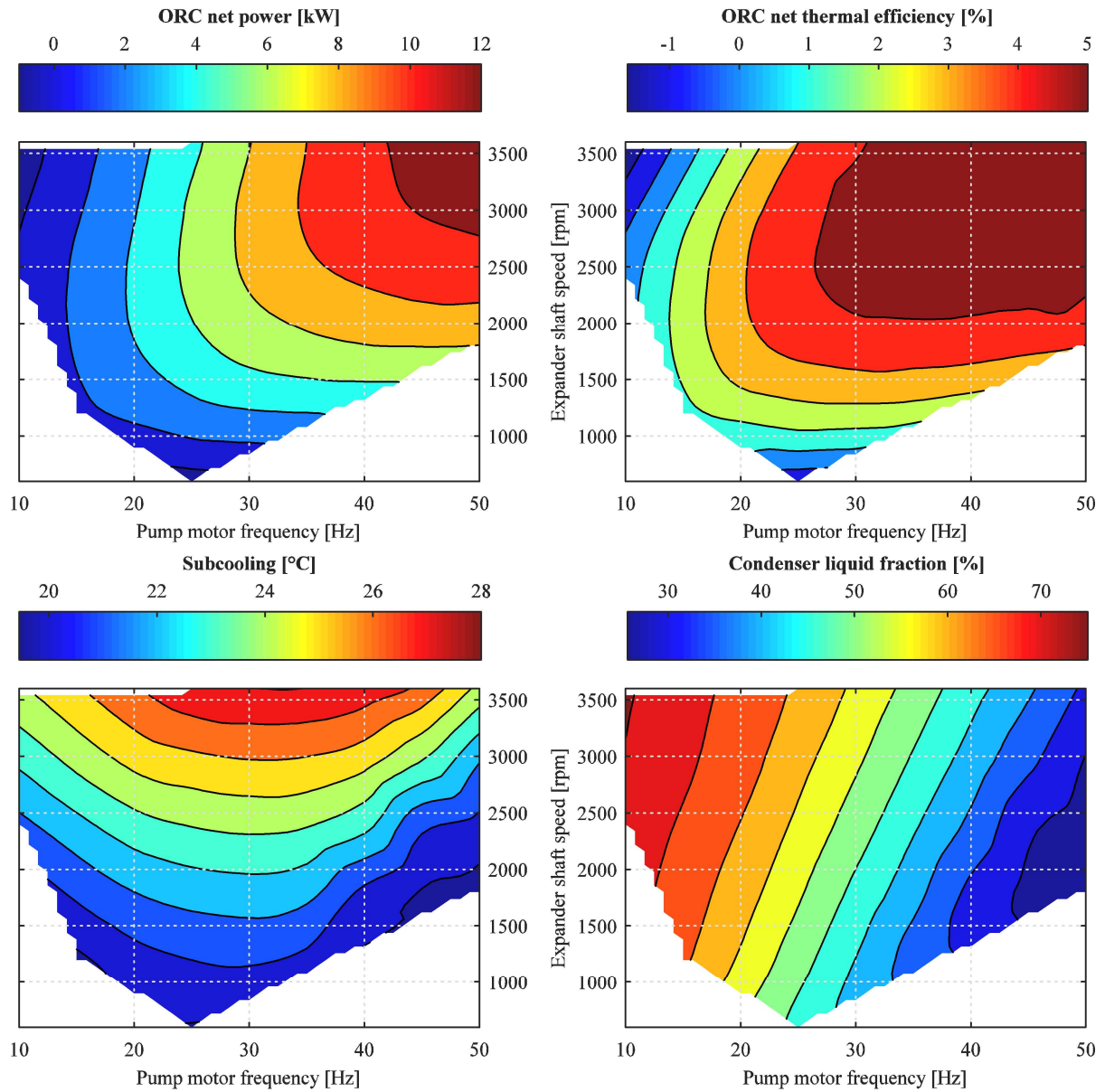


Figure VI-9: Pump and expander speed optimization for a 18 kg charge

2 Circulating fluid charge optimization

2.1 Optimum charge under variable operating conditions

As previously detailed, the working fluid charge is found to have a major impact on the condensing pressure and the subcooling, resulting in an influence over the ORC output power and efficiency. Therefore, the fluid charge circulating in the ORC might be useful parameter for subcooling and so cycle power and efficiency optimization.

In this section the subcooling is fixed at a constant 10 °C value. Simulation provides the necessary circulating fluid charge to achieve such subcooling. Starting from the previous reference case conditions, the different parameters are varied independently to evaluate their respective impacts over the optimal fluid charge. When not varied, other parameters are set to the reference case values.

Table VI-3: Parameters values for the reference case and range for the optimum fluid charge investigation.

Parameter	Reference case	Investigation range
Heat source flow rate	2 kg/s	0.25 to 4 kg/s
Heat source temperature	110 °C	80 to 150 °C
Heat sink flow rate	2 kg/s	0.5 to 4 kg/s
Heat sink temperature	20 °C	10 to 30 °C
Expander shaft speed	3000 rpm	300 to 3600 rpm
Pump motor frequency	25 Hz	7.5 to 50 Hz

Figure VI-10 shows the influence of the heat source parameters (inlet temperature and flow rate) over the optimum fluid charge. As the heat source temperature increases, the optimum fluid charge decreases. Indeed, a higher heat source temperature leads to a better heat transfer at the evaporator, thus, a higher mean enthalpy and a lower mean density at the evaporator. The impact of the heat source temperature on the low pressure part of the ORC is minimal and optimum charge variation is mainly due to evaporator charge variation.

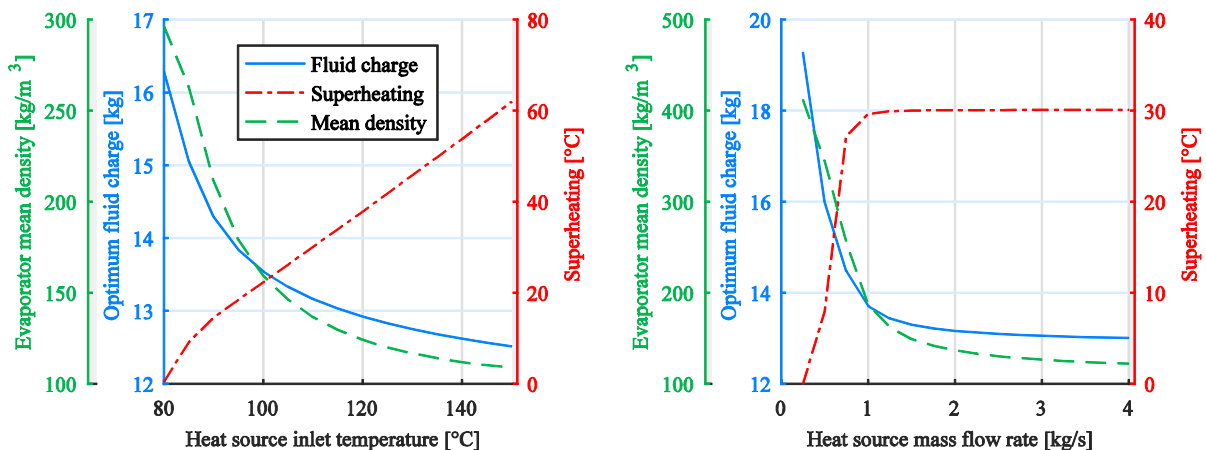


Figure VI-10: Heat source parameters influence over the optimum fluid charge

Similarly, as the heat source flow rate increases, the optimum fluids charge decreases, mainly in relation with the evaporator charge variations. Above 1 kg/s, the heat transfer is already optimized with a pinch point close to zero and a constant superheating. A higher heat source flow rate only slightly improves the heat transfer rate, and thus the mean enthalpy which decreases the mean density at the evaporator. However, below 0.5 kg/s, the evaporator heat transfer surface is not sufficient to ensure full fluid evaporation. The superheating is quickly decreasing and the pinch point location switches from the evaporator outlet to the fluid saturated liquid point. Fluid at the evaporator outlet is eventually found to be below the saturated vapor point for a heat source flow rate of 0.25 kg/s. As the heat transfer is quickly deteriorated for low heat source flow rate, the fluid mean enthalpy decreases and the mean density increases, increasing the evaporator charge.

Figure VI-11 shows the heat sink parameters influence over the optimum fluid charge. As the sink temperature increases, both the working fluid condenser outlet temperature and the fluid mean enthalpy at the condenser increases. The enthalpy increase leads to a mean density decrease. Reversely, the fluid outlet temperature increase leads to a low pressure increase since the subcooling is set to a fix value, which eventually increases the mean density at the condenser. Both effects counteract and, as a result, the optimum fluid charge marginally increases with the sink temperature, by 0.03 % per °C.

On the opposite, the heat sink flow rate increase leads both to a fluid condenser outlet temperature and mean enthalpy decrease thanks to better heat transfer. This eventually leads to a density, condenser charge as well as total charge increase with the sink flow rate.

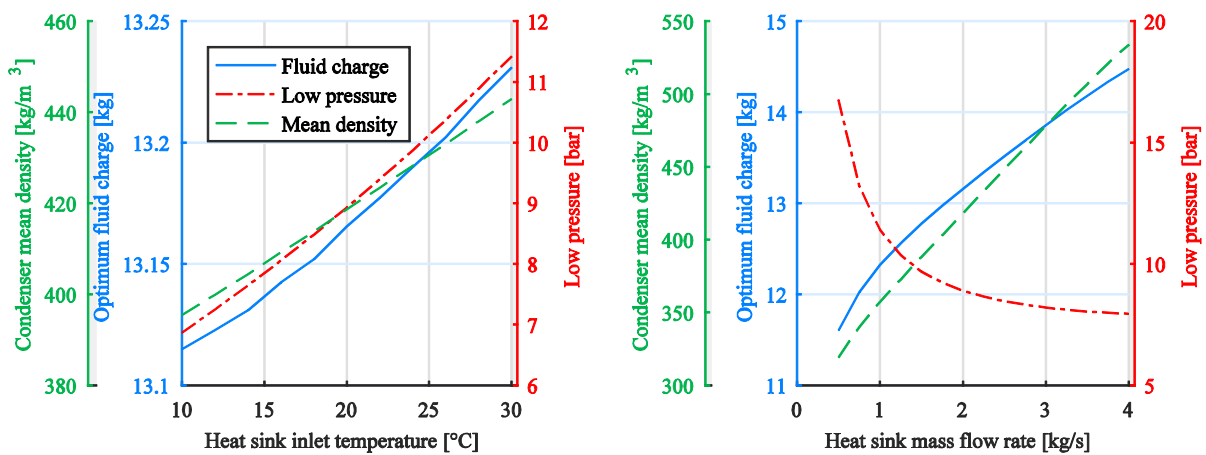


Figure VI-11: Heat sink parameters influence over the optimum fluid charge

Figure VI-12 shows the influence of the expander shaft speed over the optimum fluid charge. Expander speed mainly influences the evaporator charge through its regulation of the high pressure. As the expander speed increases, the high pressure decreases which leads to a decrease of the evaporator liquid fraction and an increase of the vapor fraction. The evaporator average density decreases and so its fluid charge.

Figure VI-13 shows the influence of the pump speed over the optimum fluid charge. Influence of the pump speed and so the working fluid mass flow rate is more complex, as many components are affected and many effects overlaps. The mass flow rate increase raises the heat load both at evaporator and the condenser, and increases the high pressure

for constant expander shaft speed which increases the mean density and charge at the evaporator.

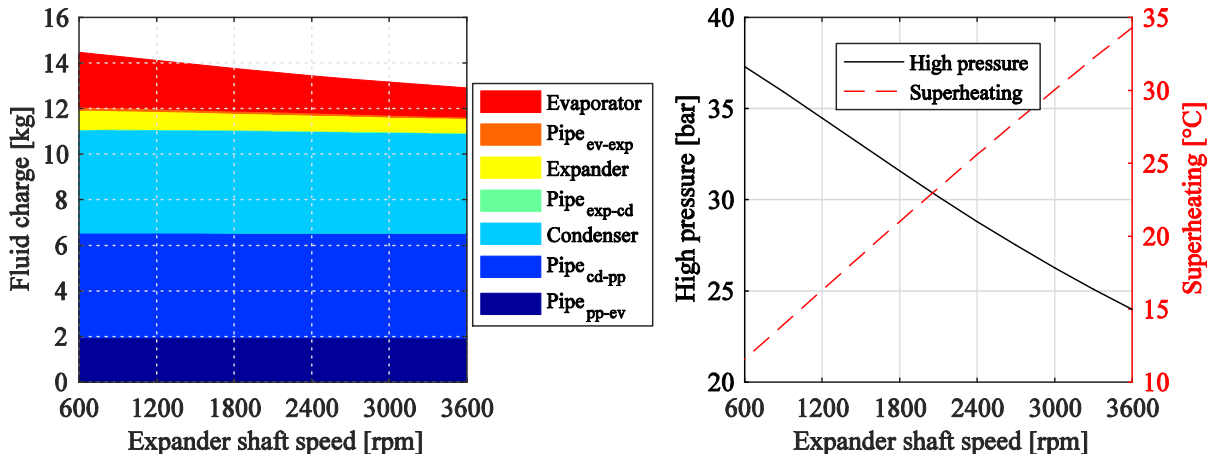


Figure VI-12: Expander speed influence over the optimum fluid charge

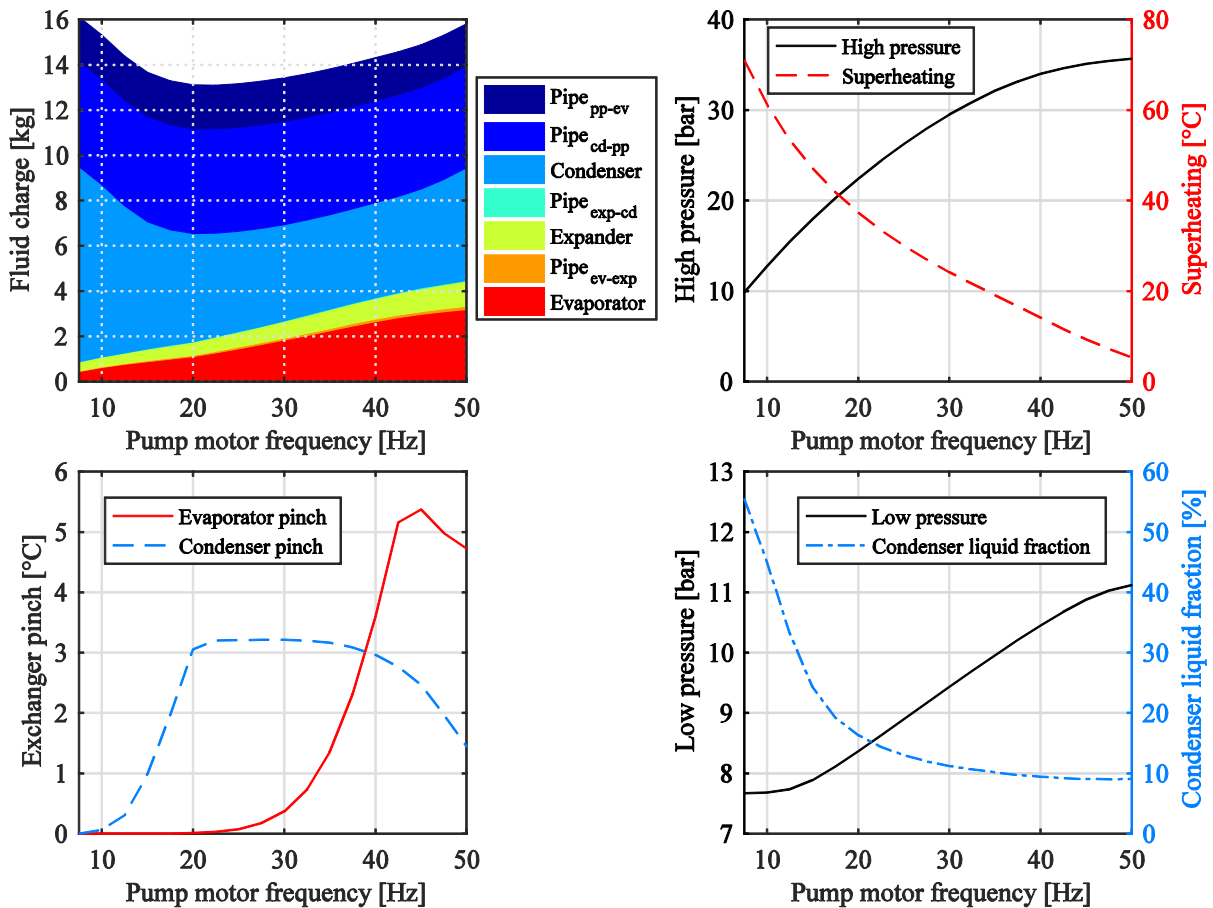


Figure VI-13: Pump speed influence over the optimum fluid charge

In addition, for pump motor frequency below 20 Hz, the condenser is found to be in the flooded configuration. Its liquid fraction and fluid charge are large, respectively above 20 % and 8 kg. The high pressure is low so the high pressure side vapor has a low density (see Figure VI-14 a: 10 Hz). As the pump motor frequency increases from the minimum to 20 Hz, the condenser is de-flooded, the condenser pinch point increases. Above 20 Hz, the

condenser pinch position starts to switch from the sink inlet to the fluid saturated vapor point. The condenser is less efficient, fluid outlet temperature slightly raises and the low pressure is increased to maintain the constant subcooling (see Figure VI-14 b-20 Hz & c-35 Hz). The condenser fluid charge is slightly decreasing.

In the meantime, the superheating is quickly decreasing both due to the high pressure increase and due to the evaporator increasing heat load which increase the evaporator pinch, but also the evaporator mean density and fluid charge. Around the pump motor frequency of 40 Hz, the evaporator pinch reaches a maximum value and the pinch location switch from the heat source inlet to the fluid saturated liquid point (see Figure VI-14 c-35 Hz & d-50 Hz). Above 45 Hz, the evaporator is overloaded and the superheating is close to zero. Since the R134a fluid is a wet fluid, its expansion through the expander reduces even more is superheating and eventually, the working fluid is found to be at saturation at the higher pump speeds (see Figure VI-14 d-50 Hz). Such saturated fluid at the condenser entry decreases its mean enthalpy and increases its mean density and fluid charge.

Finally, the minimum requested fluid charge is found to be for pump motor frequency around 20 Hz, at the point of optimized heat transfer and heat load at the condenser.

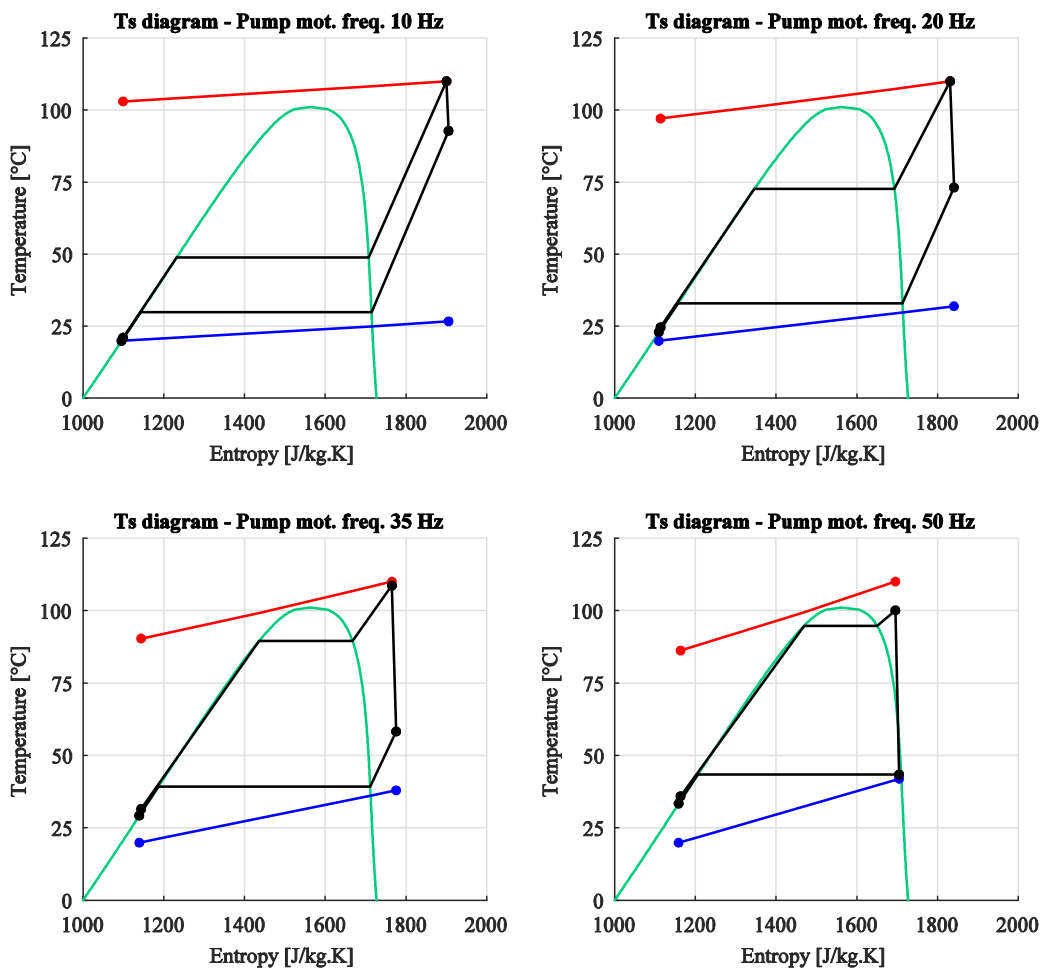


Figure VI-14: Ts diagrams for different pump speeds at the optimum fluid charge

Figure VI-15 summarizes the effects of the different parameters: heat source and sink, expander and pump shaft speeds; over the optimum fluid charge, drawn with the same scale. In addition, impacts over the ORC net power and net thermal efficiency is depicted.

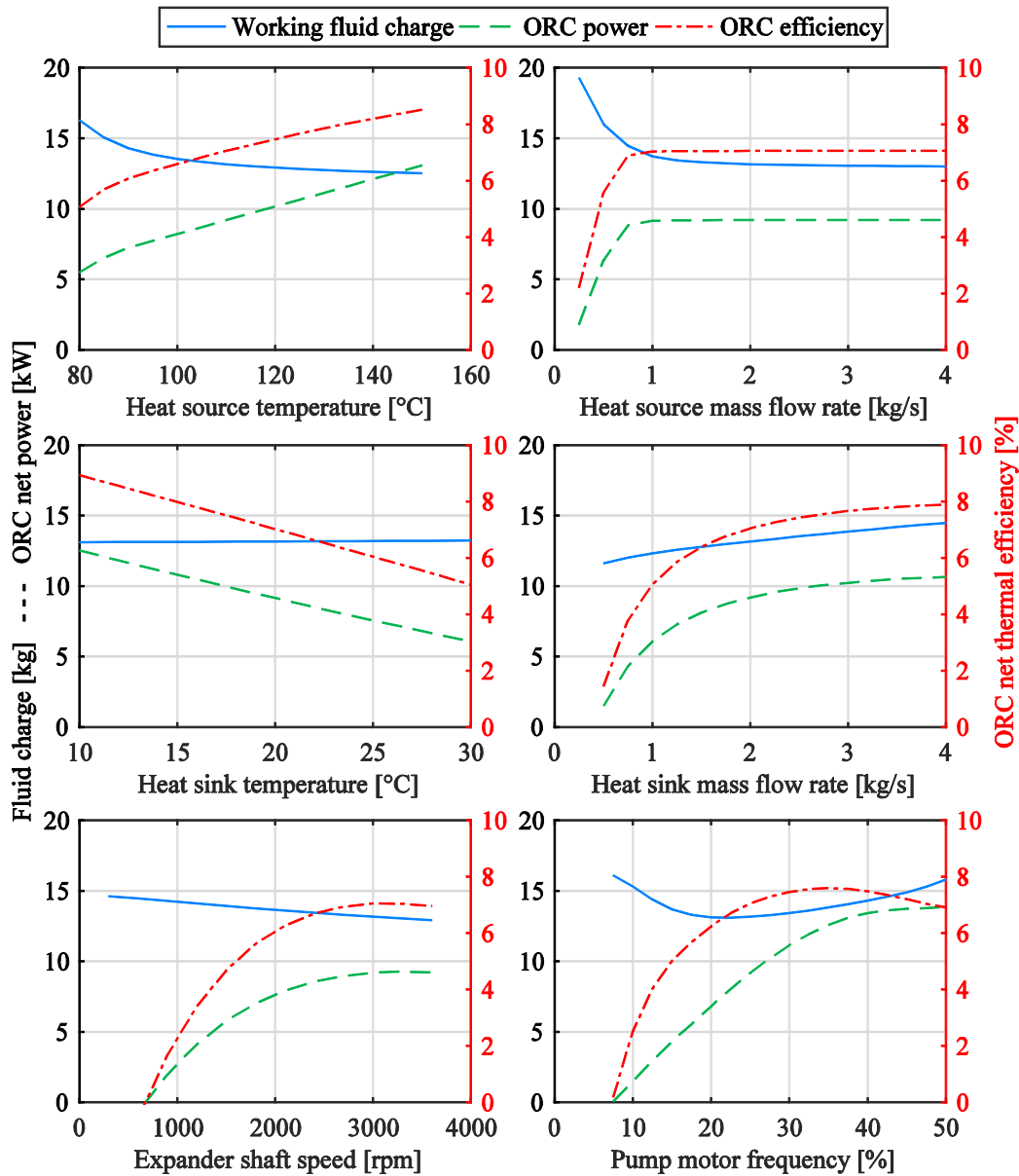


Figure VI-15: Overview of the different parameters influence on the optimum fluid charge and resulting ORC performances

Heat source temperature and flow rate is found to have a large impact over the optimum fluid charge. However, this impact is quickly reduced and even turn to be marginal at high flow rate. ORC power and efficiency constantly increase with the heat source temperature, as expected, and they reach a plateau for heat source flow rates above 0.75 kg/s.

Heat sink temperature has almost no impact over the optimum fluid charge but has a large impact over the net power and efficiency which decreases by almost 50 % for sink temperature of 10 to 30 °C. In contrast, the sink flow rate has a constant and medium impact over the optimal charge, increasing by 0.7 kg or 6 % per kg/s of sink flow rate. Sink flow

rate effect over the ORC power and efficiency can be quite large but is attenuated at large flow rates, as for the heat source flow rate but for higher flow rates.

Expander speed has a quite constant effect over the optimal charge: 0.48 kg per 100 rpm and a very large influence over the ORC power and efficiency. Very low expander speeds can even lead to negative net power and efficiency. It seems that an optimum expander speed can be found to maximize the ORC net power and efficiency, and this optimal value seems to be similar.

Pump speed is found to have a major impact over the optimal charge with many coupled or opposed effects. The optimal charge ranges from 13.1 kg to 16.1 kg and optimum pump speed can be found to minimize the charge. Pump speed also affects the ORC power and efficiency. An optimal pump speed can be found to maximize the output power and the efficiency. However, those objectives are in conflict, and are also in conflict with the charge minimization.

Table VI-4 summarizes the effect of the different variables over the fluid charge optimum and the resulting ORC net power.

Table VI-4: Summary of main variables effect over the optimal fluid charge and ORC net power

ORC parameter	Optimal fluid charge	ORC net power
Heat source flow rate	---	+ / =
Heat source temperature	--	+
Heat sink flow rate	+	+ / =
Heat sink temperature	=	-
Expander speed	-	+ + / =
Pump speed	-- / ++	+ + + / =

From this analysis of the working fluid charge optimum under various conditions, it is clear that the expander speed, the pump speed and the fluid charge should be controlled and optimized to maximize the ORC performances. Additionally, it should be noted that the present analysis strongly depends on the cycle design and the reference conditions.

2.2 ORC design and charge regulation

As previously mentioned, the heat pumps industry is trying both to minimize the total fluid charge due to economic and environmental constraints, and to optimize the fluid charge for engine performances maximization. Many criteria impact the total fluid charge and the range of optimum charge: the system architecture, the working fluid, diameter and lengths of pipes, receiver sizing and components technologies (Poggi et al. 2008).

Working fluid with low liquid density, high vaporization heat, low gas specific volume and low liquid phase specific heat would minimize the total charge. However, it should be noted that different fluids have different prices and environmental impacts, and therefore fluid resulting in the minimum charge might not be the optimal techno-economical choice.

Due to their volumes, heat exchangers receive a large fraction of the total charge and they are responsible for most of the optimum charge variation due to drastic fluid density variations during phase change. As an example, micro-channel or plate heat exchangers

have much smaller fluid volume for the same heat load than shell-and-tubes heat exchangers.

Pipes sizing and routing is also a key parameter for charge reduction. As previously shown in the simulations of the simplified CORSERE test bench (Figure VI-3), the liquid pipes (condenser to pump and pump to evaporator) could represent half the fluid charge. It should be noted, however, that CORSERE bench is a prototypes with non-optimized pipe routing and sizing.

Overall, liquid pipes volume should be minimized since the fluid density is the highest. Components exhaust and intake must be close to minimize pipe length. Pipes diameters should be properly sized according to the pressure drop allowed at the extreme operating conditions.

On the opposite of heat pumps, fluid charge located in vapor pipes should not be neglected in ORC. ORC usually runs at high pressure much closer to the critical point than heat pumps, or even above the critical point. Supercritical fluids have a relatively high density. For R134a density at the critical point is 545 kg/m^3 , almost half the $20 \text{ }^\circ\text{C}$ saturated liquid density (1226 kg/m^3). Therefore, high pressure vapor pipes could also handle a large portion of the fluid charge, especially as vapor pipes are larger to limit pressure drops for low pressure and low density vapor.

In addition, while fluid liquid density does not fluctuate between the extreme operating conditions, vapor density can largely fluctuate between different operating conditions due to the higher sensibility of the vapor to the pressure and the large temperature variations. Therefore, vapor pipes volume minimization would reduce the range of optimal charge variation between extreme operating conditions.

In the CORSERE test bench and in the simulation, a choice was made to not include a liquid receiver at the condenser outlet to absorb charge variations. The liquid receiver is a passive system which mitigates the working fluid charge fluctuations without controlling it. As previously conclude, the circulating charge control might be a lever for performances optimization through subcooling control. In particular, for compact or on-board application, the space is not sufficient to use a saturated receiver and the hydrostatic pressure from the pump inlet line to ensure sufficient subcooling at the pump inlet.

Indeed, some industries and research centers focusing on on-board internal combustion engine waste heat recovery with ORC already filed patents for charge and subcooling regulation mechanism.

For example, the US-8800285 patent (Ernst and Nelson 2012) used an isolated receiver to store or inject fluid charge in the ORC circuit. Fluid is extracted thanks to the ORC main pump and injected in the condenser thanks to an ejector or thanks to gravity or pressure difference (Figure VI-16). Similar, simpler system was already patented by (Duparchy 2011) under the patent number EP-2365192. In this patent, the receiver is isolated and connected to the ORC feed pump outlet for circulating fluid extraction into the receiver, and connected to the ORC feed pump inlet for fluid injection into the ORC circuit.

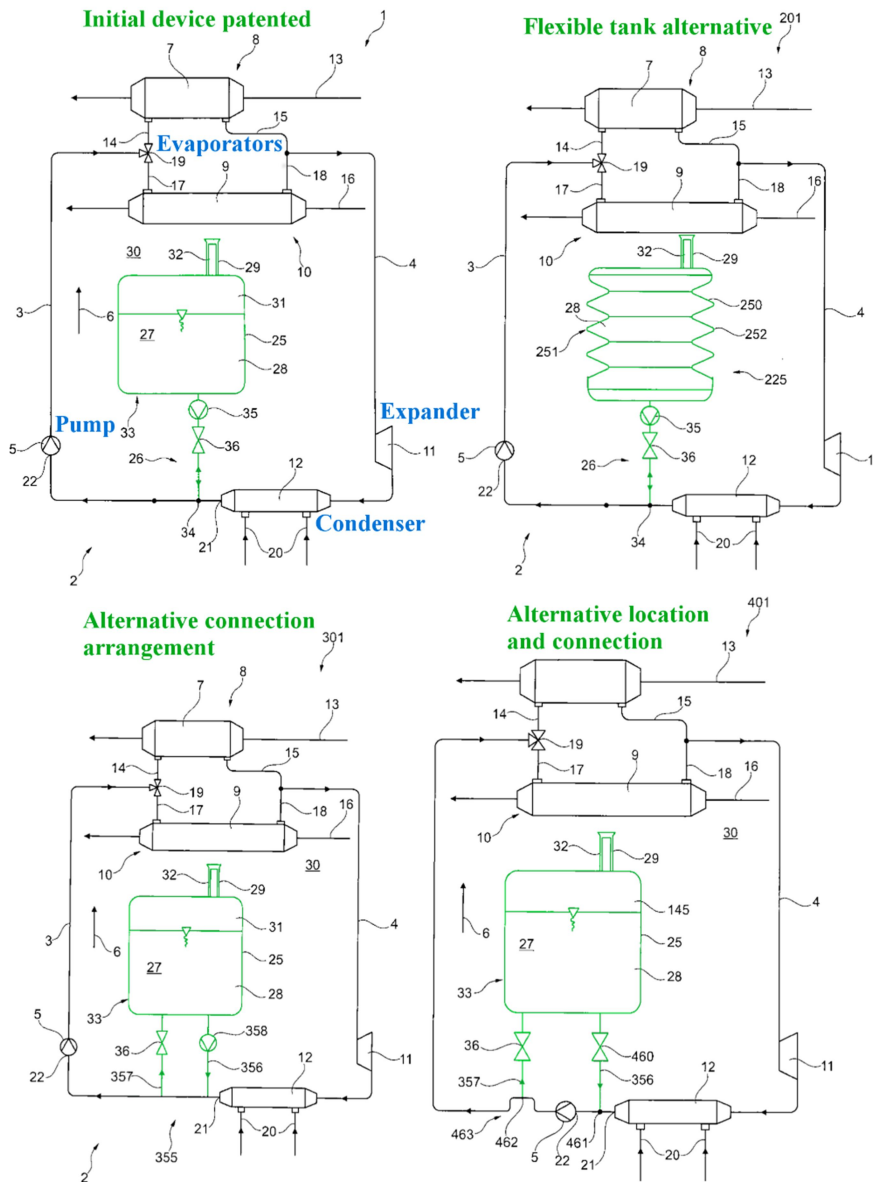


Figure VI-17: DE-102009050068 patent solutions proposed – **modified from** (Lutz, Motisi, and Bruemmer 2015)

The systems proposed usually request additional pumps and a combination of controlled valves, as well as some instrumentation and a controller to regulate the working fluid charge circulation in the ORC circuit. A new method and mechanism for circulating fluid charge regulation, was theoretically investigated and designed.

The proposed system uses only thermal energy and a set of two valves to control the ORC condensation pressure, subcooling and fluid charge in circulation in the ORC. Additionally, a mechanism was design to automatically hold the pump inlet pressure saturation margin – the NPSH – in a define range. This system prevents cavitation due to insufficient subcooling, and ORC performance deterioration due to excessive subcooling, without using instrumentation, controller or mechanical energy.

Chapter conclusion

In this chapter, the working fluid charge is investigated. The fluid charge minimization and optimization is a topic largely investigated for refrigeration and heat pumps but sparsely studied for organic Rankine cycles. Some authors experimentally pointed the influence of the fluid charge over the ORC performances.

Fluid charge is investigated through a simplified model of the CORSERE test bench, no receiver is implemented in order to maximize the fluid charge effects. At constant operating conditions, the fluid charge is found to have a large impact on the pump inlet subcooling but almost no impact on the high pressure side of the ORC. High charge leads to condenser flooding, low pressure and so subcooling increase. Low charge results in insufficient heat transfer area for proper fluid subcooling in the condenser, and therefore subcooling reduction. Excessive subcooling eventually leads to ORC performance drops, while insufficient subcooling leads to pump and flow rate decline (Chapter IV-2.2).

Then, combined effects of fluid charge, expander speed and pump speed are investigated. Expander speed increase slightly increases the low pressure and the subcooling, shifting the requested fluid charge to a lower quantity for similar subcooling. Pump speed, and so fluid flow rate increase, leads to a higher sensibility of the subcooling to the fluid charge but a lower sensibility of the low pressure. Finally, pump-expander speed performance maps are drawn for fixed fluid charge. ORC performances are maximized at maximum pump and expander speed. However, a proper fluid charge control might be necessary to ensure a sufficient and not excessive subcooling under different ORC operating conditions.

In a second step, the subcooling is fixed at 10 °C, an ideal value for proper pump operation without excessive ORC performances deterioration (Chapter IV-2.2). The resulting optimal fluid charge is computed and evaluated for a large range of heat source and heat sink conditions, as well as different pump and expander speeds.

Heat source temperature and flow rate increase tends to reduce the optimal fluid charge. On the opposite, heat sink flow rate increase leads to an optimal charge increase. However, the heat sink temperature sparsely influences the optimal charge. Expander speed reduction leads to higher pressure and higher evaporator mean density, which eventually leads to an optimal charge rise.

Influence of the pump speed and fluid mass flow rate is complex as it impacts both heat transfer efficiency at the evaporator and the condenser. It passes from a flooded condenser and excessive superheating configuration at low pump speed to an insufficient superheating with two-phase expansion configuration at the maximum pump speed.

Finally, a discussion on ORC design for total fluid charge reduction is proposed. As for heat pumps, liquid pipes volume should be reduced to a minimum. Heat exchangers technology and working fluid should be carefully selected as well. Some mechanisms and technologies for fluid charge and subcooling active regulation are presented.

Chapter VII

ORC operation

1 Machineries

1.1 Expander operation

The scroll technology has been widely investigated for expansion in small-scale ORC. First use of scroll technology as ORC expander is reported in 1994 by (Zanelli and Favrat 1994), the scroll expander was initially a standard hermetic compressor modified to run as an expander. Use of modified scroll compressor became very popular (Kane et al. 2003; Saitoh, Yamada, and Wakashima 2005; Manolakos et al. 2007; Sylvain Quoilin, Orosz, and Lemort 2008), and more than half of ORC prototypes used the scroll expander technology in the last decade (Chapter II-2). In the meantime, many models of scroll expander have been developed (Song et al. 2015): deterministic models, semi-empirical models (Lemort et al. 2009) and fully-empirical correlations (Declaye et al. 2013). Figure VII-1 shows the scroll mechanism and an exploded view of the different parts.

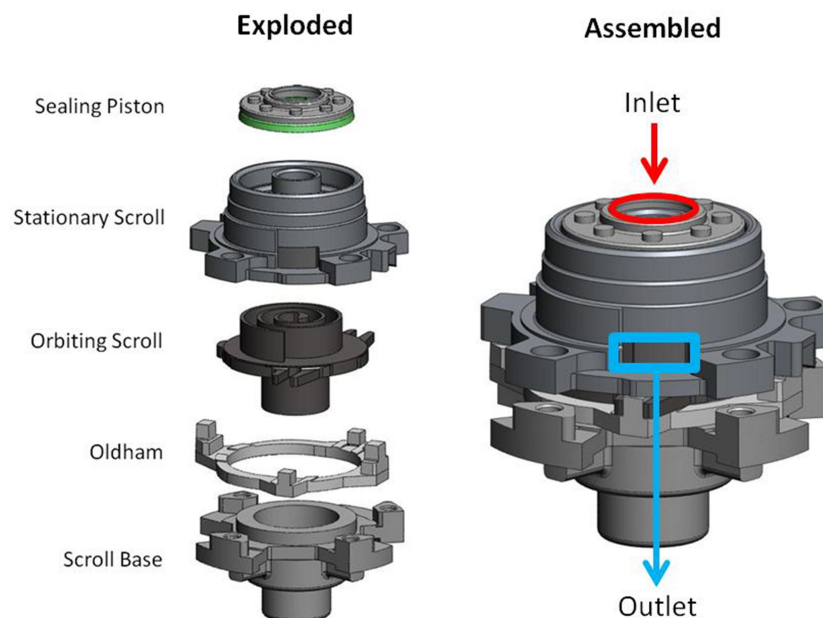


Figure VII-1: Scroll mechanism and parts – *from* (Harada 2010)

Scroll expander performances are found to be sensitive to its boundary pressure ratio. The pressure ratio should match the scroll Built-in Volume Ratio (BVR) to achieve optimal performance (Lemort et al. 2009). The BVR is the geometrical volume ratio between the suction and the exhaust of the scroll mechanism. If the pressure ratio imposed by the BVR is lower than the system pressure ratio, the pressure in the expansion chamber at the end of the expansion process (P_{ad}) is higher than the expander exhaust pressure (P_{ex}). The expander is in under-expansion, and the potential work is not fully exploited (Figure VII-2). Reversely, if the pressure ratio imposed by the scroll BVR is higher than the system pressure ratio, the pressure in the expansion chamber at the end of the expansion process is lower than the expander exhaust pressure and some work is consumed for fluid recompression.

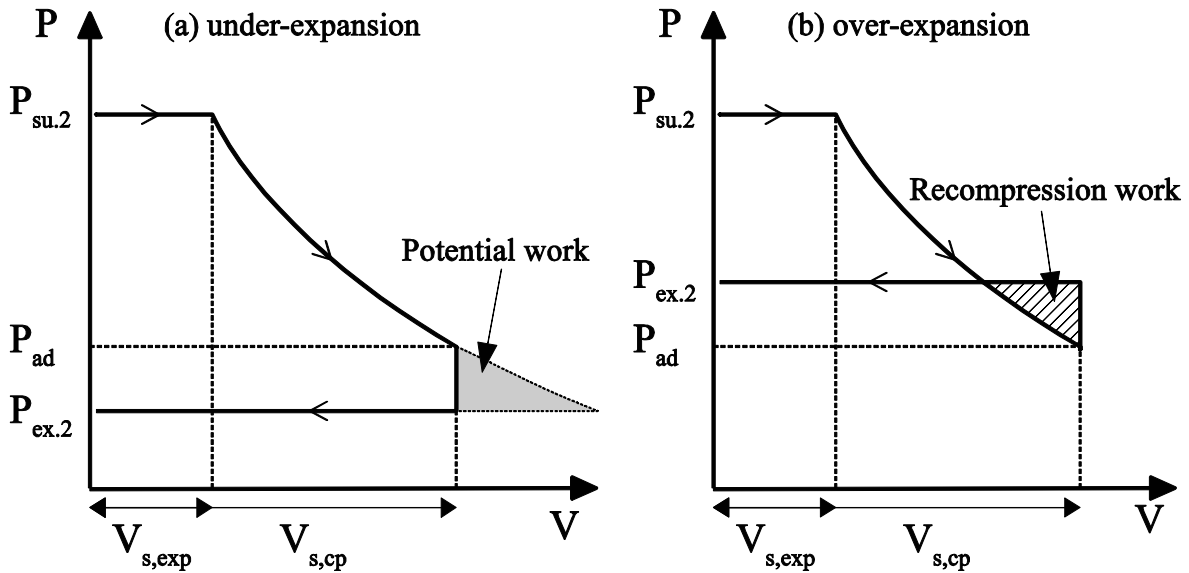


Figure VII-2: Under and over expansion process in scroll expanders from (Lemort et al. 2009)

In the present work, two similar scroll expanders are investigated. Both are Copeland © hermetic compressors modified to run as expanders in transcritical conditions. The scroll from the CPV-Rankine ORC was removed from the original casing and placed in a new casing to handle supercritical pressure. The CORSERE's scroll was kept in its original casing. However, new sealed feed-through electrical connectors were installed to handle the high pressure.

Among the modifications to convert compressors in expanders, the non-return and check valves are removed to allow reverse flow. The sealing piston is screwed to the top flange to force the fluid flow to enter in the scroll mechanism during expander start-up. Indeed, in compressor mode, the scroll first pressurizes the sealing piston chamber which lifts up the sealing piston and creates the sealing between the scroll mechanism and to top flange where the compressor exhaust is connected (Figure VII-3 a&b). In expander mode, if the sealing piston is not initially tight to the top flange, the fluid flows directly to the expander exhaust without entering and acting the scroll mechanism (Figure VII-3c).

For the CORSERE's expander, the sealing piston was not initially screwed to the top cover. Instead, a spring was placed in the piston chamber to tight the sealing piston during the start-up, as proposed by (Sylvain Quoilin, Lemort, and Lebrun 2010) and shown in Figure VII-3d. Later, the sealing piston was screwed to the top flange, where a threaded rod was added (Figure VII-3e). A specific threaded retention piece was designed to tight the sealing piston (Appendix B). Finally, the sealing piston was replaced by a home-made sealing piston after seals got damaged (Figure VII-4 & Appendix C)

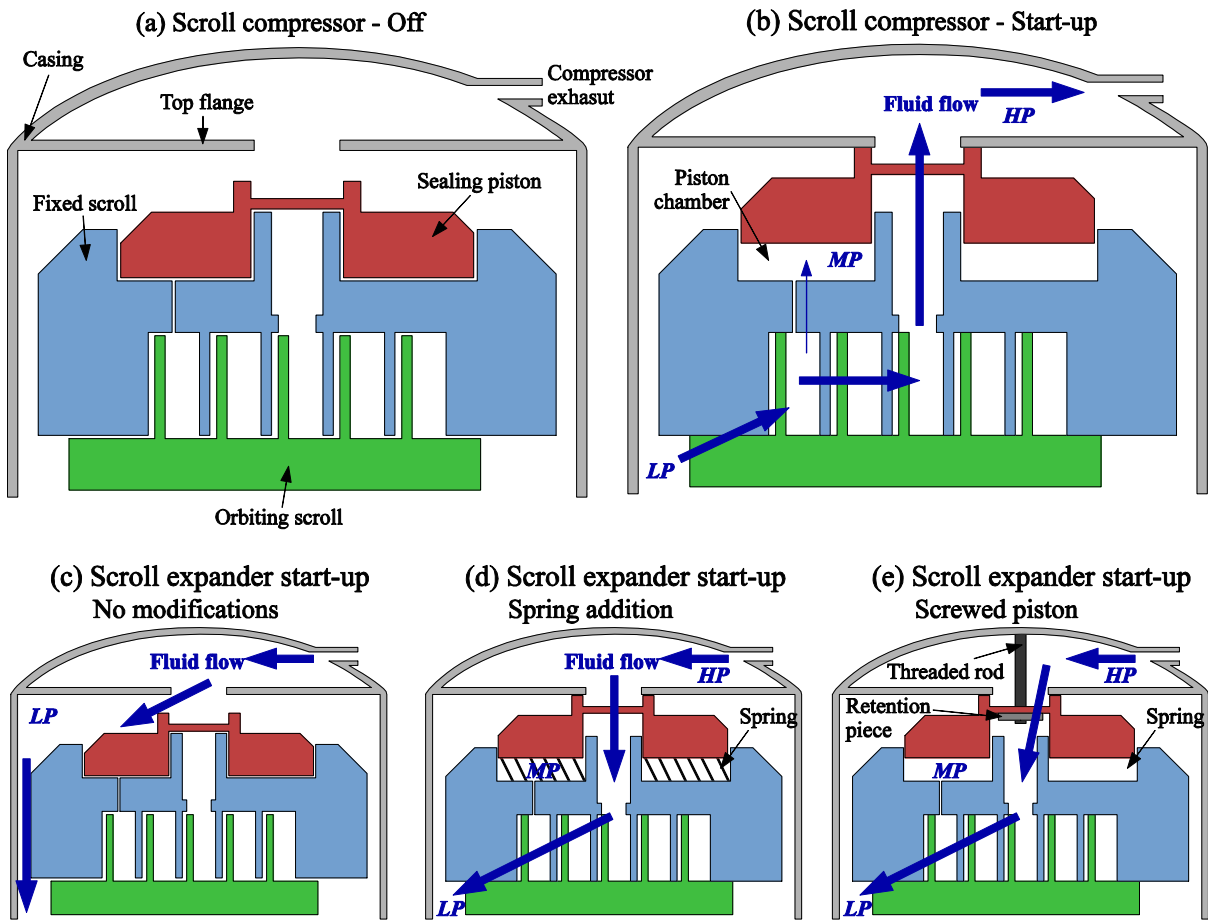


Figure VII-3: Scroll compressor and expander: parts, mechanisms and modifications

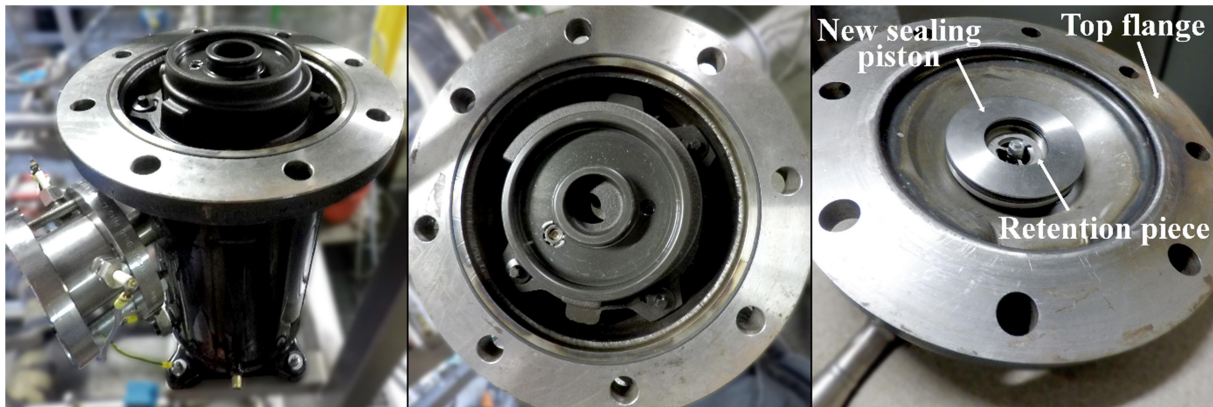


Figure VII-4: CORSERE expander pictures: a) scroll body – b) body top view – c) top flange

Both expanders were successfully tested in supercritical conditions at the expander inlet. The CORSERE expander reached a maximum of 6 kWe at the maximum flow rate of 0.76 kg/s and at supercritical entry conditions. The CPV-Rankine expander reached a maximum of 3.2 kWe for a flow rate of 0.22 kg/s. With supercritical entry conditions, the CPV-Rankine reached a gross power of 2.1 kWe, as shown in Figure VII-5. The CPV-Rankine expander operation is more widely investigated, with 87 steady-points recorded, versus 22 steady-points for CORSERE expander operation.

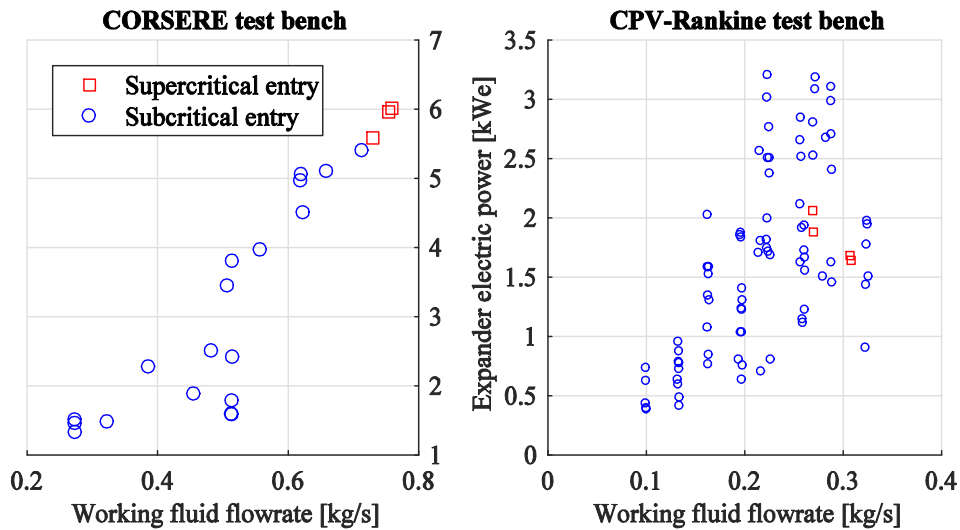


Figure VII-5: Gross electrical production of the CORSERE and CPV-Rankine scroll expanders

As expected, an optimal pressure can be found to maximize the scroll expander electrical efficiency (Figure VII-6). However, the optimum is found to be at pressure ratio around 2, while the BVR is estimated to be around 2.6. Supercritical entry conditions do not seem to affect the expander electrical efficiency.

The CPV-Rankine expander reached a maximum electrical efficiency of about 85 % (see Eq. II-1), which is a very high value compared to same scale expanders (see Chapter II-2 and Figure II-13) but mainly operates in the 40 to 70 % efficiency range. Such good efficiency might be explained by the new casing with direct injection in the scroll mechanism, reducing suction pressure losses in the top flange of the original casing (Figure VII-7).

A relation between expander electrical efficiency and expander shaft speed also appears (Figure VII-6). However, the expander shaft speed and the expander pressure ratio are also strongly related. Highest pressure are reached for low expander frequency, while inlet pressure and pressure ratio is limited for high expander frequency, leading to lower efficiency.

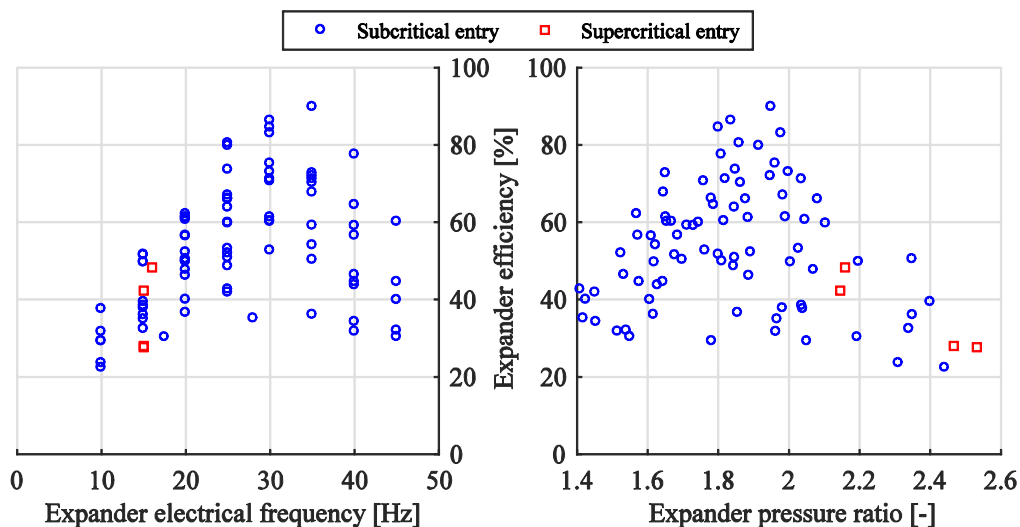


Figure VII-6: CPV-Rankine expander electrical efficiency



Figure VII-7: CPV-Rankine modified scroll expander

The mismatch between BVR and optimal pressure ratio, as well as the influence of the expander shaft speed on the expander electrical efficiency might result from the scroll expander leakages and volumetric efficiency.

Figure VII-8 shows the CPV-Rankine expander volumetric efficiency evolution with the expander frequency and boundaries pressure difference. The scroll expander volumetric efficiency is defined as:

$$\eta_{vol,exp} = \frac{\dot{\Omega}_{exp} \cdot V_{su,exp}}{\dot{m}_{exp} / \rho_{in,exp}} \quad \text{Eq. VII-1}$$

According to the semi-empirical scroll expander model from (Lemort et al. 2009), the internal leakage flow rate is directly related to the supply and exhaust pressure difference. Experimentally, the expander volumetric efficiency is actually decreasing with the pressure difference. However, the expander frequency is the main factor influencing the expander volumetric efficiency.

Indeed, if the leakage flow rate is considered proportional and only function of the pressure difference, the volumetric efficiency is actually increasing with the expander frequency as the flow rate going through the scroll mechanism is increasing for an unchanged leakage flow rate.

Comparing the volumetric and electrical efficiency of the expander, the relation between electrical efficiency and expander frequency for low frequency (10-30 Hz) seems mainly due to the volumetric efficiency and therefore internal leakages.

Furthermore, at higher expander frequency (30-50 Hz), the volumetric efficiency is still increasing and even reaches a maximum of about 95 %, but the electrical frequency decreases due to low pressure ratio.

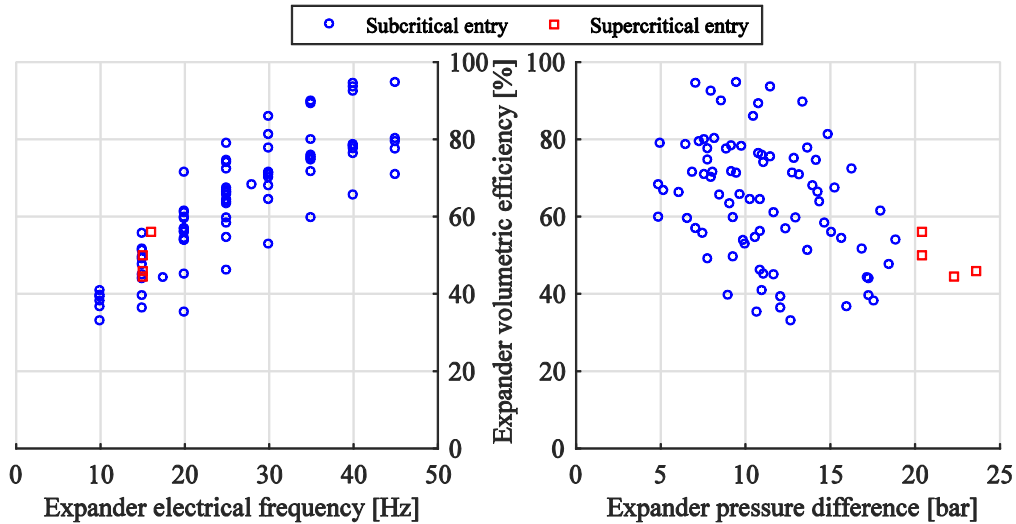


Figure VII-8: CPV-Rankine expander volumetric efficiency

Figure VII-9 shows CORSERE expander efficiency as a function of the expander electrical frequency and pressure ratio. The scroll expander efficiency also increases with its frequency. This is mainly due to internal scroll leakage reduction at higher rotating speed, as explained previously. The maximum expander efficiency is found to be 66.5 %. This good value ranks it on the top quartile of ORC expanders in the 1 to 10 kW scale, according to data from (Chapter II-2). The maximum expander efficiency corresponds to a pressure ratio of nearly 1.9, which is much lower than the estimated BVR – which is around 3 for this expander. Since the expander runs neither at the nominal frequency (50 Hz) nor at the theoretical optimum pressure ratio (3), higher efficiency could be potentially reached.

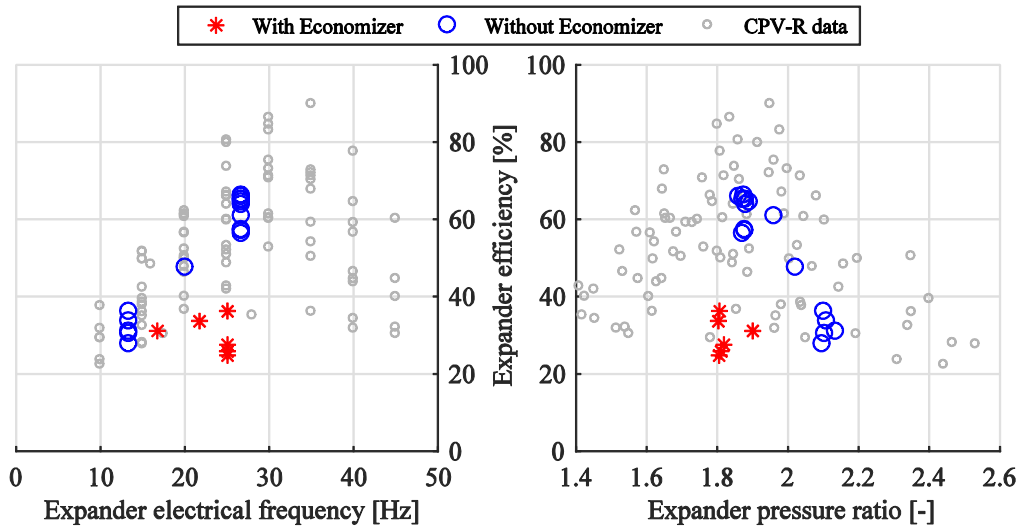


Figure VII-9: CORSERE expander electrical efficiency

In Figure VII-9, distinction is made between economizer and non-economizer configurations. The economizer configuration shows lower expander efficiency at similar expander frequency. Volumetric efficiency is similar in both configurations, so internal leakage may not be the issue. The economizer configuration results in a higher condensation pressure and therefore a lower expander pressure ratio that could explain the lower expander efficiency. Furthermore, the economizer configuration tests were performed just before an

unexpected expander failure. Therefore, scroll expander deterioration might explain the low expander efficiency in economizer configuration.

Generally speaking, both the CPV-Rankine and the CORSERE scroll expanders performed equally (see Figure VII-9). The lower maximum efficiency reached by the CORSERE expander results from the narrower range of shaft speed and pressure ratio tested. However, at similar shaft speed and pressure ratio, both expanders shown similar electrical efficiencies.

The CORSERE scroll is twice bigger than the CPV-Rankine scroll – 250 cm³ of suction volume versus 127 cm³, and the motor nominal power 50 % higher. Due to size effects, the CORSERE expander should perform slightly better than the CPV-Rankine expander. In contrast, the CPV-Rankine expander received a new casing, specifically designed for expansion operation, which results in lower pressure losses and higher efficiency.

1.2 Volumetric machineries – flow rate balance

The pump operation and performances of the ORC prototypes were already discussed in the dedicated chapter (Chapter IV). In the present section, a discussion is proposed on the flow rate equilibrium between two volumetric engines: the reciprocating pump and the scroll expander.

If fluid leakages in both machineries are neglected – in first order – each engine tends to impose its own flow rate to the system. One might wonder how the system reaches a stationary state. Both engines impose a volumetric flow rate, proportional to their shaft speed, while in steady state, the mass flow rates in both engines must be equal. Therefore:

$$\dot{m}_{exp} = \dot{m}_{pp} \Leftrightarrow \dot{V}_{in,exp} \cdot \rho(T; P)_{in,exp} = \dot{V}_{in,pp} \cdot \rho(T; P)_{in,pp} \quad \text{Eq. VII-2}$$

The fluid is assumed to be in liquid state at the pump inlet and vapor state at the expander inlet. In addition, we will consider perfect heat exchangers (evaporator and condenser) and therefore the pump and expander inlet temperatures are assumed unchanged whatever the fluid mass flow rate and pressure levels. In a first order, the liquid fluid can be considered as incompressible, therefore the pump inlet density is only function of the inlet temperature, so does the fluid mass flow rate.

Then, as the expander inlet temperature is imposed by the heat transfer in the evaporator, the expander inlet pressure is function of the expander inlet volumetric flow rate, itself function of the suction volume $V_{su,exp}$ of the expander and the expander shaft speed Ω_{exp} .

In the ideal case of working fluid associated to an ideal gas, at the expander inlet, the density can be expressed as a function of the temperature and pressure, with M_{wf} the working fluid molar mass and R the universal perfect gas constant:

$$\rho_{in,exp} = \frac{M_{wf}}{R} \cdot \frac{P_{in,exp}}{T_{in,exp}} \quad \text{Eq. VII-3}$$

For the liquid fluid, we will use the volumetric thermal expansion coefficient (α_V) of the saturated liquid at the reference temperature T_0 . For a temperature $T=T_0+\delta T$, the density ρ can be expressed using the saturated liquid density ρ_0 :

$$\rho_{in,pp} = \frac{\rho_0}{1+\alpha_V \cdot (T_{in,pp}-T_0)} \quad \text{Eq. VII-4}$$

From Eq. VII-2, we can relate the pump and expander inlet temperature and shaft speeds with the expander inlet pressure.

$$\dot{\Omega}_{exp} \cdot V_{su,exp} \cdot \frac{M_{wf}}{R} \cdot \frac{P_{in,exp}}{T_{in,exp}} = \dot{\Omega}_{pp} \cdot V_{stroke,pp} \cdot \frac{\rho_0}{1+\alpha_V \cdot (T_{in,pp}-T_0)} \quad \text{Eq. VII-5}$$

This volumetric flow rate balance is simulated for the CORSERE and the CPV-Rankine test benches. The equilibrium is simulated for three different pump shaft frequency: 10, 30 and 50 Hz and for different expander inlet temperature. The expander inlet pressure function of the expander shaft frequency is drawn.

For accuracy reasons and since the fluid at the expander inlet is near or in supercritical conditions, fluid thermo-physical properties are directly computed using *CoolProp* instead of the ideal gas law.

In this realistic simulation of the test benches operation, machineries leakages are taken into account. For the pump, the semi-empirical model previously presented is used to compute the volumetric efficiency. Note, subcooling is assumed to be large enough to neglect volumetric efficiency degradation due to cavitation.

Additionally, an empirical correlation is used for the expander volumetric efficiency. This efficiency is assumed to be only function of the expander shaft frequency f_{exp} and described by the following equation, with a the empirical coefficient estimated at 0.0437 s for the CORSERE bench and 0.0436 s for the CPV-Rankine bench. The correlation and the experimental data are plotted in Figure VII-10. Influence of the pressure ratio or pressure difference on the expander volumetric efficiency was not clear enough to adapt a correlation from them.

$$\eta_{vol,exp} = 1 - \exp(-a \cdot f_{exp}) \quad \text{Eq. VII-6}$$

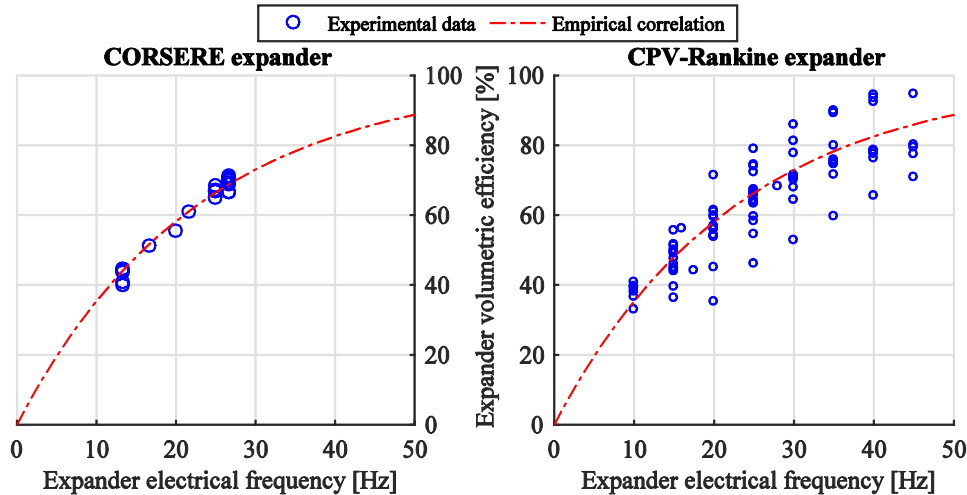


Figure VII-10: CORSERE & CPV-Rankine expanders volumetric efficiency and empirical correlation

The CORSERE simulation results for the different pump shaft speeds and expander inlet temperatures are shown in Figure VII-11. For temperatures below the critical temperature, pressure increase is limited to avoid two-phase fluid at the expander inlet, and so the expander frequency reduction is limited.

Sensibility of the high pressure to the temperature is found to be quasi-linear, as expected by the ideal gas theory. However, sensibility of the high pressure to the expander frequency increases as the temperature increases. In the same way, as pump shaft speed increases, the high pressure is more sensitive to an expander speed or inlet temperature change, which may result in control issues.

The CORSERE test bench has a maximum operating pressure of 50 bar and a critical pressure of 40.59 bar. To run in transcritical conditions, the range of temperature, pump and expander speed are limited. At 130 °C of expander inlet temperature and a pump motor frequency of 30 Hz, the expander frequency should range between 10 and 30 Hz; at 50 Hz pump motor frequency, it should range between 40 and 50 Hz.

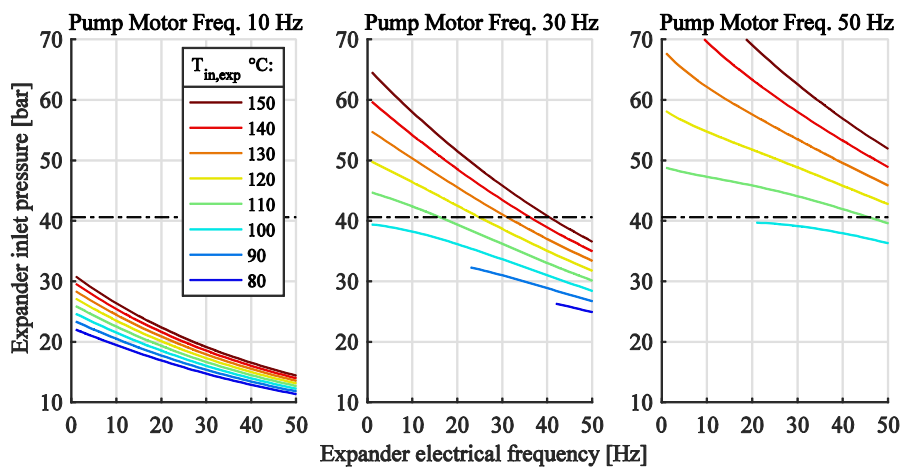


Figure VII-11: CORSERE expander and pump flow rate equilibrium

In the same way, the CPV-Rankine simulation results are shown in Figure VII-12. Same trends than the CORSERE test bench can be observed. However, in the CPV-Rankine bench, the hot source inlet temperature should be limited at 100 °C to prevent solar PV cells deterioration. Therefore, to run in transcritical conditions, the pump motor frequency should be kept at 50 Hz, and the expander frequency below 30 Hz.

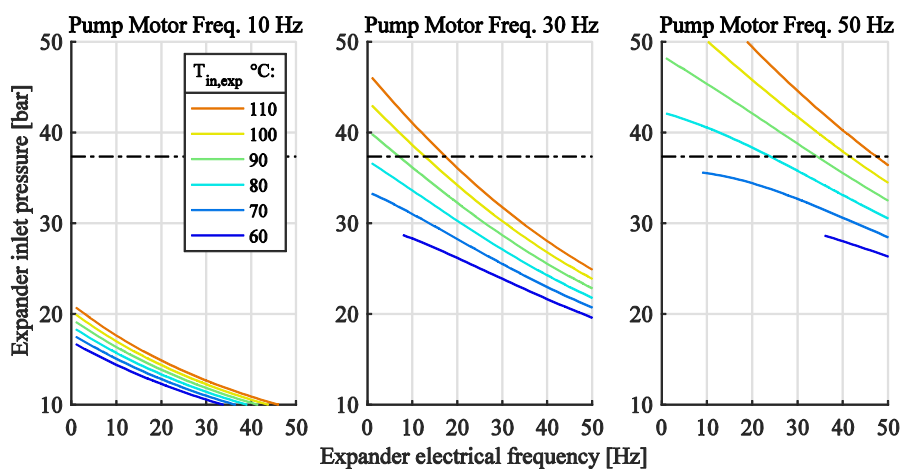


Figure VII-12: CPV-Rankine expander and pump flow rate equilibrium

2 Cycle performances analysis

2.1 ORC efficiency: analysis and comparison

In the previous sections, the main components of the ORC, i.e. the expander and evaporator, were investigated and their performances analyzed. In the present section, the cycle performances are analyzed from an energetic and exergetic standpoint.

Figure VII-13a shows the CORSERE ORC net efficiencies evolution with the relative pressure at the expander inlet. The net thermal efficiency reaches a maximum of only 1.0 %, corresponding to 4.24 % of the Carnot optimum efficiency. At low relative pressure and working fluid flow rates, the net production is even negative. For open source types, the net exergetic recovery efficiency reaches a maximum of 1.81 %. However, the hot water flow rate is high, with a small temperature drop of 20 K in average, which is more typical to closed source types.

The ORC performs better at 90 % of the critical pressure, however different ORC control parameters are simultaneously changed and therefore, relation between a single parameter and the ORC performances is arduous to distinguish. Nevertheless, Figure VII-13b shows a strong relation between expander efficiency and ORC performances. Similar correlation between expander and ORC efficiency was already stated through ORC statistical analysis (Chapter II-2.3).

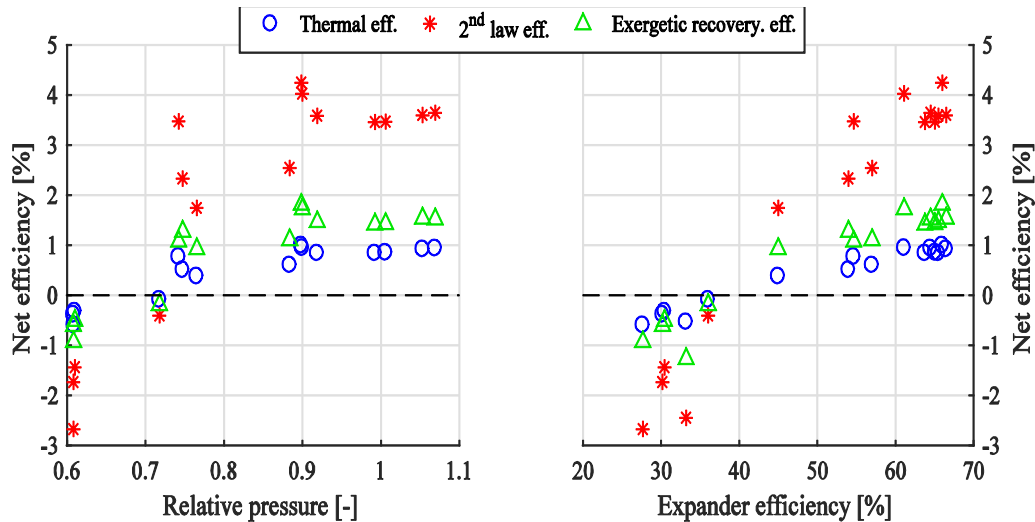


Figure VII-13: CORSERE net efficiencies function of: (a) relative pressure (b) expander efficiency

Figure VII-14 depicts the back work ratio and back work ratio efficiency, which is the ratio between the measured BWR and the ideal BWR with isentropic compression and expansion. The CORSERE ORC has a very high BWR with a minimum of 74 %, which is much higher than other ORC in the same power range (15-40 %). This high BWR has two origins, first the relatively low pump efficiency, which combined with the good but not sufficient expander efficiency results in a low back work ratio efficiency of 30 %. Second, ORC has inherent higher BWR when running close and above the critical point (Sylvain Quoilin et al. 2013)(Chapter IV-1.3) .

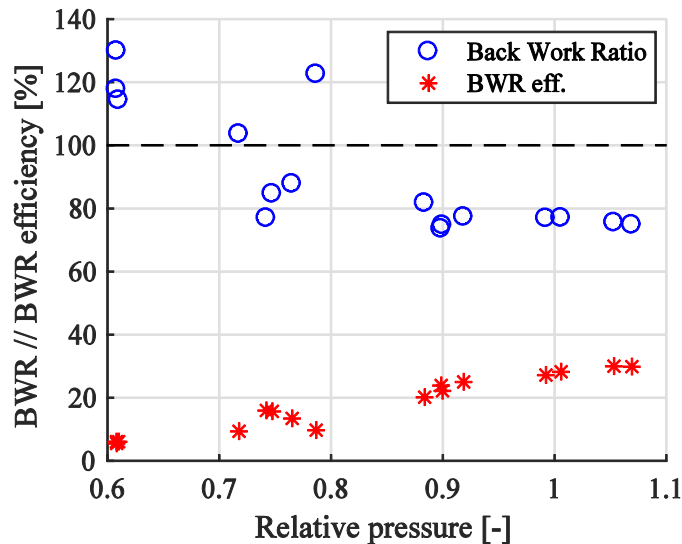


Figure VII-14: CORSERE Back Work Ratio and BWR efficiency evolution with the relative pressure

The CPV-Rankine test bench is analyzed in depth, since more data points are available and for a wider range of running conditions. The ORC net efficiency reaches a maximum of 4.2 % thermal efficiency at a pressure ratio of 1.95, as shown in Figure VII-15. At constant pressure ratio, ORC thermal efficiency increases with the expander frequency, but a minor improvement is reported above 30 Hz. At constant expander speed, the thermal efficiency increases with the pressure ratio, which is directly related to the expander efficiency shown previously, with an optimum pressure ratio of around 2. However, such pressure ratio is only achieved for low expander speed. For high expander speed, pressure ratio is limited by the pump maximum flow rate as discussed in Chapter VII-1.2. Thermal efficiency of 5 to 6 % could be expected at nominal expander frequency and optimum pressure ratio.

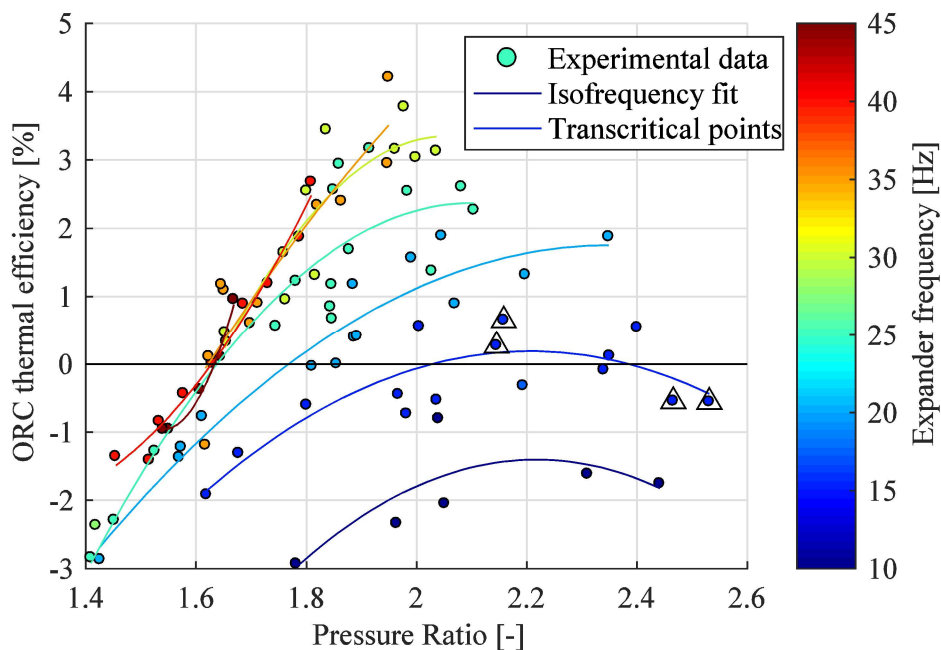


Figure VII-15: CPV-Rankine net thermal efficiency function of the pressure ratio

The exergetic efficiency as a function of relative pressure for constant hot source temperature of 95 °C is depicted in Figure VII-16. The maximum exergetic efficiency increases with pump frequency and the optimum pressure increases with the pump frequency. However, the reduced cycle efficiency at high pressure is induced by the low expander efficiency (as a result of low expander frequency). Considering only data with expander frequency above 25 Hz, the exergetic efficiency constantly increases with the relative pressure.

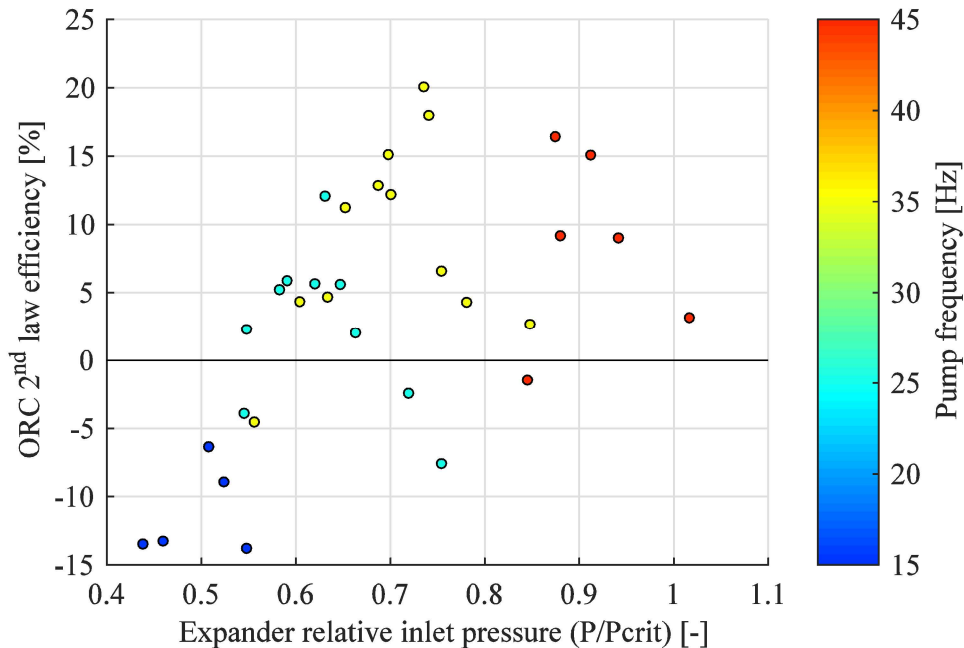


Figure VII-16: CPV-Rankine 2nd law efficiency function of expander inlet relative pressure

For each hot source temperature (65 °C, 80 °C, 95 °C and 100 °C), the maximum exergetic efficiency points are presented and linked with the pressure-temperature map, as shown in Figure VII-17. This map can be used to estimate the optimum pressure of this specific ORC test bench, for different hot fluid temperature levels, and estimates 2nd law efficiency reachable. The optimum pressure is increasing with maximum temperature, but the optimum 2nd law efficiency seems to be limited below 20 %. The maximum 2nd law net efficiency is reached for working fluid supercritical temperature at the expander inlet but subcritical pressure. But as largely discussed previously, low cycle efficiency at supercritical pressure seems mostly due to mismatch between pump and expander nominal flow rates (Chapter VII-1.2).

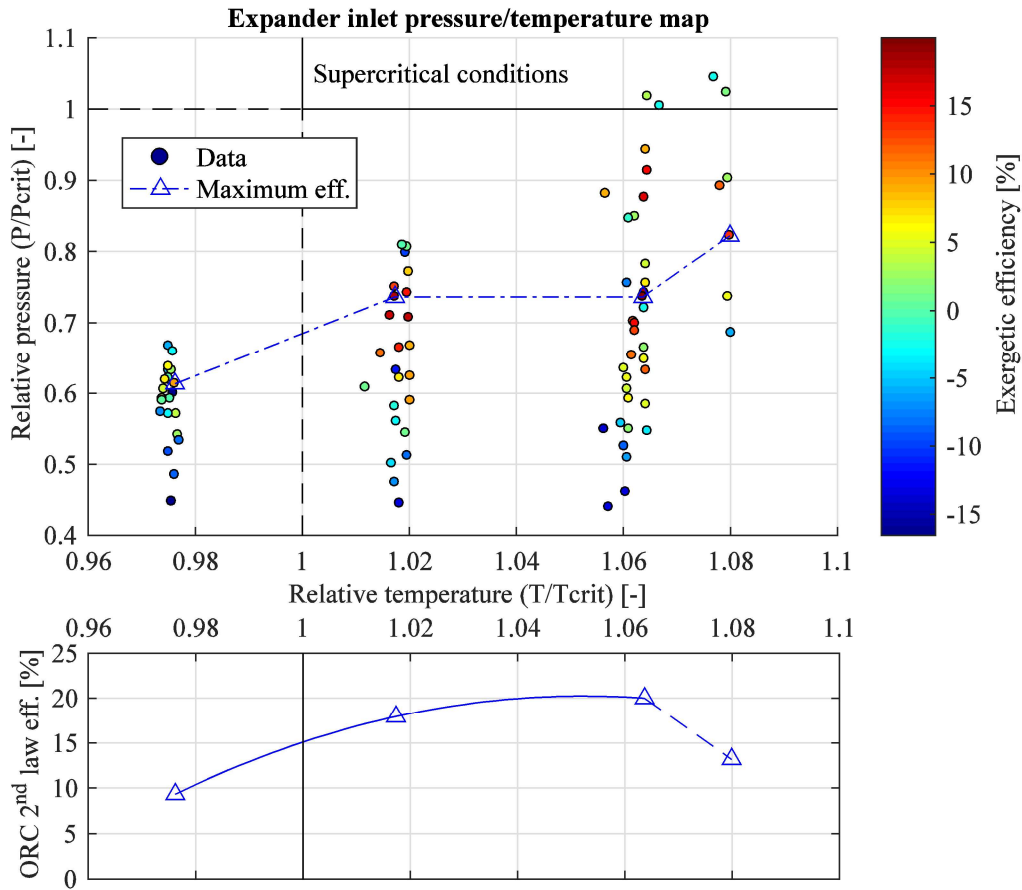


Figure VII-17: CPV-Rankine 2nd law efficiency in the relative pressure-temperature map

The two ORC performances are compared with other experimental ORC of the same power range (1-10 kWe) using the previously introduced database (Chapter II-2). Since the database is computed with gross efficiencies, the expander production is used as the ORC gross power for efficiencies computation. Figure VII-18 shows the distribution of 1-10 kWe experimental ORCs ordered by growing efficiency, for both the thermal, 2nd law and exergetic recovery efficiency.

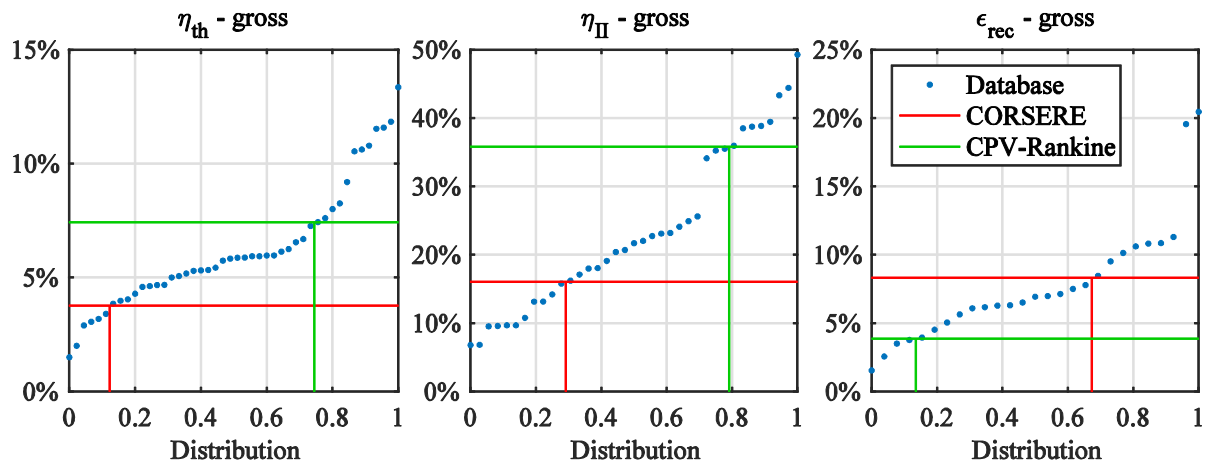


Figure VII-18: ORCs comparison with state-of-the-art prototypes

Even considering the gross power, the maximum thermal efficiency of the CORSERE test bench is only 3.8 %, it places this ORC on the bottom 12 % ORC. Considering the 2nd law efficiency which rectify the efficiency from the hot source temperature inlet, the present ORC is on the bottom 29 % ORC with a 16 % efficiency. However, for the exergetic recovery efficiency, the present ORC is on the top 33 % ORC with 8.3 % of efficiency, while its full potential may not yet be reached.

However, the CPV-Rankine test bench performs well for the closed source efficiencies. It reaches a 7.4 % gross thermal efficiency, ranking it on the top quarter of all ORCs. Considering the 2nd law efficiency, which annihilate the hot source temperature effect, the CPV-Rankine bench reaches a 35.8 % efficient, ranking it on the top fifth. Although, the test bench is not optimized for heat recovery. Its exergetic recovery efficiency reaches only 3.9 %, much less than the CORSERE test bench and on the bottom tenth of ORC prototypes.

2.2 Exergetic analysis

Exergy is a useful tool for analysis of thermodynamic process such as organic Rankine systems and it is a complement to classic energetic analysis to address issues and identify improvement opportunities (Mago et al. 2008; Grosu et al. 2016). Exergetic flow diagram shows the transfer of exergy between components and their internal exergy destruction. In Figure VII-19, the exergetic flow diagram of the CORSERE test bench at the point of highest efficiency (thermal, 2nd law and exergetic recovery) is drawn. For scale reasons, the minimum exergy is taken as the reference (or zero) exergy, for each fluid. For cold water, its inlet exergy, for working fluid, the pump inlet exergy and for hot water, its outlet exergy. Therefore, the non-recovered exergy of the hot water is not shown, and, for information, equals 45 kW. So, the hot water recoverable exergy ΔE_{\max} equals 73.6 kW.

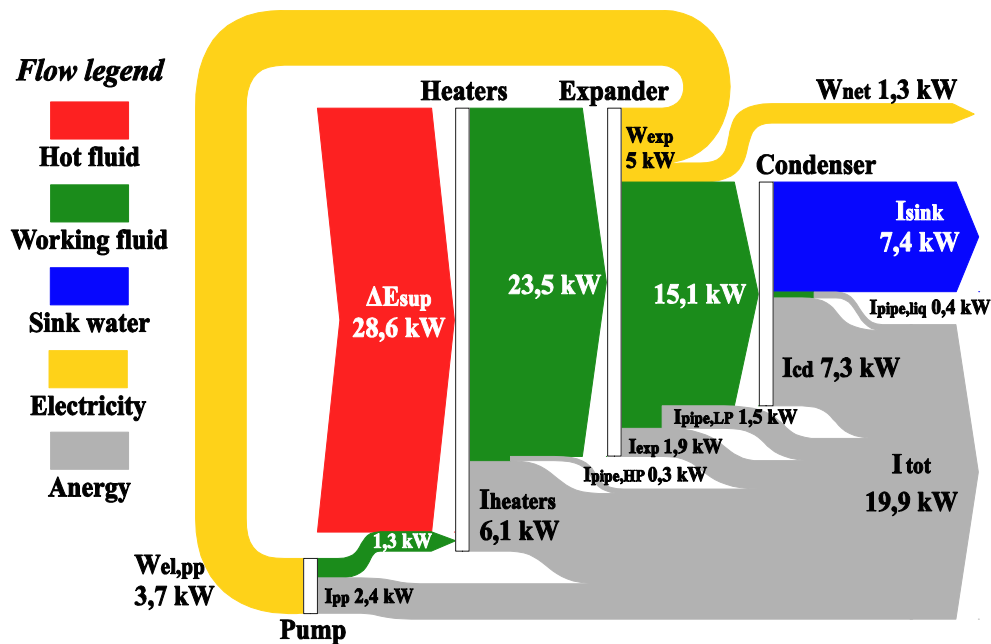


Figure VII-19: Detailed exergetic flow diagram of the CORSERE bench at the most efficient point

As previously mentioned in the dedicated chapter, the pump efficiency is low, 65 % of its input exergy is destroyed and it consumes a large portion of the expander production, but it is only the 3rd component in terms of absolute exergy destruction. The heaters (pre heater and evaporator) are in second position of exergy destruction but destroy only 21 % of their hot water supplied exergy ΔE_{sup} . The HP pipe exergy destruction accounts for heaters and pipe pressure drops, as well as HP pipes thermal losses, but is in last position for absolute exergy destruction. The expander is the main component with the smaller exergy destruction. However the low pressure pipes and condenser pressure drops, grouped under the pipe LP denomination, causes relatively large exergy destruction. This part of the ORC has the highest fluid velocity in the pipes; since the fluid has the lowest density (low pressure and high temperature vapor). Larger, shorter and more direct piping could reduce the destroyed exergy.

The condenser accounts for the largest portion of exergy destruction, especially when counting the sink exergy in the exergy destruction. The sink exergy could be reduced by increasing the cold water flow rate. Doubling the cold water flow rate would decrease the cold water outlet temperature from 55.7 °C to 37.4 °C for the same heat power extracted at the condenser, and would reduce the sink exergy from 7.4 kW to 3.9 kW. But the condenser heat transfer exergy destruction would equally increase from 7.3 to 10.8 kW.

Then, the only way to reduce the condenser exergy destruction would be to decrease the condensation pressure. As shown in Figure VII-20a, the condenser specific exergy destruction increases with the condensation pressure and the superheating at the condenser inlet. The use of economizer allows de-superheating the low pressure fluid and recovering some exergy to pre-heat the high pressure fluid, reducing the condenser exergy destruction.

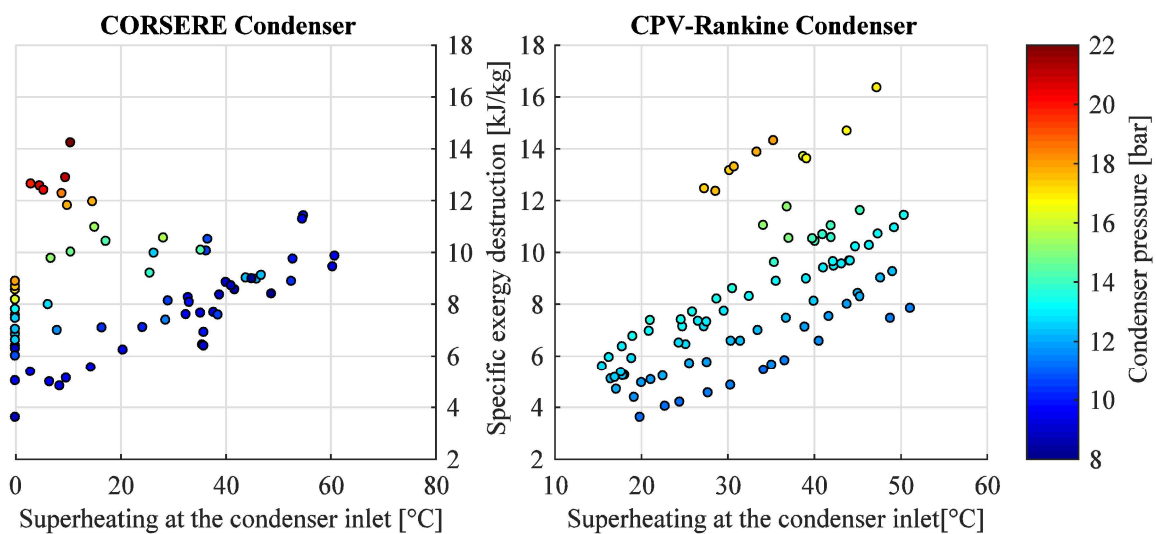


Figure VII-20: Condenser exergy destruction analysis: (a) CORSERE (b) CPV-Rankine

In the meantime, while the condensation pressure would improve the exergetic efficiency of the condenser, the pump subcooling should be carefully monitored. The actual subcooling is 16 °C or 3.7 bar of net positive suction head (NPSH) and could be reduced to 5 °C or 1.1 bar of NPSH, without pump troubleshooting (Chapter IV-2.2), however the pump inlet temperature could hardly be reduced since there is already a temperature difference of 5 °C at the condenser between the working fluid outlet and cold water inlet.

Liquid pipe pressure drops between the condenser and the pump account for a small exergy destruction. However, those pressure drops induces a higher condensation pressure and therefore are partly accountable for the high exergy destruction at the condenser. The total pressure drop is found to be nearly 7.4 bar, and then, the actual equivalent subcooling at the condenser outlet is 38 °C. Reducing this pressure drop could drastically decrease the condenser exergy destruction, and increase the expander output power.

The Figure VII-21 compares four different cases study, and shows the proportion of supplied exergy ΔE_{sup} destroyed on each component. All pipe losses are grouped under the Pressure Drops denomination. The optimum case is the point of maximum efficiency previously analyzed. The main parameters of each case study are summarized in Table VII-1.

Table VII-1: CORSERE exergetic performances – case study summary

Parameter	Transcritical	Optimum	Low Pressure	Economizer
Hot water inlet temperature [°C]	120.1	108.8	104.4	103.7
Hot water flow rate [kg/s]	1.66	1.53	0.98	1.00
Hot water supplied exergy [kW]	37.90	28.59	13.72	12.34
Working fluid flow rate [kg/s]	0.759	0.620	0.274	0.324
Relative pressure [-]	1.07	0.90	0.61	0.65
Expander frequency [Hz]	26.7	26.7	13.4	16.7
Cold water flow rate [kg/s]	0.84	0.84	0.85	0.53
Condenser outlet subcooling [K]	43.1	37.7	21.6	31.6

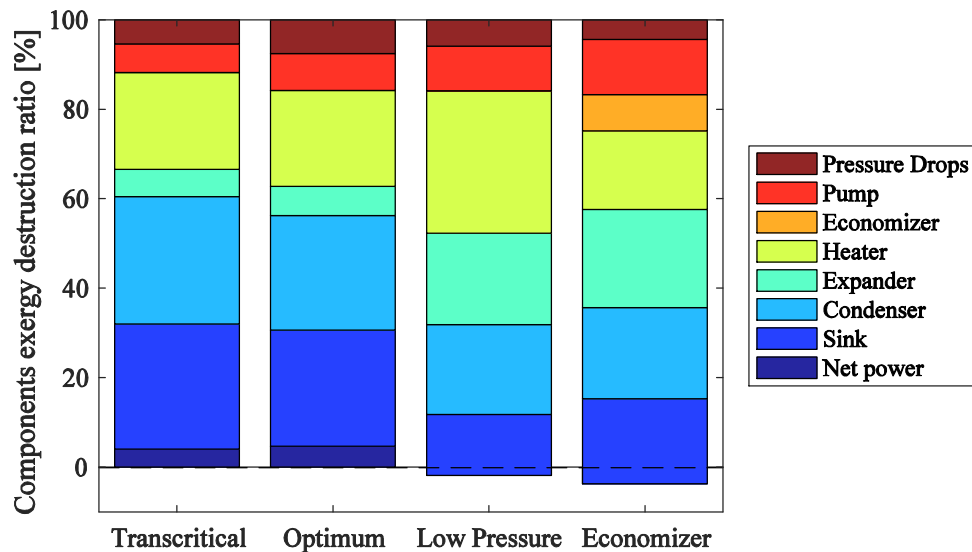


Figure VII-21: CORSERE bench - components exergetic destruction ratio for different case study

The transcritical case has low pump exergy destruction ratio due to higher pump efficiency at high pressure. Transcritical running condition also leads to lower pressure drop exergy destruction, probably because of the higher fluid density. However, it has similar heater and expander destruction ratio compared to the optimum reference case. The gain on the pump and pipes are lost at the condenser. Since the transcritical case has higher flow rate and liquid pressure drop are higher, resulting in higher condensation pressure and condenser subcooling.

The low pressure case has lower condenser subcooling and therefore lower exergy destruction at the condenser. However, its lower pressure results in higher heater and pump exergy destruction ratio. Combined with a low frequency, the expander has a low efficiency, and so, a high exergy destruction ratio.

The economizer case can be compared with the low pressure case since they have similar input parameters. The use of economizer reduces by 45 % the ratio of exergy destroyed by at heaters and by 20 % the heating exergy destruction (sum of the economizer and heaters exergy destruction). They have similar exergy destruction ratio at the expander, but the economizer case has higher exergy destruction ratio at the condenser and sink combined, while the economizer should reduce the condenser exergy destruction. This may be due to the lower cold water flow rate and higher condenser subcooling.

Figure VII-22 shows exergetic flow diagram of the CPV-Rankine test bench. Figure VII-22a shows the optimum subcritical point (point of maximum cycle efficiency), and Figure VII-22b a transcritical point for a similar supplied exergy of 9.1 kW, with a heat input 43 kWth at 95 °C in both cases. The supplied exergy is used as a base index of 100 for this diagram.

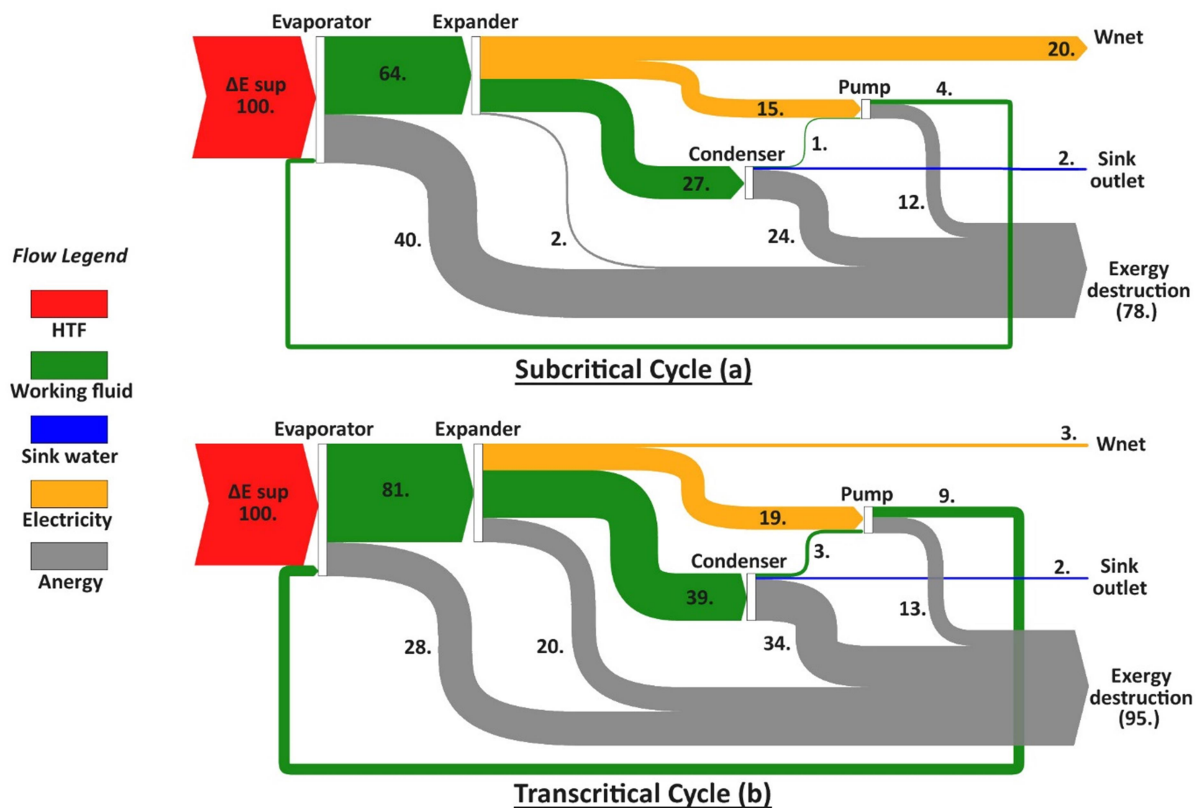


Figure VII-22: CPV-R exergetic flow diagram: (a) subcritical optimum case (b) transcritical case

Most of the exergy destruction occurs in the two heat exchangers (evaporator and condenser). The exergy loss in the evaporator occurs because of the high average temperature difference between the HTF and the organic fluid. In transcritical operation, the pressure is increased and the mean temperature difference reduced. Therefore, exergy destruction in the evaporator is 30 % lower (see Figure V-14).

In the condenser, there is no valorization of the rejected heat. Even if superheating at the expander outlet is lower for transcritical case, condenser exergy destruction is 40 % higher because of the condensation pressure increases of 2.5 bar. As for the CORSERE test bench, influence of the condenser inlet superheats and condensation pressure over the exergy destruction in the CPV-Rankine condenser is shown in Figure VII-20b. Lower condensation pressure could be achieved with a better design and control of the condensation process. The use of an economizer for recovering the superheating power at the expander outlet could save 10 % to 30% of the heat input and reduce exergy destruction both in the condenser and evaporator.

Exergy destruction in the expander is much higher in the transcritical case, mainly because the expander frequency is very low – 15 Hz in average – in order to reach supercritical conditions at the expander inlet. Such operating conditions resulted to low expander efficiency.

For transcritical operation, the pump exergy destruction sparsely increased, which was not expected, since the provided hydraulic power in this case is 60 % higher than in the subcritical case. This is because of the high static losses in the pump power system (Chapter IV-1).

2.3 ORC dynamics

The CORSERE test bench dynamics is investigated experimentally and using the Modelica/Dymola model. The experimental test bench and its dedicated heating and cooling auxiliaries have inherent dynamics, so pure steps might not be obtained experimentally. In particular, the hot source temperature dynamics is slower than all other ORC dynamics. Therefore it can only be investigated using a model. On the opposite, as already discussed in Chapter III-3.3, the model uses a fictive receiver in order to run, which disturbs the ORC low pressure response to a step.

Figure VII-23 shows CORSERE dynamic behavior for two increasing steps of working fluid flow rates. Experimental and model data are compared for the pre-heater temperatures, condenser temperatures and ORC pressures. The model is found to have similar time and amplitude response than the experiment for the different variables, except for the low pressure as previously discussed. Experimentally, the high pressure increases as fast as the working fluid. The low pressure experienced almost no change.

Heat source and heat sink flow rate steps could be easily performed experimentally. Figure VII-24 shows a downward step of the heat source flow rate from 5 to 2.75 m³/h. Raw and normalized variables are plotted. In the normalized signal, the variable pre-step value is used as the zero and the stabilized value as the unitary.

The ORC response is fast but with some oscillations. Since the pinch point is almost null in both cases, the evaporator outlet temperature is directly related to the hot fluid inlet temperature. Downstream of the evaporator, temperature variations are due to oscillations of the hot source temperature. The high pressure is also found to oscillate with the heat source flow rate step.

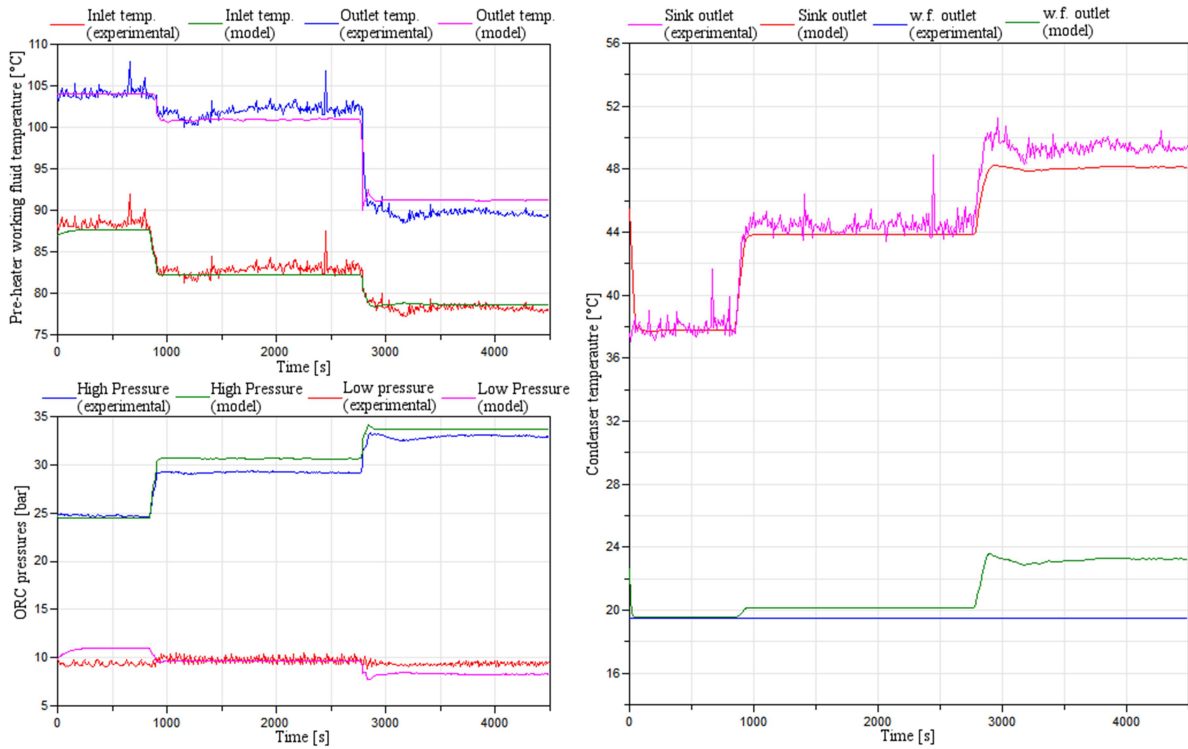


Figure VII-23: CORSERE working fluid flow rate steps - Experiment & Model comparison

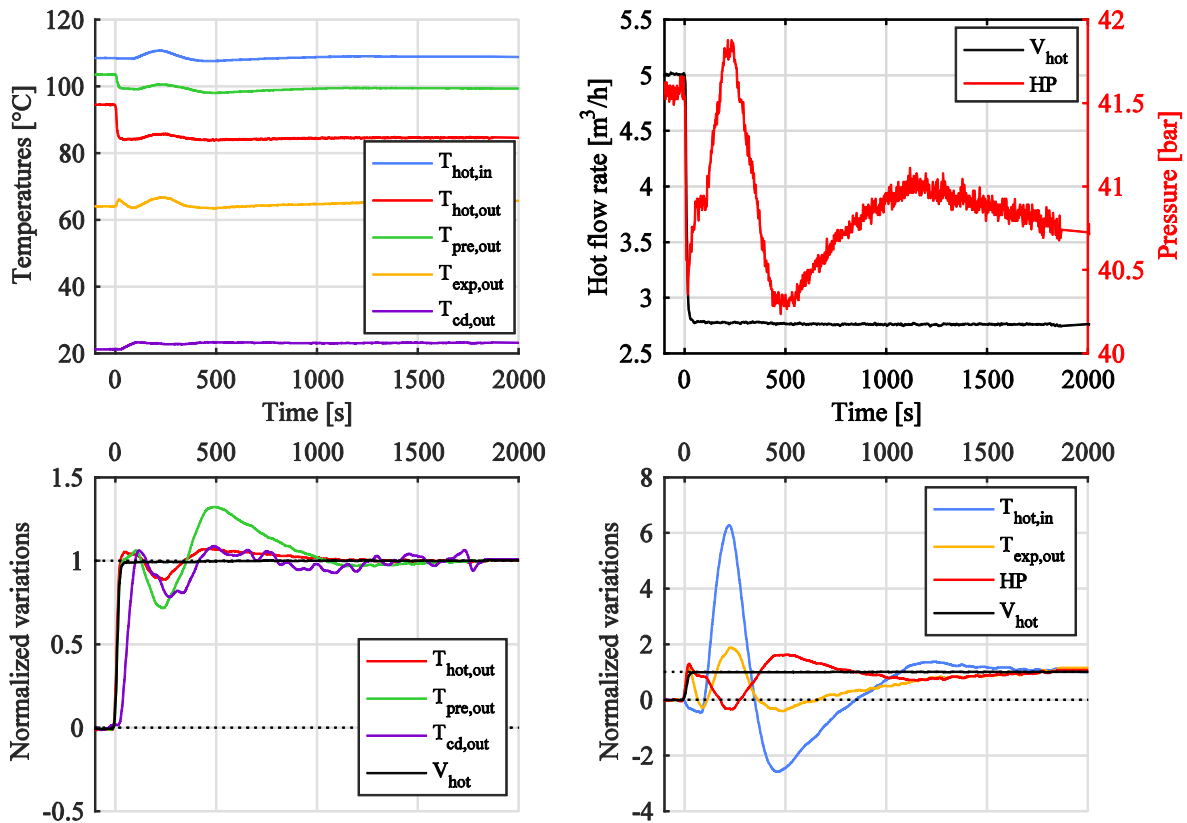


Figure VII-24: CORSERE bench - heat source flow rate downward step

Similarly, Figure VII-25 shows an upward step of the heat sink flow rate, from 1.5 to 3 m³/h. Only the working fluid and cold fluid condenser outlet temperatures are found to be influenced by the heat sink flow rate step, as well as the ORC pressures. In particular, the low pressure experienced a drastic decrease, corresponding to the behavior expected from the charge-sensitive model (Chapter VI). The high pressure experiences minimal variations but some oscillations. Low pressure 5 % settling time and ramp time are respectively 32 s and 22 s, which is faster than the working fluid and cold water temperature, both 43 s for the 5 % settling time and 27 s for the ramp time.

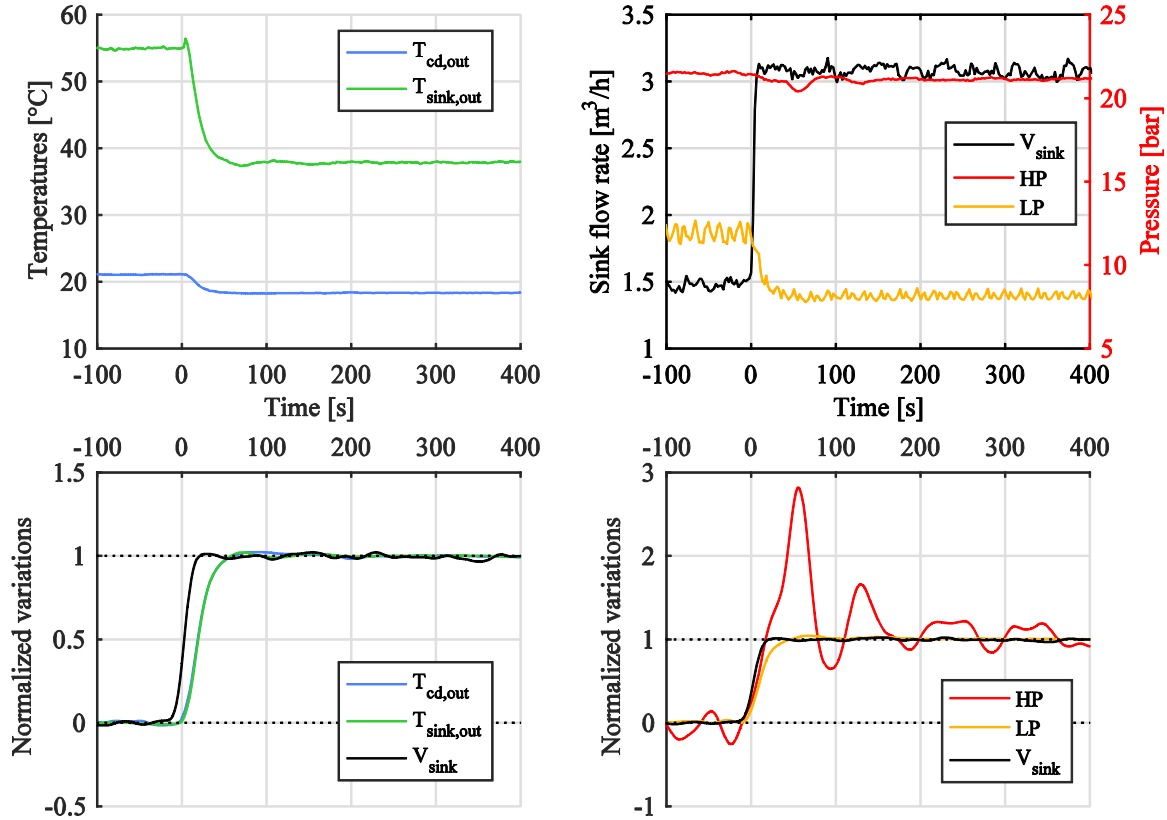


Figure VII-25: CORSERE bench - heat sink flow rate upward step

Chapter conclusion

In this chapter, the Organic Rankine Cycle operation is investigated, focusing on the machineries and then on the complete cycle. Both the CORSERE and the CPV-Rankine test benches are used for the discussion.

First, the two machineries: the scroll expander and the diaphragm are studied. The scroll mechanism is exposed and compressor to expander modifications are discussed. Then, the expander energetic and volumetric efficiencies are analyzed and associated. Expander frequency is found to have a major impact on scroll volumetric efficiency and therefore its global energetic efficiency.

Since both the scroll expander and the diaphragm pump are volumetric engines, their combined behavior is a topic of interest. A careful matching investigation of both engines should be conducted during the design phase to prevent part-load operation of one or the other machinery and the resulting performance deterioration. Especially for transcritical ORC, as the expander inlet density drastically changes.

Then, the complete cycle behavior and performances are investigated with an energetic and exergetic standpoint. The CORSERE bench only reached a 1.0 % of net thermal efficiency, corresponding to 4.2 % of the Carnot thermodynamic maximum efficiency, and 1.8 % of net exergetic recovery efficiency. The CPV-Rankine reached respectively 4.2 % and 20 % for the net thermal and 2nd law efficiency.

A comparison of benches gross efficiencies with other 1 to 10 kWe prototypes is exposed. The CORSERE bench ranks respectively on the bottom 12 % and 29 % in terms of gross thermal and 2nd law efficiency. But it ranks on the top third for exergetic recovery efficiency which is its design application. Conversely, the CPV-Rankine bench, which was designed for a closed source application (thermal solar), ranks on the top quarter for thermal efficiency and top fifth for 2nd law efficiency illustrating the potential of high pressure and transcritical cycles. However, it ranks on the bottom tenth with regards to the exergetic recovery efficiency, but the prototype was not tested for typical heat recovery inputs.

An exergetic analysis of both cycles allowed identifying optimization potential. In particular, the condenser and the condensing pressure should be carefully investigated to keep the subcooling as low as possible but above the pump technical limits. Transcritical running condition can drastically reduce exergy destruction at the evaporator, which is preponderant component for exergetic losses.

Finally, the CORSERE test bench dynamic response to steps is investigated, using both experimental data and dynamic simulations. Flow rate variations are specifically discussed. The system time response is generally less than a minute, pressures variations are faster than thermal variations. In addition, some oscillations can be observed for some variables. They are not always related to the ORC system but also to the heating system regulation.

Chapter VIII

Conclusion

The energy sector is facing major challenges in the upcoming century to ensure a low-carbon and climate-resilient economy. On one side, energy demand, driven by the world population and economic growth, is rising. On the other side, its major impact on the global warming issue needs to be addressed. Among the solutions to overcome these challenges, renewable energies and process energy efficiency could be partially fulfilled by the use of the Organic Rankine Cycle (ORC) technology.

The organic Rankine cycle is a heat to power conversion technology used since the 19th century to transform energy from a variety of sources such as geothermal, solar, biomass or waste heat recovered from the industrial process or internal combustion engines. Current range of commercial ORC goes from 10 kWe to 10 MWe converting heat sources between 80 °C and 300 °C, but this range is extending as new applications are developed such as ocean thermal energy conversion, micro-CHP or vehicle engine heat recovery. Researches on ORC increased in the last decades, focusing on design optimization, fluid selection, expander technologies or dynamic control.

The present thesis is centered on the use of Organic Rankine Cycle for low-grade heat conversion into electricity. The specific case of the transcritical ORC configuration being the main thread, different topics are investigated such as reciprocating pump operation, supercritical heat transfer, working fluid charge influence and global ORC behaviors.

The first part of this work aims to provide a clear framework of the thermodynamic applied to ORC and its related applications. Through an energetic and exergetic standpoint, the different power types involved in the ORC system are detailed. Starting from those different powers, components and cycle efficiencies are defined.

A differentiation is proposed between classic closed-source applications, such as biomass and solar fuel sources, where the input can be assimilated to a heat flux and the heat source input temperature is directly related to the heat source output; and the open-source applications, such as geothermal energy and waste heat recovery, where the input is assimilated to a fluid flow, with an imposed flow rate and/or input energy.

Three definitions are selected to monitor ORC global performances: The classical thermal efficiency, and energetic efficiency; the second law efficiency, here defined as the ratio of thermal to Carnot efficiency and approximation of the exergetic efficiency; the exergetic recovery efficiency, specifically designed to report ORC performances for open-source application.

In order to have an overview of the current ORC state-of-the-art, a database of ORC prototypes is created. This database gathers qualitative and quantitative data on ORC components and plants. The performance criteria previously introduced are applied to the database references to perform an objective comparison.

Through the database analysis, a view of current and new research trends as well as opportunities for innovation can be identified. Using statistical methodology, innovative ORC performances can be evaluated and compared with classic ORC; while the main parameters influencing the ORC performances, the ORC power scale and the expander efficiency, can be identified.

This preliminary analysis is used as the starting point to identify topics of interest for the present thesis, but it also leads to new perspectives:

- While transcritical ORC is identified as a promising cycle for waste heat recovery and is the focus of the present work, zeotropic fluid mixtures are also a promising ORC evolution for waste heat recovery which should be further investigated.
- The lack of standards for power and efficiency definitions, in the scientific and the industrial community, is an issue that must be addressed to further develop the ORC technology.
- The experimental database is released under an open-source license². Therefore, extensions and updates of the database are open to other researchers.

In order to address the different issues and investigate the selected research topics, different tools are used. Four experimental test bench are used, for different purposes:

- CORSERE: a complete ORC, using R134a as working fluid and a scroll expander. Designed to run in transcritical conditions, it can be switched from simple to regenerative configuration. This test bench is at the core of the present work and is largely investigated: pump operation, dynamic and charge-sensitive modeling, heat transfer investigation, ORC performances and behavior analysis.
- CPV-Rankine: a transcritical ORC prototype installed at the Agricultural University of Athens. It uses R404a as working fluid and a modified scroll compressor as expander. The bench is first tested on a controlled laboratory environment and then connected to concentrated solar panel field. This test bench is used for pump energetic model validation, and transcritical ORC performances investigation in various conditions.
- SURCOUF: a fluid loop, without expander, designed for heat transfer investigation. It uses R134a as circulating fluid and is mainly used for supercritical heat transfer study and reciprocating pump investigation.
- Solammor: an ammonia-water absorption chiller, only used for reciprocating pump model validation.

In parallel, different numerical tools are used. The software, *Engineering Equation Solver* is used for simple thermodynamic simulation and optimization. The *Matlab* and *Scilab* software, coupled with the *CoolProp* fluid properties library, are used for experimental data processing. Scripts for steady-state and transient identification are coded. The data reconciliation method is applied to steady-points in order to improve measured and calculated parameters precision.

² Available at <https://doi.org/10.5281/zenodo.400556>

The *ORCmKit*, a library for steady-state ORC modeling, is used under the *Matlab* environment. The library includes void-fraction correlations to estimate the fluid charge in the heat exchangers. Therefore, charge-sensitive model of ORC test bench can be computed and the charge influence investigated.

Dynamic modeling is performed with the *ThermoCycle* library, coded with the *Modelica* language and used under the *Dymola* environment. This tool is able to simulate the ORC dynamic response but is not charge sensitive at the moment.

However, the different libraries and models are not able to run transcritical cycles. Transition from subcritical to supercritical conditions lead to many different numerical issues, the first one being infinite fluid properties derivatives, resulting in model convergence issues. Further work should be done to upgrade and validate dynamic and charge-sensitive model for transcritical ORC.

The ORC working fluid pump is not largely investigated in the literature. Meanwhile, pump performances and behavior can have a large impact on the general ORC performances, especially transcritical ORC. In a first step, the energetic performance of reciprocating pump for ORC is investigated. A semi-empirical model is proposed, coupling correlations of the literature for the electric part, from the manufacturer for the pump part and completed with field investigations of the pump operation.

The model is validated on four different test benches, running with various working fluids, with different pump and motor sizes. The model is able to estimate the pump electric consumption at full and part load, under various speeds, with a deviation below 5 %. Then, impact of pump energetic performance on the ORC design and operation is discussed. The influence of pump and its driving motor oversizing is highlighted. Excessive oversizing results in operation under low load and low efficiency, especially for small-scale units.

In a second step, the volumetric performances of the pump are investigated. Through a literature analysis, the effects of fluid properties such as isentropic compressibility or viscosity, over the volumetric efficiency are discussed. A semi-empirical model for volumetric efficiency is also exposed, but no robust validation could be achieved.

Finally, the pump cavitation is discussed. A high minimum cavitation margins results in ORC performance deterioration, especially for low-grade heat sources. The pump cavitation is experimentally investigated and shown results similar to manufacturer data for water. A correlation is proposed and validated to adjust the pump volumetric efficiency deterioration due to the pump cavitation.

The ORC pump presents many research and development perspectives:

- Develop and investigate a pump specifically dedicated to ORC. For example, a pump directly coupled to the expander shaft, as for the *Tri-o-gen* © ORC units.
- In depth investigation of local pump cavitation mechanisms with organic fluid, for both volumetric and centrifugal pumps, and its impact (erosion, vibrations).
- Development of alternatives to ORC mechanical pumps, such as pumpless ORC (Yamada, Watanabe, and Hoshi 2013) or thermofluidic pumps (Richardson 2016).

Supercritical heat transfer is a complex subject. Many different phenomena are involved and fluid thermo-physical properties undergo drastic changes. In the literature, supercritical heat transfer are mostly investigated for water and CO₂. The first experimental setup used for heat transfer investigation is a smooth tube, homogeneously heated by a controlled power electric cord and dedicated to heat transfer investigation. Different tests are performed: subcooling fluid entry and near-critical temperature fluid entry.

Experimental heat transfer coefficients are compared with different literature correlations, using the Nusselt number. For subcooled fluid entry, Sieder-Tate correlation is found to better estimate experimental values, except for points with wall temperature exceeding the supercritical temperature. For near-critical fluid entry, heat transfer coefficient is found to largely differ from literature correlations developed for supercritical heat transfer. Indeed, near-critical heat transfer is still a misunderstood topic and uncertainty on measured and calculated parameters are large.

In the present configuration and test conditions, the flow and heat transfer are found to be a mixed opposed convection. Correlations for such flow are tested (Bruch; Fewster) and adapted. For subcooled fluid entry, the adapted correlation is found to better match the experimental Nusselt even for wall temperature above supercritical conditions, while for near-critical fluid entry, Bruch correlation gave acceptable results.

In a second step, a commercial brazed plate heat exchanger is investigated under supercritical conditions. Supercritical global heat transfer coefficient is found to range between the liquid and the two-phase heat transfer coefficients. On an exergetic efficiency standpoint, evaporator performances are enhanced as the pressure increases to the supercritical pressure.

Supercritical heat transfer investigations lead to perspectives for future work:

- Deeper investigations of the plate heat exchanger in supercritical conditions, under various flow rates, pressure and inlet temperature conditions.
- Near-critical heat transfer should be further investigated, using a dedicated experimental set-up, with a high precision instrumentation or numerical CFD tools.

The fluid charge minimization and optimization is a topic largely investigated for refrigeration and heat pumps but sparsely studied for organic Rankine cycles. Eventually, some authors experimentally pointed the influence of the fluid charge over the ORC performances. Fluid charge is investigated using the *ORCmKit* modeling library under the *Matlab* environment. A complete model of the CORSERE test bench is used for library and components parameters validation. However, a simplified model, i.e. with only the basic components and without pressure losses, is used to investigate the fluid charge influence.

At constant operating conditions, the fluid charge is found to have a large impact on the pump inlet subcooling but almost no impact on the high pressure side of the ORC. High charge leads to condenser flooding, low pressure and so subcooling increase. Low charge results in insufficient heat transfer area for proper fluid subcooling in the condenser, and therefore subcooling reduction. Excessive subcooling eventually leads to ORC performance drops, while insufficient subcooling leads to pump and flow rate decline.

Then, combined effects of fluid charge, expander speed and pump speed are investigated. ORC performance is maximized at maximum pump and expander speed. However, a proper fluid charge control might be necessary to ensure a sufficient and not excessive subcooling under different ORC operating conditions.

In a second step, the optimal fluid charge is calculated, assuming an optimal subcooling of 10 °C. Heat source temperature and flow rate increase tends to reduce the optimal fluid charge. On the opposite, heat sink flow rate increase leads to an optimal charge increase. However, the heat sink temperature sparsely influences the optimal charge. Expander speed reduction leads to higher pressure, higher evaporator mean density and optimal charge rise. By impacting both the evaporator and the condenser, working fluid flow rate variations lead to complex impact over the optimal fluid charge. Finally, a discussion on ORC design for fluid charge reduction is proposed. Current and new mechanisms and solutions for fluid charge and subcooling active regulations are introduced.

Investigation of the fluid charge results in different perspectives for technological development and broader investigations:

- Fluid charge influence over the ORC behavior and performances should be further investigated through experiments and the model compared with experimental data.
- Influence of the fluid and its thermo-physical properties over the optimal charge value and variation could be investigated as well.
- The *ORCmKit* library could be adapted to simulate transcritical ORC. Optimal charge variations are expected to be increased for transcritical cycle as fluid density undergoes large variations.
- The proposed mechanism for circulating fluid charge regulation should be designed and experimentally tested.

Lastly, the complete ORC performances and behavior are discussed, with a focus on the transcritical operation. Both the CORSERE and the CPV-Rankine test benches are used for the discussion. In a first step, scroll expanders performances are discussed. Scroll shaft speed is found to largely impact the expander volumetric and energetic efficiency. Then, flow rate equilibrium between the scroll expander and the diaphragm pump is investigated, as both engines are volumetric technologies. Flow rate matching should be carefully study at the design phase, especially for transcritical ORC, to prevent part-load operation of one or the other machinery.

Cycle performances are investigated with an energetic and exergetic standpoint, using the three different cycle efficiencies highlighted in the first part of the thesis. The CORSERE bench only reached a 1.0 % of net thermal efficiency, corresponding to 4.2 % of the Carnot thermodynamic maximum efficiency, and 1.8 % of net exergetic recovery efficiency. The CPV-Rankine reached respectively 4.2 % and 20 % for the net thermal and 2nd law efficiency.

The database of ORC prototypes is used to compare the tested benches with other ORC of the same power range. The CORSERE bench ranks respectively on the bottom 12 % and

29 % in terms of gross thermal and 2nd law efficiency. But it ranks on the top third for exergetic recovery efficiency which is its design application. Conversely, the CPV-Rankine bench, designed for a closed source application (thermal solar), ranks on the top quarter for thermal efficiency and top fifth for 2nd law efficiency illustrating the potential of high pressure and transcritical cycles.

Then, an exergetic analysis of both cycles is performed to identify optimization potential. Condenser pressure and subcooling should be carefully monitored and controlled, through charge regulation, to ensure maximal ORC performances. On the other side, transcritical operating conditions can drastically reduce exergy destruction at the evaporator, which is a preponderant component for exergetic losses.

Finally, the ORC dynamics is investigated using both experimental data and dynamic simulations. Flow rate variations of the heat source, the heat sink and the working fluid are specifically discussed.

ORC general behavior investigation leads to different perspectives, both for the present transcritical ORC setups and future ORC:

- The CORSERE test bench performances could be improved by removing fouled filters which leads to high pressure losses at the condenser outlet. Then, further investigation of transcritical operation should be performed.
- In the CPV-Rankine test bench, a bigger pump or faster driving motor should be placed to investigate cycle performances under transcritical conditions and nominal expander speed.
- Design of transcritical ORC should be carefully performed to properly match pump and expander flow rates. A fluid charge regulation could ensure smooth and optimal operation of test bench both under subcritical and transcritical operations.

A number of papers focusing on parametric investigation of ORC technology have shown that transcritical configuration or zeotropic fluid mixtures could improve the ability of ORC plants to efficiently recover and convert sensible heat from open sources, when considering their exergetic potential. The transcritical ORC, by operating at high pressure, with fluid at supercritical condition, poses new challenges and opportunities for scientific research and technological development.

The pumping system performances become preponderant to ensure global ORC performances, its design should be carefully carried out and ORC architecture modifications investigated (mechanical expander-to-pump coupling; ejector). Supercritical heat transfer improves the global heat exchanger efficiency; nevertheless local heat transfer investigation, especially near the critical point is required. Furthermore, the management of the working fluid charge represents a real lever for ORC performances optimization under various operating conditions.

Evaluating the techno-economical potential of the transcritical ORC technology for waste heat recovery, including the proposed improvements, will be necessary to convince stakeholders to further develop and investigate this technology.

References

- ADEME. 2015. *La chaleur fatale industrielle*.
- Afshari, Faraz, Omer Comakli, Nesrin Adiguzel, and Sendogan Karagoz. 2016. "Optimal Charge Amount for Different Refrigerants in Air-to-Water Heat Pumps." *Iranian Journal of Science and Technology, Transactions of Mechanical Engineering* 40 (4):325–35. doi:10.1007/s40997-016-0028-2.
- Almeida, Anibal De, Hugh Falkner, Joao Fong, and Keeran Jugdoyal. 2014. "EuP Lot 30 - Electric Motors and Drives." Final Report. European Commission.
- Apra, C., A. Greco, and A. Maiorino. 2015. "An Experimental Study on Charge Optimization of a Trans-Critical CO₂ Cycle." *International Journal of Environmental Science and Technology* 12 (3):1097–1106. doi:10.1007/s13762-014-0502-6.
- Astolfi, Marco, Matteo C. Romano, Paola Bombarda, and Ennio Macchi. 2014. "Binary ORC (Organic Rankine Cycles) Power Plants for the Exploitation of Medium–low Temperature Geothermal Sources – Part B: Techno-Economic Optimization." *Energy* 66 (March):435–46. doi:10.1016/j.energy.2013.11.057.
- Bamorovat Abadi, Gholamreza, and Kyung Chun Kim. 2017. "Investigation of Organic Rankine Cycles with Zeotropic Mixtures as a Working Fluid: Advantages and Issues." *Renewable and Sustainable Energy Reviews* 73 (June):1000–1013. doi:10.1016/j.rser.2017.02.020.
- Bamorovat Abadi, Gholamreza, Eunkoo Yun, and Kyung Chun Kim. 2015. "Experimental Study of a 1 Kw Organic Rankine Cycle with a Zeotropic Mixture of R245fa/R134a." *Energy* 93 (December):2363–73. doi:10.1016/j.energy.2015.10.092.
- Bao, Junjiang, and Li Zhao. 2013. "A Review of Working Fluid and Expander Selections for Organic Rankine Cycle." *Renewable and Sustainable Energy Reviews* 24 (August):325–42. doi:10.1016/j.rser.2013.03.040.
- Bell, Ian H., Jorrit Wronski, Sylvain Quoilin, and Vincent Lemort. 2014. "Pure and Pseudo-Pure Fluid Thermophysical Property Evaluation and the Open-Source Thermophysical Property Library CoolProp." *Industrial & Engineering Chemistry Research* 53 (6):2498–2508. doi:10.1021/ie4033999.
- Bendig, Matthias, François Maréchal, and Daniel Favrat. 2013. "Defining 'Waste Heat' for Industrial Processes." *Applied Thermal Engineering*, 15th Conference on Process Integration, Modelling and Optimisation for Energy Saving and Pollution Reduction, 61 (1):134–42. doi:10.1016/j.applthermaleng.2013.03.020.
- Borsukiewicz-Gozdur, Aleksandra. 2013. "Exergy Analysis for Maximizing Power of Organic Rankine Cycle Power Plant Driven by Open Type Energy Source." *Energy* 62 (December):73–81. doi:10.1016/j.energy.2013.03.096.
- Braimakis, Konstantinos, and Sotirios Karellas. 2017. "Integrated Thermoeconomic Optimization of Standard and Regenerative ORC for Different Heat Source Types and Capacities." *Energy* 121 (February):570–98. doi:10.1016/j.energy.2017.01.042.
- Branchini, Lisa, Andrea De Pascale, and Antonio Peretto. 2013. "Systematic Comparison of ORC Configurations by Means of Comprehensive Performance Indexes." *Applied Thermal Engineering* 61 (2):129–40. doi:10.1016/j.applthermaleng.2013.07.039.
- Bruch, A., A. Bontemps, and S. Colasson. 2009. "Experimental Investigation of Heat Transfer of Supercritical Carbon Dioxide Flowing in a Cooled Vertical Tube." *International Journal of Heat and Mass Transfer* 52 (11–12):2589–98. doi:10.1016/j.ijheatmasstransfer.2008.12.021.
- Bruch, Arnaud. 2006. "Optimisation des composants échangeurs dans les machines frigorifiques fonctionnant au dioxyde de carbone." PhD Mécanique et Energétique, Grenoble: Université Joseph Fourier.
- Carnot, Sadi. 1824. *Réflexions sur la puissance motrice du feu et sur les machines propres à développer cette puissance*. Bachelier Libraire.
- Casci, C., G. Angelino, P. Ferrari, M. Gaia, G. Giglioli, and E. Macchi. 1981. "Heat Recovery in a Ceramic Kiln with an Organic Rankine Cycle Engine." *Journal of Heat Recovery Systems* 1 (2):125–31. doi:10.1016/0198-7593(81)90027-8.
- Chang, Jen-Chieh, Tzu-Chen Hung, Ya-Ling He, and Wenping Zhang. 2015. "Experimental Study on Low-Temperature Organic Rankine Cycle Utilizing Scroll Type Expander." *Applied Energy* 155 (October):150–59. doi:10.1016/j.apenergy.2015.05.118.
- Chang, Young Soo, Jae Kyoo Jang, Byung Ha Kang, and Sukhyun Kim. 2014. "Experimental Study on Effects of POE Oil on R134a Evaporation Heat Transfer in Plate Heat Exchanger." *Transactions of the Korean Society of Mechanical Engineers B* 38 (3):255–62. doi:10.3795/KSME-B.2014.38.3.255.
- Chargerès, Bernard De, and Robet Rey. 2009. "Pompes volumétriques pour liquides." *Techniques de l'Ingénieur*.

References

- Chen, Huijuan, D. Yogi Goswami, and Elias K. Stefanakos. 2010. "A Review of Thermodynamic Cycles and Working Fluids for the Conversion of Low-Grade Heat." *Renewable and Sustainable Energy Reviews* 14 (9):3059–67. doi:10.1016/j.rser.2010.07.006.
- Cipolla, G. 1980. "Experimental Rankine Cycle Engine Designed for Utilization of Low Temperature, Low Pressure Heat." In *New Ways to Save Energy*, 809–22. Springer. doi:10.1007/978-94-009-8990-0_86.
- Colonna, Piero, Emiliano Casati, Carsten Trapp, Tiemo Mathijssen, Jaakko Larjola, Teemu Turunen-Saaresti, and Antti Uusitalo. 2015. "Organic Rankine Cycle Power Systems: From the Concept to Current Technology, Applications, and an Outlook to the Future." *Journal of Engineering for Gas Turbines and Power* 137 (10):100801–19. doi:10.1115/1.4029884.
- Corberán, José-M., Israel Martínez-Galván, Santiago Martínez-Ballester, José González-Maciá, and Rafael Royo-Pastor. 2011. "Influence of the Source and Sink Temperatures on the Optimal Refrigerant Charge of a Water-to-Water Heat Pump." *International Journal of Refrigeration* 34 (4):881–92. doi:10.1016/j.ijrefrig.2011.01.009.
- Declaye, Sébastien, Sylvain Quoilin, Ludovic Guillaume, and Vincent Lemort. 2013. "Experimental Study on an Open-Drive Scroll Expander Integrated into an ORC (Organic Rankine Cycle) System with R245fa as Working Fluid." *Energy* 55 (June):173–83. doi:10.1016/j.energy.2013.04.003.
- Demierre, Jonathan, Antonio Rubino, and Juerg Schifffmann. 2015. "Modeling and Experimental Investigation of an Oil-Free Microcompressor-Turbine Unit for an Organic Rankine Cycle Driven Heat Pump." *Journal of Engineering for Gas Turbines and Power-Transactions of the Asme* 137 (3):032602. doi:10.1115/1.4028391.
- Deprez, Wim, Joris Lemmens, Dirk Vanhooydonck, Wim Symens, Kurt Stockman, Steve Dereyne, and Johan Driesen. 2010. "Iso Efficiency Contours as a Concept to Characterize Variable Speed Drive Efficiency." In . Rome: IEEE. doi: 10.1109/ICELMACH.2010.5607991.
- DiBella, Francis A., Luco R. DiNanno, and Michael D. Koplów. 1983. "Laboratory and On-Highway Testing of Diesel Organic Rankine Compound Long-Haul Vehicle Engine." In *SAE Technical Paper*. SAE International. doi:10.4271/830122.
- Dickes, Rémi, Olivier Dumont, Rémi Daccord, Sylvain Quoilin, and Vincent Lemort. 2017. "Modelling of Organic Rankine Cycle Power Systems in off-Design Conditions: An Experimentally-Validated Comparative Study." *Energy* 123 (March):710–27. doi:10.1016/j.energy.2017.01.130.
- DiPippo, Ronald. 2004. "Second Law Assessment of Binary Plants Generating Power from Low-Temperature Geothermal Fluids." *Geothermics* 33 (5):565–86. doi:10.1016/j.geothermics.2003.10.003.
- . 2007. "Ideal Thermal Efficiency for Geothermal Binary Plants." *Geothermics* 36 (3):276–85. doi:10.1016/j.geothermics.2007.03.002.
- Dittus, F.W., and L. M. K Boelter. 1930. *Heat Transfer in Automobile Radiators of the Tubular Type*. Vol. 2. 13. University of California Press.
- Domanski, P., and D. Didion. 1983. "Computer Modeling of the Vapor Compression Cycle with Constant Flow Area Expansion Device." ark:/67531/metadc38337.
- Dumont, Olivier, Sylvain Quoilin, and Vincent Lemort. 2015. "Experimental Investigation of a Reversible Heat Pump/organic Rankine Cycle Unit Designed to Be Coupled with a Passive House to Get a Net Zero Energy Building." *International Journal of Refrigeration* 54 (June):190–203. doi:10.1016/j.ijrefrig.2015.03.008.
- . 2016. "Importance of the Reconciliation Method to Handle Experimental Data in Refrigeration and Power Cycle: Application to a Reversible Heat Pump/organic Rankine Cycle Unit Integrated in a Positive Energy Building." *International Journal of Energy and Environmental Engineering* 7 (2):137–43. doi:10.1007/s40095-016-0206-4.
- Duparchy, Alexandre. 2011. Dispositif de contrôle du fluide de travail circulant dans un circuit fermé fonctionnant selon un cycle de Rankine et procédé pour un tel dispositif. EP2365192B1, issued September 14, 2011.
- Elson, Amelia, Rick Tidball, and Anne Hampson. 2015. "Waste Heat to Power Market Assessment." ORNL/TM--2014/620. Oak Ridge National Laboratory (ORNL), Oak Ridge, TN (United States). Building Technologies Research and Integration Center (BTRIC); <https://www.osti.gov/scitech/biblio/1185773>.
- Enertime, ENSAM, CEA, and Separex. 2012. "Etude SURORC." ADEME.
- Ernst, Timothy C., and Christopher R. Nelson. 2012. Rankine cycle waste heat recovery system. US8800285 (B2), issued August 23, 2012.
- Eyerer, Sebastian, Christoph Wieland, Annelies Vandersickel, and Hartmut Spliethoff. 2016. "Experimental Study of an ORC (Organic Rankine Cycle) and Analysis of R1233zd-E as a Drop-in Replacement for R245fa for Low Temperature Heat Utilization." *Energy* 103 (May):660–71. doi:10.1016/j.energy.2016.03.034.
- Fewster, Jonathan. 1976. "Mixed Forced and Free Convective Heat Transfer to Supercritical Pressure Fluids Flowing in Vertical Pipes." Ph.D., The University of Manchester. <http://ethos.bl.uk/OrderDetails.do?uin=uk.bl.ethos.524682>.
- Fisher, R. A. 1925. *Statistical Methods For Research Workers*. Edinburgh: Olivier & Boyd.
- Forman, Clemens, Ibrahim Kolawole Muritala, Robert Pardemann, and Bernd Meyer. 2016. "Estimating the Global Waste Heat Potential." *Renewable and Sustainable Energy Reviews* 57 (May):1568–79. doi:10.1016/j.rser.2015.12.192.

- Fu, Ben-Ran, Sung-Wei Hsu, and Chih-His Liu. 2014. "Trends in Patent Applications Relating to Organic Rankine Cycle." *Procedia Engineering* 79:249–57. doi:10.1016/j.proeng.2014.06.339.
- Galindo, J., S. Ruiz, V. Dolz, L. Royo-Pascual, R. Haller, B. Nicolas, and Y. Glavatskaya. 2015. "Experimental and Thermodynamic Analysis of a Bottoming Organic Rankine Cycle (ORC) of Gasoline Engine Using Swash-Plate Expander." *Energy Conversion and Management* 103 (October):519–32. doi:10.1016/j.enconman.2015.06.085.
- Gao, P., L.W. Wang, R.Z. Wang, L. Jiang, and Z.S. Zhou. 2015. "Experimental Investigation on a Small Pumpless ORC (organic Rankine Cycle) System Driven by the Low Temperature Heat Source." *Energy* 91 (November):324–33. doi:10.1016/j.energy.2015.08.076.
- Gibbs, Josiah Willard. 1873. *A Method of Geometrical Representation of the Thermodynamic Properties of Substances by Means of Surfaces*. Vol. 2. Transactions of the Connecticut Academy of Arts and Sciences.
- Gnielinski, V. 1976. "New Equations for Heat and Mass Transfer in the Turbulent Flow in Pipes and Channels." *International Chemical Engineering* 16:359–68.
- Godson, Lazarus, B. Raja, D. Mohan Lal, and S. Wongwises. 2010. "Enhancement of Heat Transfer Using nanofluids—An Overview." *Renewable and Sustainable Energy Reviews* 14 (2):629–41. doi:10.1016/j.rser.2009.10.004.
- Grosu, Lavinia, Andreea Marin, Alexandru Dobrovicescu, and Diogo Queiros-Conde. 2016. "Exergy Analysis of a Solar Combined Cycle: Organic Rankine Cycle and Absorption Cooling System." *International Journal of Energy and Environmental Engineering* 7 (4):449–59. doi:10.1007/s40095-015-0168-y.
- Guillaume, Ludovic, Arnaud Legros, Adriano Desideri, and Vincent Lemort. 2016. "Performance of a Radial-Inflow Turbine Integrated in an ORC System and Designed for a WHR on Truck Application: An Experimental Comparison between R245fa and R1233zd." *Applied Energy*, March. doi:10.1016/j.apenergy.2016.03.012.
- Harada, K.J. 2010. "Development of a Small Scale Scroll Expander." Master of Science, Oregon State University. <http://ir.library.oregonstate.edu/jspui/handle/1957/18837>.
- Hsieh, Jui-Ching, Ben-Ran Fu, Ta-Wei Wang, Yi Cheng, Yuh-Ren Lee, and Jen-Chieh Chang. 2017. "Design and Preliminary Results of a 20-kW Transcritical Organic Rankine Cycle with a Screw Expander for Low-Grade Waste Heat Recovery." *Applied Thermal Engineering* 110 (January):1120–27. doi:10.1016/j.applthermaleng.2016.09.047.
- Huang, Dan, Zan Wu, Bengt Sundén, and Wei Li. 2016. "A Brief Review on Convection Heat Transfer of Fluids at Supercritical Pressures in Tubes and the Recent Progress." *Applied Energy* 162 (January):494–505. doi:10.1016/j.apenergy.2015.10.080.
- Hughmark, G. A. 1965. "Holdup and Heat Transfer in Horizontal Slug Gas-Liquid Flow." *Chemical Engineering Science* 20 (12):1007–10. doi:10.1016/0009-2509(65)80101-4.
- Imran, Muhammad, Muhammad Usman, Byung-Sik Park, and Dong-Hyun Lee. 2016. "Volumetric Expanders for Low Grade Heat and Waste Heat Recovery Applications." *Renewable and Sustainable Energy Reviews* 57 (May):1090–1109. doi:10.1016/j.rser.2015.12.139.
- International Electrotechnical Commission. 2010. "IEC 60034-31: Guide for the Selection and Application of Energy Efficient Motors Including Variable-Speed Applications."
- International Energy Agency. 2016a. "Energy Technology Perspectives." www.iea.org/etp2016.
- . 2016b. "International Energy Outlook 2016." <https://www.eia.gov/outlooks/ieo/world.cfm>.
- . 2017. "Spot Prices for Crude Oil and Petroleum Products."
- Jackson, J. D. 2002. "Consideration of the Heat Transfer Properties of Supercritical Pressure Water in Connection with the Cooling of Advanced Nuclear Reactors." http://inis.iaea.org/Search/search.aspx?orig_q=RN:34084057.
- Jackson, J.D., and W.B. Hall. 1979. "Influences of Buoyancy on Heat Transfer to Fluids Flowing in Vertical Tubes under Turbulent Conditions." *In Turbulent Forced Convection in Channels and Bundles, Hemisphere* 2:613–40.
- Johnston, D. Nigel. 1991. "Numerical Modelling of Reciprocating Pumps with Self-Acting Valves." *Proceedings of the Institution of Mechanical Engineers, Part I: Journal of Systems and Control Engineering* 205 (2):87–96.
- Jung, Hyung-Chul, Leighton Taylor, and Susan Krumdieck. 2015. "An Experimental and Modelling Study of a 1 kW Organic Rankine Cycle Unit with Mixture Working Fluid." *Energy* 81 (March):601–14. doi:10.1016/j.energy.2015.01.003.
- Kane, M, D Larrain, D Favrat, and Y Allani. 2003. "Small Hybrid Solar Power System." *Energy* 28 (14):1427–43. doi:10.1016/S0360-5442(03)00127-0.
- Kari, Ranta. 2009. "AC Drive Comes with Losses - Technical Description." ABB Drives.
- Kim, Minsung, Seok Ho Yoon, Piotr A. Domanski, and W. Vance Payne. 2008. "Design of a Steady-State Detector for Fault Detection and Diagnosis of a Residential Air Conditioner." *International Journal of Refrigeration* 31 (5):790–99. doi:10.1016/j.ijrefrig.2007.11.008.
- Klein, S.A. 2015. "Engineering Equation Solver (EES)." F-Chart Software.
- Kosmadakis, George, Arnaud Landelle, Marija Lazova, Dimitris Manolakos, Alihan Kaya, Henk Huisseune, Christos-Spyridon Karavas, et al. 2016. "Experimental Testing of a Low-Temperature Organic Rankine Cycle (ORC) Engine Coupled with Concentrating PV/thermal Collectors: Laboratory and Field Tests." *Energy* 117 (December):222–36. doi:10.1016/j.energy.2016.10.047.

References

- Krasnoshchekov, E., V. Protopopov, F. Van, and I. Kuraeva. 1967. "Experimental Investigation of Heat Transfer for Carbon Dioxide in the Supercritical Region." In *Gazley Jr., C., Harnett, J., Ecker, E. (Eds.), Proc. 2nd All-Soviet Union Conf. on Heat and Mass Transfer. Minsk, Belarus, May 1964*, 1:26–35. Rand Report R-451-PR.
- Krebs, Eugen, Thomas Streule, and Manuel Jung. 2011. Internal combustion engine has cooling circuit and Clausius-Rankine cycle for waste heat recovery, where Clausius-Rankine cycle is connected with cooling circuit in heat transmitting manner by heat exchanger device. DE102009050068, issued April 21, 2011.
- Landelle, Arnaud, and Nicolas Tauveron. 2016. "Experimental ORC Database - v2016.12." Repository. Zenodo.org. December 2016. doi:10.5281/zenodo.218252.
- Landelle, Arnaud, Nicolas Tauveron, Philippe Haberschill, Rémi Revellin, and Stéphane Colasson. 2017. "Organic Rankine Cycle Design and Performance Comparison Based on Experimental Database." *Applied Energy*. doi:10.1016/j.apenergy.2017.04.012.
- Larjola, J. 1995. "Electricity from Industrial Waste Heat Using High-Speed Organic Rankine Cycle (ORC)." *International Journal of Production Economics*, Proceedings of the 12th International Conference on Production Research, 41 (1–3):227–35. doi:10.1016/0925-5273(94)00098-0.
- Lawrence Livermore National Laboratory. 2007. *Estimated International Energy Flows*.
- Layssac, Thibaut, Claudia Capo, Stéphane Lips, Alfonso William Mauro, and Rémi Revellin. 2017. "Prediction of Symmetry during Intermittent and Annular Horizontal Two-Phase Flows." *International Journal of Multiphase Flow* 95 (October):91–100. doi:10.1016/j.ijmultiphaseflow.2017.05.010.
- Lazova, Marija, Henk Huisseune, Alihan Kaya, Steven Lecompte, George Kosmadakis, and Michel De Paepe. 2016. "Performance Evaluation of a Helical Coil Heat Exchanger Working under Supercritical Conditions in a Solar Organic Rankine Cycle Installation." *Energies* 9 (6):432. doi:10.3390/en9060432.
- Lecompte, Steven, Henk Huisseune, Martijn van den Broek, Bruno Vanslambrouck, and Michel De Paepe. 2015. "Review of Organic Rankine Cycle (ORC) Architectures for Waste Heat Recovery." *Renewable and Sustainable Energy Reviews* 47 (July):448–61. doi:10.1016/j.rser.2015.03.089.
- Lemort, Vincent, Sylvain Quoilin, Cristian Cuevas, and Jean Lebrun. 2009. "Testing and Modeling a Scroll Expander Integrated into an Organic Rankine Cycle." *Applied Thermal Engineering* 29 (14-15):3094–3102. doi:10.1016/j.applthermaleng.2009.04.013.
- Leontaritis, Aris-Dimitrios, Platon Pallis, Sotirios Karellas, Aikaterini Papastergiou, Nikolaos Antoniou, Panagiotis Vourliotis, Nikolaos Matthaios Kakalis, and George Dimopoulos. 2015. "Experimental Study on a Low Temperature ORC Unit for Onboard Waste Heat Recovery from Marine Diesel Engines." In *ASME-ORC*. Brussels. www.asme-orc2015.be/online/proceedings/display_manuscript/55.htm.
- Liao, S. M., and T. S. Zhao. 2002. "An Experimental Investigation of Convection Heat Transfer to Supercritical Carbon Dioxide in Miniature Tubes." *International Journal of Heat and Mass Transfer* 45 (25):5025–34. doi:10.1016/S0017-9310(02)00206-5.
- Li, Tailu, Jialing Zhu, Wencheng Fu, and Kaiyong Hu. 2015. "Experimental Comparison of R245fa and R245fa/R601a for Organic Rankine Cycle Using Scroll Expander." *International Journal of Energy Research* 39 (2):202–14. doi:10.1002/er.3228.
- Li, Yunhua, Mingsheng Liu, Josephine Lau, and Bei Zhang. 2015. "A Novel Method to Determine the Motor Efficiency under Variable Speed Operations and Partial Load Conditions." *Applied Energy* 144 (April):234–40. doi:10.1016/j.apenergy.2015.01.064.
- Lockhart, RW, and RC Martinelli. 1949. "Proposed Correlation of Data for Isothermal Two-Phase, Two-Component Flow in Pipes." *Chem. Eng. Prog* 45 (1):39–48.
- Lutz, Rainer, Giovanna Motisi, and Richard Bruemmer. 2015. Device and method for recovering waste heat energy and a utility vehicle. DE102014223626, issued May 21, 2015.
- Mago, P. J., K. K. Srinivasan, L. M. Chamra, and C. Somayaji. 2008. "An Examination of Exergy Destruction in Organic Rankine Cycles." *International Journal of Energy Research* 32 (10):926–38. doi:10.1002/er.1406.
- Maizza, V., and A. Maizza. 2001. "Unconventional Working Fluids in Organic Rankine-Cycles for Waste Energy Recovery Systems." *Applied Thermal Engineering* 21 (3):381–90. doi:10.1016/S1359-4311(00)00044-2.
- Manolacos, D., G. Papadakis, S. Kyritsis, and K. Bouzianas. 2007. "Experimental Evaluation of an Autonomous Low-Temperature Solar Rankine Cycle System for Reverse Osmosis Desalination." *Desalination, EuroMed 2006 Conference on Desalination Strategies in South Mediterranean Countries*, 203 (1–3):366–74. doi:10.1016/j.desal.2006.04.018.
- Marmolejo-Correa, Danahe, and Truls Gundersen. 2012. "A Comparison of Exergy Efficiency Definitions with Focus on Low Temperature Processes." *Energy* 44 (1):477–89. doi:10.1016/j.energy.2012.06.001.
- Miao, Zheng, Jinliang Xu, Xufei Yang, and Jinghuang Zou. 2015. "Operation and Performance of a Low Temperature Organic Rankine Cycle." *Applied Thermal Engineering* 75 (January):1065–75. doi:10.1016/j.applthermaleng.2014.10.065.

- Miller, John E. 1995. *The Reciprocating Pump Theory, Design, And Use*. 2nd Edition. Krieger Publishing Co. <http://fr.scribd.com/doc/190770608/The-Reciprocating-Pump-Theory-Design-And-Use-John-E-Miller-2nd-Edition#scribd>.
- Molés, Francisco, Joaquín Navarro-Esbri, Bernardo Peris, and Adrián Mota-Babiloni. 2016. “Experimental Evaluation of HCFO-1233zd-E as HFC-245fa Replacement in an Organic Rankine Cycle System for Low Temperature Heat Sources.” *Applied Thermal Engineering* 98 (April):954–61. doi:10.1016/j.applthermaleng.2016.01.011.
- Petukhov, B. S. 1970. “Heat Transfer and Friction in Turbulent Pipe Flow with Variable Physical Properties.” *Advances in Heat Transfer* 6 (January):503–64. doi:10.1016/S0065-2717(08)70153-9.
- Poggi, F., H. Macchi-Tejeda, D. Leducq, and A. Bontemps. 2008. “Refrigerant Charge in Refrigerating Systems and Strategies of Charge Reduction.” *International Journal of Refrigeration* 31 (3):353–70. doi:10.1016/j.ijrefrig.2007.05.014.
- Popular Mechanics. 1930. *Power from the Sea*. Hearst Magazines.
- Premoli, A, D Francesco, and A Prina. 1970. “An Empirical Correlation for Evaluating Two-Phase Mixture Density under Adiabatic Conditions.” In *European Two-Phase Flow Group Meeting, Milan, Italy*, 51.
- Pytilinski, J. T. 1978. “Solar Energy Installations for Pumping Irrigation Water.” *Solar Energy* 21 (4):255–62. doi:10.1016/0038-092X(78)90001-4.
- Quoilin, S. 2007. “Experimental Study and Modeling of a Low Temperature Rankine Cycle for Small Scale Cogeneration .” Electro-Mechanical Engineer, Faculty of Applied Sciences - Thermodynamics Laboratory: University of Liege.
- Quoilin, Sylvain, Martijn Van Den Broek, Sébastien Declaye, Pierre Dewallef, and Vincent Lemort. 2013. “Techno-Economic Survey of Organic Rankine Cycle (ORC) Systems.” *Renewable and Sustainable Energy Reviews* 22 (June):168–86. doi:10.1016/j.rser.2013.01.028.
- Quoilin, Sylvain, Sébastien Declaye, Arnaud Legros, Ludovic Guillaume, and Vincent Lemort. 2012. “Working Fluid Selection and Operating Maps for Organic Rankine Cycle Expansion Machines.” In *International Compressor Engineering Conference*, 1546. Perdue. doi:http://orbi.ulg.ac.be/handle/2268/128663.
- Quoilin, Sylvain, Sébastien Declaye, Bertrand F. Tchanche, and Vincent Lemort. 2011. “Thermo-Economic Optimization of Waste Heat Recovery Organic Rankine Cycles.” *Applied Thermal Engineering* 31 (14–15):2885–93. doi:10.1016/j.applthermaleng.2011.05.014.
- Quoilin, Sylvain, Adriano Desideri, Jorrit Wronski, Ian Bell, and Vincent Lemort. 2014. “ThermoCycle: A Modelica Library for the Simulation of Thermodynamic Systems.” <http://orbi.ulg.ac.be/handle/2268/162325>.
- Quoilin, Sylvain, Vincent Lemort, and Jean Lebrun. 2010. “Experimental Study and Modeling of an Organic Rankine Cycle Using Scroll Expander.” *Applied Energy* 87 (4):1260–68. doi:10.1016/j.apenergy.2009.06.026.
- Quoilin, Sylvain, Matthew Orosz, and Vincent Lemort. 2008. “Modeling and Experimental Investigation of an Organic Rankine Cycle Using Scroll Expander for Small Scale Solar Applications.” In *International Conference on Solar Heating, Cooling, and Buildings*. Lisbon. doi:http://orbi.ulg.ac.be/handle/2268/1298.
- Rant, Zoran. 1956. “Exergie, Ein Neues Wort Fur ‘Technische Arbeitsfähigkeit.’” *Forschung Auf Dem Gebiete Des Ingenieurwesens* 22:36–37.
- Richardson, E.S. 2016. “Thermodynamic Performance of New Thermofluidic Feed Pumps for Organic Rankine Cycle Applications.” *Applied Energy* 161 (January):75–84. doi:10.1016/j.apenergy.2015.10.004.
- Saitoh, Takeo S., Noboru Yamada, and Shinichiro Wakashima. 2005. “Study of Solar Organic Rankine Cycle System Using Scroll Expander.” In *Transactions of the Japan Society of Mechanical Engineers Series C*, 71(703):986–92. doi:10.1299/kikaib.71.986.
- Schuster, a., S. Karellas, and R. Aumann. 2010. “Efficiency Optimization Potential in Supercritical Organic Rankine Cycles.” *Energy* 35 (2):1033–39. doi:10.1016/j.energy.2009.06.019.
- Shen, Zhi, Dong Yang, Haiyan Xie, Xin Nie, Wanyu Liu, and Siyang Wang. 2016. “Flow and Heat Transfer Characteristics of High-Pressure Water Flowing in a Vertical Upward Smooth Tube at Low Mass Flux Conditions.” *Applied Thermal Engineering* 102 (June):391–401. doi:10.1016/j.applthermaleng.2016.03.150.
- Sieder, E. N., and G. E. Tate. 1936. “Heat Transfer and Pressure Drop of Liquids in Tubes.” *Industrial & Engineering Chemistry* 28 (12):1429–35. doi:10.1021/ie50324a027.
- Smague, Pascal. 2015. Dispositif de contrôle d’un circuit fermé fonctionnant selon un cycle de Rankine et procédé utilisant un tel dispositif. EP2933444, issued October 21, 2015.
- Song, Panpan, Mingshan Wei, Lei Shi, Syed Noman Danish, and Chaochen Ma. 2015. “A Review of Scroll Expanders for Organic Rankine Cycle Systems.” *Applied Thermal Engineering* 75 (January):54–64. doi:10.1016/j.applthermaleng.2014.05.094.
- Spearman, C. 1904. “The Proof and Measurement of Association between Two Things.” *The American Journal of Psychology* 15 (1):72–101. doi:10.2307/1412159.
- Tackett, H.H., J.A. Cripe, and G. Dyson. 2008. “Positive Displacement Reciprocating Pump Fundamentals - Power and Direct Acting Types.”

References

- Tartière, Thomas. n.d. "World Overview of the Organic Rankine Cycle Technology." ORC World Map. Accessed March 22, 2017. <http://orc-world-map.org/>.
- Tartière, Thomas, and Marco Astolfi. 2017. "A World Overview of the Organic Rankine Cycle Market." In *IV International Seminar on ORC Power Systems*. Milano.
- Tauveron, Nicolas, Stéphane Colasson, Jérôme Bentivoglio, Arnaud Landelle, and Tommy Aime. 2014. "Rapport Final Projet SSORC." Rapport technique DTBH/DL/2014-158. CEA LITEN.
- Tauveron, Nicolas, Stéphane Colasson, and J.-A. Gruss. 2015. "Conversion of Waste Heat to Electricity: Cartography of Possible Cycles due to Hot Source Characteristics." In *Proceedings of ECOS 2015*. Pau.
- Taylor, Barry N., and Chris E. Kuyatt. 1994. *Guidelines for Evaluating and Expressing the Uncertainty of NIST Measurement Results*. National Institute of Standards and Technology Technical Note 1297. www.nist.gov/document/tn1297spdf.
- Toffolo, Andrea, Andrea Lazzaretto, Giovanni Manente, and Marco Paci. 2014. "A Multi-Criteria Approach for the Optimal Selection of Working Fluid and Design Parameters in Organic Rankine Cycle Systems." *Applied Energy* 121 (May):219–32. doi:10.1016/j.apenergy.2014.01.089.
- Triché, Delphine, Sylvain Bonnot, Maxime Perier-Muzet, François Boudéhenn, Hélène Demasles, and Nadia Caney. 2017. "Experimental and Numerical Study of a Falling Film Absorber in an Ammonia-Water Absorption Chiller." *International Journal of Heat and Mass Transfer* 111 (August):374–85. doi:10.1016/j.ijheatmasstransfer.2017.04.008.
- Tsatsaronis, George. 2007. "Definitions and Nomenclature in Exergy Analysis and Exergoeconomics." *Energy*, ECOS 05. 18th International Conference on Efficiency, Cost, Optimization, Simulation, and Environmental Impact of Energy Systems ECOS 05, 32 (4):249–53. doi:10.1016/j.energy.2006.07.002.
- Turunen-Saaresti, Teemu, Jin Tang, Jos van Buijtenen, and Jaakko Larjola. 2006. "Experimental and Numerical Study of Real-Gas Flow in a Supersonic ORC Turbine Nozzle," January, 1527–33. doi:10.1115/GT2006-91118.
- United Nations Department of Economic and Social Affairs, Population Division. 2015. "World Population Prospects: The 2015 Revision." <https://esa.un.org/unpd/wpp/Download/Standard/Population/>.
- Wang, Yuping, Xing Liu, Xiaoyi Ding, and Yiwu Weng. 2016. "Experimental Investigation on the Performance of ORC Power System Using Zeotropic Mixture R601a/R600a: ORC Power System Using R601a/R600a." *International Journal of Energy Research*. doi:10.1002/er.3664.
- Woldesemayat, Melkamu A., and Afshin J. Ghajar. 2007. "Comparison of Void Fraction Correlations for Different Flow Patterns in Horizontal and Upward Inclined Pipes." *International Journal of Multiphase Flow* 33 (4):347–70. doi:10.1016/j.ijmultiphaseflow.2006.09.004.
- Woudstra, Nico. 2004. "Value Diagrams and Exergy Efficiencies."
- Woudstra, Nico, Theo Woudstra, Armando Pirone, and Teus van der Stelt. 2010. "Thermodynamic Evaluation of Combined Cycle Plants." *Energy Conversion and Management* 51 (5):1099–1110. doi:10.1016/j.enconman.2009.12.016.
- Xu, R.-J., H. Xi, and Y.-L. He. 2013. "Experimental study on the performance of the organic rankine cycles with and without internal heat regeneration." *Kung Cheng Je Wu Li Hsueh Pao/Journal of Engineering Thermophysics* 34 (2):205–10.
- Yamada, Noboru, Masataka Watanabe, and Akira Hoshi. 2013. "Experiment on Pumpless Rankine-Type Cycle with Scroll Expander." *Energy* 49 (January):137–45. doi:10.1016/j.energy.2012.10.027.
- Yang, Xufei, Jinliang Xu, Zheng Miao, Jinghuang Zou, and Chao Yu. 2015. "Operation of an Organic Rankine Cycle Dependent on Pumping Flow Rates and Expander Torques." *Energy*. doi:10.1016/j.energy.2015.07.121.
- Yekoladio, P. J., T. Bello-Ochende, and J. P. Meyer. 2015. "Thermodynamic Analysis and Performance Optimization of Organic Rankine Cycles for the Conversion of Low-to-Moderate Grade Geothermal Heat." *International Journal of Energy Research* 39 (9):1256–71. doi:10.1002/er.3326.
- Zabek, Daniel, John Penton, and David Reay. 2013. "Optimization of Waste Heat Utilization in Oil Field Development Employing a Transcritical Organic Rankine Cycle (ORC) for Electricity Generation." *Applied Thermal Engineering* 59 (1-2):363–69. doi:10.1016/j.applthermaleng.2013.06.001.
- Zanelli, Robert, and Daniel Favrat. 1994. "Experimental Investigation of a Hermetic Scroll Expander-Generator." In *International Compressor Engineering Conference*, 1021. Perdue. doi:<http://docs.lib.purdue.edu/icec/1021>.
- Zhang, Siyu, Hanyang Gu, Xu Cheng, and Zhenqin Xiong. 2014. "Experimental Study on Heat Transfer of Supercritical Freon Flowing Upward in a Circular Tube." *Nuclear Engineering and Design* 280 (December):305–15. doi:10.1016/j.nucengdes.2014.09.017.
- Ziviani, Davide, Asfaw Beyene, and Mauro Venturini. 2014. "Advances and Challenges in ORC Systems Modeling for Low Grade Thermal Energy Recovery." *Applied Energy* 121 (May):79–95. doi:10.1016/j.apenergy.2014.01.074.
- Ziviani, Davide, Brandon J. Woodland, Emeline Georges, Eckhard A. Groll, James E. Braun, W. Travis Horton, Martijn van den Broek, and Michel De Paepe. 2016. "Development and a Validation of a Charge Sensitive Organic Rankine Cycle (ORC) Simulation Tool." *Energies* 9 (6):389. doi:10.3390/en9060389.
- Zivi, S. M. 1964. "Estimation of Steady-State Steam Void-Fraction by Means of the Principle of Minimum Entropy Production." *Journal of Heat Transfer* 86 (2):247–51. doi:10.1115/1.3687113.

Appendixes

Appendix A: Database complete layout description

Section	Sub section	Parameter name	Parameter Description
Main Database Sheet			
Paper ID		Name	First author name
		Year	Publication year
		Link	DOI or URL
		Title	Paper title
		N°	Paper unique identifier
ORC ID		N°	ORC unit unique identifier
		Flu	Unit fluid ID
		Exp.	Unit expander ID
		HS	Unit hot source ID
Filter		Paper	Paper duplicate filter
		Unit	Unit duplicate filter
		Fluid	Fluid duplicate filter
		Expander	Expander duplicate filter
		Hot-Source	Hot Source duplicate filter
		U/F	Unit & Fluid duplicate filter
		U/E	Unit & Expander duplicate filter
		U/HS	Unit & Hot Source duplicate filter
		U/F/E	Unit & Fluid & Expander duplicate filter
General Info.		Year	Year of publication
		Country	Country of the unit (first author)
		Univ.	Institution of the first author
		Targeted	Aimed application - if specified
		Specificity	Specific application or configuration (if any)
		CHP	If dedicated to Combine Heat & Power
Working Fluid		Flu/Name	Working fluid name
		Flu/Cat	Working fluid category
		Flu/Transcritical	If operates in critical conditions
		Flu/Tcrit	Critical temperature [°C]
		Flu/Perit	Critical pressure [bar]
		Flu/Ksi	Saturation slope (see Fluid Listing Sheet) [kJ/kg]
		Flu/Type	Type of fluid (dry / isentropic / wet / zeotropic)

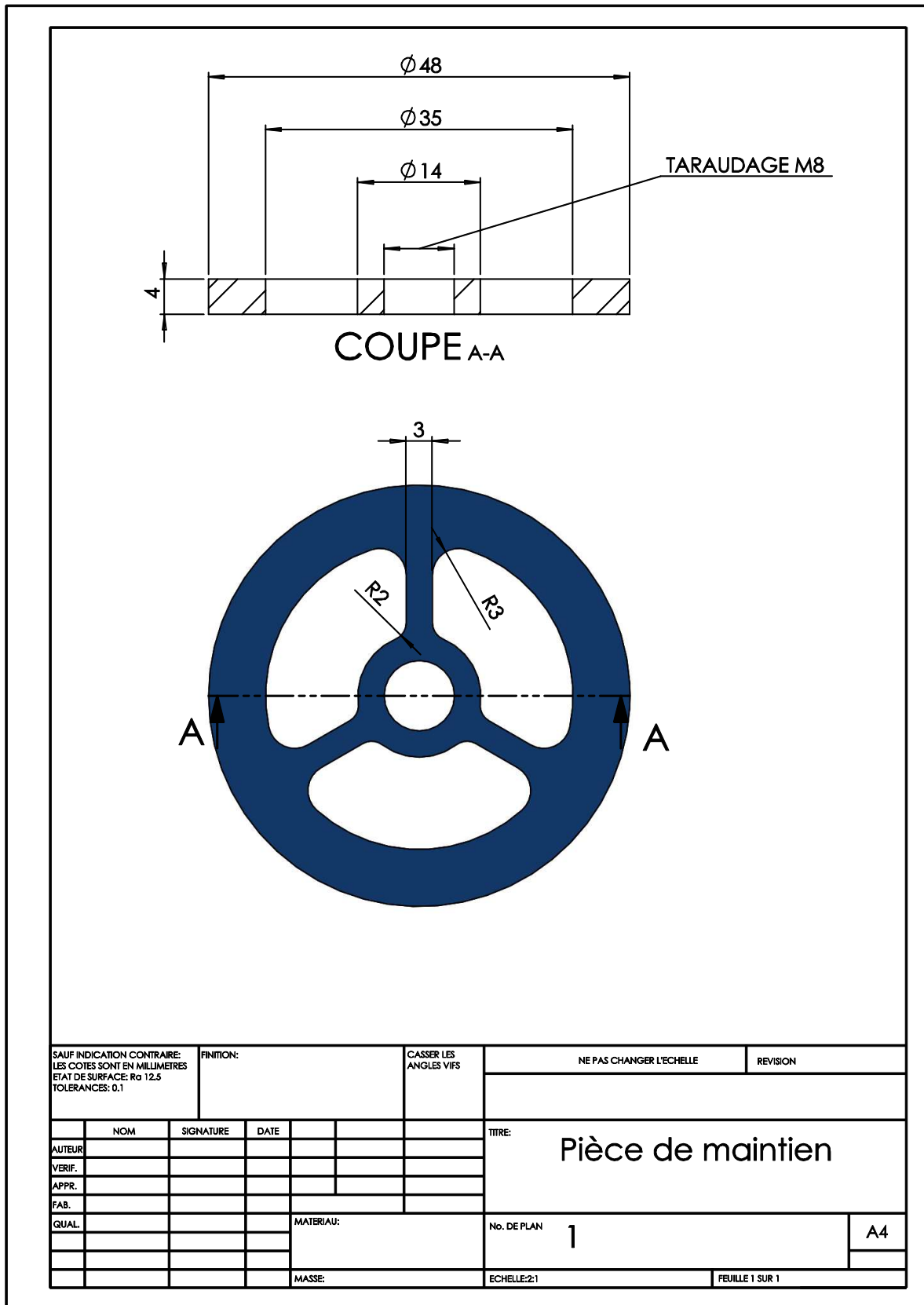
Working Fluid Conditions	Tmax °C	Cycle/Th - Cycle/Th +	Expander inlet / Evaporator outlet temperature [°C]
	Superheating °C	Cycle/Supheat - Cycle/Supheat +	Expander inlet superheating [°C]
	Tmin °C	Cycle/Tl - Cycle/Tl +	Condenser outlet / Pump inlet temperature [°C]
	Subcooling °C	Cycle/Subcool - Cycle/Subcool +	Pump inlet subcooling [°C]
	HP bar	Cycle/HP - Cycle/HP +	High Pressure [bar]
	LP bar	Cycle/LP - Cycle/LP +	Low Pressure [bar]
Heat Source	Temperature (°C)	HS/Origin HS/T - HS/T +	Primary heating energy source Hot fluid temperature (at evaporator inlet) [°C]
	Power (kW)	HS/Pth - HS/Pth +	Heat power [kWth]
	Flowrate (kg/s)	HS/Flow - HS/Flow +	Hot fluid flow rate [kg/s]
		HS/Fluid	Hot fluid type
Cold Source	Temperature (°C)	CS/Origin CS/T - CS/T +	Cooling energy source Cold fluid temperature [°C]
	Power (kW)	CS/Pth - CS/Pth +	Cooling power [kWth]
	Flowrate (kg/s)	CS/Flow - CS/Flow +	Cold fluid flow rate [kg/s]
		CS/Fluid	Cold fluid type
ORC Power & Efficiency	Net Power (kW)	Cycle/Pnet - Cycle/Pnet +	ORC net power output [kW]
		Cycle/Pnet def	Definition of the power output
	Eta Th Cycle	Cycle/e1 - Cycle/e1 +	ORC energetic efficiency
		Cycle/e1 def	Definition of the energetic efficiency
	Eff Exergetic	Cycle/e2 - Cycle/e2 +	ORC exergetic efficiency
		Cycle/e2 def	Definition of the exergetic efficiency
	ORC Efficiency	Cycle/Eff.Gross.Mech	ORC gross mechanical efficiency (m/s or m/f)
		Cycle/Eff.Gross.Elec	ORC gross electrical efficiency (e/s or e/f)
Cycle/Eff.Net.Elec		ORC net electrical efficiency (e-e/s or e-e/f)	
	Cycle/Eff.Carnot	ORC carnot efficiency (based on heat & cold temp.)	

Pump	Pump/Type	Technology	
	Pump/Driver	Driving mechanism	
	Pump/Control	Flow control	
	Pump/Name	Commercial name	
	Pump/ Nom Pel	Nominal power [kW]	
	Flow Rate (kg/s)	Pump/Flow -	Working fluid flow rate [kg/s]
		Pump/Flow +	
	Power	Pump/Speed	Maximum shaft speed [rpm]
		Pump/Pel -	Electric power [kW]
		Pump/Pel +	
Pump/Pad		Adiabatic power [kW]	
Efficiency	Pump/Phy	Hydraulic power [kW]	
	Pump/Eff.el	Electrical efficiency (Phy/Pel)	
	Pump/Eff.is	Isentropic efficiency (Phy/Pad)	
	Pump/Comments	Other comments about the pump	
Evaporator	Eva/Type	Technology	
	Eva/Name	Commercial name	
	Eva/Area	Heat exchange area [m ²]	
	Eva/Other Carac	Other geometrical data	
	Efficiency	Eva/Eff	Heat exchanger efficiency
		Eva/dP	Pressure drop (mbar)
Expander	Exp/Type	Technology	
	Exp/Generator	Generator technology	
	Exp/Control	Expander control	
	Exp/Name	Commercial name	
	Nominal Power	Exp/Nom Pel	Nominal electric power [kW]
		Exp/Nom Pm	Nominal mechanical power [kW]
	Swept Volume	Exp/BVR	Built-in Volume Ratio (if any)
		Exp/Vol Comp	Suction volume in compressor mode [cm ³]
		Exp/Vol Exp.	Suction volume in expander mode [cm ³]
	Shaft Speed	Exp/Speed -	Shaft rotational speed [rpm]
		Exp/Speed p	
	Pressure Ratio	Exp/PR -	Pressure ratio
		Exp/PR +	
	Power	Exp/Pel -	Electric power [kW]
		Exp/Pel +	
		Exp/Pme -	Mechanic power [kW]
		Exp/Pme +	
		Exp/Pad -	Adiabatic power [kW]
Exp/Pad p			
Exp/Pel.Cor		Estimated electric power [kW]	
Exp/Pscale		Expander power scale [kW]	

Efficiency	Exp/Eff.el -	Electrical efficiency (Pel/Pis)
	Exp/Eff.el +	
	Exp/Eff.me -	Mechanical efficiency (Pme/Pis)
	Exp/Eff.me +	
	Exp/Eff.is -	Isentropic efficiency (Pad/Pis)
	Exp/Eff.is +	
	Exp/Eff.ad.hermetic -	Adiabatic efficiency for hermetic expander (Pel/Pad)
	Exp/Eff.ad.hermetic +	
	Exp/Eff.ad.open -	Adiabatic eff. for non-hermetic expander (Pme/Pad)
	Exp/Eff.ad.open +	
Exp/e gen -	Generator efficiency (Pel/Pme)	
Exp/e gen +		
Gen.Eff.Correl	Generator efficiency from empirical correlation	
FF -	Filling Factor ($V_{real} / V_{theoretical}$)	
FF +		
	Exp/Comments	Other comments about the expander
Condenser	Cond/Type	Technology
	Cond/Name	Commercial name
	Cond/Area	Heat exchange area [m ²]
	Cond/Other Carac.	Other geometrical data
	Cond/Eff	Heat exchanger efficiency
	Cond/dP	Pressure drop (mbar)
Lubrication	Oil/Separator	Oil and working fluid separator (at exp outlet)
	Oil/Pump	Lubrication oil pump
	Oil/Tank	Oil tank
	Oil/Cooler	Oil cooler
	Oil/Filter	Oil filter
	Oil/ExpInjection	Lubrication injection methods
	Oil/Mix	Lubrication methods
	Oil/Comments	Other comments about lubrication
Regen.	IHE/Type	Technology
	IHE/Name	Commercial name
	IHE/Eff	Heat exchanger efficiency
Additional Components	Add/Other	Other components added to the cycle
	Add/Subcooler	Subcooler (in addition of the condenser)
	Add/PrefeedPump	Pre-feed pump prior to the main pump
	Add/Bumper	Pulsation damper (at pump outlet)
	Add/Filter	Filter for working fluid
	Add/Vapor Tank Sep	Tank or vapor separator at evaporator outlet
	Add/Liquid Tank	Working fluid tank at condenser outlet

Operating Point Sheet		
Point ID	N°	Operating point unique identifier
	Type	Type of operating point
	Type of Target	Type of target application (open/closed)
Efficiencies	En. Closed	ORC thermal efficiency
	Ex. Closed	ORC second law efficiency
	En. Open	ORC recovery efficiency
	Ex. Open	ORC exergetic recovery efficiency
Heat Source	$T_{hot,in}$	Hot fluid evaporator inlet temperature [°C]
	$T_{hot,out}$	Hot fluid evaporator outlet temperature [°C]
	m_{hot}	Hot fluid flow rate [kg/s]
	Q_{hot}	Heat power [kWth]
	$type$	Hot fluid type
Cold Source	$T_{sink,in}$	Cold fluid temperature [°C]
	$T_{sink,out}$	Cold fluid outlet temperature [°C]
	m_{sink}	Cold fluid flow rate [kg/s]
	Q_{sink}	Cooling power [kWth]
	Type	Cold fluid type
Working Fluid	$T_{exp,in}$	Expander inlet temperature [°C]
	$T_{exp,out}$	Expander outlet temperature [°C]
	$T_{cond,out}$	Condenser outlet / Pump inlet temperature [°C]
	HP	High Pressure [bar]
	LP	Low Pressure [bar]
	m_{fluid}	Working fluid flow rate [kg/s]
	Type	Working fluid name
Expander	Type	Expander technology
	P_{ad}	Adiabatic power [kW]
	P_{mech}	Mechanic power [kW]
	P_{elec}	Electric power [kW]
	Pelec Cor	Estimated electric power [kW]
Pump	P_{hy}	Hydraulic power [kW]
	P_{ad}	Adiabatic power [kW]
	P_{elec}	Electric power [kW]

Appendix B: Retention piece plan

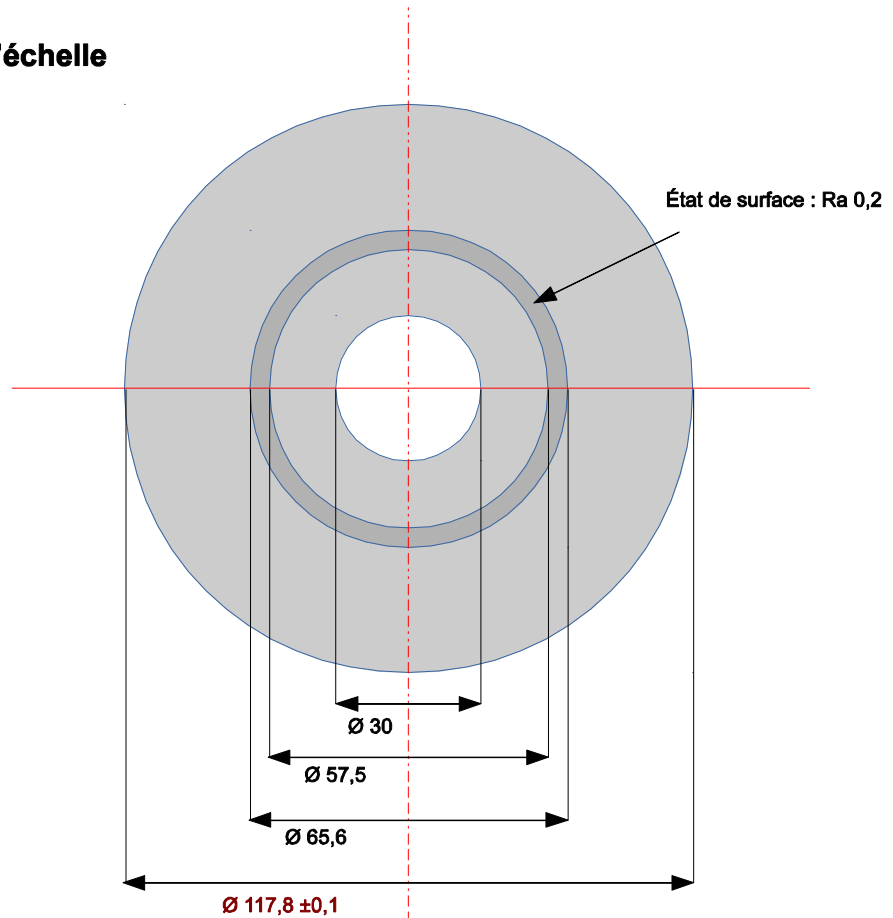


Appendix C: Redesign sealing piston

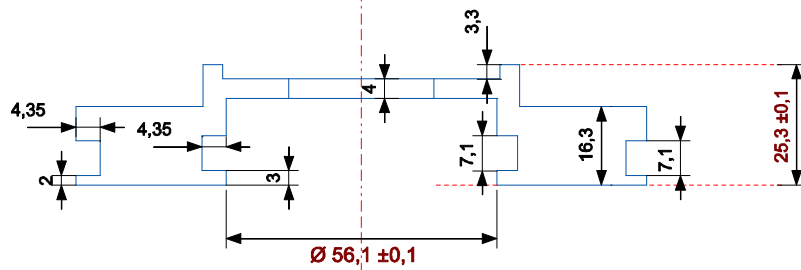
Schéma pas à l'échelle

Matériau : Inox

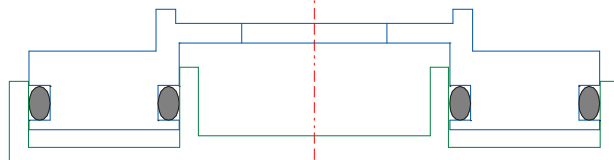
Vue dessus



Vue en coupe



Assemblage





FOLIO ADMINISTRATIF

THESE DE L'UNIVERSITE DE LYON OPEREE AU SEIN DE L'INSA LYON

NOM : LANDELLE

DATE de SOUTENANCE : 12/10/2017

Prénoms : Arnaud

TITRE : Experimental and numerical study of transcritical Organic Rankine Cycles for low-grade heat conversion into electricity from various sources

NATURE : Doctorat

Numéro d'ordre : 2017LYSEI090

Ecole doctorale : ED 162 - Mécanique, Énergétique, Génie Civil, Acoustique

Spécialité : Thermique Énergétique

RESUME : The Organic Rankine Cycle (ORC) is a technology used for low-grade thermal energy conversion into electricity. Transcritical ORC has been identified as a solution for efficient waste heat recovery. However, few experimental tests have been conducted to confirm the interest of transcritical ORC and investigate its operational behaviors. The work presented focuses on the operation and the optimization of subcritical and transcritical Organic Rankine Cycles for low-grade heat conversion into electricity from various heat sources (solar, industrial waste heat).

First, the thermodynamic framework of the ORC technology is presented. Energetic and exergetic performance criteria, appropriate to each type of input source, are introduced and selected. The criteria are later applied to a database of ORC prototypes, in order to objectively analyze the state-of-the-art.

In a second step, the experimental and numerical tools, specifically developed or used in the present thesis, are presented. Three subcritical and transcritical ORC test benches (hosted by CEA and AUA) provided experimental data. Numerical models were developed under different environments: Matlab for steady-state modeling, data processing and energy/exergy analysis. The Modelica/Dymola environment for system dynamics and transient operations.

Lastly, the different tools are exploited to investigate four different topics:

- The ORC pump operation is investigated, both under an energetic and volumetric standpoint, while semi-empirical models and correlations are exposed.
- Supercritical heat transfers are explored. Global and local heat transfer coefficients are estimated and analyzed under supercritical conditions, while literature correlations are introduced for comparison.
- Working fluid charge influence over the ORC performance and behavior is investigated. Optimal fluid charge is estimated under various operating conditions and mechanisms for charge active regulation are exposed.
- ORC system performances and behavior are discussed. Through both an energetic and exergetic standpoint, performance are compared with the state-of-the-art, while optimization opportunities are identified through an exergetic analysis.

MOTS-CLÉS : Organic Rankine Cycle ; Transcritical ; Experiment ; Waste Heat Recovery ; Solar ; Database ; Feed pump ; Heat transfer ; Fluid charge ; Exergy ; Dynamic ;

Laboratoires de recherche :

Laboratoire des Systèmes Thermiques et Thermodynamiques (CEA/DRT/LITEN/DTBH/SBRT/LS2T)
Centre d'Énergétique et de Thermique de Lyon (CETHIL, UMR 5008)

Directeur de thèse: REVELLIN, Rémi – Professeur – INSA-Lyon
TAUVERON, Nicolas – Ingénieur de recherche, HDR – CEA-Liten

Président de jury : LEMORT, Vincent – Professeur – Université de Liège

Composition du jury : GROSU, Lavinia – Maître de Conférence, HDR – Université Paris Nanterre (Rapporteur)
LANZETTA, François – Professeur – Université de Franche-Comté (Rapporteur)
HABERSCHILL, Philippe – Maître de Conférence, HDR – INSA-Lyon (Examineur)